Experimental investigations into mineral-buffered solubility and speciation in supercritical fluids:

The systems SiO_2–H_2O and

Cu–Cu_2O–MgO–SiO_2–HCl–H_2O

by

Alistair Campbell Hack

A thesis submitted for the degree of

Doctor of Philosophy

of The Australian National University

Canberra
August 2003

Declaration

This thesis contains the results of research undertaken at the Research School of Earth Sciences, The Australian National University. Except where acknowledged otherwise, the research and interpretation described in this thesis are my own. No part of this thesis has been submitted to any other University.

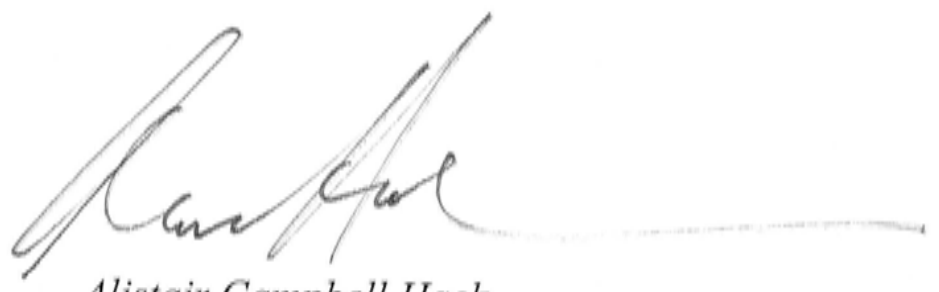

Alistair Campbell Hack

Acknowledgments

I would like to especially thank my supervisor John Mavrogenes for his friendship, infectious enthusiasm, sense of humour and support throughout the course of my studies. Similarly, I am indebted to my friend and co-supervisor Andrew Berry for guidance and assistance.

Special thanks to Bill Hibberson, Dean Scott and Paul Willis for not only sharing their technical expertise but also their virtuous patience, pragmatism, encouragement and friendships which extend beyond the RSES high-pressure laboratory.

Mike Shelley and Charlotte Allen are thanked for instruction, the smooth running of the LA-ICP-MS facility, assistance with analysis-related experiments, and numerous helpful conversations. Mike is also thanked for his interest in the experimental side of this project, particularly in the early stages.

Andrew Christy is thanked for sharing his enthusiasm for minerals and assistance with quench solution analyses. Graeme Mortimer is thanked for assistance with solution preparations.

Numerous discussions, peripheral and otherwise, with Jörg Hermann, Steve Eggins, Hugh O'Neill, Nick Ware and Bob Loucks were constructive and very appreciated. Special thanks to Uli Faul, Richard Arculus, Thomas Ulrich, Dagmar Kelly and the larger RSES Petrochemistry and Experimental Petrology Group and its many visitors. Dave Ellis is thanked for providing access to the Department of Geology hydrothermal cold-seal laboratory. Friendly and constructive discussions with Weihua Liu and D.C. "Bear" McPhail during the later stages of this study were an unexpected source of encouragement for which I am grateful.

Steve Sutton and Matt Newville at the Advanced Photon Source (APS), Chicago, are thanked for their assistance with X-ray absorption experiments. The Assess to Major Research Facilities Program is thanked for providing travel funds to the APS.

Chris Ryan at CSIRO is thanked for assistance with PIXE analyses. Terry Mernagh at Geoscience Australia is thanked for assistance with laser Raman measurements.

Fellow office mates, Stephan Klemme, Jörg, Xi "Louie" Liu, Silvano "Mate" Sommacal, and others, Chuck Magee, Naomi Douglas, Mark "Rootus" Richardson,

Kath Farmer, Linda Glass, Wilfred Lus, Chris Heath and "the Wig" have been integral in making RSES and life so enjoyable. Likewise, thanks to all of my friends; among others, Dan Rayner, Andrew Brown, Roger Biddle, Ash Lester, Andrew McFadzean and especially Linda Devine.

This dissertation was undertaken on award of a J.C. Jaeger Scholarship, RSES.

I acknowledge and am very grateful for the endless encouragement and support of my family.

ABSTRACT

A series of experiments focussing on mineral-buffered solubility and solute speciation in high-pressure and high-temperature supercritical fluids were undertaken. A newly derived technique for synthesising fluid inclusions under mineral-buffered conditions in a piston-cylinder apparatus is described.

The pressure-volume-temperature-composition properties (P–V–T–X) of SiO_2–H_2O fluids were investigated using synthetic quartz-hosted fluid inclusions. Fluid volume measurements were used to constrain activity-composition *(a–X)* relations of SiO_2–H_2O solutions. The data suggest that changes in dissolved silica speciation may not be the only cause of differences between existing quartz and silica-unsaturated mineral solubility datasets up ~ 2.0 GPa, and that the activity of H_2O may also need to be considered explicitly even in dilute solutions (*e.g.* 1–5 mol% dissolved SiO_2) at P above approximately 0.5 GPa.

Aspects of quantitative fluid inclusion analysis by laser ablation inductively coupled plasma mass spectrometry (LA-ICP-MS) and methods for obtaining reliable solubility data from experimentally produced fluid inclusions were critically assessed using synthetic quartz-hosted fluid inclusions. Fluid inclusion analysis by LA-ICP-MS was compared directly with proton induced X-ray emission (PIXE). Fluid inclusion analysis by LA-ICP-MS is shown to be accurate despite having an intrinsic relative precision of approximately ± 50%. This precision is comparable to other quantitative individual inclusion analytical methods (*e.g.* PIXE and synchrotron X-ray fluorescence) though LA-ICP-MS generally has much lower detection limits. The relatively low analytical precision inherent to current fluid inclusion measurement techniques is more than acceptable, however, because mineral solubilities and trace element fluid compositions vary over orders of magnitude. Uniform fluid inclusion compositions in mineral-buffered solubility experiments provide evidence that major element fluid-mineral equilibrium is attained on a time-scale comparable to hydrothermal fracture annealing in quartz. Trace element behaviour appears comparatively sluggish by comparison especially where mineral-fluid exchange involves coupled substitutions or where the trace element is essentially incompatible in the coexisting solid phases.

Mineral-buffered solubility and copper(I) speciation in the quartz-saturated part of the Cu_2O–MgO–SiO_2–HCl–H_2O system was determined using synthetic fluid inclusions. Fluid inclusions were synthesised over a wide range of salinity (0.29–11.3 mol/kg Cl), T (525–850 °C) and P (0.3–1.7 GPa). Quench solution Mg compositions (presumably unmodified by quenching because of low concentrations and known high solubility of $MgCl_2$) were determined by SN-ICP-AES. These independently measured Mg concentrations were used to quantify concentrations from fluid inclusion composition ratios (representative high P–T fluid samples) measured by LA-ICP-MS. Fluid inclusions from numerous experiments were independently analysed by PIXE. X-ray absorption spectroscopy was undertaken to further characterise copper(I) speciation in the supercritical fluids. Solubility data was regressed independently to obtain speciation details and selected thermodynamic parameters.

Solubility of the assemblage native copper-cuprite-quartz-talc (Cu–Cpr–Tc–Qz) increases with salinity at constant T and P (in highest T experiments enstatite (Ens) was stable, so the fluid was buffered by Cu–Cpr–Ens–Qz). Hydroxide copper(I) complexes and polynuclear species are negligible in these fluids and chlorocopper(I) complexes predominate over the entire range of Cl concentration investigated. Similarly, chloromagnesium(II) complexes predominate over all experimental conditions investigated. Fluid Cu/Cl decreases with increasing Cl and T at constant P. Low Cu:Cl (*e.g.* ~ 1:4) suggests chlorocopper(I) complexing is important but cannot be explained by models containing conventional $CuCl_n^{1-n}$ complexes as the formation of $CuCl_n^{1-n}$ complexes with $n >$ ~ 1 results in an apparent net charge imbalance for these experimental fluids, violating the neutrality constraint. Two possible solutions to this problem were identified.

Cu solubilities are consistent with increasingly higher-order, neutral chlorocopper(I) complexes ($CuCl(HCl)^0_{n-1\,(aq)}$) predominating with increasing salinity and T at constant P. A least squares fit to both the Cl and T series solubility data is best satisfied by complexes with up to $n = 4$. For $CuCl^0_{(aq)}$, the complex formation log K value differs up to approximately one log unit from theoretical calculations based on experimental data acquired at much lower T and P; for higher-order complexes no comparisons may be made.

Alternatively, because a–X relations of even simple multi-component supercritical fluids are essentially unknown at high-P, it is equally plausible that $HCl^0_{(aq)}$

becomes disproportionately stable relative to $CuCl^0_{(aq)}$ at high salinities and with increasing T at fixed P. In this case, the experimental data could be fit using a conventional speciation model where activity coefficients (γ_i) for neutral species (i) vary independently, such that $\gamma_{HCl^0_{(aq)}} / \gamma_{CuCl^0_{(aq)}}$ becomes less than unity at high Cl concentrations and with increasing T at constant P.

At 710 °C Cu–Cpr–Tc–Qz solubility in aqueous fluid containing 1 mol/kg Cl increases with P to at least 1.7 GPa. Conspicuously, with increasing P (> ~ 0.5 GPa) Tc solubility increases and molal Cu concentrations exceed those of Cl. The isothermal Cu solubility isopleth parallels that of quartz solubility in the simple SiO_2–H_2O system. Solubility trends suggest that the stability of copper(I) hydroxide complexes (*e.g.* $CuOH^0_{(aq)}$) shifts to higher salinities such that H_2O may become an effective ligand at high-P.

High-T, in situ X-ray absorption near edge structure (XANES) spectroscopy experiments were undertaken on single homogenised synthetic fluid inclusions to further characterise chlorocopper(I) coordination environment in supercritical fluids as a function of salinity, T and mineral-buffer assemblage. Cu K-edge XANES spectra indicate the presence of highly coordinated chlorocopper(I) complexes (*e.g.* Cu:Cl, 1:3–4) predominating at high salinity, whereas lower-order linear Cu–Cl coordination predominates at lower salinities in fluids buffered by native copper-cuprite-talc-quartz. This is consistent with the interpretation of the solubility data. At equivalent salinity, T and P conditions, spectra for fluids buffered by native copper-orthoclase-sillimanite-quartz-magnetite-hematite show no evidence for higher-order chlorocopper(I) complexes. Preliminary extended X-ray absorption fine structure (EXAFS) data for these latter inclusions indicates that $CuCl_2^-$ predominates. The stability of higher-order complexes is strongly coupled to HCl concentrations, which at constant P and T is determined by both the specific mineral assemblage and total salinity.

This is the first spectroscopic evidence for highly coordinated chlorocopper(I) complexes in supercritical fluids and the speciation dependence on the buffering mineral assemblage. Similarly, this is the first experimental confirmation that copper concentrations in mineral-buffered fluids can be extremely high, *e.g.* ~ 10 wt.%, something which until now was only speculated.

The results were applied to mineral transport and deposition in porphyry copper deposits. The general solubility trends are consistent with the observed absence

of hydrothermal Cu deposits above ~ 500 °C and suggest that cooling below ~ 500 °C may be a particularly effective mechanism for precipitating ore metals; noting that many chemical equilibria are in operation and all are irrevocably but independently coupled to T such that considering changes in T alone is likely to be too simplistic for understanding natural phenomenon, but is suggestive of why T should be such a key variable. The predominance of chlorocopper(I) complexing combined with increasing coordination with increasing salinity suggest that fluid mixing between brines and more dilute heated groundwater under mineral-buffered conditions may not be an effective ore deposition mechanism and may even result in under-saturation. This is because mixing under mineral-buffered conditions reduces both the metal and ligand concentrations simultaneously. More generally the results provide insight into hydrous mineral solubilities at high-P and the potential bearing this has on the origin of the subduction zone geochemical signature of arc magmas.

–CONTENTS–

Experimental investigations into mineral-buffered solubility and speciation in supercritical fluids: The systems SiO_2–H_2O and Cu–Cu_2O–MgO–SiO_2–HCl–H_2O

Declaration I

Acknowledgments II

Abstract IV

Contents VIII

Prelude 1

Remarks on the structure of the thesis 2

Part 1

High-pressure and high-temperature fluid inclusion synthesis using a piston-cylinder apparatus and *PVTX* relations in the SiO_2–H_2O system

Abstract 3

1. Introduction 5

2. Experimental method 8

2.1 Capsule and piston-cylinder assembly 8

2.2 Temperature 13

2.3 Pressure 16

2.3.1 Introduction and calibration approach 16

2.3.2 Experimental 20

2.3.3 Low pressure PVT results, 630–800 °C: Sources of error and friction behaviour in a piston-cylinder apparatus 22

3. A note on synthetic fluid inclusions and attainment of fluid-mineral equilibrium in multi-component systems: Major elements 26

4. Insights into the activity-composition relations of the SiO_2–H_2O system at high-pressure from *PVTX* measurements using synthetic quartz-hosted fluid inclusions **29**

4.1 Introduction 29

4.2 Determination of activity-composition relations using *PVT* measurements 35

4.3 Experimental conditions investigated and remarks on the limitations of the technique 36

4.4 Experimental data 39

4.5 Discussion 41

4.5.1 Equation of state of water *41*

4.5.2 Comparison of end-member properties, ideal fluids and measurements - Another look at the data *43*

4.5.3 Partial molar properties of components in SiO_2–H_2O fluids - Implications for silica speciation *46*

4.5.4 Hydrous, silica-poor melts or silica-bearing aqueous fluids? *48*

4.5.5 Implications for fluid inclusion PVT studies *51*

4.5.6 Other evidence for "strange behaviour" in high-pressure mineral-saturated fluids *53*

Part 2

Factors affecting accuracy and precision of the quantitative analysis of individual fluid inclusions by laser ablation inductively coupled plasma mass spectrometry

Abstract **54**

1. Introduction **57**

2. Experimental **59**

2.1 Samples 59

2.1.1 Analogue epoxy- and quartz-hosted aqueous inclusions *59*

2.1.2 Synthetic quartz-hosted fluid inclusions *59*

2.2 Instrument 61

2.2.1 Sample ablation *62*

2.2.2 ICP-MS data collection method *62*

3. LA-ICP-MS data reduction procedure for inclusions **64**

3.1 Host signal correction 64

3.2 Extended ablation: down-hole mass fractionation correction 66

3.3 Some notes on interferences 67

3.3.1 Host-related analytical interferences *67*

3.3.2 Inclusion-related analytical interferences *68*

4. Quantification of element ratios and absolute concentrations in fluid inclusions **69**

5. Results and discussion **71**

5.1 Calibration effects related to using unknowns and reference standards with different physical properties and different compositions 71

5.2 On the limit of signal quantification in LA-ICP-MS fluid inclusion analysis 76

5.3 Surface contamination 78

5.4 The effect of using different ICP-torch types and carrier gas compositions 84

5.5 Effect of different ablation conditions 87

5.6 Ablation behaviour of quartz and its potential bearing on analytical precision 91

5.7 Comparison of synthetic fluid inclusion and quenched solution compositions: another look at the accuracy of LA-ICP-MS measurements 93

5.8 Comparison of LA-ICP-MS and PIXE fluid inclusion analysis techniques 97

5.9 Another note on synthetic fluid inclusions and the attainment of fluid-mineral equilibrium in multi-component systems: Trace elements 99

5.10 A discussion of methods for obtaining absolute concentrations from natural and synthetic fluid inclusions by LA-ICP-MS 101

5.10.1 Natural fluid inclusions *101*

5.10.2 Synthetic fluid inclusions *103*

5.10.3 Independent complementary techniques *104*

5.10.4 An alternative, "internal standard-less" method for quantitative fluid inclusion LA-ICP-MS *104*

Part 3

Copper(I) solubility and speciation in mineral-buffered supercritical fluids: A synthetic fluid inclusion study

Abstract **107**

1. Introduction **110**

1.2 Previous investigations of copper(I)-chloride speciation and solubility 112

1.2.1 Summary *112*

1.2.2 Notes on high-temperature studies *113*

2. Background theory: Solubility, speciation and multi-component solution equilibria **119**

3. Experimental **121**

3.1 Mineral-buffered fluid inclusion synthesis and analysis 121

3.2 Fluid inclusion petrography 124

3.3 Precision and accuracy of the solubility data 126

4. Mineral solubility: Effect of chloride and speciation **127**

4.1 Experimental data 127

4.2 Data Interpretation 130

4.2.1 Calculation of mineral solubility and Cu–Mg–H–Cl speciation *130*

4.2.2 Data regression method *137*

4.2.3 Mg–O–H–Cl speciation: Further discussion of the thermodynamic data required from the literature *138*

4.2.4 Comparison with extrapolations of previous "low-temperature" (< 350 °C) copper(I) species data *141*

4.2.5 Copper(I) speciation, derived equilibrium constants and discussion *145*

4.2.6 Summary: Solubility and chlorocopper(I) complexing at constant pressure and temperature *156*

5. Mineral solubility: Effect of temperature (524 to 850 °C) on high-pressure supercritical fluids **157**

5.1 Experimental data 157

5.2 Data Interpretation 160

5.2.1 Cu–Mg–O–H–Cl speciation and solubility: Comparison with existing thermodynamic predictions *160*

5.2.2 Cu–Cpr–Tc–Qz solubility (I): Data selection and empirical regression *163*

5.2.3 Cu–Cpr–Tc–Qz solubility (II): Speciation, derivation of equilibrium constants, and other thermodynamic properties as a function of temperature *166*

5.2.4 Cu–Cpr–Ens–Qz solubility: Limitations imposed by analytical uncertainty and comparison with extrapolated equilibrium constants obtained from this study *172*

6. Mineral solubility: Effect of pressure to 1.7 GPa **176**

6.1 Experimental data 176

6.2 Data Interpretation 178

6.2.1 Cu–Mg–O–H–Cl speciation and solubility: Comparison with and limitations of existing thermodynamic models *178*

6.2.2 Mineral solubility and speciation in supercritical aqueous fluid at very high-pressure *180*

7. Mineral solubility: Summary of *P–T–X* solubility data and speciation **184**

8. Laser Raman microspectroscopy: Fluid inclusions and minerals from solubility experiments **185**

9. High-temperature, in situ X-ray absorption spectroscopy of individual synthetic fluid inclusions: Further investigation of chlorocopper(I) speciation **188**

9.1 X-ray absorption near-edge structure (XANES) spectroscopy: Background and experimental method 188

9.2 Fluid inclusion samples 191

9.3 Results and interpretation 193

9.3.1 Cu K-edge normalised and derivative XANES features *193*

9.3.2 Cu^0 and Cu^{2+}: artefacts related to beam-induced damage *194*

9.3.3 Chlorocopper(I) speciation derived from "undamaged" XANES spectra *196*

9.4 Summary 200

10. Application to supercritical hydrothermal phenomena **201**

10.1 Magmatic hydrothermal fluids: Transport and deposition of porphyry copper ores 201

10.1.1 Copper concentrations in magmatic fluids *201*

10.1.2 Geological observations relating to porphyry copper systems *202*

10.1.3 Fluid mixing at supercritical conditions *204*

10.1.4 Isobaric cooling of supercritical ore fluid *207*

10.1.5 Decompression of supercritical ore fluid and vapour-liquid partitioning in "boiling" hydrothermal fluids *210*

10.2 High-pressure metamorphic fluids: Subduction geochemical signatures and the stability and solubility of hydrous minerals 214

10.2.1 Release of LILE, LREE, Th from subducted lithosphere *215*

11. Conclusions and future studies **219**

References **222**

PRELUDE

"...to many petrologists a volatile component is exactly like a Maxwell demon; it does just what one may wish it to do." **N.L. Bowen (1928)**

Indeed, perhaps the most poorly understood of all geologically significant phases is the high-pressure supercritical fluid[1]. The hydrothermal fluid phase is enigmatic simply because it is ephemeral by nature, in contrast to mineral and silicate melt phases which are usually preserved and amenable to sampling and study using conventional methods. Fluid-rock interactions are preserved chemically and texturally in hydrothermal alteration around ore deposits, metamorphic veins, regional metasomatism, isotopic anomalies, and decoupled trace element signatures in magmatic arc rocks (*e.g.* Barnes 1979; Debout and Barton 1989; Ague 1994; Ferry 1994; Carroll and Holloway 1994; Arculus 1994; Newton and Manning 2002). Samples of the causative agent may be preserved as fluid inclusions within the effected rocks, but have been difficult to study because they are small and necessarily occur below the sample surface making them difficult if not impossible to analyse by most conventional methods. Recent microanalytical advances such as laser ablation inductively coupled plasma mass spectrometry and X-ray absorption and fluoresce spectroscopy, however, have begun enabling detailed chemical information to be obtained in situ from single natural and synthetic fluid inclusions (*e.g.* Heinrich *et al.* 1999; Mavrogenes *et al.* 1995; Loucks and Mavrogenes 1999; Mavrogenes *et al.* 2002).

The study of alteration assemblages and fluid inclusions provides useful information on phase relations and possible fluid compositions at the formation conditions. Natural samples, however, do not provide *a priori* information on their temperature and pressure of equilibration. Rather, it is high-temperature and high-

[1] In this context supercritical refers to any fluid above its critical point which defines the condition where liquid and vapour phases become completely miscible. The critical point is determined by pressure and temperature and fluid composition. The critical point of pure H_2O occurs at 374 °C and 22.1 MPa (Haar *et al.* 1984). For the H_2O–NaCl system a critical curve exists, its termination is determined by the bulk fluid composition (*e.g.* Sourirajan and Kennedy 1962; Bodnar *et al.* 1985).

pressure experimental studies that underpin our understanding and interpretation of the rock-fluid phase relations that are observed.

Recognising this, a method to synthesise fluid inclusions in complex mineral-buffered systems in a piston-cylinder apparatus, providing access to previously experimentally unobtainable pressure-temperature conditions, was developed. A complementary study in quantitative fluid inclusion analysis by laser ablation inductively coupled plasma mass spectrometry was undertaken. Accordingly, this work was followed by a series of fluid inclusion synthesis experiments in simple mineral-buffered systems (principally, SiO_2–H_2O and Cu–Cu_2O–MgO–SiO_2–HCl–H_2O) to obtain solubility and fluid speciation details. This data was used to extract thermodynamic parameters for the aqueous species identified. In principle, the information from these and similar experimental investigations can be used for rigorous extrapolation to different pressures, temperatures and compositions. In this way, the nature of previously enigmatic fluid-rock interactions may be quantitatively explained.

Remarks on the structure of the thesis

The results are presented in three separate but complementary sections. Parts 1 and 2 describe experimental and analytical techniques that were developed and represent a substantial component of this study. Some related findings are also given. The thesis culminates with Part 3 in which the results and interpretation of mineral-buffered solubility experiments using synthetic fluid inclusions are detailed. Each part is structured with the approximate form of a scientific paper; abstracts are given at the beginning of each part. The references are placed together at the end. Some repetition may occur, especially in the introductory sections and where further clarity is required. The most important results are summarised in the conclusions.

PART 1

High-pressure and high-temperature fluid inclusion synthesis using a piston-cylinder apparatus and *PVTX* relations in the SiO_2–H_2O system

Abstract

A technique is described to trap synthetic aqueous fluid (and silicate melt) inclusions over the pressure (P) and temperature (T) range accessible by a piston-cylinder apparatus. The method combines the use of a large volume, piston-cylinder assembly with a thick-walled, cold-sealed capsule design. With this capsule relatively large volume experiments can be undertaken. This allows the use of complex buffering techniques and relatively large crystals for trapping inclusions. P and T calibrations indicate that experimental conditions may be controlled with comparable precision to a conventional cold-seal hydrothermal apparatus, typically used for fluid inclusion synthesis. From the P calibration data it seems clear that internal friction within piston-cylinder assemblies is a time-dependant phenomenon, such that the friction can be expected to decay over the duration of a typical fluid inclusion synthesis run to an essentially friction-free state.

Geochemical evidence obtained from laser ablation inductively coupled plasma mass spectrometry of individual fluid inclusions is presented that establishes that fluid-mineral equilibrium is readily attained in mineral-buffered fluid inclusion synthesis experiments.

An application to the determination of activity–composition (a–X) relations in the system SiO_2–H_2O at high pressures from *PVTX* properties is also presented. Recent silica solubility studies at quartz-saturated and under-saturated conditions have suggested polymerisation of the dissolved silica species is responsible for discrepancies between the existing datasets, despite low solute concentrations (*e.g.* < 5 mol %). The *PVT* measurements of quartz-saturated fluids of this study indicate the volume of SiO_2–H_2O mixtures may deviate significantly from ideal behaviour at high-P (*e.g.* > 0.5 GPa). This is most plausibly explained by minor variation in the partial molar volume of H_2O in the mixture relative to pure H_2O (*i.e.* $\overline{V}_{H_2O}^{fluid} \neq \overline{V}_{H_2O}^{pure}$); the excess volumes are

positive and sufficiently large that they are not sensibly reconciled by silica polymerisation because the SiO_2 component is too minor in these fluids. This effect is not apparent at low-P (*e.g.* < 0.5 GPa), consistent with previous quartz-hosted fluid inclusion PVT studies. It appears the activity of H_2O along with the effect of dissolved silica polymerisation needs to be considered explicitly, even in dilute fluids, at high-P.

This experimental technique, combined with recent developments in single fluid inclusion analytical techniques, provides a means of tackling current, seemingly intractable problems concerning fluid- and related phenomena at deep crustal and upper mantle P and T conditions.

1. Introduction

Fluids have been implicated in many geological processes from controlling the location and extent of melting at subduction zones to hydrothermal ore genesis and earthquake generation. In fact, fluids appear to be so inseparable from rock-forming processes that it is difficult to overstate the importance of understanding aqueous fluids. For instance, the quantification of hydrothermal mass fluxes and processes, along with subsolidus and melting phase relations in the upper mantle and crust requires knowledge of mineral solubilities, chemical speciation and pressure-volume-temperature (*PVT*) properties of fluids. In principle, the necessary details should be readily obtained by experimentation combined with investigation of natural fluid inclusions, as these contain the sole direct information on natural high-pressure (*P*) and temperature (*T*) fluids. However, our current understanding barely scratches the surface. Simply, the paucity of relevant information is due to the limitations of traditional experimental approaches and, until recently, analytical difficulties in extracting detailed chemical and isotopic information from natural single fluid inclusions. Typical experimental difficulties include fluid modification due to precipitation of dissolved silicate components or back-reaction of fluids with buffering phases during quenching or, as is the case for in situ spectroscopic methods, the physical limits of the sample cell. Moreover, deciphering the fluid inclusion record alone, despite its promise, is not a panacea for an absence of experimental techniques capable of sampling fluids at crustal and upper mantle conditions. For instance, fluids entrapped in relatively high *PT* metamorphic rocks are scarce and of uncertain origin since they rarely survive exhumation to the surface unmodified. Thus, the rarity and equivocal provenance of fluids encapsulated in natural high-*P* and *T* samples, means the nature of fluids in these extreme, yet common, environments will remain largely enigmatic without direct experimental investigation.

Experimental fluid inclusion synthesis provides an elegant means of isolating fluids at the high-*P* and *T* run conditions avoiding the usual fluid modification problems associated with quenching. The technique relies on ambient fluids becoming trapped and preserved as inclusions at growth irregularities that inevitably develop during fracture healing, and recrystallisation and overgrowth of crystal surfaces. Indeed several decades of experiments in hydrothermal- and gas-media apparatus have firmly established that this technique provides a reliable means of sampling fluids at high-*P*

and *T*. Moreover, the technique is not restricted to investigations of single phase, supercritical fluids, but can also be used to trap both vapour- and liquid inclusions in non-quenchable, subcritical, two-phase fluid systems as well as sample coexisting hydrous silicate melt and aqueous fluid as inclusions (Bodnar *et al.* 1985; Student and Bodnar 1999). This ability to study both single phase and immiscible fluid phases, individually is not possible by any other technique and so lends it a significant advantage as the complete breadth of hydrothermal phenomena may be investigated by a single method.

Despite the potential of this technique, most previous synthetic inclusion studies have been generally restricted to *P* less than 0.5 GPa, *T* below 800 °C and to relatively simple fluid compositions. These apparent limitations are not because there is some intrinsic problem with the approach, rather it is a reflection of the constraints imposed by conventional hydrothermal- and gas-media apparatus, the standard devices used to undertake these experiments, and those associated with traditional single inclusion analytical techniques. Therefore, it seems sensible to adapt devices already used extensively in experimental petrology for determining phase equilibria at deep crust and upper mantle conditions, to the task of fluid inclusion synthesis. Similarly, the use of recent instrumental developments should be taken advantage of, such as laser ablation inductively coupled plasma mass spectrometry (LA-ICP-MS; *e.g.* Gunther *et al.* 1998, *this study*), proton induced X-ray emission spectroscopy (PIXE; *e.g.* Anderson *et al.* 1989, Heinrich *et al.* 1992, *this study*) and synchrotron X-ray fluorescence and absorption spectroscopic techniques (*e.g.* SXRF Mavrogenes *et al.* 1995; XANES/EXAFS Mayanovic *et al.* 1995, 1997, and Mavrogenes *et al.* 2002, *this study*), in combination with traditional methods to extract a more comprehensive set of information from single inclusions.

One apparatus which is ideally suited for fluid inclusion experiments over a more extensive *T* and *P* range is the piston-cylinder (Boyd and England 1960), however, it has seen only very limited use in this application (Brodholt and Wood 1994; Ballhaus *et al.* 1994; Frost and Wood 1997; Shmulovich and Graham 1999; Withers *et al.* 2000). This presumably stems from the generally small sample volume in standard piston-cylinder arrangements, compared to gas-media apparatus. Such factors present a challenge since fluid inclusion synthesis generally requires large sample volumes to contain fragile single crystals and other charge materials. However, typical piston-cylinder experiments use capsules which are small, and because of their size are prone

to failure or crushing of single crystals during the experiment or upon quenching, preventing entrapment of abundant, well-formed inclusions within reasonable experimental run times. Also the usual method of sealing capsules by arc welding tends to be somewhat unreliable, as some volatilisation is common and can result in unknown mass losses and changes to the bulk composition of the sample.

Therefore, to avoid the inherent difficulties associated with standard piston-cylinder capsule and welding methods, a simple, large volume, cold-sealed capsule technique was developed that can be used in a piston-cylinder apparatus for fluid inclusion synthesis and any other experiments requiring large volumes.

2. Experimental method

In order to readily transfer established fluid inclusion synthesis procedures (*e.g.* Sterner and Bodnar 1984) to a piston-cylinder apparatus, the available sample volume was increased by using a 30 mm internal diameter pressure vessel on a 500 tonne end-loaded press. However, to take advantage of the total sample volume, new capsule and pressure assembly configurations were specifically developed.

2.1 Capsule and piston-cylinder assembly

The capsule is comprised of a thick-walled capsule body, open at one end and a separate lid (Figure 1.1). Both parts are fashioned so the capsule can be swaged, to form an effective cold-seal, by applying some pressure prior to mounting the full cell assembly into a piston-cylinder apparatus. By following this procedure the usual problems encountered with welding are mitigated and sample loading procedures simplified compared to standard or "open" capsule methods (*e.g.* Brodholt and Wood 1994, Ayers *et al.* 1992), as not only is the capsule sealed, the seal can be inspected before running the experiment.

The lid fits closely inside the capsule body where it is supported by a ledge recessed into the inside diameter of the opening. The depth of the ledge is such that with the lid inserted, a lip extends above the upper outer surface of the lid by about 1.5 mm. This lip is swaged, or crimped down, over the lid, giving the capsule a watertight seal. A hydraulic press is used to operate a simple swaging device to create the seal. The swaging device consists of a brass die, to support the capsule, and a piston-like swage tool is used to roll the lip inwards and over the lid, cold-sealing the capsule (Figure 1.2). The hole in the die is the same diameter as the capsule and its thickness equivalent to the distance from the base of the capsule, to the top outer surface of the lid. The swage tool has at one end a circular depression with rounded edges, its diameter equal to the outer diameter of the capsule, its depth the same as the lip thickness. It is important that the lid, the supporting ledge and swaging lip of the capsule are clean to ensure a proper seal.

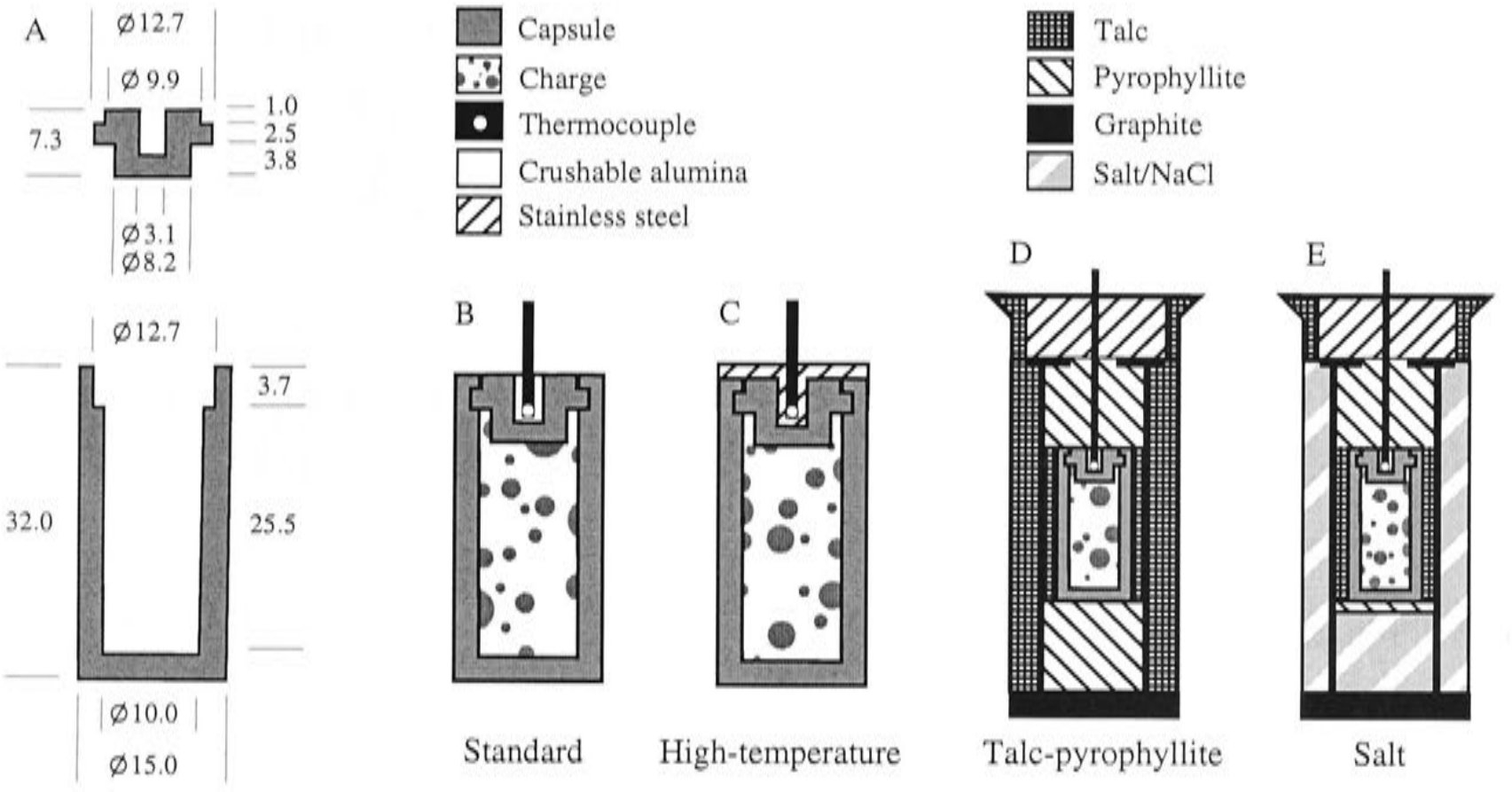

Figure 1.1 Capsule and assembly design for large volume hydrothermal experiments in a piston cylinder. (A) Cross sectional view of standard capsule body and lid. Dimensions in millimetres. (B) Standard capsule. (C) Modified standard capsule, for running capsule materials that become extremely ductile at high-*T*, like copper, it is necessary to add a steel "cap" to prevent contamination of thermocouple and generally restrict mobility at the top of the capsule to attain high-*P* and *T*. (D) Standard talc-pyrophyllite pressure assembly. (E) Standard salt pressure assembly.

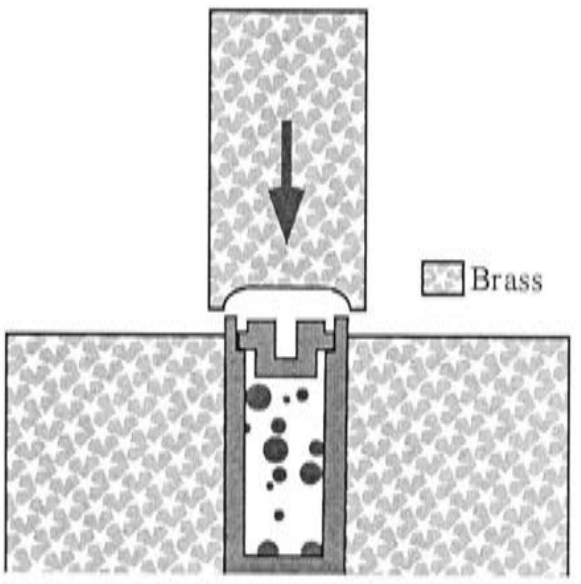

Figure 1.2 Schematic of swaging device for cold sealing capsules (cross sectional view, includes capsule not yet sealed).

The unusual shape of the lid is essential for reliable thermocouple and general behaviour of the assembly. The well recessed into the lid houses the thermocouple. As explained in detail below, this feature is required for accurate *T* control for a capsule of this size. To minimise thermocouple drift due to contamination, the thermocouple and tubing are isolated from the capsule by a crushable alumina sleeve with a small amount of alumina powder packed into the base of the well. The raised portion of the lid

prevents material collapsing into the void, which is otherwise created by the rolled lip that forms the capsule seal and the remaining exposed lid surface. If space above the lid is not occupied, it collapses during or shortly after pressurisation of the cell and often results in thermocouple failure.

It was found that copper capsules can be mobile at relatively high-T (> 800 °C). This is undesirable as it complicates attempts to achieve high-P because copper, although solid, tends to migrate into boundaries between cell components. In particular it was noticed that copper from the lid region can flow into the pyrophyllite top spacer through the thermocouple housing causing thermocouple drift and loss of capsule integrity. This problem was overcome by improving the seal between the top of the capsule and the thermocouple/pyrophyllite spacer by fitting a single piece steel disk with a short hollow spine that houses the thermocouple assemblage and inserts into the normal thermocouple lid recess (Figure 1.1). Powdered alumina is packed around the thermocouple tip to prevent contamination from the capsule.

Although most of the experiments were conducted in copper capsules, other metals (*e.g.* Ag) or alloys (*e.g.* Ni–Cu, Cu–Pd, Ag–Pd) could be utilised for capsule construction depending on T and chemical constraints. Alternatively, the capsule could be lined with a noble metal sleeve or other material if desired.

Two pressure medium configurations, utilising talc, pyrophyllite and salt components, were used successfully for hydrothermal and fluid inclusion experiments (Figure 1.1). The talc-pyrophyllite assembly consists of a talc outer sleeve, a graphite heater and an inner talc sleeve surrounding the capsule. Fire hardened (1050 °C) pyrophyllite spacers were placed above and below the capsule. A graphite disk covers the base of the assembly and a thinner graphite disk was placed at the top of the assembly. The upper and lower graphite disks increase the reliability of forming a heating circuit through the cell.

The salt assembly consists of an outer sleeve of NaCl into which a graphite heater sleeve is inserted. Again, a talc sleeve surrounds the capsule, isolating it from the heater. A hardened pyrophyllite spacer sits above, and a thin pyrophyllite disk below the capsule. The thin pyrophyllite disk separates the capsule from an NaCl spacer. Graphite disks are placed at the top and bottom of the cell. All NaCl components were pressed to > 95% of the theoretical density.

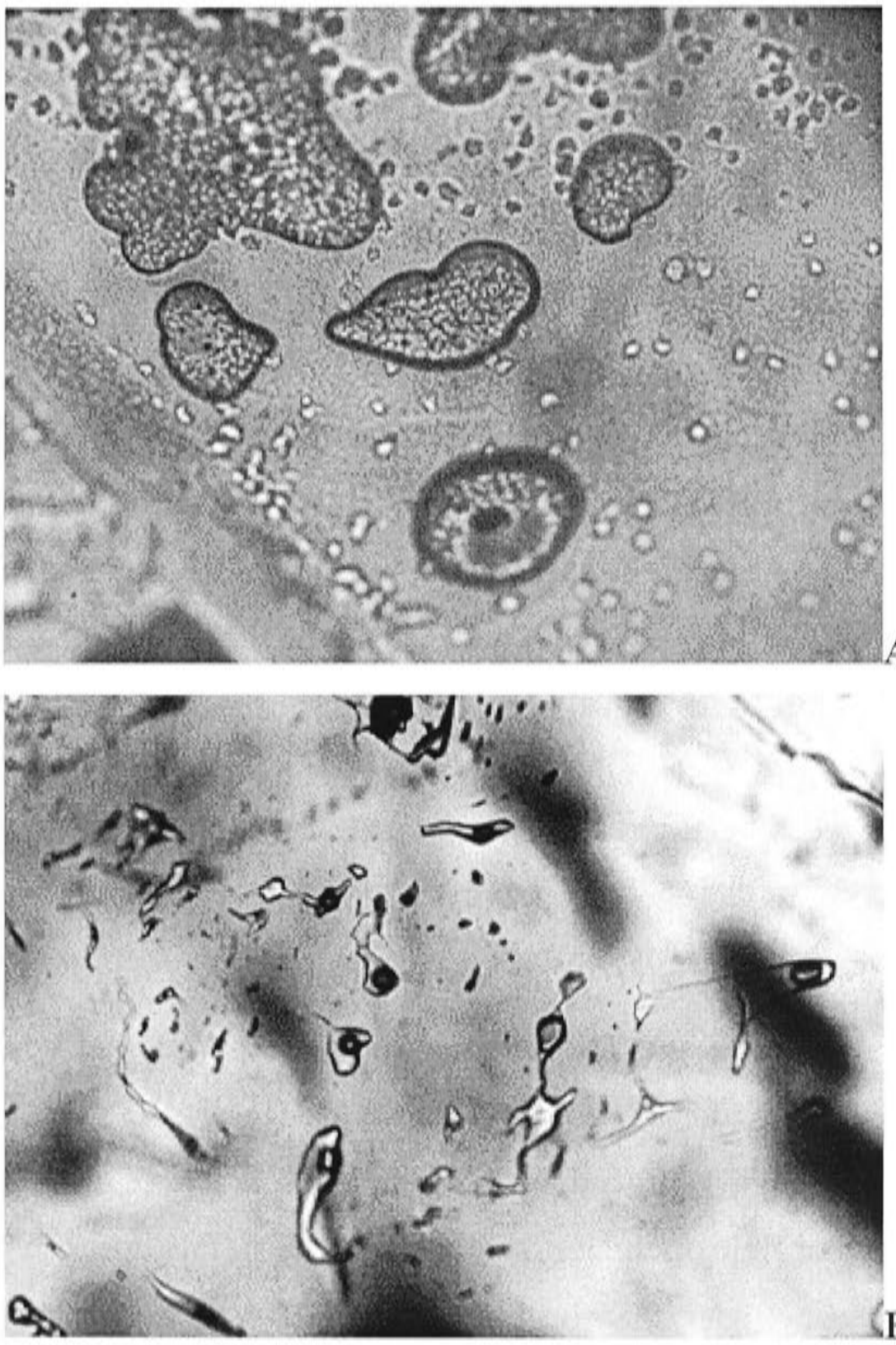

Figure 1.3 An example of coexisting silicate melt (A) and aqueous vapour phase (B) inclusions hosted in quartz. Sample synthesised in a piston-cylinder apparatus at 850 °C and 0.5 GPa using the technique described in the text. Images are approximately 300 μm across.

Experience has shown that aqueous fluid and silicate melt inclusion synthesis in a piston-cylinder apparatus (*e.g.* Figure 1.3), using the capsule and assembly configuration described, can be performed reliably using a "piston-out" routine, as described. Firstly, 0.2 to 0.3 GPa was applied to the cell prior to heating. This ensures that the lid remains sealed en route to the experimental conditions. *T* was ramped at 50 °C per minute to the desired run condition; *P* was added synchronously such that the *P–T–time* path followed a slightly over-pressured, pure water isochore, appropriate to the desired run *P* and *T*. In general, however, the simple addition of *T*, usually above about 400 °C, saw the cell *P* rise due to the increasing fluid pressure at approximately constant volume. This confirmed that the capsule had sealed and the assembly

approached isochoric behaviour on the way to the final run conditions. P was adjusted at the final run T and kept constant for the run duration, by manual adjustment if necessary. Runs were quenched at 50 °C per minute to avoid thermal shocking of the sample and rupture of fluid inclusions. For the majority of the runs, during the quench process, P was decreased by thermal contraction, along the cooling path. However, more controlled quenching along an approximate isochore may be advisable for some conditions to avoid decrepitation or crushing inclusions (*e.g.* very high-P). T ramp rates and T during the run were controlled automatically via a programmable Eurotherm power controller connected to the thermocouple. The consequence of using relatively low quench rates was not investigated, but is not thought to affect results as isochore-like P-T paths were followed. This is because: 1) this procedure reduces the chances of inclusion deformation (which would produce erroneous PVT fluid inclusion data); and 2) bulk fluid inclusion composition is not expected to be modified provided the inclusions remained intact during the quench process and is ensured as far as possible by cooling along an isochore appropriate to the P-T conditions.

Calibration of T and P accuracy for the experimental configuration was ascertained by a series of runs as described below.

Although standard procedures, described elsewhere (*e.g.* Sterner and Bodnar 1984), were used for fluid inclusion synthesis, some points specific to thick-walled capsules in a piston-cylinder are worth mentioning. It was found that minimising the potential volume change (positive or negative) of the capsule during the experiment improved the experimental reliability. A near constant capsule volume is desirable for two reasons: 1) to ensure crystals are not crushed; and, 2) reduce the possibility of capsule over-expansion causing fluid loss. This was achieved by calculating the total available sample volume, from the physical dimensions of the capsule body and lid, prior to loading the capsule. After determining the empty capsule volume, the mass of solids and fluids required to produce a bulk capsule isochore equal to or slightly less than that estimated for the conditions of the experiment can be calculated.

2.2 Temperature

Several temperature (T) calibration experiments were conducted to determine T gradients and the thermocouple position providing the most reliable control. Copper calibration capsules were fitted with three thermocouples at different locations within the cell. All calibration experiments were run in standard talc-pyrophyllite assemblies. Rather than use a solid copper capsule, analogue charge materials were placed inside the capsules to simulate normal experimental conditions. Also, to determine whether the charge materials affect the thermal structure of the capsule, two types of analogue charge were used; pyrophyllite and quartz sand + water. T was measured simultaneously across the capsule, at 10 to 30 °C intervals from 200 to 950 °C using $Pt_{94}Rh_6$–$Pt_{70}Rh_{30}$ (type-B) thermocouples, inserted axially into the assembly. Thermocouples were inside four-bore high-purity Al_2O_3 tubing and surrounded by a slightly larger crushable alumina sleeve to prevent contamination related thermocouple drift. Type-B thermocouples, although slightly less sensitive, are less susceptible to contamination than other more commonly used thermocouples, such as Pt–$Pt_{90}Rh_{10}$ (type-S) or Pt–$Pt_{87}Rh_{13}$ (type-R). No correction for P was applied to thermocouple measurements.

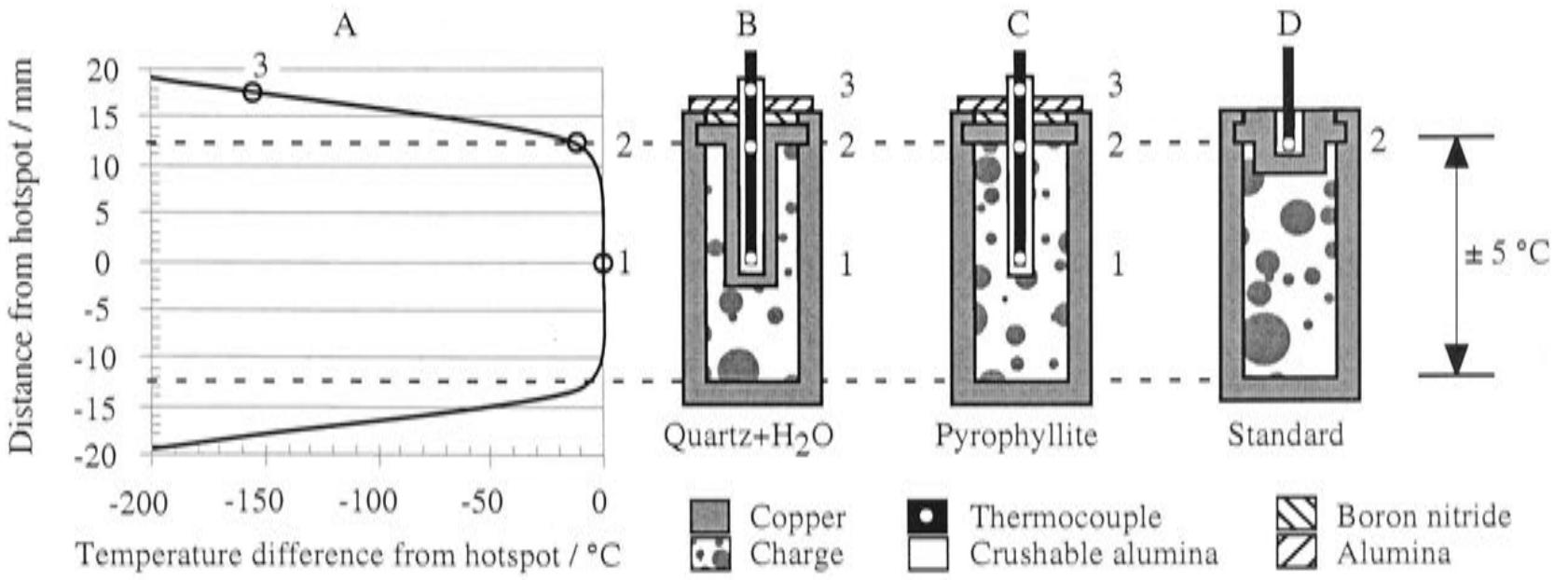

Figure 1.4 (A) T gradient measured at 850 °C over 30mm long copper capsule, in a talc-pyrophyllite assembly. Comparison of modified T calibration capsules containing analogue charges, quartz sand + water (B) and solid pyrophyllite (C) with the standard capsule configuration (D). Numbers refer to the different thermocouple positions measured. All Figures are to scale.

Experiments containing an analogue charge of quartz sand and water required a special lid to house the thermocouple within the capsule while retaining a high-P and T fluid phase throughout the calibration run. This was achieved using a single piece flat

lid with a hollow spine extending into the capsule, just beyond the centre for thermocouple access (Figure 1.4B). On the other hand, a simple flat lid with a hole through it was all that was required for pyrophyllite charge calibration (Figure 1.4C). Both lid types were swaged onto the capsules to form the usual cold-seal, as described previously.

Calibration data show that despite the relatively large size of the capsule, T over its length is remarkably uniform, about ±5 °C over the entire T range investigated (Figure 1.4A, Figure 1.5). Boettcher and Kerrick (1971) report that T errors in hydrothermal-bomb apparatus are also on the order of ± 5 °C. The near constant T distribution over the capsule length is attributed to the large mass and high thermal conductivity of copper. However, in stark contrast, an extreme thermal gradient, > 30 °C/mm, is evident immediately adjacent to the capsule ends. Consequently, thermocouple placement is critical for accurate T control and, perhaps not surprisingly, it was found that this could be best achieved by embedding the thermocouple within the body of the capsule itself, rather than in a more traditional position outside the capsule (Figure 1.4D).

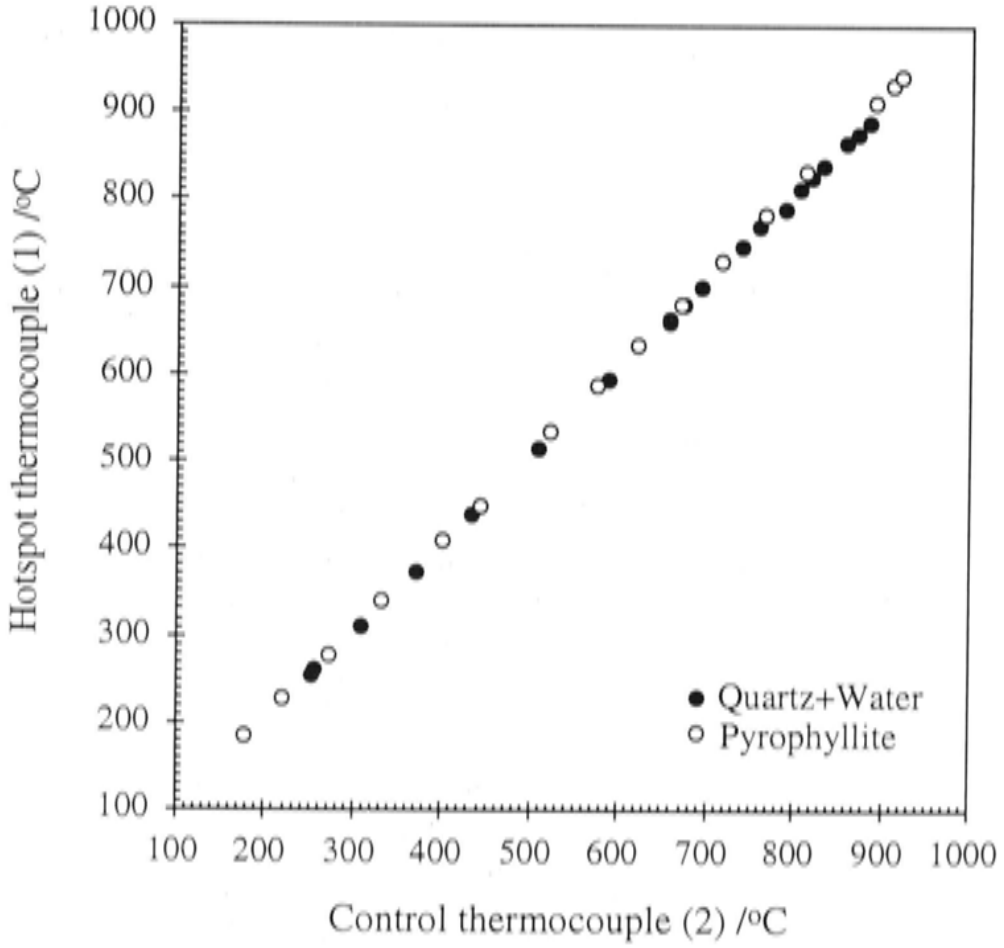

Figure 1.5 Comparison of T calibration measurements across the copper capsules for pyrophyllite (open symbol) and quartz sand + water (filled symbol) charges. Numbers in parentheses refer to thermocouple positions shown in Figure 1.4.

Figure 1.5 provides a comparison of T measurements made at different positions in copper capsules containing different charge types. The data show that the

thermal structure of the capsule is not significantly affected by major differences in experimental charge materials.

2.3 Pressure

2.3.1 Introduction and calibration approach

Pressure in a piston-cylinder apparatus is calculated simply from the applied load, in this case oil pressure, and the effective dimensions of the ram and piston. Typically, the accuracy and precision of the measurement is about 1–3%. This, however, requires that uncertainty in the applied force-pressure relation is known and corrected.

It is generally believed that P uncertainties in a piston-cylinder apparatus largely depend on how well the internal friction-related P loss is characterised for the type of assembly used. These so-called "friction losses" are attributed to a variety of sources such as the interaction between the cylinder wall and the piston and, especially, to the effects resulting from the use of cell components with variable compressibility. Although friction effects have been calibrated for a number of salt- and talc assembly types, "low-friction" and "high-friction" respectively, these calibrations are generally based on short duration high-T experiments in standard assemblies and are assumed to be independent of T, P, assembly size and run time (*e.g.* Green *et al.* 1966; Boettcher *et al.* 1981; Bohlen and Boettcher 1982; McDade *et al.* 2002). However, since large assemblies (30 mm) were used and fluid inclusion synthesis requires more time than many conventional experiments, the applicability of previous calibrations is uncertain. Moreover, work by Bose and Ganguly (1995) casts doubt on the friction correction concept that pervades the literature. Their data indicates that assembly friction in fact decays with time, more or less independent of assembly configuration, and so P corrections become negligible for long (> 24 hours) duration piston-cylinder experiments.

With these thoughts in mind, a series of experiments was undertaken to calibrate the P loss, if any, due to friction for extended duration experiments, as required for fluid inclusion synthesis, in copper capsules within talc-pyrophyllite and NaCl type assemblies[2].

---

[2] Experience has shown, while robust at ambient conditions, copper capsules anneal and deform rapidly at even moderate T (~ 350 °C) so that despite the large mass of the capsue, its shear strength is not considered to have any significant effect on the overall assembly.

Rather than calibrating P by the usual way of locating a known phase transition or other reaction position, a fluid inclusion technique was used to calculate the true experimental P from the known PVT properties of pure water. The calibration technique depends upon accurate knowledge of the experimental T, which was calibrated independently earlier, and the specific volume of water at the run conditions to calculate an isochore for the fluid in the inclusion and solve for P (Figure 1.6). Simply, any difference between the nominal and isochore-derived P would, ordinarily, be interpreted as a friction-related discrepancy which should be corrected for. That previous investigations demonstrate that fluid inclusion isochores reliably measure fluid volume as a function of P and T (Bodnar and Sterner 1985; Sterner and Bodnar 1991; Brodholt and Wood 1994; Frost and Wood 1997; Withers *et al.* 2000) should validate the use of fluid inclusions as a P calibration method. This technique of course, requires that the solubility of the host is low enough to have a negligible effect on the fluid properties. For the quartz-water system this requires that the volume of the real fluid $\left(\overline{V}_{fluid}^{PTX}\right)$ is essentially equal to that of pure H_2O $\left(\overline{V}_{H_2O}^{pure}\right)$. This could be justified on the basis that X_{H_2O} is close to unity.

The extent to which this assumption may reasonably hold to higher P and T can be gauged from the experiments of Bodnar and Sterner (1985) and Sterner and Bodnar (1991). They measured the PVT properties of water from 0.1 to 0.6 GPa and 300 to 700 °C using quartz-hosted fluid inclusions (synthesised in cold-sealed, externally heated, gas pressure media apparatus, where P error due to friction can be reasonably assumed to be negligible). These data indicate that the effect of dissolved silica on H_2O isochores is negligible, and thus the assumption is acceptable, at least up to 0.6 GPa and 700 °C, at the precision of the measurements.

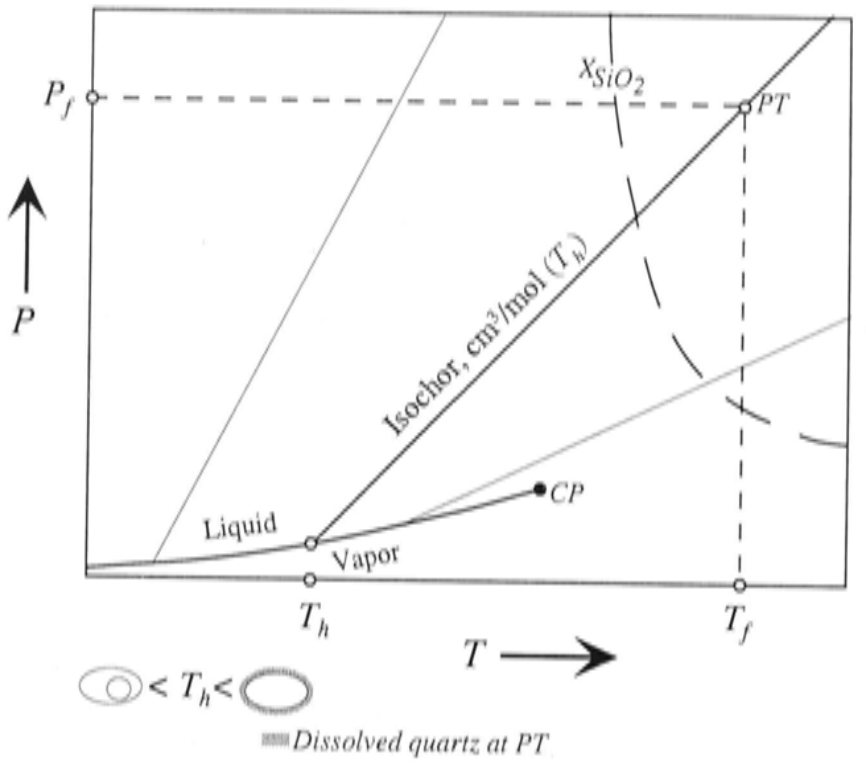

Figure 1.6 Schematic diagram illustrating *P* calibration approach. Abbreviations refer to fluid inclusion homogenisation *T* (T_h), *T* of formation or run temperature (T_f) and *P* of formation (P_f, or actual experimental *P*) as predicted from the isochore extending from T_h. H_2O phase relations shown, *CP* refers to the critical point of pure H_2O. The ideal case where friction is negligible is shown, *i.e.* the nominal run conditions (open circle) intersect the isochore. A quartz solubility isopleth (X_{SiO2}, X refers to mole fraction dissolved silica) is indicated. A schematic depiction of fluid inclusion petrography as a function of *T* is also shown.

On the other hand, the simplification that $\overline{V}_{fluid}^{PTX} \approx \overline{V}_{H_2O}^{pure}$ is unnecessary, because the solubility of quartz in H_2O is well known to 900 °C and 2.0 GPa (Manning 1994) and previous fluid inclusion work demonstrates that quartz-saturated water along the liquid-vapour curve can be treated as essentially pure H_2O. Thus, it is possible to calculate the molar volume of the real H_2O + SiO_2 fluid mixture. Technically, the molar volume should be corrected for the amount of quartz dissolved from inclusion walls between T_h and the formation *P* and *T*. Although this correction is small at low-*P* - correcting the volumes measured by Bodnar and Sterner (1985) and Sterner and Bodnar (1991) for quartz dissolution would not change their general conclusion - it is nonetheless valid. The calculation, from T_h measurements, of the real fluid volume at the *P* and *T* of interest then takes the form,

$$\overline{V}_{fluid}^{PTX} = \left(\overline{V}_{H_2O}^{T_h} + V_{SiO_{2(aq)}}^{T_h\ precipitated}\right) \cdot \Delta V_{Qz}^{PT}$$

where, $\overline{V}_{fluid}^{PTX}$ is the volume of the real fluid (H_2O + $SiO_{2\ (aq)}$), in cm^3/mol, $\overline{V}_{H_2O}^{T_h}$ is the molar volume of pure water on the liquid-vapour curve corresponding to the

homogenisation temperature (T_h). $V_{SiO_{2(aq)}}^{T_h\ precipitated}$ is the volume increase per mole of water of the inclusion between T_h and the formation P and T due to quartz dissolution from the walls of the inclusion. $V_{Qz}^{Th\ precipitated}$ can be calculated from solubility data and the relation, $V_{SiO_{2(aq)}}^{Th\ precipitated} = \overline{V}_{Qz}^{Th} \cdot m_{SiO_{2(aq)}}^{PT} / 55.51$, where $\overline{V}_{Qz}^{Th}$ is the molar volume of quartz at T_h, $m_{SiO_{2(aq)}}^{PT}$ is the concentration of dissolved silica at P and T in mol/kg units, and 55.51 represents the number of moles of H_2O in 1000 g of water. ΔV_{Qz}^{PT} is the fractional change in the volume of quartz between T_h and the P and T of the experiment (also known as the T and P of formation, T_f and P_f, respectively).

Although fluid inclusion *PVT* experiments were carried out over a wide range of P and T conditions, only the low-P experiments have been used for calibration purposes, since only these overlap with the P and T region for which the effect of dissolved silica is known to be negligible and thus allow direct volumetric comparison of the fluid and pure water without significant error. These conditions also coincide with those at which the majority of fluid inclusion work to be presented in *PART 3* were conducted. In contrast, the *PVT* data obtained at higher P are discussed separately (*PART 1, §4*), as they indicate SiO_2–H_2O interaction in the fluid becomes significant, such that the fluid can no longer be treated as essentially pure water, despite containing similar concentrations of dissolved silica as in the low-pressure experiments. That is, composition related phenomena must be considered at these conditions, *e.g.* $\overline{V}_{H_2O}^{pure} \neq \overline{V}_{H_2O}^{fluid}$. Thus, for the sake of accuracy and consistency, the effect of dissolved silica will be taken into account in the volume measurements of all experiments.

2.3.2 Experimental

Capsules were loaded with pure water, pre-cracked quartz and a small amount of silica powder (slightly less than the mass predicted for saturation). During the experiment, fluid inclusions were formed along healed fractures. Almost all of the *PVT* experiments were at *P* and *T* conditions where the density of water is less than 1 g/cm^3, so that at ambient conditions fluid inclusions contain a vapour bubble. Because the pure water system is univariant everywhere along the vapour-saturation curve, T_h uniquely defines both the homogenisation *P* and, importantly, the specific volume of water used for determining the isochore (Figure 1.6). For water densities between 1 and 1.25 g/cm^3 fluid inclusions contain no vapour bubble at ambient conditions, thus isochores must be determined from freezing point depression measurements, which are, however, more difficult to obtain reliably (*PART 1, §4.3*). In any case, extrapolation along the isochore to T_f gives the experimental pressure, P_f.

Samples were mounted in epoxy and doubly polished, then removed from the epoxy. T_h was determined by microthermometry measurements on individual fluid inclusions using a Fluid Inc. adapted USGS gas-flow heating/freezing stage. Synthetic fluid inclusions were used to calibrate the stage *T*. Accuracy of heating measurements was determined to be ±1 °C. For all T_h experiments the thermocouple tip was positioned as near as possible to the inclusion being heated to minimise any potential errors related to small thermal gradients within the sample cell, the distance between the thermocouple and inclusion was less than 1 mm. T_h was found by heating the sample until the bubble disappeared completely. Complete versus incomplete homogenisation was easily distinguished by differences in bubble behaviour on cooling. For example, the true homogenisation is reached when the bubble reappears by a sudden nucleation and only after significant under cooling of the sample, approximately 20 °C or more below T_h, whereas, incomplete homogenisation is characterised by the vapour bubble growing back steadily on cooling.

The *PVT* data used to find the fluid density at T_h on the pure water liquid-vapour phase boundary was taken from Haar *et al.* (1984). In order to determine the density of water at the *P* and *T* of the experiment, however, a small correction must be applied to account for the volume change of the host phase that occurs from the T_h and ambient *P* ($P_{ambient}$) to the experimental conditions (T_f, P_f). Specific volumes determined at T_h were corrected by determining the percentage volume increase of

quartz from T_h, $P_{ambient}$ to T_f, P_f, using the thermodynamic data of Berman (1988), and increasing the specific volume found at T_h by an equal amount. The effect of quartz dissolution on the inclusion volume was calculated from the empirical quartz solubility equation of Manning (1994).

2.3.3 Low pressure PVT results, 630–800 °C: Sources of error and friction behaviour in a piston-cylinder apparatus

Experimental results are given in Table 1.1. There are at least three main sources of error in the measurements, arising from uncertainty in the nominal P (σ_P), T (σ_T), and the range of T_h measured for each sample (σ_{T_h}). However, for completeness, error in the volume properties of the host ($\sigma_{V_{quartz}}$) and fluid composition error ($\sigma_{X_{fluid}}$, where X is the mole fraction), since the measurements more accurately describe PVT relations in the SiO_2–H_2O system, also contribute to the overall error and should be included. Thus, total error is expressed by,

$$\sigma^2_{\overline{V}^{PTX}_{fluid}} = \sigma^2_T\left(\frac{\partial V_{fluid}}{\partial T}\right)^2 + \sigma^2_P\left(\frac{\partial V_{fluid}}{\partial P}\right)^2 + \sigma^2_{V_{quartz}}\left(\frac{\partial V_{fluid}}{\partial V_{quartz}}\right)^2 + \sigma^2_{X_{fluid}}\left(\frac{\partial V_{fluid}}{\partial X_{fluid}}\right)^2 + \sigma^2_{Th,n-1} \qquad [1.1]$$

Any remaining errors are likely to be insignificant. P and T uncertainties were considered to be equivalent to the total observed variation during the experiment and with an additional ± 5 °C added to the uncertainty to account for the measured thermal gradient across the capsule. The PVT properties of quartz were assigned an arbitrary, but generous, 5 % error, based on the observed differences between various equations of state (EOS; *e.g.* Hosieni 1985, Berman 1988, Dorogokupets 1995, Mao *et al.* 2001). The quartz solubility error is estimated to be 0.020 mol/kg (± 1 σ, Manning 1994). However, by far the largest and most significant uncertainty relates to the precision of the T_h measurement (Table 1.1).

A potential further complication thought worth investigating was the effect of different capsule materials. Specifically, a double capsule technique was utilised to investigate if dissolution of the copper capsule, although minor, might affect the PVT properties of the fluid. Practically, these experiments involved trapping "pure H_2O" fluid inclusions in quartz in a smaller, carbon arc welded, platinum capsule (outside diameter 5 mm, inside diameter 4.5 mm, length ≤ 20 mm) placed inside a standard copper capsule. In addition, there was sufficient volume in the standard capsule to contain pre-cracked quartz, silica powder and water, allowing a direct comparison of the two capsule environments. The water in the copper capsule provided a hydrostatic P environment, transmitting the external P through to the flexible inner platinum capsule

so that there is no P differential between the two capsules. Platinum was chosen because it is well tested for synthetic fluid inclusion experiments (*e.g.* Bodnar and Sterner 1985; Brodholt and Wood 1994).

Table 1.1 Fluid inclusion *PVT* data used to investigate friction effects in a piston-cylinder apparatus

Run	Asssembly	P/MPa	T/ °C	T_h^{ave}	n	σ_{T_h}	$\overline{V}^{T_h}_{\min}$	$\overline{V}^{T_h}_{\max}$	$\overline{V}^{T_h}_{ave}$	$\overline{V}^{PT}_{fluid}$	$X^{PT}_{SiO_{2(aq)}}$	$\overline{V}^{PTX}_{fluid}$	$\sigma^{PTX}_{\overline{V}}$
R143	Talc/Cu	354(6)	796(13)	327	13	8.2	26.52	29.20	27.72	27.92	0.0095	28.14	1.33
R166	Talc/Cu	344(3)	629(6)	295	8	1.9	24.74	25.08	24.94	25.05	0.0043	25.14	0.48
R168*	NaCl/Pt	364(6)	700(6)	321	10	2.1	26.08	27.53	27.10	27.23	0.0064	27.38	0.65

Notes: Assembly refers to the piston-cylinder cell type and capsule material used. * Indicates double capsule experiment, Pt capsule data given. Figures in parentheses indicate the uncertainty in the experimental P (MPa) and T (°C). T_h^{ave} is the average homogenisation temperature, and σ_{T_h} is one standard deviation on T_h^{ave}. $\overline{V}^{T_h}_{\min}$, $\overline{V}^{T_h}_{\max}$ and $\overline{V}^{T_h}_{ave}$ are the minimum, maximum and average fluid volumes obtained from T_h measurements in units of cm^3/mol. $\overline{V}^{PT}_{fluid}$ is $\overline{V}^{T_h}_{ave}$ corrected for the expansivity and compressibility of quartz. $\overline{V}^{PTX}_{fluid}$ is, $\overline{V}^{PT}_{fluid}$ further corrected for silica solubility, $X^{PT}_{SiO_{2(aq)}}$ (specified in mole fraction $SiO_{2\,(aq)}$), as appropriate, and $\sigma^{PTX}_{\overline{V}}$ is the uncertainty in the fluid volume measurement in cm^3/mol.

The quartz solubility correction to the fluid volume measurement is minor, particularly in the context of the overall measurement uncertainty. The magnitude of the correction can be evaluated by comparing the composition corrected fluid volumes, $\overline{V}^{PTX}_{fluid}$, with the uncorrected volumes, $\overline{V}^{PT}_{fluid}$, in Table 1.1. The compositional correction is minor because quartz solubility is relatively low at the experimental conditions.

In Figure 1.7 the position of each isochore corresponding to the measured $\overline{V}^{PTX}_{fluid}$, is plotted in P–T space along with the conditions of each experiment. The uncertainty in P, related to the precision of the $\overline{V}^{PTX}_{fluid}$ measurement, is shown at the T of the experiment. Figure 1.8 is an alternative presentation of the data, where the measured fluid volume from each sample is compared directly with that of pure water $\left(\overline{V}^{pure}_{H_2O}\right)$ calculated from the MRK-type EOS given by Holland and Powell (1998), at the same P and T. Uncertainties in $\overline{V}^{pure}_{H_2O}$ arise from the minor variations in P, and to a lesser degree T, observed during the runs (Table 1.1), the error component attached to the PVT properties of pure water, predicted by the EOS, was ignored, as the same calculations using other EOS appropriate to the conditions (*e.g.* Burnham *et al.* 1969, Kerrick and Jacobs 1981, Holland and Powell 1991) yield similar results indicating that it is not likely to be a significant source of error.

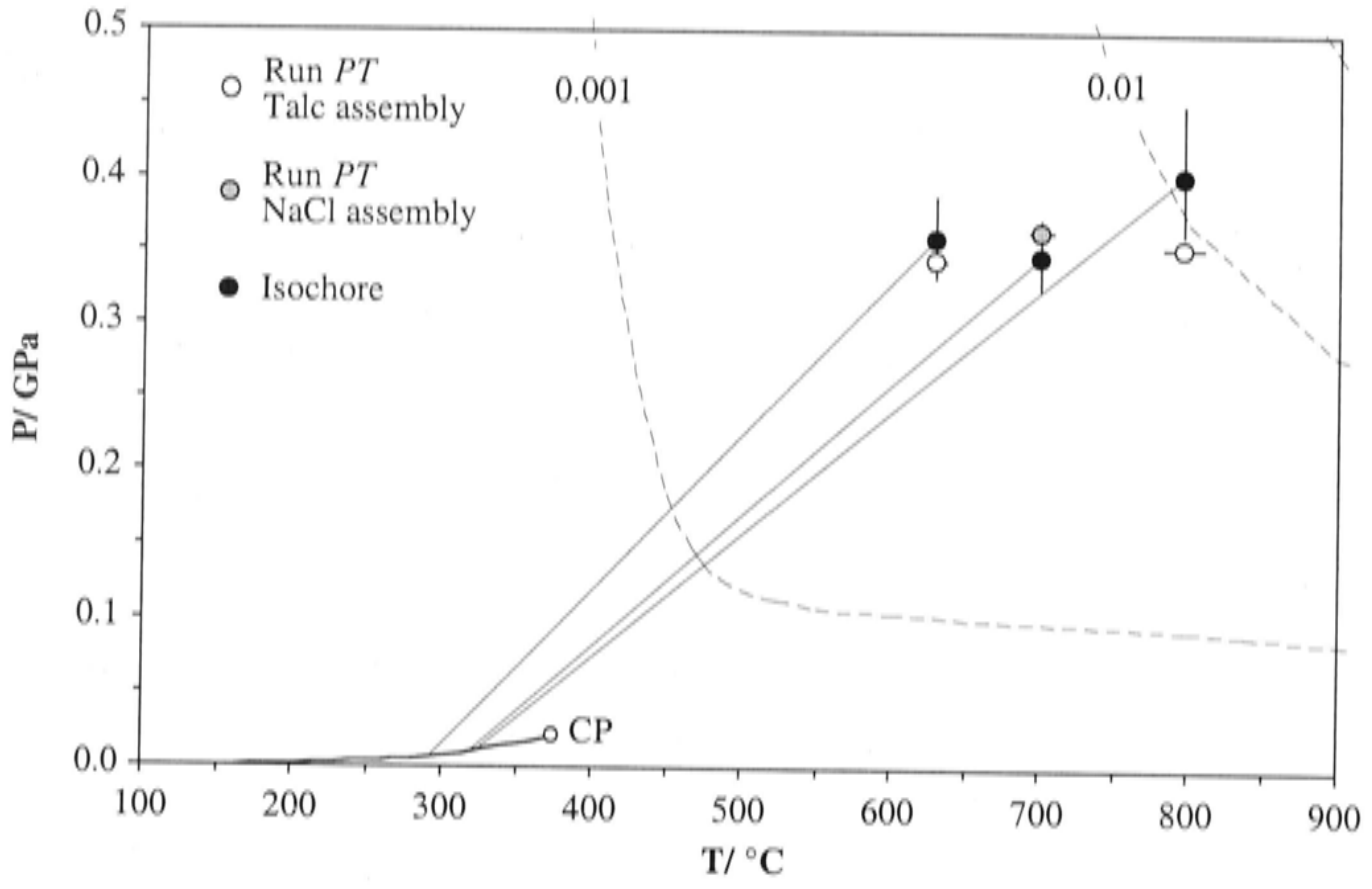

Figure 1.7 Comparison of the nominal experimental conditions with the average corrected *P* determined from the fluid inclusion isochore as a function of *P* and *T*. Experimental and measurement uncertainties are shown. Isochore extrapolated (solid line) from T_h on the pure water liquid-vapour curve using equation of Holland and Powell (1998). Piston-cylinder assembly type indicated. Quartz solubility mole fraction isopleths (0.001 and 0.01; dashed lines) shown (Manning 1994). The pure water liquid-vapour curve terminates at the critical point (CP).

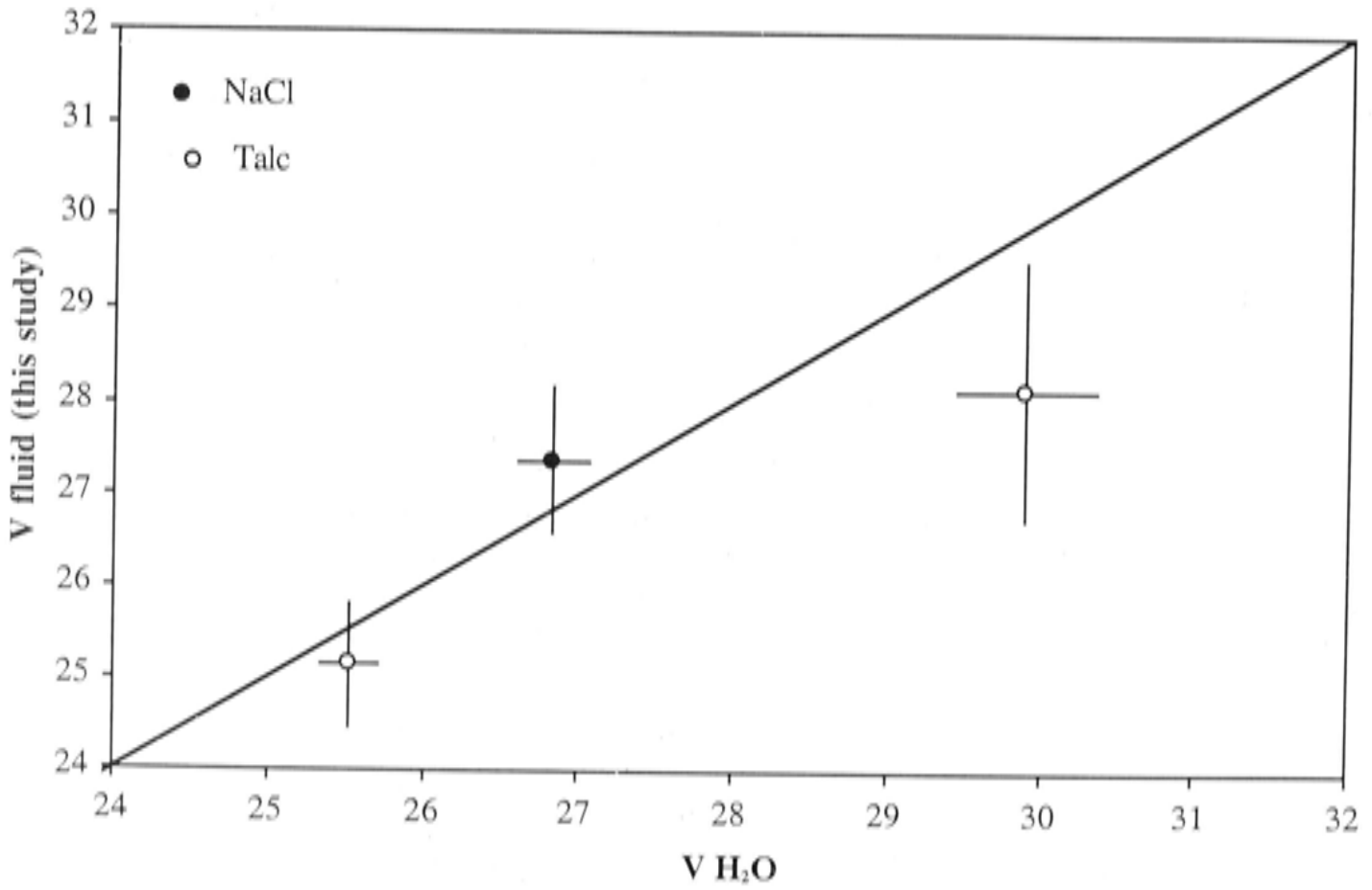

Figure 1.8 Comparison of the measured fluid volume, V_{fluid} ($=\overline{V}^{PTX}_{fluid}$), and the volume of pure water, V_{H_2O}, the same *P* and *T*. Units are cm^3/mol. Assembly type used indicated. V_{H_2O} predicted using the EOS of Holland and Powell (1998) associated errors reflects uncertainty in the run conditions.

These low-P experiments resulted in corrected fluid volumes that are indistinguishable from the volume of pure water at the same P and T with due consideration of the small experimental uncertainties. This is true, regardless of capsule material[3] or pressure assembly type. This indicates that the small amount of dissolved copper (not determined) and silica at these conditions, has no measurable effect on the PVT properties of the fluid and, importantly, that friction is negligible in our large volume piston-cylinder device. This latter finding is consistent with the work of Bose and Ganguly (1995), that is, friction is a time-dependent phenomenon that effectively decays to zero during long runs. Perhaps it is also significant that their data indicate that internal friction decay becomes more rapid as assembly size increases. Consequently, it seems that the friction correction concept is inapplicable when undertaking large volume, long-duration piston-cylinder runs (> 24 hours, *e.g.* fluid inclusion synthesis experiments), in either NaCl or talc-pyrophyllite assemblies at low-P. Specifically, no friction correction is required under these conditions.

[3] Unfortunately, T_h data could not be obtained from the quartz contained in the Cu capsule in R168 due to a lack of inclusions (crushed during run) and only Pt capsule data is available. Regardless, since inclusion data from all capsule and assembly types coincide with the nominal PT conditions, the effect of capsule material on the fluid PVT properties seems negligible in comparison with the uncertainties. Moreover, a similar conclusion is reached from higher-pressure PVT experiments, for which data from both capsules is available.

3. A note on synthetic fluid inclusions and attainment of fluid-mineral equilibrium in multi-component systems: Major elements

As mentioned earlier, the fluid inclusion method is in principle ideally suited to the study of mineral solubilities, however, one crucial requisite is that fluid-mineral equilibrium is achieved over the duration of the experiment. The length of time required to establish fluid-mineral equilibrium is usually determined by replicate experiments of different duration (*e.g.* Kennedy *et al.* 1962, Seward 1976 and Xiao *et al.* 1998). However, for inclusion experiments using pre-fractured minerals - the usual approach, the timing of fluid trapping cannot be controlled[4]. So, the question arises as to whether use of pre-cracked phases results in premature entrapment of non-equilibrated fluids in mineral-buffered experiments and should an in situ-fracturing or other method that delays the formation of fluid inclusions be used instead. This question is resolved simply by examining the compositional variation amongst individual fluid inclusion populations, since each inclusion represents an independent fluid sample potentially trapped at different, but unknown, times during the experiment.

To assess the compositional variability and thus attainment of equilibrium by fluids trapped using pre-fractured quartz in mineral-buffered experiments, LA-ICP-MS analysis was used to quantitatively measure the major and trace element concentration ratios of individual fluid inclusions (see *PART 2* for instrument and analytical technique details). Piston-cylinder experiments were undertaken using cold-sealed copper capsules and talc-pyrophyllite assemblies, as described above. Fluid inclusions were buffered by the assemblage quartz-orthoclase-sillimanite-magnetite-hematite-copper at ~ 700 °C and 0.35 GPa. Chloride was added as sylvite, KCl, to the starting fluid along with a range of trace elements. Cu, K, Na, and Sr were analysed. Cl and Fe could not be measured using the LA-ICP-MS instrument at RSES at the time owing to the presence of a prohibitively high-background from adjacent masses and interfering

---

[4] Although an in situ fracturing technique, which allows extended reaction times before inclusion trapping, has been developed for cold-seal, hydrothermal pressure media apparatus, it requires a rapid transit of the quartz α–β transition by changing the pressure (or temperature) to facilitate fracturing (Sterner 1992). Because of the relative fragility of piston-cylinder assemblies and differential response of each cell component to changes in pressure and temperature this technique was not attempted using our piston-cylinder apparatus. Regardless, attainment of equilibrium can still be demonstrated (see text).

molecular species respectively[5]. Petrographic examination after the run showed that fluid inclusions contain a vapour bubble, small sylvite and larger copper-salt daughter crystals (quench precipitates). All inclusions exhibit uniform phase ratios and re-homogenise on heating.

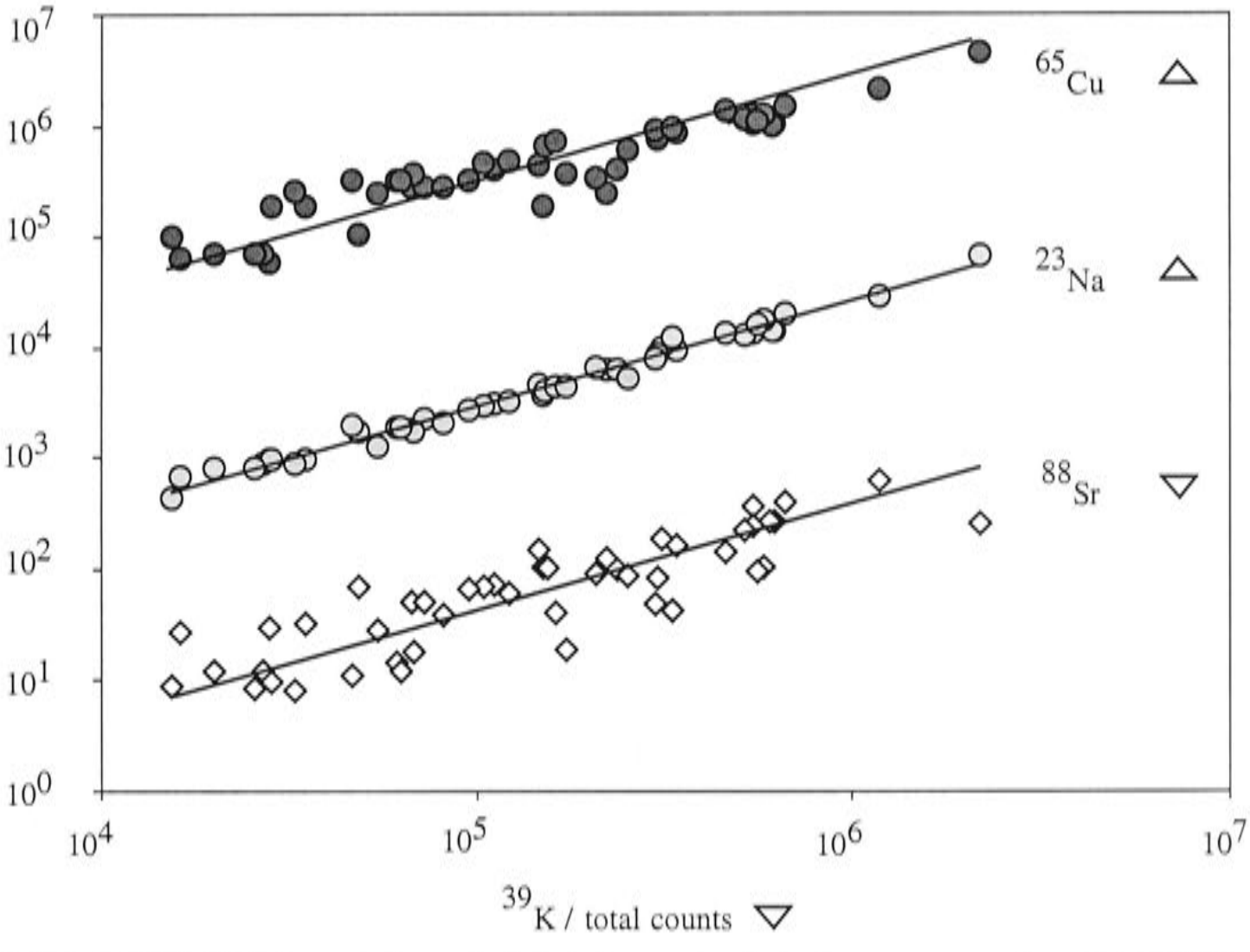

Figure 1.9 LA-ICP-MS time-integrated total counts data for measured masses ^{65}Cu, ^{23}Na, ^{88}Sr versus ^{39}K obtained from 47 individual fluid inclusions grown under mineral-buffered conditions in a piston-cylinder apparatus (AH87). The data are corrected for background counts. Compositional variation is within the analytical precision, consistent with fluid-mineral equilibrium. The direction taken to achieve measured ratios, relative to the initial fluid composition is indicated by the symbols △ and ▽which refer to initially under- and over-saturated fluid concentrations respectively.

LA-ICP-MS data for individual inclusions from a single experiment is presented in Figure 1.9 (further data related to trace element behaviour in this sample is presented in *PART 2, §5.12*). Because fluid inclusions release a transient signal on ablation, the total time-integrated intensity ratios are required for quantitative analysis. LA-ICP-MS total integrated signal intensity, which varies over about 2.5 orders of magnitude, can be used as a proxy for inclusion size as it is directly proportional to the

---

[5] At the time these measurements were made, the laser was coupled with a modified VG PQ2+ quadrupole ICP-MS. This ICP-MS, has subsequently been replaced by a more sensitive instrument (*PART 2*).

volume/mass of the analysed inclusion. Although some scatter in the data is apparent, the observed compositional variation is within the intrinsic precision of the LA-ICP-MS fluid inclusion analytical technique (*PART 2*). Therefore, no evidence was found to suggest that fluids are being trapped prematurely. Following this, it is reasonable to conclude that at the T and P of the experiment, fluid-mineral equilibrium is established rapidly at least on the time-scales associated with the hydrothermal healing of fractures and resultant stranding of fluid inclusions in quartz for the mineral-buffering assemblage used. In explanation, it is suggested that the prograde solubility of quartz results in active dissolution of fracture surfaces and conspires to prevent the early formation of inclusions thereby providing sufficient time for other mineral components to react and equilibrate with the fluid. Indeed, assuming initially silica under-saturated fluid conditions, healing of fractures should (in theory) only begin once the fluid attains the equilibrium dissolved silica concentration, a value which is dependant also on the concentration of the other solution components and so will be constantly changing until the entire system (major components at least) equilibrates.

4. Insights into the activity-composition relations of the SiO_2–H_2O system at high-pressure from *PVTX* measurements using synthetic quartz-hosted fluid inclusions

"The leading thermodynamic properties of a fluid are determined by the relations which exist between the volume, pressure, temperature, energy and entropy of a given mass of fluid in a state of thermodynamic equilibrium." **J.W. Gibbs (1906)**

4.1 Introduction

Silica solubility and SiO_2–H_2O phase relations are better understood than any other hydrothermal system. The experimental and theoretical effort expended on this system reflects its direct geological relevance and the fact that it provides a basic framework on which the behaviour of more complex rock-fluid systems can be understood. Given the extensive published literature, the reader could be forgiven for wondering what is left to know about this system? Yet, surprisingly, there remain fundamental gaps in our understanding of SiO_2–H_2O interactions. For instance, although quartz solubility has been comprehensively determined to 900 °C and 2.0 GPa (*e.g.* Kennedy 1950; Weill and Fyfe 1964; Anderson and Burnham 1965; Crerar and Anderson 1971; Fournier and Potter 1982; Manning 1994), the data are limited compositionally (up to a few mole percent), given that complete miscibility between hydrous SiO_2 melt and SiO_2-rich aqueous fluid is known to occur above the upper critical end point of 1080 °C and 0.97 GPa (Kennedy *et al.* 1962). Furthermore, activity-composition (a–X) relations have not been directly measured over the range of conditions spanned by current solubility data, let alone near or beyond the upper critical end point. For reference, the *PTX* topology of the SiO_2–H_2O system is shown in Figure 1.10. This figure was calculated using the quartz solubility data of Kennedy (1950), Kennedy *et al.* (1962), Nakamura (1974), and Manning (1994), pure water phase relations were taken from Haar *et al.* (1984), remaining parts of the diagram from Jackson (1976) and Guissani and Guillot (1996). Although details of the fields containing two immiscible fluids are experimentally unknown their general behaviour can be inferred based on simple phase relation requirements.

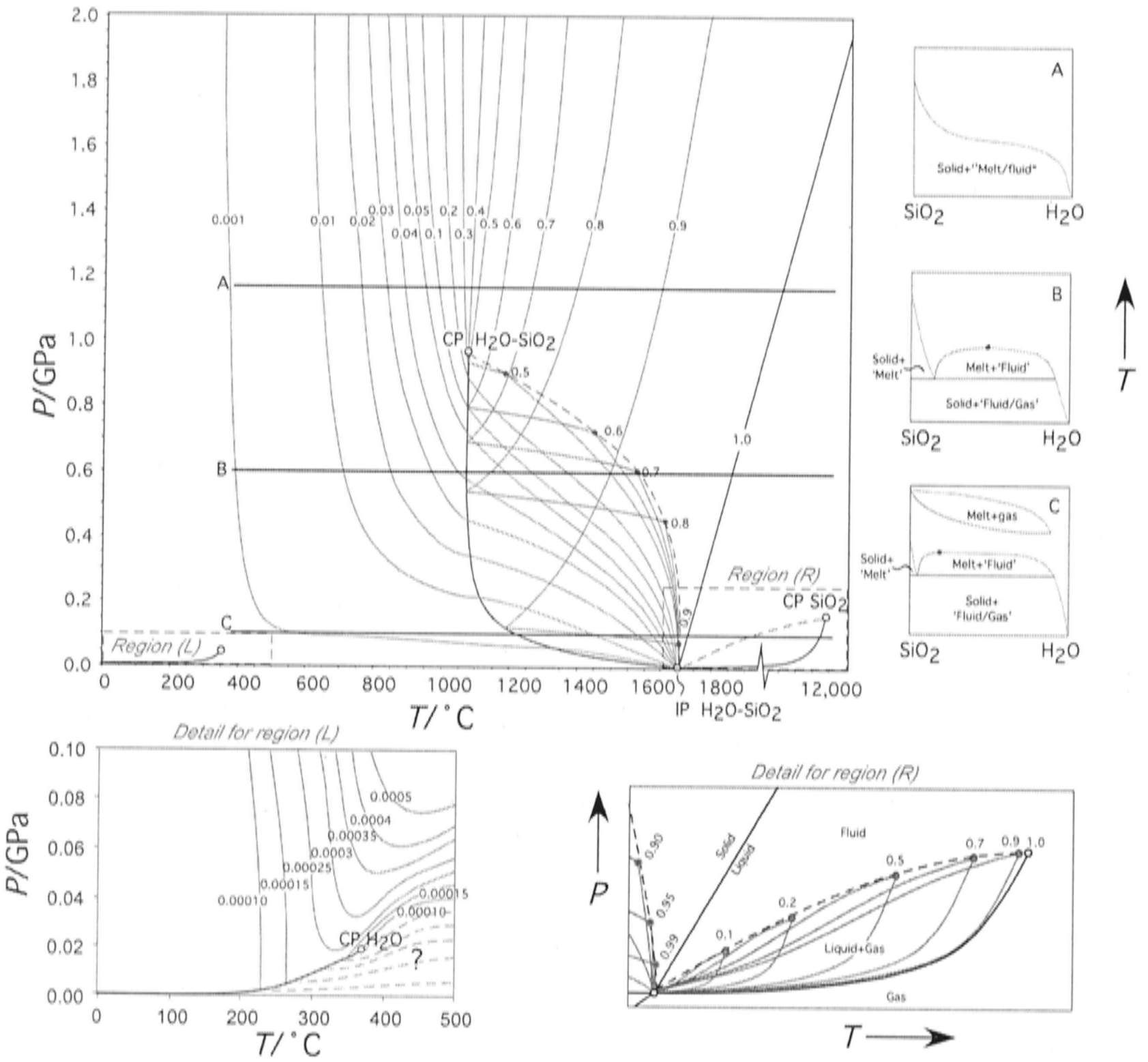

Figure 1.10 Solubility and phase relations of the SiO_2–H_2O system as function of P and T. Experimentally determined SiO_2 solubility isopleths (mole fraction units; Kennedy 1950; Nakamura 1974; Manning 1994) and important phase boundaries indicated (black lines). Critical end points (CP) in the pure H_2O (Haar *et al.* 1984), pure SiO_2 (Guissani and Guillot 1996) and SiO_2–H_2O (Kennedy *et al.* 1962) systems shown, as is an inferred invariant point (IP) in the SiO_2–H_2O system. For convenience, schematic isobaric T–X phase relations also shown for several P (sections A, B and C). Quartz solubility and other compositional isopleths are colour coded to their respective phase as given by isobaric T–X sections. Some features on these figures are inferred, such as isopleth values and their positions in the two PT regions in which immiscible fluids may occur and the specific locations of the upper termination of these fields, above which a complete continuum between hydrous SiO_2 melt and SiO_2-rich aqueous fluid exists (*i.e.* a single supercritical fluid phase).

Quartz solubility data can be used to interpret aqueous silica speciation and to obtain thermodynamic properties. These properties, together with standard thermodynamic data for other rock-forming minerals, allow calculation of SiO_2 solubilities in quartz-under saturated assemblages, for example, appropriate to the upper mantle. However, extraction of this kind of information requires understanding of a–X

relations in SiO_2–H_2O fluids. Initial thermodynamic investigations of quartz solubility (Walther and Helgeson 1977) led to the conclusion that the activity of H_2O is close to unity and that the activity coefficient of total dissolved silica $\left(\gamma_{SiO_2}^{fluid}\right)$, relative to the conventional infinitely dilute solution standard state, also remains unity up to a few mole percent SiO_2. The general expression describing this *a–X* relation is,

$$a_{SiO_2}^{fluid} = \gamma_{SiO_2}^{fluid} \cdot m_{SiO_2}^{fluid}$$

where, $a_{SiO_2}^{fluid}$, $\gamma_{SiO_2}^{fluid}$ and $m_{SiO_2}^{fluid}$ refer to the activity, the activity coefficient describing SiO_2–H_2O interactions, and the concentration of aqueous silica in mol/kg, respectively. In other words, *a–X* relations in SiO_2–H_2O fluids are considered essentially ideal in nature over the range of existing measurements, that is $a_{SiO_2}^{fluid} = m_{SiO_2}^{fluid}$ (*cf.* Manning 1994; Wasserman *et al.* 1995).

The hydration of dissolved silica in quartz-saturated H_2O was investigated to 0.5 GPa and 900 °C by Walther and Orville (1983) using existing quartz solubility data in CO_2–H_2O mixtures[6] and their own data for Ar–H_2O fluids. The general quartz solubility reaction was considered, as in previous and subsequent studies,

$$SiO_{2\,(quartz)} + nH_2O = SiO_2 \cdot nH_2O_{(aq)} \qquad [1.2]$$

where, $SiO_2 \cdot nH_2O_{(aq)}$ refers to the dissolved silica species and n denotes the total hydration number. Like Walther and Helgeson (1977), they also arrived at the conclusion, that the dominant aqueous silica species was a neutral complex represented by the formula $Si(OH)_4^0$ with one to three hydrogen-bonded (solvated) H_2O molecules (*i.e.* $Si(OH)_4^0 \cdot n_sH_2O$, where n_s refers to the number of solvated water molecules in the hydration shell). A similar investigation of *a–X* relations using CO_2–H_2O and NaCl–H_2O mixtures was undertaken by Newton and Manning (2000). They also identified $Si(OH)_4^0$ solvated by one to three H_2O molecules as the dominant complex controlling quartz solubility at 800 °C and 1.0 GPa from their CO_2–H_2O data. Interpretation of the NaCl–H_2O data is not straightforward as there is significant

[6] Most of these CO_2–H_2O experimental data are contained in an unpublished M.S. thesis (Shettel 1974).

uncertainty as to whether NaCl can be considered inert or if it is involved in silica complexation (Anderson and Burnham 1983; Xie and Walther 1993; Newton and Manning 2000). It should be noted that these studies cover most of the compositional space, if not P and T, encompassed by the existing solubility data, and suggest that silica speciation is essentially constant over this range. Importantly, it should also be emphasised that these "conventional" interpretations of the silica hydration state rely entirely on the assumption that the solute is dissolved as monomers with the stoichiometry SiO_2, if this is not the case and dimers or higher polymers occur the solution becomes non-unique.

Indeed, recently questions have been raised over the nature of SiO_2–H_2O interactions and the "conventional" monomeric view of the solute from two independent directions.

The first is that calculations using conventional aqueous silica properties with $\gamma_{SiO_2}^{fluid} = 1$, combined with standard thermodynamic data for minerals, grossly over estimate recent phase equilibrium data and silica solubility measurements in the quartz-undersaturated part of the MgO–SiO_2–H_2O system (Manning and Boettcher 1994; Zhang and Frantz 2000; Newton and Manning 2002). The data in question refer to silica solubility buffered by the equilibrium,

$$Mg_2Si_2O_{6\,(enstatite)} = Mg_2SiO_{4\,(forsterite)} + SiO_{2\,(aq)} \qquad [1.3]$$

where, $SiO_{2\,(aq)}$ represents the solvated silica species independent of the hydration state (Walther and Helgeson 1977) in equilibrium with enstatite and forsterite. As in the case of quartz solubility, the identity of the silica complex is ignored if solvation is accounted for implicitly in the thermodynamic properties. This simplification is justified if the activity of H_2O is close to unity. These enstatite + forsterite solubility data cover the ranges, 700 to 1310 °C and 0.4 to 2.0 GPa, similar to the solubility measurements in the SiO_2–H_2O system, albeit somewhat less comprehensively. There is, however, a degree of consistency between the silica under-saturated and quartz solubility datasets at low-P, as the 0.1 GPa solubility data of Hemley *et al.* (1977) for equilibrium [1.3], are predicted assuming the conventional $Si(OH)_4^0$ species properties and $\gamma_{SiO_2}^{fluid} = 1$, as inferred from the quartz data.

In order to reconcile the discrepancy between the unexpectedly low silica solubility in enstatite + forsterite buffered H_2O with that predicted from the quartz solubility data, both Zhang and Frantz (2000) and Newton and Manning (2002) argued that, despite the low concentrations of total dissolved silica (*e.g.* < 1 mol% SiO_2 at 900 °C, 1.0 GPa), $\gamma_{SiO_2}^{fluid}$ was much less than unity, and that this was almost certainly due to polymerisation of the aqueous silica. Newton and Manning (2002) went further, calculating the required $\gamma_{SiO_2}^{fluid}$ for a number of polymerisation models such that the various solubility datasets came to agreement. It was pointed out, however, that the existing data did not define a unique solution and that the inclusion of additional solvation effects to the simple aqueous monomer ($Si(OH)_4^0 \cdot n_s H_2O$, *e.g.* Walther and Orville 1983) at a given P and T would produce an equally consistent solution.

Essentially the same conclusion, that the existing speciation model was inadequate for explaining the full range of observed phenomena, was reached by Zotov and Keppler (2000, 2002) using an entirely different approach. They undertook in situ Raman spectroscopy experiments to 900 °C and 1.4 GPa of quartz-saturated H_2O using an externally-heated diamond anvil apparatus. Although the spectra are clearly dominated over the complete range of conditions investigated by sharp band at 760–785 cm^{-1} corresponding to the $Si(OH)_4^0$ species, above about 0.5 GPa new spectral features, diffuse broad peaks at 630, 920 and 230 cm^{-1}, were observed. These observations were taken to imply a fundamental change in the solute structure occurring at ~ 0.5 GPa, contrary to the usual assumption (*e.g.* Manning 1994), but supported by the enstatite solubility results. Again, progressive silica polymerisation with increasing P and T was used to explain the appearance of the new spectral bands. Specifically, Zotov and Keppler (2000, 2002) assigned the new bands, on the basis of ab initio molecular orbital calculations, to an $H_6Si_2O_{7\,(aq)}^0$ molecule, which it was argued formed via the dehydration reaction, $2Si(OH)_{4\,(aq)}^0 = H_6Si_2O_{7\,(aq)}^0 + H_2O$. This general interpretation of the Raman data may be consistent with the interpretations based on existing solubility data.

Although the various data sets are entirely appropriate for constraining a–X relations, they do not uniquely define them. It is clear, however, that in detail the underlying assumptions of ideal solution behaviour currently used to interpret quartz

solubility are inadequate. Explaining the observed non-ideality[7] by polymerisation of the dissolved silica (Zhang and Frantz 2000; Zotov and Keppler 2000; Newton and Manning 2002; Zotov and Keppler 2002) is an attractive option as above 1.0 GPa, in the SiO_2–H_2O system, a continuum exists between dilute H_2O-rich fluids and hydrous silica melt, in which the silica is likely to be dominantly polymerised (Figure 1.10). Indeed, this reality demands the inclusion of polymerisation, but what is equally obvious is that the activity of H_2O must also be explicitly treated as the dissolved silica content increases rapidly to melt-like concentrations near the upper critical point and the mole fraction of water departs significantly from unity.

Leaving aside complications associated with supercritical behaviour for the moment, as these can only be addressed by future solubility and activity determinations, understanding the nature of the existing measurements in the SiO_2–H_2O system, and relevant others, is the first step towards a holistic model but remains limited by the lack of experimental a–X data at high-P and T.

---

[7] 'Non-ideality' refers to the need to resort to the use of activity coefficients for dissolved silica which vary from the ideal value of one as a function of its concentration in order to reconcile the different silica solubility datasets within a traditional monomer species solution model (*e.g.* as used by Walther and Orville 1983).

4.2 Determination of activity-composition relations using *PVT* measurements

Activity-composition (*a–X*) relations are routinely obtained in two-component fluids by measuring the *PVT* properties of known mixtures of the two components (*e.g.* CO_2–H_2O, Sterner and Bodnar 1991; Frost and Wood 1997). In principle, SiO_2 + H_2O fluids can be studied in a completely analogous way.

Earlier it was shown that fluid volumes in the SiO_2–H_2O system are readily measurable using quartz-hosted fluid inclusions, though it was argued that quartz-saturated fluid volumes at *P* less than about 0.5 GPa are essentially indistinguishable from pure H_2O, because solubilities are very low (*PART 1, §2.3*). However, further *PVTX* type experiments at higher *P* at comparable total dissolved silica concentrations, produced fluids with apparently anomalous volumes, but it was noted these varied systematically with respect to *PTX* conditions. Since the low-*P* experiments established the force-pressure relation in a piston-cylinder apparatus as being essentially friction-free, a situation likely to remain true at higher *P*, it can be concluded that the experimental *P* (and *T*) is well known. The volumetric properties of the SiO_2–H_2O fluid at high-*P* and *T*, on the other hand, are unknown.

Fluid inclusion measurements appear to be sufficiently sensitive to fluid volume that they can be used to measure *PVT* relations. Such measurements in conjunction with solubility data, as pointed out by Anderson and Burnham (1962), provide another vantage point from which to view SiO_2–H_2O interactions and derive silica speciation details and thermodynamic properties. Thus, a series of *PVTX* measurements of quartz-saturated fluids were carried out in order to help further constrain *a–X* relations in the simple system. The details of the experimental method, measurement procedure and error calculation used for determining the *PVTX* properties are as described in *PART 1, §2.3*.

4.3 Experimental conditions investigated and remarks on the limitations of the technique

The range of *PVTX* conditions amenable to study in the SiO_2–H_2O system using quartz-hosted fluid inclusions are limited by the sensitivity of the measurements to fluid volumes, intrinsic physical strength of the host mineral, the general phase relations of the system and the extent to which these are known.

At low-*P*, where quartz-saturated fluids have low dissolved SiO_2 concentrations (to a mole percent or so), the fluid inclusion technique simply is not sensitive enough to discriminate between the volumetric properties of SiO_2–H_2O fluids and pure water (Bodnar and Sterner 1985; Sterner and Bodnar 1991; *this study*). However, at higher *P* and with increasing solute concentrations, fluid inclusions can be used to provide reasonable volume measurements of the fluid mixture.

Fluid inclusions trapped at *P* and *T* where the density of H_2O is 1 to 1.25 g/cm^3, quenched along an isochoric path to ambient conditions will remain a single liquid phase, such that no vapour bubble nucleates on cooling. At fluid densities above 1.25 g/cm^3, solid ice (several polymorphs are possible depending on the *P*) is the stable phase at ambient *T*. All such high-density fluid inclusions (> 1 g/cm^3) are internally over-pressured at ambient conditions. In this case, liquid densities may be determined from freezing point depression measurements. The *P* exerted by high-density fluid can be enormous, *e.g.* H_2O at the highest liquid densities stable at 25 °C exerts almost 1 GPa on the host mineral (Wagner *et al.* 1994). Because quartz has a limited strength, extremely dense fluids at ambient conditions simply cannot be quenched as they rupture from internal over-pressuring on cooling. Fluid inclusions in quartz rarely survive differential stresses over about 0.15 GPa, limiting the use of quartz to pure water densities generally less than ~ 1.1 g/cm^3 and without any problems at densities < 1 g/cm^3 (Figure 1.11). The same problem, decrepitation, is observed in high-*T* heating experiments on lower density fluid inclusions once the inclusion leaves the liquid-vapour coexistence curve. A further difficulty in studying high-density liquid H_2O inclusions is that freezing point depression measurements are complicated by metastable ice nucleation and optical identification of the ice polymorphs (Evans 1967; Haselton *et al.* 1995) such that liquid H_2O densities along the ice melting curve are difficult (but not impossible) to determine by this method (*e.g.* Withers *et al.* 2000).

Although *PVT* properties may be obtained by the quartz-hosted fluid inclusion method outside of the "ultra-high density region" (> ~ 1 g/cm^3), the interpretation of such measurements is somewhat limited by our understanding of the fluid composition at the *T* and *P* of interest. Since quartz solubility data exist only to 900 °C and 2.0 GPa (Manning 1994) and along the upper three-phase curve (vapour-saturated SiO_2–H_2O solidus; Kennedy *et al.* 1962) this constrains the immediate usefulness of any volumetric measurements to this region. The vapour-saturated hydrous silica melt region is probably beyond the practical bounds of this technique, as quartz is only stable together with hydrous SiO_2 melt (Liq_1, in Figure 1.10) and not with the H_2O-rich fluid phase (Figure 1.11).

With regards to the determination of the *PVT* properties of fluids in the ultra-high-density region (and possibly the vapour-saturated SiO_2-hydrous melt region), slight modification of the experimental technique described by Larrieu and Ayers (1997), to mineral-saturated conditions rather than pure fluids may prove to be useful. The method involves the measurement of the initial and deformed volume of a thick-walled metal capsule (similar in design to the one used in this study) after the experiment in order to extract the *PVT* fluid properties. Combined with standard weight loss-type solubility measurements in the same experiment, mineral-saturated fluid *PVTX* determinations could be made. Alternatively, redox sensors that are sensitive to the activity of water, like the type described by Taylor *et al.* (1992) and Pownceby and O'Neill (1994, 1995, 2000), could be used.

The experimental conditions investigated were thus limited to those for which solubility data exist and, generally, to the region for which the density of H_2O is less than 1 g/cm^3 (Figure 1.11).

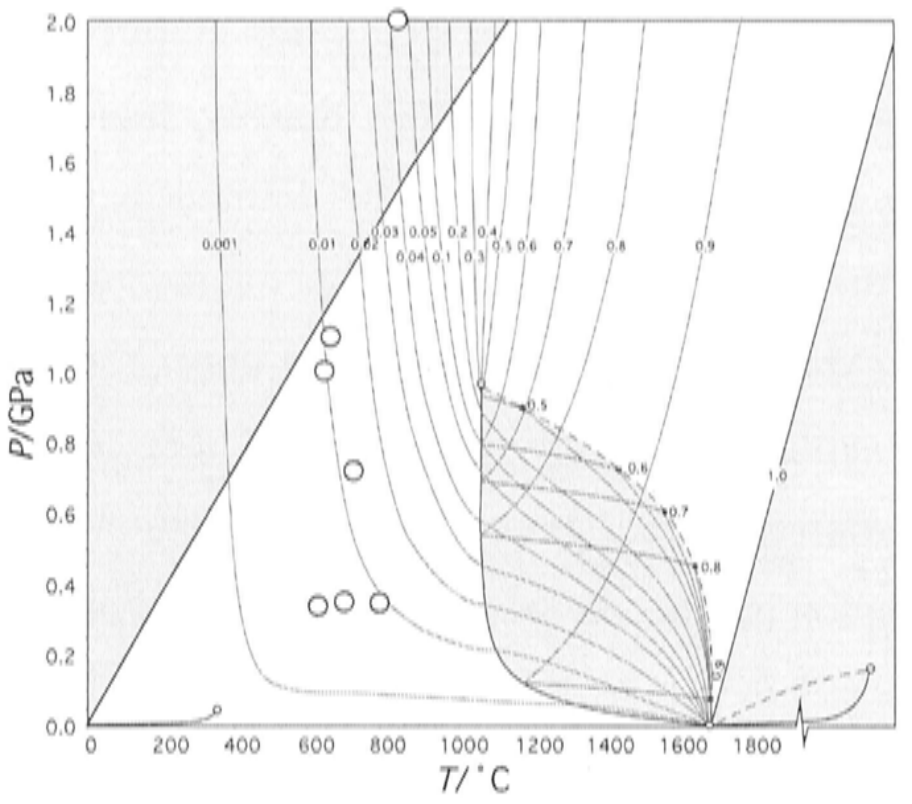

Figure 1.11 ***P*** **and** ***T*** **diagram indicating region accessible to fluid inclusion study of the** ***PVTX*** **properties of quartz-saturated H_2O (at least in principle). Solid dots mark the location of the experiments undertaken in this study. Shaded areas represent "forbidden" regions and include the vapour-saturated melt field in the SiO_2–H_2O system, the region for which the density of pure H_2O fluid is greater than 1 g/cm^3 (calculated using the EOS of Holland and Powell, 1998) and the liquid-only region above the pure SiO_2 liquidus. Other features are as described in Figure 1.10.**

4.4 Experimental data

Fluid inclusion *PVTX* measurements, and their uncertainty, for quartz-saturated SiO_2–H_2O fluids are given in Table 1.2. Figures 1.12 and 1.13 illustrate the extent to which SiO_2–H_2O fluid volumes deviate from those of pure H_2O. In Figure 1.12 fluid volume data are represented in terms of the position of the apparent isochore in P and T space, calculated from the T_h measurement assuming the fluid behaved as pure H_2O, and compared with the actual run conditions. The data obtained at low-P (~ 0.35 GPa series, plotted similarly in Figure 1.7) are also shown together with quartz solubility isopleths. Figure 1.13 compares directly the measured fluid volume with that of pure H_2O, calculated using the EOS of Holland and Powell (1998), at the same conditions.

Table 1.2 Fluid inclusion *PVTX* data for SiO_2–H_2O fluids at high-pressure

Run	Assembly	T/°C	P/ GPa	T_h^{ave}	n	σ_{T_h}	$\overline{V}^{T_h}_{\min}$	$\overline{V}^{T_h}_{\max}$	$\overline{V}^{T_h}_{ave}$	$\overline{V}^{PT}_{fluid}$	$X^{PT}_{SiO_{2(aq)}}$	$\overline{V}^{PTX}_{fluid}$	$\sigma^{PTX}_{\overline{V}}$
R144	Talc/Cu	665 (8)	1.091 (0.012)	163.5	4	1.3	19.90	19.97	19.94	19.94	0.0114	20.20	0.46
R147	Talc/Cu	725 (8)	0.715 (0.003)	250.0	6	3.0	22.43	22.68	22.55	22.62	0.0126	22.91	0.57
R165*	Talc/Pt	665 (6)	1.104 (0.005)	156.7	7	4.7	19.69	19.92	19.81	19.81	0.0115	20.07	0.46
R167*	NaCl/Pt	650 (6)	1.001 (0.006)	161.9	8	0.7	19.88	19.92	19.90	19.91	0.0099	20.13	0.46
R188**	NaCl/Pt	850 (10)	2.000 (0.006)	-19.3	3	0.9	16.51	16.59	16.57	16.57	0.0464	17.67	0.46

Notes: Volume measurements in units of cm^3/mol. * Double capsule experiment using a standard pure Cu primary capsule, inner Pt capsule data given. ** Double capsule experiment using a pure Ag primary capsule, inner Pt capsule freezing point depression (final melting) data given as H_2O density > 1 g/cm^3 at ambient conditions in this run. H_2O ice melting curves and liquid densities along it, required for determining the R188 isochore, were calculated from Wagner *et al.* (1994) and the EOS of Saul and Wagner (1989) respectively. Refer to Table 1.1 notes for other information relating to this table.

The effect of the capsule material on the measured fluid volumes appears to be negligible as $\overline{V}^{PTX}_{fluid}$ measurements from R144 (Cu capsule) and R165 (Pt capsule), that were run at similar P and T conditions and using the same cell assembly, are within error of each other (Table 1.2).

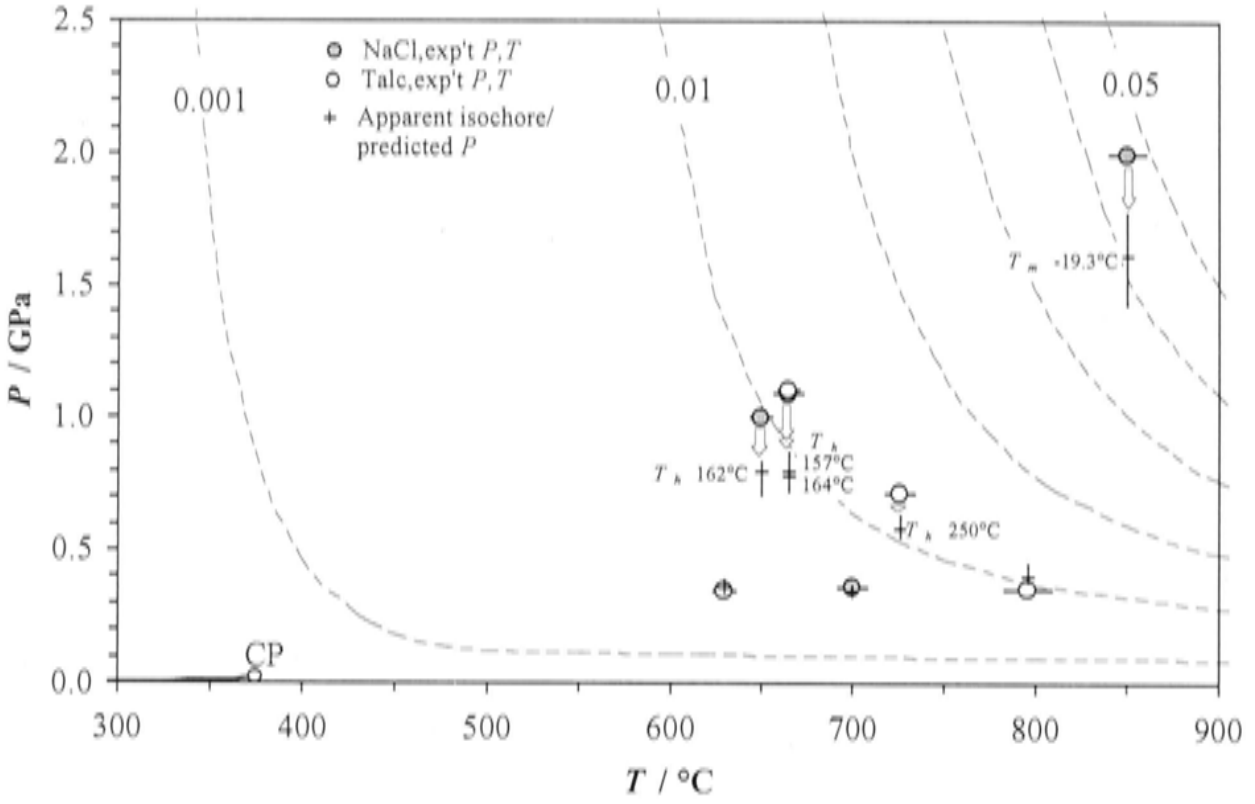

Figure 1.12 Comparison of the predicted *P* and actual experimental *P* and *T* conditions. Crosses ("apparent isochore/predicted *P*") give the position and uncertainty in *P* of the apparent isochore assuming a "pure H_2O fluid" at the experimental *T* (Holland and Powell 1998). Arrows indicate the apparent isochore offset direction relative to P_fT_f. T_h (>0.35 GPa) given for reference. Experiments at ~ 0.35 GPa are those used for assessing possible friction error effects. Critical point of pure water (CP) and various quartz solubility isopleths (mole fraction; Manning 1994) are also shown.

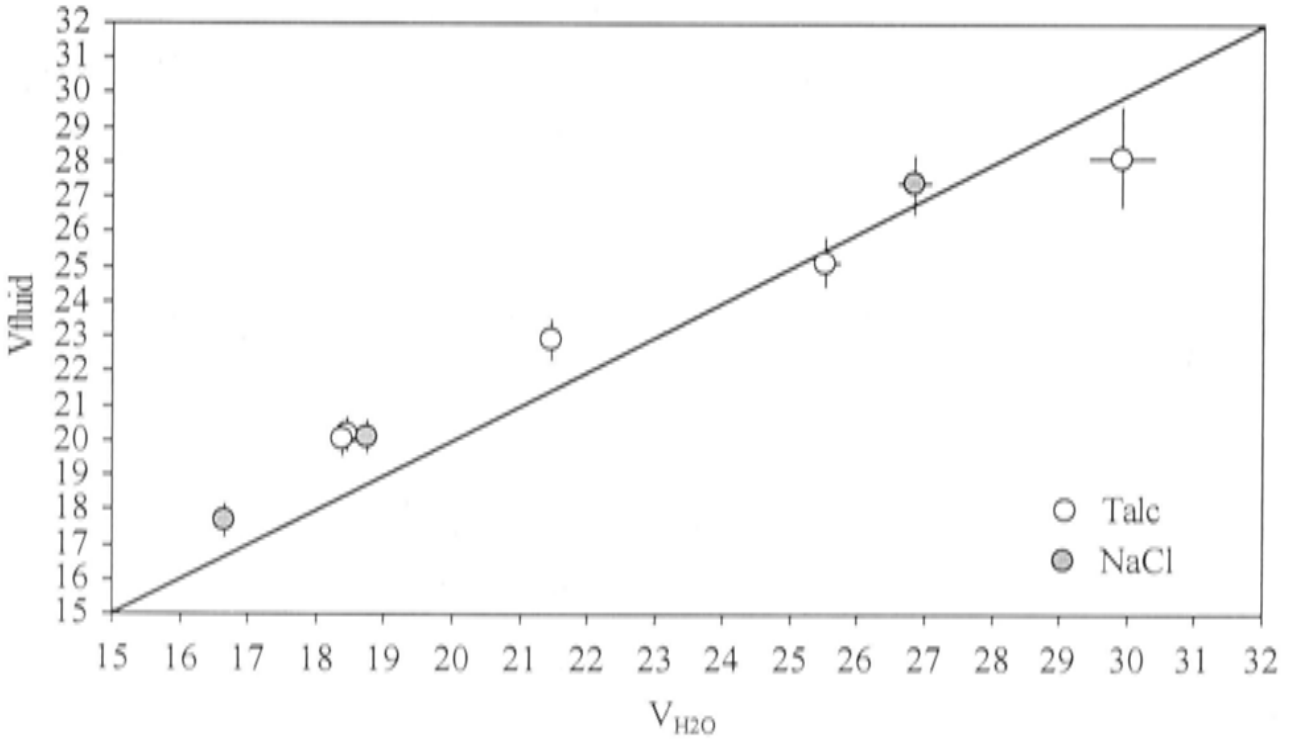

Figure 1.13 Comparison of the measured SiO_2–H_2O fluid volume (Vfluid = $\overline{V}_{fluid}^{PTX}$) and the volume of pure H_2O (V_{H_2O}) at the same *P* and *T*. V_{H_2O} calculated using the EOS of Holland Powell (1998). Errors associated with V_{H_2O} correspond to the small uncertainties in the experimental *PT* conditions and are smaller than the symbols in some instances. Piston-cylinder assembly type in which each experiment was undertaken is indicated. Low-*P*, ~ 0.35 GPa data generally overlap 1:1 line within their uncertainty.

4.5 Discussion

There is a distinct difference between the calculated volume of pure water and the measured volume of SiO_2–H_2O fluids at high-*P*. This raises the question, what can be inferred from these data? To answer this, the complete two-component system should be considered (unlike at low-*P*; *PART 1, §2.3*). However, before moving towards an interpretation of the data, a discussion of a possible alternative explanation is warranted.

4.5.1 Equation of state of water

Concerns that such anomalous volumes may be the result of internal friction effects in a piston-cylinder apparatus are found to be groundless, as such phenomena would likely be more pronounced in the low-*P* data but, as pointed out earlier, they are not.

Another potential explanation for the data is that the equation of state (EOS) for pure water by which the measured fluid isochores are extrapolated to the experimental conditions is in error at these conditions, namely Holland and Powell (1998), indeed relatively small errors in the EOS volume translates into a large *P* uncertainty, as illustrated in Figure 1.12. It is well known that there is substantial variation between pure water EOS, especially at high-*P* (>1.5 GPa; *cf.* Withers *et al.* 2000). However, the original formulation of the equation given by Holland and Powell (1991) fit the available measured volume data in the range 0–5.0 GPa and 100–1400 °C to ±0.49% (average absolute deviation). The Holland and Powell (1998) equation of state, contains some minor revisions to the original fit parameters, to adjust the equation into accordance with new data that had become available, and represents the most recent form. Although the fitting was optimised for fugacity determination, because extraction of reliable free energies for H_2O was their primary aim, the stated precision at which volumes may be calculated, compared to experimental values, is still well within the measurement uncertainty at which fluid volumes can be determined using the fluid inclusion technique. In addition, few other EOS provide a continuous, consistent coverage of the full range of *P* and *T* space covered by the experiments presented here, and so, complications that might arise from the use of multiple independent equations to interpret the data set are avoided.

Although a deficiency in the EOS for pure water cannot be definitively ruled out, there is good reason to believe that these data represent reliable volume measurements of SiO_2–H_2O fluid mixtures at elevated P and T.

4.5.2 Comparison of end-member properties, ideal fluids and measurements - Another look at the data

The volume of a real SiO_2–H_2O fluid can be described, conveniently, as the sum of the molar properties of the two components,

$$\overline{V}_{fluid}^{PTX} = X_{H_2O} \cdot \overline{V}_{H_2O}^{fluid} + X_{SiO_2} \cdot \overline{V}_{SiO_2}^{fluid} \qquad [1.4]$$

Since all parameters in Equation [1.4] are known from experimental measurement, except for $\overline{V}_{SiO_2}^{fluid}$ and $\overline{V}_{H_2O}^{fluid}$ the source of the deviation must lie within these terms. Although these values cannot be obtained independently from the available data, the plausible possibilities are limited, as will be shown.

In Equation [1.4] the effects on volume caused by SiO_2–H_2O interactions are implicitly accounted for, that is, the volume terms refer to the actual partial molar properties of the components, not the pure substances. An alternate expression can be written describing the real fluid volume in terms of the properties of the pure substances, SiO_2 and H_2O, in their liquid states, which are known experimentally. Additional terms, namely, activity coefficients $\left(\gamma_i^{fluid}\right)$, are then used to correct for any non-ideal behaviour when the end-member components are mixed,

$$\overline{V}_{fluid}^{PTX} = \left(\gamma_{H_2O}^{fluid} \cdot X_{H_2O} \cdot \overline{V}_{H_2O}^{end\ member}\right) + \left(\gamma_{SiO_2}^{fluid} \cdot X_{SiO_2} \cdot \overline{V}_{SiO_2}^{end\ member}\right) \qquad [1.5]$$

By assuming that $\gamma_i^{fluid} = 1$, Equation [1.5] simplifies to give the expression for the ideal SiO_2–H_2O fluid[8],

$$\overline{V}_{fluid}^{ideal} = \left(X_{H_2O} \cdot \overline{V}_{H_2O}^{end\ member}\right) + \left(X_{SiO_2} \cdot \overline{V}_{SiO_2}^{end\ member}\right) \qquad [1.6]$$

---

[8] The ideal fluid function can be related to the real fluid volume via a standard expression,
$\overline{V}_{fluid}^{PTX} = \overline{V}_{fluid}^{ideal} + \overline{V}_{fluid}^{excess}$

Here, the γ_i^{fluid} terms are combined in the excess volume parameter, $\overline{V}_{fluid}^{excess}$.

It is instructive to contrast the real fluid volume against the calculated ideal volume and that of the end-members, as this potentially allows the dominant unknown terms, $\overline{V}_{SiO_2}^{fluid}$ and/or $\overline{V}_{H_2O}^{fluid}$, to be identified. The partial molar properties of the various pure liquid end-member components at the P and T of interest, along with the experimental conditions, fluid composition and calculated ideal fluid volume are presented in Table 1.3.

Table 1.3 Partial volume data for various components in the SiO_2–H_2O system and calculated ideal quartz-saturated fluid volumes at high-pressure

Experimental *PTX* fluid details				Liquid state end-member partial molar volumes				Calculated ideal fluid volumes[5]	
Run	T/°C	P/GPa	$X_{SiO_{2(aq)}}^{PT}$	$\overline{V}_{H_2O}^{pure}$ [1]	$\overline{V}_{H_2O}^{melt}$ [2]	$\overline{V}_{SiO_2}^{liquid}$ [3]	$\overline{V}_{SiO_2}^{melt}$ [4]	$\overline{V}_{SiO_2-H_2O\ melt}^{ideal}$	$\overline{V}_{fluid}^{ideal}$
R144	665	1.091	0.0114	18.45	16.28	25.11	25.40	16.39	18.51
R147	725	0.715	0.0126	21.45	18.04	25.25	25.73	18.14	21.49
R165	665	1.104	0.0115	18.39	16.24	25.11	25.39	16.35	18.47
R167	650	1.001	0.0099	18.75	16.42	25.08	25.48	16.51	18.81
R188	850	2.000	0.0464	16.67	15.17	25.51	24.61	15.61	17.08

Notes: 1) Partial molar volume of pure H_2O at the P and T of interest (Holland Powell 1998);
2) Partial molar volume of H_2O in a hypothetical silicate melt at the P and T of interest (Ochs and Lange 1997);
3) Partial molar volume of pure SiO_2 in its liquid state (albeit supercooled) at the P and T of interest (Mao *et al.* 2001);
4) Partial molar volume of SiO_2 in a hypothetical silicate melt at the P and T of interest (Gaetani *et al.* 1998); and
5) Calculated using expression [1.6], $\overline{V}_{fluid}^{ideal}$ and $\overline{V}_{SiO_2-H_2O\ melt}^{ideal}$ are the fluid volumes calculated assuming ideal mixing between either the pure liquid SiO_2 and H_2O end-members or the partial molar properties of the components as determined for silicate melts.

A number of features are especially apparent when the data in the Table 1.3 are examined graphically. Figure 1.14 illustrates the relation between the end-member components, an ideal mixture of these and the experimental measurement. Shown in Figure 1.15 is the relation between the measured fluid volume relative to the predicted ideal fluid volume as a function of the dissolved silica concentration at the P and T of interest.

It is clear from Figure 1.14 that the fluids considered in this study are sufficiently dilute that the $X_{H_2O} \cdot \overline{V}_{H_2O}^{fluid}$ term dominates the volume expression [1.4], but also, it is significant that the $\overline{V}_{SiO_2}^{fluid}$ term is unlikely to account for the volume changes necessary to satisfy the volume excesses determined, if $\overline{V}_{SiO_2}^{liquid}$ is any indication.

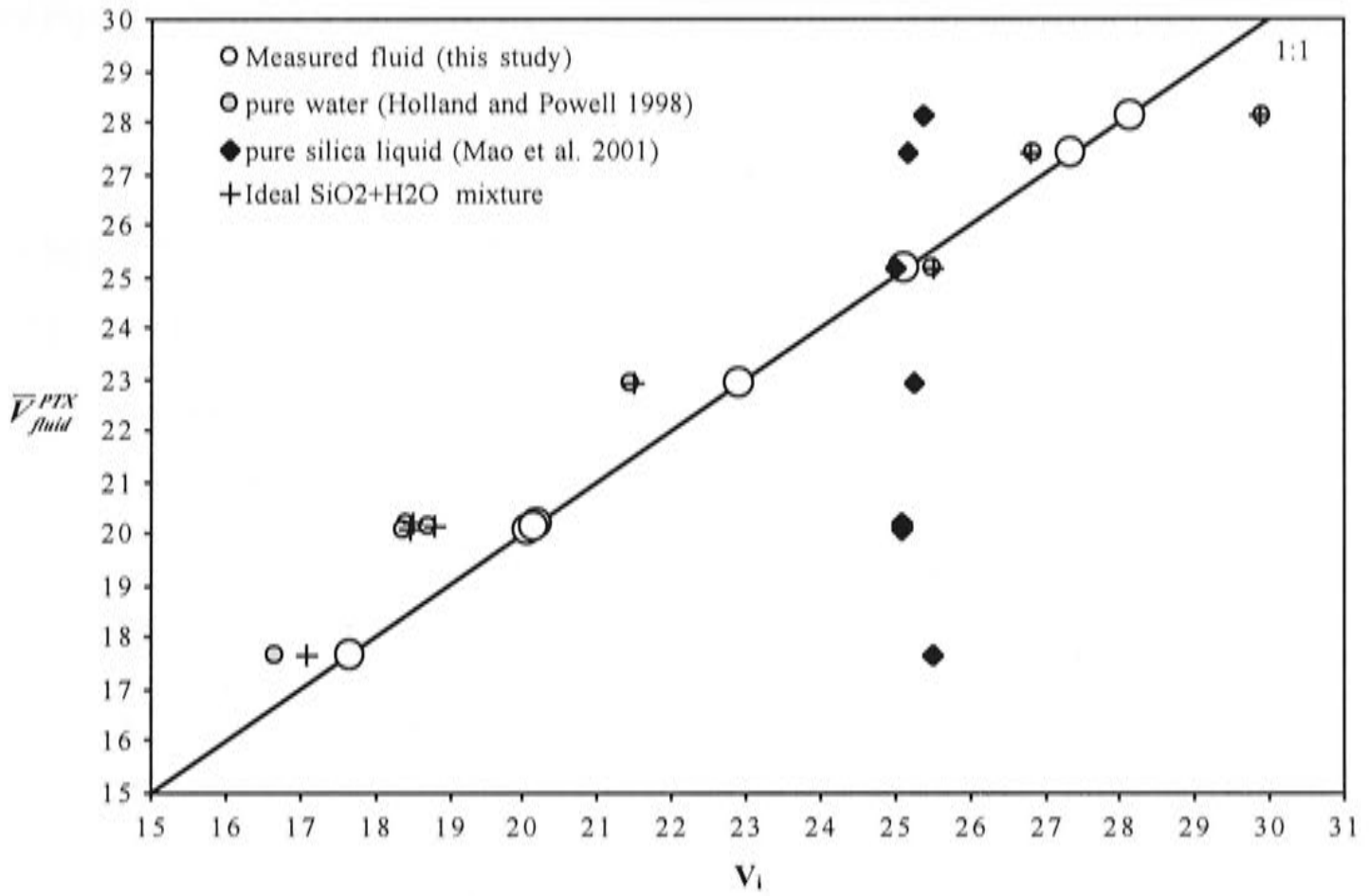

Figure 1.14 Comparison of the experimentally measured SiO_2–H_2O fluid volume, $\overline{V}^{PTX}_{fluid}$, the volume of pure silica liquid and pure H_2O end-members and the volume of an ideal mixture of the pure components (V_i) at the same *P* and *T* (Table 1.3). Units are cm^3/mol. Low-*P*, ~ 0.35 GPa, *PVTX* fluid data also plotted. Solid line (1:1) indicates the case where the calculated and measured fluid volumes would coincide.

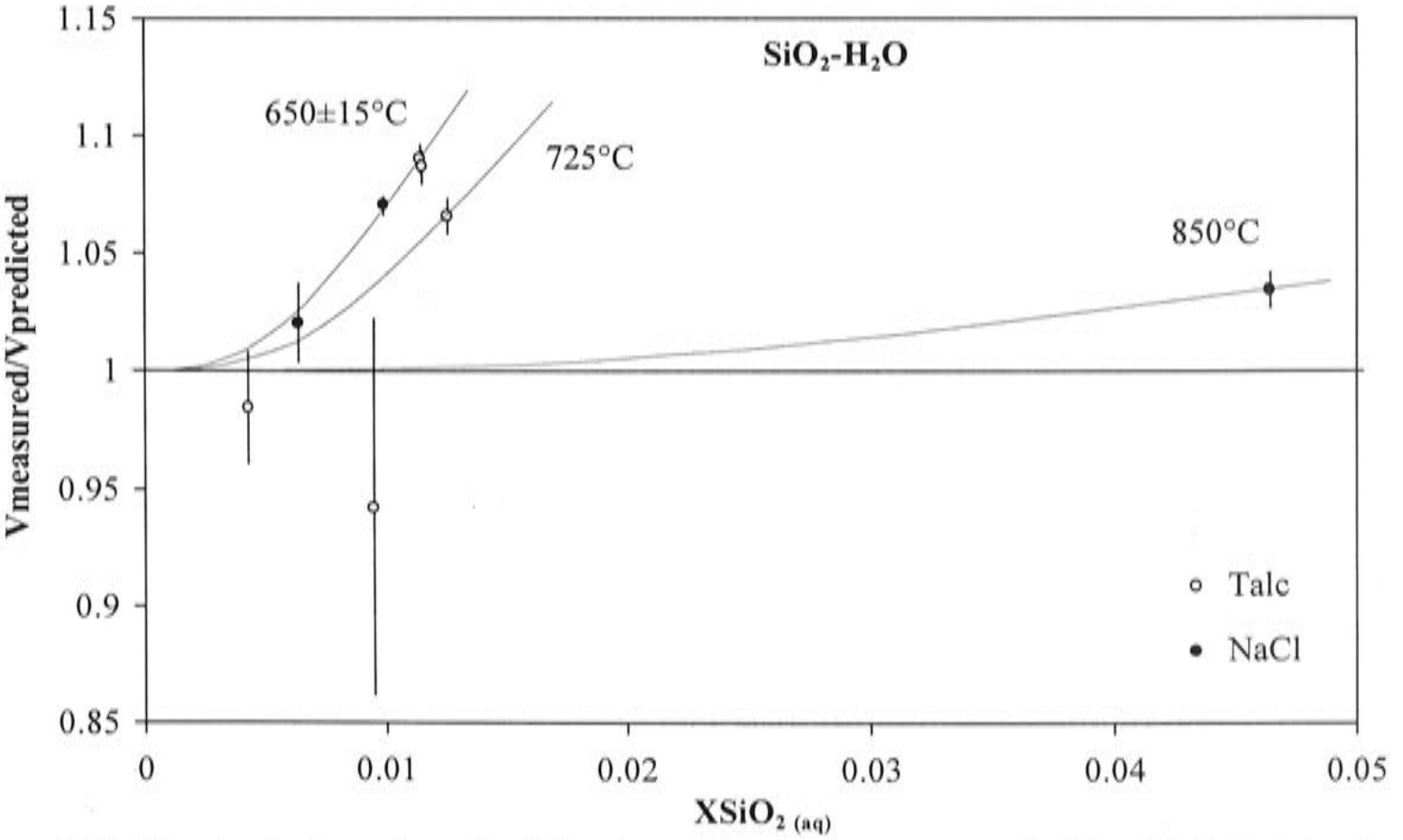

Figure 1.15 The deviation, described by the ratio, of the measured SiO_2–H_2O fluid volume, $V_{measured}$ (Table 1.2), from that predicted, $V_{predicted}$ (= $\overline{V}^{ideal}_{fluid}$; Table 1.3) along various isotherms is shown as a function of fluid composition (where, $X_{SiO_2\ (aq)}$ is total dissolved silica in mole fraction units). The three data points essentially within error of the predicted fluid volume are low-*P* experiments (~ 0.35 GPa). Fluid composition was calculated from the empirical equation of Manning (1994). Isothermal trendlines fit by eye. Piston-cylinder assembly-type indicated.

4.5.3 Partial molar properties of components in SiO_2–H_2O fluids - Implications for silica speciation

Although there are too few *PVTX* measurements to formulate a quantitative model describing *a*–*X* relations in the SiO_2–H_2O system, the data nonetheless provide a significant insight to the nature of SiO_2–H_2O interactions in high-*P* fluids.

The data indicate that quartz-saturated, H_2O-dominant fluids at *P* above 0.5 GPa are substantially less compressible, so slightly *less* dense (g/cm^3), than either pure water or an ideal mixture, at the same conditions. Importantly, the excess fluid volumes implied by the data, relative to an ideal mixture of pure H_2O and SiO_2 liquid at the same conditions, at high-*P* are so large (ranging to at least 10 volume percent; Figure 1.15) they cannot be the result of the dissolved silica alone. For example, because the molar quantity of dissolved SiO_2 is so low (less than a few mole percent) in these fluids, the relatively small total volume difference between the ideal and measured volume would require unreasonable volumetric changes in the dissolved silica species, *i.e.*, $\overline{V}^{fluid}_{SiO_2\ (aq)}$ in Equation [1.4]. In fact, if $\overline{V}^{fluid}_{H_2O}$ is assumed in the usual fashion to be equal to $\overline{V}^{pure}_{H_2O}$, it would require $\overline{V}^{fluid}_{SiO_2\ (aq)}$ to enlarge with increasing *P* and greatly exceed the molar volume of the coexisting quartz polymorph. This is not physically reasonable.

Alternatively, a comparatively small difference between $\overline{V}^{fluid}_{H_2O}$ and $\overline{V}^{pure}_{H_2O}$, with $\overline{V}^{fluid}_{SiO_2\ (aq)}$ remaining approximately constant, delivers a solution that seems far more sensible. A minor digression, the finding that $\overline{V}^{fluid}_{H_2O} \neq \overline{V}^{pure}_{H_2O}$ in H_2O–SiO_2 mixtures, is also generally consistent with experimental determinations of $\overline{V}^{fluid}_{H_2O}$ from solubility relations in concentrated multi-component fluids at very-high *T* and *P* (Mysen and Acton 1999; Mysen and Wheeler 2000; Mysen 2002).

Thus, the observations of this study mean that the usual assumption that the partial molar volume of the H_2O component in the fluid is effectively that of pure H_2O, because the solutions are dilute, cannot be sustained (*cf.* Walther and Helgeson 1977; Walther and Orville 1983; Wasserman *et al.* 1995; Zhang and Frantz 2000; Zotov and Keppler 2000; Newton and Manning 2002; Zotov and Keppler 2002). Although recent solubility and in situ spectroscopic observations argue strongly in favour of solute polymerisation (*e.g.* Zhang and Frantz 2000; Zotov and Keppler 2000; Newton and Manning 2002; Zotov and Keppler 2002) an is a phenomena is not disputed here, the

positive excess volumes of mixing observed in this study argue equally for the explicit recognition of the properties of the solvent in thermodynamic description of SiO_2–H_2O fluids, since it (the solvent) also contributes an excess energy to the system. Deviations from "ideal" behaviour are apparent in each of the independent datasets and shed their own light on the nature of SiO_2–H_2O interactions. The most significant point to draw from the present observations, and not glimpsed by previous studies, is that non-ideality in these fluids cannot be tied solely to the identity of SiO_2–H_2O complexes at high-P.

It is well known that Si prefers tetrahedral coordination environments that are not prone to large changes in volume as a function T and P, if silicate minerals and SiO_2-rich liquids are any indication (*e.g.* Table 1.3; Figure 1.14). It follows that SiO_2 dissolved in H_2O should also share this characteristic, whether it be as polymerised silica, hydrous melt-like species or more isolated SiO_2–H_2O complexes (*e.g.* $Si(OH)_4^0 \cdot n_s H_2O$). In this case, it is unlikely that the SiO_2 component should display rapid volume changes over modest P and T ranges. H_2O, on the other hand, is well known for rapidly changing in volume as a function of P and T (*e.g.* Figure 1.14), even so only a minor adjustment is required in quartz-saturated fluids.

The data then seem to suggest that silica, although a minor component in these fluids, is bringing some kind of structural ordering to the H_2O-rich fluid (aqueous SiO_2 and H_2O are in a reaction relation after all) and causing it to be slightly less compressible than in its pure state and more like a hydrous silicate melt (in terms of its expansivity and compressibility at least). Perhaps high-P induces a structural ordering in SiO_2–H_2O fluids akin to that displayed by ice, that is, the structure is expanded relative to the pure liquid.

4.5.4 Hydrous, silica-poor melts or silica-bearing aqueous fluids?

The partial molar volumes of H_2O and SiO_2 as dissolved in silicate melt, $\overline{V}_{H_2O}^{melt}$ and $\overline{V}_{SiO_2}^{melt}$, represent an alternative choice of end-member properties by which to calculate the ideal SiO_2–H_2O fluid volume. These properties are known experimentally to vary as a simple function of P and T and also appear to vary little over large ranges of melt composition (Lange and Carmichael 1987; Lange and Carmichael 1990; Ochs and Lange 1997; Gaetani *et al.* 1998). Hence, the behaviour of silicate melt components may be potentially useful for understanding H_2O-rich fluids as well as more SiO_2-rich compositions, especially given that hydrous silica melt isopleths extend into the supercritical fluid region (Figure 1.10).

Although there is a remarkably consistent linear correlation between the ideal melt and the real fluid volumes, silicate melt components appear to be a poor choice of end-members, if only for the sake of simplicity (Figure 1.16). For example, the calculated ideal hydrous silica melt volume and that measured show extreme divergence at low fluid densities. Similarly, recognising that fluid and melt volumes are indistinguishable beyond the upper critical point, the comparatively low ideal fluid volume calculated at the upper critical point $PVTX$ conditions cannot easily be reconciled with the data which suggest this convergence is at much higher fluid densities (Figure 1.16). These features are not amenable to a simple solution, especially when compared with the potential ease of explanation, not to mention eventual mathematical treatment, if the pure liquid end-member substances at the P and T of interest are used to predict SiO_2–H_2O fluid properties (Figure 1.17).

Figure 1.17 compares the fluid volumes predicted from the properties of the pure liquid end-members at the T and P of interest with the corresponding measurement. Clearly, the use of the ideal pure liquid standard state at the P and T of interest provides a much closer approximation of the properties of the real fluid than the use of partial molar silicate melt components. This suggests that such fluids in this region are still best thought of as low-density silica-bearing aqueous liquids and not hydrous silica melts. Minor differences between $\overline{V}_{H_2O}^{fluid}$ and $\overline{V}_{H_2O}^{pure}$ are the most likely source of the discrepancy between calculated and measured values. Also shown on Figure 1.17 is the volume for the fluid at the upper critical point, calculated using both melt component (Ochs and Lange 1997; Gaetani *et al.* 1998) and pure liquid properties

(Mao *et al.* 2001; Holland and Powell 1998), the fluid *PTX* details from Kennedy *et al.* (1962). These two points presumably bracket the density of the upper critical SiO_2–H_2O fluid isochore.

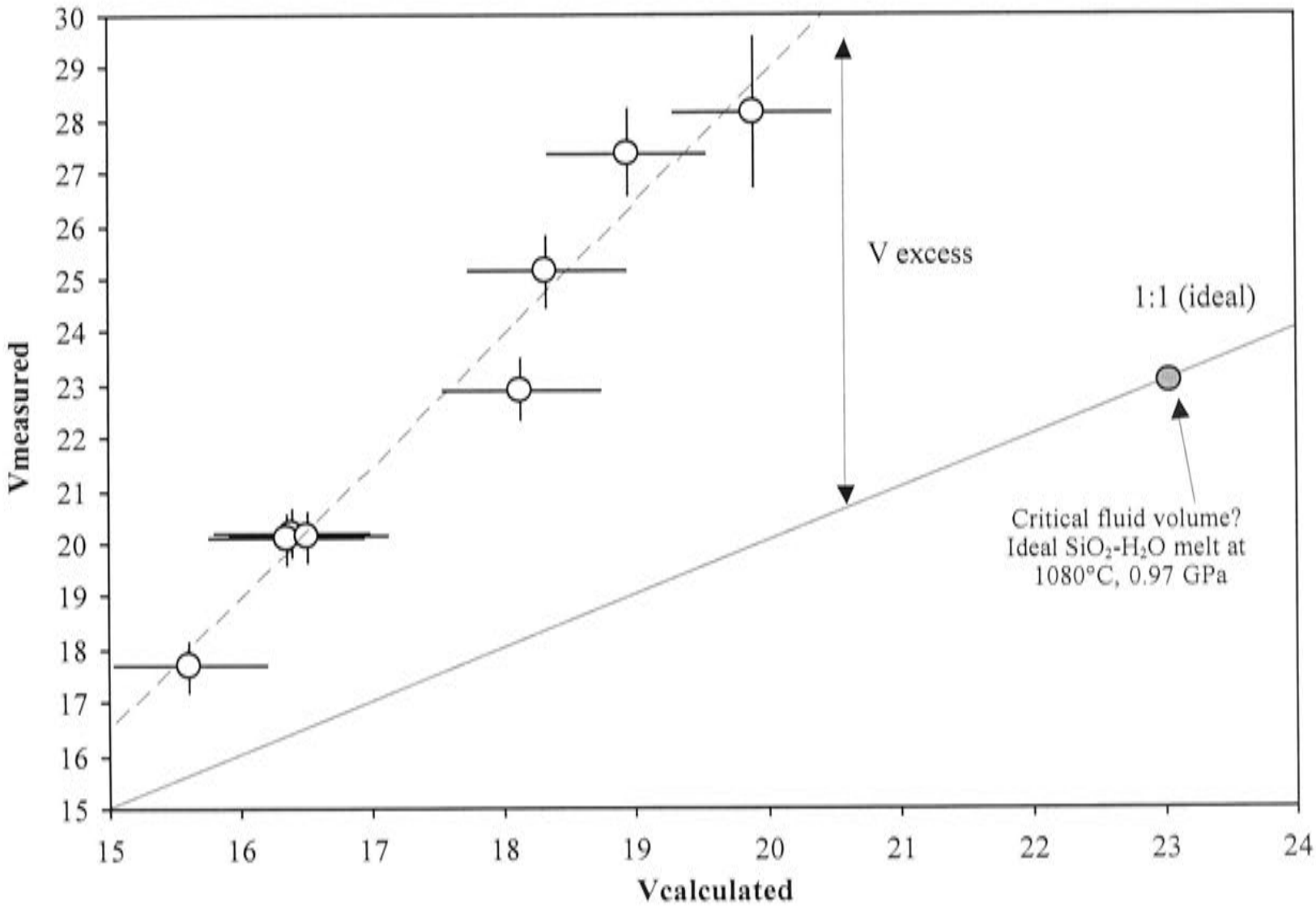

Figure 1.16 The experimentally measured fluid volume, $V_{measured}$ ($=\overline{V}^{PTX}_{fluid}$), plotted against that of an ideal SiO_2–H_2O melt, $V_{calculated}$ ($=\overline{V}^{ideal}_{SiO_2-H_2O\ melt}$), calculated from the partial molar properties of silica and H_2O dissolved in a silicate melt (Table 1.3). Units are in cm^3/mol. Low-*P*, ~ 0.35 GPa, *PVTX* fluid data also plotted. $V_{calculated}$ errors correspond to the uncertainty in the experimental conditions and the thermodynamic properties. Solid line (1:1) indicates where the calculated and measured volumes would coincide. The shaded point denotes the critical fluid volume derived using the partial molar melt properties of SiO_2 and H_2O (Table 1.3), critical fluid *PTX* details taken from Kennedy *et al.* (1962).

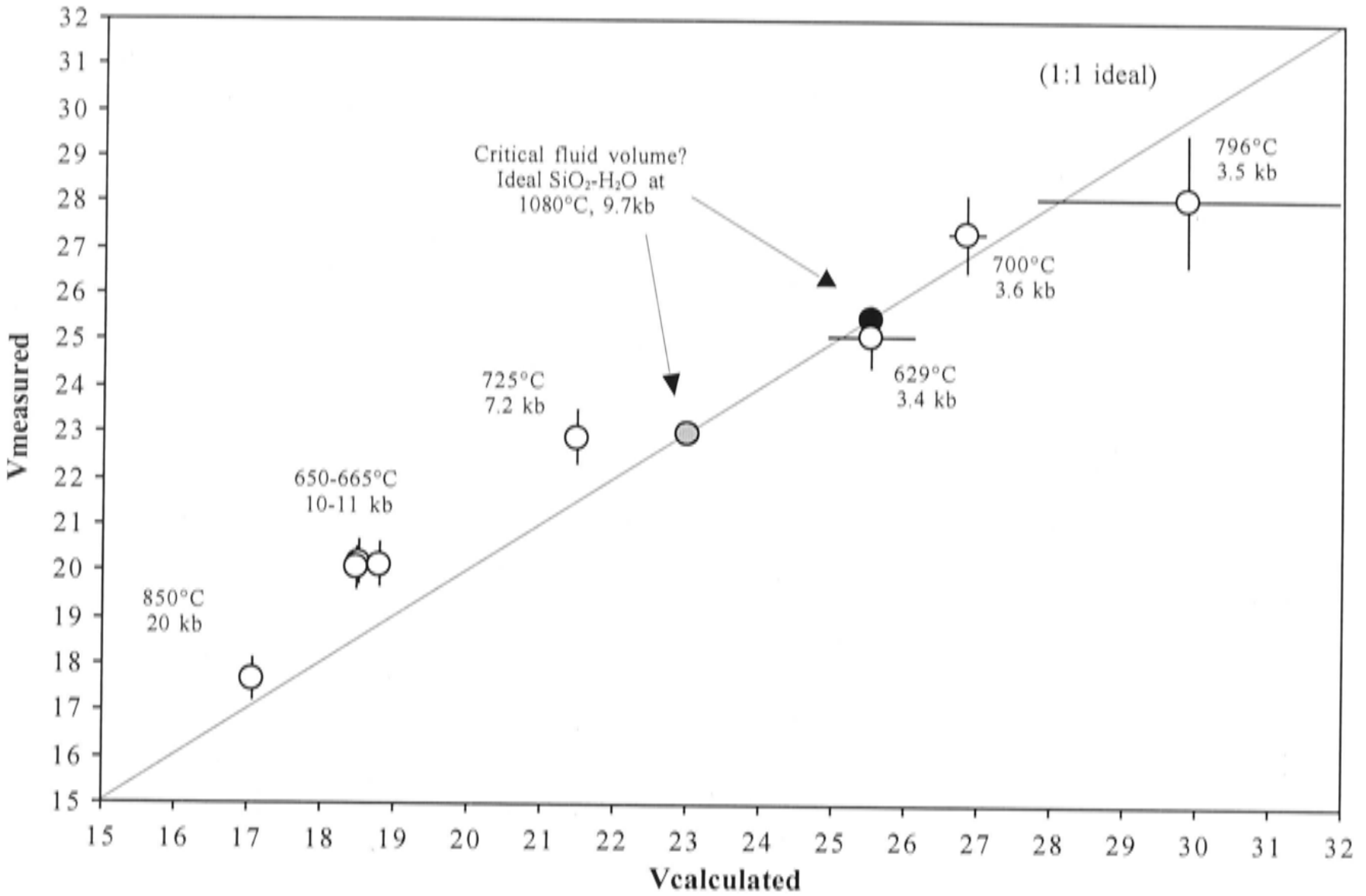

Figure 1.17 The measured fluid volume, $V_{measured}$ ($=\overline{V}_{fluid}^{PTX}$), plotted against the volume of an ideal SiO_2–H_2O fluid, $V_{calculated}$ ($=\overline{V}_{fluid}^{ideal}$), calculated from the partial molar properties of a mixture of pure silica liquid and pure H_2O (Table 1.3). Units are in cm^3/mol. Low-*P*, ~ 0.35 GPa, *PVTX* fluid data also plotted. $V_{calculated}$ errors correspond to the uncertainty in the experimental conditions and the thermodynamic properties (plotted symbols may be larger than the total uncertainty). Solid line (1:1) indicates the case where the calculated and measured volumes would coincide. Solid and grey points denote, respectively, the critical fluid volume as calculated for ideal mixtures of the pure liquid end-members and as derived using the partial molar melt properties of SiO_2 and H_2O (Table 1.3), critical fluid *PTX* details from Kennedy *et al.* (1962).

In any case, volumetric data, as obtained here, suggests that in addition to configurational changes in the trace solute components as inferred from the various solubility and in situ spectroscopic data there is also a positive excess volume of mixing associated with these fluids. Non-ideal mixing of dissolved silicate components in water and polymerisation of these components into melt-like structures, especially at higher concentrations, may be the norm at high-*P*.

4.5.5 Implications for fluid inclusion PVT studies

If, as it has been argued, there is significant interaction between solvent and solutes, even at trace concentrations at high-*P*, the possibility arises that volume determinations purporting to be of pure H_2O based on phase equilibrium or fluid inclusion-type measurements (*e.g.* Johnson and Walker 1993; Brodholt and Wood 1994; Withers *et al.* 2000) are likely to be in error. Alternatively, differences between fluid inclusion or phase equilibrium measurements and EOS predictions reflect real variations in the properties of different mineral-saturated fluids. In this case, EOS that are constrained by fluid inclusion experimental results need to incorporate the effects of solute-solvent interactions in the values predicted by them.

Comparison of H_2O volumes predicted by the Brodholt and Wood (1993) and Holland and Powell (1998) EOS reveals that the former expression predicts volumes that are systematically larger than the latter, by a few percent. Although the Brodholt and Wood (1993) EOS was developed using molecular simulations, its validity at high-*P* was argued on the basis that fluid inclusion measurements of nominally pure water were in close agreement (Brodholt and Wood 1994). This coincidence may be fortuitous given the fluid inclusion measurements (the only volume data available at the high-*P* and *T* of interest) were potentially biased by the presence of dissolved alumina.

As might be expected, the use of the Brodholt and Wood (1993) EOS to calculate H_2O–SiO_2 fluid volumes reduces the difference between the predicted and fluid inclusion measured values, but still does not completely eliminate the differences and the general pattern of the volume mismatch remains. Similarly, it has been noted that the Brodholt and Wood (1993) equation for pure water fits some experimentally determined phase equilibria slightly better than other EOS at high-*P* (Pawley 1994; Schmidt and Poli 1994) but anomalies also remain.

The internal consistency between fluid inclusion measurements and phase equilibrium experiments, on the other hand, is not particularly surprising given the mineral-saturated state of the fluid in each case. Thus, EOS fit to such measurements, or EOS that are independently derived but consistent with fluid inclusion and/or phase equilibrium experiments (*e.g.* Brodholt and Wood 1993), may well provide a better approximation of the fluid properties in mineral-buffered systems, but probably not because they accurately describe pure H_2O.

Because corundum-hosted fluid inclusion volumes for nominally pure H_2O (*e.g.* Brodholt and Wood 1994; Withers *et al.* 2000), appear to be close to what is observed for quartz-saturated fluids, it could be interpreted that Al_2O_3, although assumed to be substantially less soluble than SiO_2 at high-*P*, has a similar but smaller effect on the solvent properties as $SiO_{2(aq)}$. Could this be the general effect associated with dissolving any of the major rock-forming components in aqueous fluids at high-*P*?

4.5.6 Other evidence for "strange behaviour" in high-pressure mineral-saturated fluids

Several other independent lines of evidence also suggest that the activity of H_2O (a_{H_2O}) in high-P fluids containing solutes deviates significantly from that of an ideal solution. Aranovich and Newton (1996, 1997) documented essentially ideal mixing between NaCl–H_2O, KCl–H_2O and NaCl–KCl–H_2O mixtures at low-P at T from about 550 to 900 °C. However, they also showed that with increasing P, above about 0.2 GPa, that a_{H_2O} decreases very rapidly, approaching the square of the mole fraction in the fluid $\left(a_{H_2O} = X_{H_2O}^2\right)$. A significant further point is that this phenomenon is *independent* of the solute concentration. This effect was attributed to P-induced dissociation of the alkali salt component. Regardless, these studies clearly showed that the simple relation, $a_{H_2O} = X_{H_2O}$, cannot be assumed to hold at high-P in electrolyte-bearing fluids.

Further evidence that dissolution of mineral components in H_2O at high T and P may be the cause of discrepancies between calculated and experimentally determined reactions can be inferred from the observations of Pawley *et al.* (1996) and Holland *et al.* (1996). This series of studies examined the thermal expansion and compressibility of various hydrous phases in order to better understand their high P stabilities and hence their importance in subduction-related processes. On the basis of the disagreement they found between the experimental measurements and thermodynamic predictions they suggested that "the properties of H_2O might change in hitherto unexpected ways at very high pressure" (Holland *et al.* 1996). It is entirely possible that this so-called unexpected behaviour of H_2O is due to the unaccounted for effect that dissolved mineral components have on a_{H_2O} at higher P.

The observations made here are potentially more widely applicable, in that they may explain perennially encountered petrological problems related to high-P hydrothermal phenomena, critical behaviour and the stability of hydrous phases. Perhaps the interpretation of the limited data has gone too far, but there is at present no good reason why such possibilities should not be considered. In doing so, who knows what exciting new insights can be gained about hydrothermal processes from natural samples and fluid-saturated experimental data pertaining to deep crust and upper mantle environments.

PART 2

Factors affecting accuracy and precision of the quantitative analysis of individual fluid inclusions by laser ablation inductively coupled plasma mass spectrometry

Abstract

Aspects of laser (ArF 193 nm) ablation inductively coupled plasma mass spectrometry (LA-ICP-MS) that affect the accuracy and precision of fluid inclusion analyses have been investigated. These include: physical and compositional matrix effects, inclusion signal corrections, sample carrier gas composition and ICP-MS configuration, ablation rate and the derivation of internal standards for determining absolute element concentrations. A summary of the main findings follows.

Matrix-related calibration effects are generally not significant when using silicate glasses as calibration reference materials for the analysis of quartz-hosted fluid inclusions. However, calibration errors, arising from interferences usually considered negligible, can be observed where extreme compositional differences between fluid inclusions and standards occur.

Extended duration ablation leads to highly fractionated ablation yields as the aspect ratio of the developing pit increases. Because fluid inclusions occur at different depths in the sample, a down hole fractionation correction must be made. This is achieved by co-locating the equivalent inclusion depth interval on the bracketing standards, also used to monitor and correct for instrumental drift. The relative time from beginning of ablation to the start of the inclusion signal is used as a proxy for depth in both materials.

Transient fluid inclusion signals should also be corrected for host signal contributions. This involves modelling the behaviour of individual analyte masses over the inclusion signal interval. In this way, the mass specific down hole signal attenuation and inter-mass fractionation that occurs with depth is corrected.

Deposition of ablation-related condensate material on the sample substrate is inevitable, even when ablating in a helium atmosphere. Such deposits can severely compromise the quality of data obtained from shallow inclusions, where the surface signal cannot be resolved from, or overlaps, the inclusion signal. Experiments show

that the effectiveness of removing ablation condensate-type contamination by single light pulses is low, as there is some recondensation of material after each pulse over the ablation site. Thus, rejecting data obtained from shallow inclusions is recommended, where the surface component of the analysis cannot be clearly separated from the true inclusion signal.

Synthetic fluid inclusion samples were analysed by LA-ICP-MS using different sample carrier gas compositions and ICP-torch configurations. The results indicate that there is no significant difference in the measured fluid composition between the instrument conditions. However, the analytical set-up strongly influences analyte mass backgrounds and sensitivity and therefore the analytical conditions need to be chosen according to the selected analytes.

Optimum fluid inclusion sampling conditions occur over a relatively narrow range of ablation frequency. There is an improvement in the definition of the inclusion signal along with improved signal to background intensity ratio that occurs with increasing ablation frequency. This improvement, however, is increasingly offset by the deleterious effects associated with rapid excavation and sampling at high-aspect ratio ablation sites, resulting in shorter, usable analysis intervals (*i.e.* time) with the data containing lower spatial resolution, due to signal smoothing, and the increasing difficulties in co-locating analytical depths between samples and bracketing standards.

A series of concentrated, daughter crystal-bearing and dilute fluid-only synthetic quartz-hosted fluid inclusions were analysed using the same ablation beam diameter. In contrast with the study by Günther *et al.* (1998), no difference was found in the analytical accuracy or precision between solute saturated and solution-only inclusions.

It is demonstrated using synthetic fluid inclusions that the analytical uncertainty for major and trace element measurements on individual LA-ICP-MS analyses is approximately 30–50% (± 1 sigma relative). This analytical precision is comparable to other micro-analytical techniques. Consequently, robust measurements of fluid composition can only obtained if replicate analyses are made on multiple individual inclusions of a single population. The analytical accuracy was tested by analysing the same inclusions with proton induced X-ray emission (PIXE). The two methods give, within their respective analytical uncertainties, identical quantitative fluid compositions.

The method of internal standardisation is crucial to accurate quantification of fluid inclusion compositions. Quantification involving the addition of "inert" trace elements to mineral-buffered solubility experiments is not as robust as previously thought (*e.g.* Loucks and Mavrogenes 1999) and is not recommended without verification. A reliable technique was developed for synthetic inclusion studies. Specifically, it involves independent measurement of the quench solution to obtain an internal standard in the fluid inclusions. Systematic errors are an inevitable consequence of using simple model systems to calibrate thermometry measurements on more complex natural inclusions. A technique is described for extricating quantitative absolute concentrations from LA-ICP-MS data, based on the measurement of fluid inclusion volume.

1. Introduction

Geological fluids are fugitive by nature, such that they are effectively vanished from the rock by the time it is sampled. Fluid relicts, however, are commonly captured as inclusions in minerals during their growth or by annealing of fluid-filled fractures in hydrothermal systems (*e.g.* Roedder 1984). Such inclusions are important because they contain the only direct information we have on fluid parameters such as composition, which is possibly the most crucial information necessary for constraining the origins and nature of hydrothermal mass fluxes and processes. However, detailed chemical and isotopic information has been difficult to obtain from fluid inclusions because they are small (*e.g.* ~ 10^{-10} g) and solute concentrations commonly vary over several orders of magnitude, down to extremely low levels.

Although fluid concentration ratio measurements can be made using conventional crush-leach and other bulk fluid inclusion sampling techniques, these data are often difficult to interpret (Roedder 1984). This is because they generally represent time-integrated fluid compositions due to the coexistence of multiple, compositionally distinct, inclusion populations even within small samples.

Individual inclusion analysis techniques do not suffer from this problem and potentially allow a detailed time-resolved fluid record to be constructed for a given sample. This advantage has stimulated the development of various techniques to routinely measure the major and trace element compositions of both natural and synthetic single fluid inclusions. Of these, laser ablation inductively coupled plasma mass spectrometry (LA-ICP-MS), which involves the destructive analysis of entire fluid inclusions (fluid plus precipitated daughter products), has received considerable attention in recent literature (*e.g.* Günther *et al.* 1998; Audétat *et al.* 1998; Ulrich *et al.* 1999; Heinrich *et al.* 1999; Schäfer *et al.* 1999; Loucks and Mavrogenes 1999; Audétat *et al.* 2000a,b; Ulrich *et al.* 2001). LA-ICP-MS is ideally suited to the acquisition of detailed compositional data from individual fluid inclusions as current ICP-MS instruments are capable of measuring a large range of elements (> 65), have high sensitivity and low backgrounds, affording $\mu g.g^{-1}$ detection limits for many elements, and allow quantification of the full concentration range spanned by trace and major solutes in hydrothermal fluids. However, despite its increasingly widespread application there remain aspects of quantitative fluid inclusion analysis by LA-ICP-MS that warrant further scrutiny.

A series of experiments were carried out, involving a range of analogue- and quartz-hosted synthetic fluid inclusion samples, to investigate various factors that affect the quantification of major and trace element ratios and absolute concentrations in aqueous fluid inclusions by LA-ICP-MS analysis. This investigation has examined:

a) Matrix- and composition-related effects resulting from the use of non-matching calibration standards and fluid inclusion host phases;
b) The effect of modifying the sample carrier gas composition and using different ICP torch configurations;
c) The effect of varying the sample ablation conditions (ablation rate, sampling depth);
d) Analysis procedures for aqueous fluid-only and daughter crystal-bearing inclusions;
e) The composition of synthetic fluid inclusions is compared with the starting fluid and quench solution compositions; and,
f) Compare quantitative inclusion compositions obtained by LA-ICP-MS with proton induced X-ray emission (PIXE) techniques.

The experimental results provide a solid basis on which to assess both the accuracy and precision of quantitative LA-ICP-MS fluid inclusion analysis and the methods that deliver the best quality data for both natural and synthetic fluid inclusions. The limitations and advantages of various current fluid inclusion data reduction procedures are also discussed.

2. Experimental

2.1 Samples

2.1.1 Analogue epoxy- and quartz-hosted aqueous inclusions

To investigate whether different fluid inclusion or their host materials require matrix-matched calibration standards, analogue fluid inclusions were prepared in both epoxy and natural inclusion-free quartz. The analogue inclusions were formed in two polished 26 mm diameter epoxy mounts, one of which contained a 2 mm thick chip of quartz. Relatively widely spaced (~ 0.5 mm) holes were ablated in both epoxy and polished quartz mounts using the ArF excimer laser. The hole width to depth ratio was approximately one. These pits (29 to 150 μm diameter) were then filled with known concentration multi-element solutions. Finally, the filled holes were sealed over by a layer of Kapton adhesive tape to prevent uncontrolled evaporation while in the Ar–He atmosphere of the ablation cell and better approximate actual inclusion ablation behaviour. The epoxy, natural quartz and sealing tape were all previously determined by LA-ICP-MS not to contain any of the elements of interest.

2.1.2 Synthetic quartz-hosted fluid inclusions

A variety of synthetic quartz-hosted fluid inclusions were made experimentally at high-P and T to assess the accuracy and precision of quantitative fluid inclusion measurements by LA-ICP-MS. Two kinds of synthetic quartz-hosted fluid inclusions were prepared. The first runs were in simple KCl±NaCl±$CaCl_2$–H_2O systems, these are referred to as the "non-buffered" runs. A range of trace elements was added to several of these experiments. The second series of experiments were conducted under mineral-buffered conditions in the system Cu–Fe–K–Na–H–Cl–H_2O and included a range of dissolved trace elements.

High-purity copper capsules were used to contain the experimental charges, which were prepared gravimetrically. Major elements, K, Na and Ca, were loaded directly as analytical-grade chloride salts, along with pure de-ionised water, inclusion-free pre-fractured quartz and, where appropriate, the fluid-buffering mineral phases.

Trace elements were added to the capsule in solution. Trace element solutions were prepared gravimetrically from 1000 mg/L analytical standard solutions diluted with pure water. The copper capsules, once loaded, were cold-sealed, ensuring no solute components were lost before running the sample in a 30 mm talc-pyrophyllite assembly in a piston-cylinder apparatus. Quartz + fluid only (*i.e.* "non-buffered") experiments were run at 850 °C and 1.1 GPa for 3 to 4 days, while mineral-buffered experiments were run at the more moderate, although near-solidus for the buffering assemblage, conditions of ~ 700 °C and 0.35 GPa for 10 to 14 days. Further details of the procedure for fluid inclusion synthesis in a piston-cylinder apparatus and sample preparation are described in *PART 1*.

2.2 Instrument

The LA-ICP-MS instrument used in this study consists of an ultraviolet ArF (λ=193 nm) excimer laser (Lambda Physik LPX 120I) and custom-built sample ablation cell flushed with Ar and He. The cell is coupled, via a signal smoothing manifold, to an Agilent 7500 series quadrupole ICP-MS (Figure 2.1). A colour camera linked to a video monitor provides uninterrupted viewing throughout the ablation process. The system uses simple image projection optics with a long working distance objective that gives a large depth of field (~ 500 μm). This instrument is located at the Research School of Earth Sciences, The Australian National University. Further details of the instrument design and configuration are given by Loucks *et al.* (1995) and Eggins *et al.* (1998a,b), though the current instrument has been improved by replacement of the previous quadrupole ICP-MS with the more sensitive Agilent 7500 series quadrupole ICP-MS.

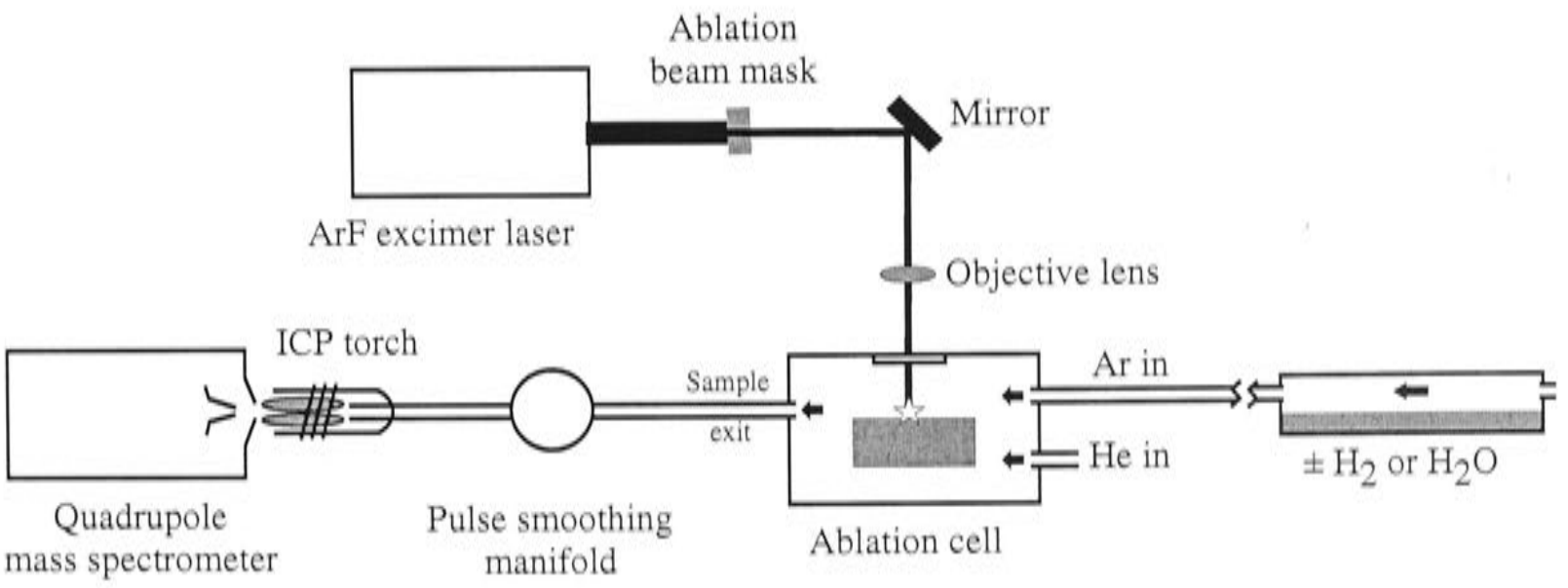

Figure 2.1 Schematic of the LA-ICP-MS instrument configuration (modified after Eggins *et al.* 1998a).

2.2.1 Sample ablation

Fluid inclusion samples and calibration materials were ablated using a circular cross-section beam, pulsed at 20 or 25 Hz. The beam size was held constant during ablation and selected as appropriate using a beam mask, normally 20 to 70 μm diameter, so as to sample entire individual inclusions (Figure 2.1).

2.2.2 ICP-MS data collection method

A short transient signal is typically generated by the ablation of individual fluid inclusions (*e.g.* 5 to 30 seconds). To resolve the separate components of the analysis, time-resolved data was collected sequentially at one point per mass peak with dwell time per mass set at 10 to 20 ms and with counting carried out in dual detector (pulse and analogue) mode on a single collector ICP-MS. The number of isotopes measured was kept to a minimum (< 15) depending on the sample requirements. These operational conditions maximise the counting efficiency and, combined with our use of a signal smoothing manifold, minimise "spectral skew" (Pettke *et al.* 2000).

Spectral skew is a counting error associated with non-representative sampling of the fluid inclusion signal by the ICP-MS; it is essentially the deviation of the measured peak area from the true peak area. This error stems from the transient nature of the inclusion signal and because in quadrupole mass spectrometry, analyte masses are sampled sequentially rather than simultaneously. Consequently, high-frequency fluctuations in signal intensity for a given mass can go undetected between mass sweeps if mass dwell times are excessive or too many isotopes are selected. The potential error resulting from spectral skew can be significant.

A blank sample carrier gas interval was measured for between 10 and 30 seconds prior to the start of sample ablation to determine the instrument background signal. The sample ablation time typically lasted about 60 to 100 seconds.

Laser sampling- and instrument-induced element fractionation are an intrinsic part of LA-ICP-MS analysis. Instrumental drift and ablation-related element fractionation processes can be routinely determined and compensated for by regular bracketing analysed samples with measurements of an external calibration standard (*e.g.* hourly). Instrument-related drift is corrected assuming linearity between analyses of the standard. The same sampling conditions, *i.e.*, ablation energy and frequency, carrier gas

and ICP-torch conditions, should be used for standards and unknowns. The soda-lime aluminosilicate glasses NIST SRM 610 and 612 were used for calibration (NBS 1970; Pearce *et al.* 1997).

Sample carrier gas flow and plasma conditions were tuned for optimum sensitivity, *i.e.* counts/μg/g, on analyte masses for each analytical session and subject to ThO/Th < 0.5%.

3. LA-ICP-MS data reduction procedure for inclusions

Extracting quantitative fluid inclusion data from raw LA-ICP-MS signals requires corrections for signal contributions directly related to the host material as well as mass fractionation effects related to "deep" extended ablation. Methods described below were developed during this study.

3.1 Host signal correction

Most fluid inclusion-hosts are likely to contain some elements that also occur in the inclusion. For example, Li is a common trace element in natural quartz and fluid inclusions. In such instances, the background subtraction for the inclusion must include the host-derived signal in addition to the gas/instrument background. The host-related background/interference subtraction takes the form,

$$I_{i(t)}^{Inclusion} = I_{i(t)}^{Raw} - I_{i(t)}^{host\ model} \qquad [2.1]$$

where, $I_{i(t)}^{Inclusion}$ is the background corrected fluid inclusion signal intensity for mass *i*, $I_{i(t)}^{Raw}$ is the raw signal intensity of the inclusion and $I_{i(t)}^{host\ model}$ is the intensity calculated from the host signal model that corresponds to the inclusion signal interval (*t*). In this context, intensities (*I*) refer to the total integrated signal intensity over the inclusion measurement interval, Equation [2.2].

$$I_{i(t)}^{Component} = \sum_{i}^{n} i_i^{Component} \qquad [2.2]$$

where $I_{i(t)}^{Component}$ refers to the total signal intensity of mass *i* for the superscripted signal component (*i.e.* host model, inclusion and raw), and $i_i^{Component}$ refers to individual signal intensity measurements of mass *i* and the summation is over *n* number of measurements corresponding to the length of the inclusion signal (*t*).

It was found that $I_{i(t)}^{host\ model}$ can be adequately calculated over relatively long, down hole, ablation intervals by fitting a logarithmic-linear Equation [2.3] to two or more relatively short host-only ablation intervals in the same analysis,

$$\log\left(i_i^{host\ model}\right) = m \cdot \left(t_{seconds}\right) + b \qquad [2.3]$$

where, $i_i^{host\ model}$ is the calculated inclusion host ablation signal intensity of mass i for a given measurement at time slice, $t_{seconds}$, in appropriate counts per time units, m and b are fitted parameters describing the down hole signal attenuation and absolute host signal intensity. By calculating this model directly from the raw host signal, a separate correction for the gas/instrument background signal is made redundant, as the model automatically incorporates both components (host and gas) of the inclusion background signal. The background removal procedure is illustrated in Figure 2.2. More detailed descriptions of the host signal profile may provide even better results in some circumstances.

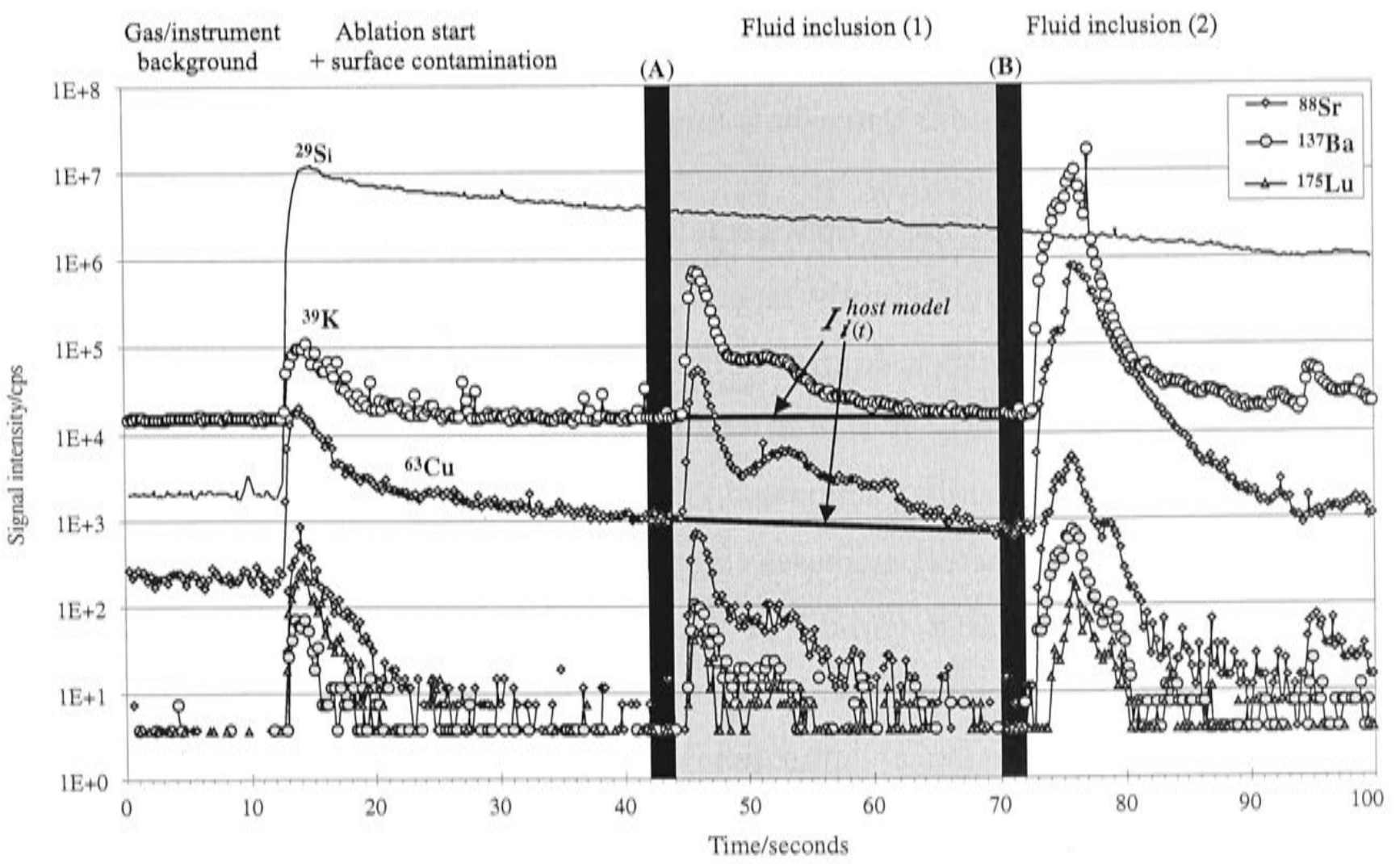

Figure 2.2 Typical fluid inclusion time-resolved LA-ICP-MS data (counts per second) obtained from natural quartz. The initial blank carrier gas/instrument background interval is followed by the quartz ablation interval (indicated by ^{29}Si signal). Following the surface contamination signal which is coincident with the start of ablation, at least two individual fluid inclusions can be observed. The interval containing fluid inclusion "1" is shaded light grey, darker shaded bands either side of this indicate the two intervals (denoted A and B) from which the total, host + gas, inclusion background $\left(I_{i(t)}^{host\ model}\right)$ was calculated. For clarity, only calculated backgrounds for K and Cu are shown.

Calculation of the inclusion signal background from the host signal interval in this way, although not quite as convenient as taking a simple gas/instrument background, is both theoretically and practically justified. Alternative host background correction procedures have been suggested by Schäfer *et al.* (1999) based on the measurement of a single mass, *e.g.* $^{29}Si^{+}$, which only occurs in the host, and using it as a proxy for the behaviour of all other masses in the host. Note, however, the latter method does not account for the observed inter-mass fractionation during progressive ablation and so the quality of analyses processed in this way is degraded.

3.2 Extended ablation: down-hole mass fractionation correction

The long focal length optics employed with the laser ablation system at RSES allows very deep, though slightly tapered, flat-bottom holes to be excavated. This contrasts with some other configurations that restrict analyses to very shallow inclusions (*e.g.* ~ 20 μm). A side effect of deep ablation, however, is that it can be associated with significantly fractionated yields for different elements as the aspect ratio of the hole (depth/diameter) increases (Eggins *et al.* 1998a). Because fluid inclusions may be encountered at a variety of depths, compensation for down-hole signal attenuation and mass fractionation is necessary. This correction is made by correlating the inclusion depth (using ablation time) with equivalent depths in the bracketing standard analyses. The assumption that ablation time and depth is equivalent in both the sample and unknown is reasonable where both target materials are ablated under the same conditions and are known to ablate at similar rates.

By using a higher laser pulse frequency and larger beam diameter the onset of fractionation is delayed (allowing sampling to greater depths), but is not eliminated. In any case, correcting depth-related fractionation is a worthwhile and simple matter.

3.3 Some notes on interferences

3.3.1 Host-related analytical interferences

Quartz (SiO_2) generally contains few elements likely to contaminate fluid inclusion analyses, making host corrections largely unnecessary, yet several interferences have been observed which are additional to any instrument or other calibration-related phenomena. Quartz-related interferences stem both from the high intensity of the individual silicon isotope signals and production of various silicon oxide species that cause relatively high-backgrounds over both the adjacent masses (related to the intrinsic mass resolution, or abundance sensitivity, of the ICP-MS) and, of course, the coincident masses. In particular, some Al, Ca and Cu isotopes are potentially affected by silica-related interferences (Table 2.1).

Table 2.1 Some potential analytical interferences, related to the ablation of quartz

Analyte isotope	Interfering species
$^{27}Al^+$	$^{28}Si^{+,\clubsuit}$
$^{43}Ca^+$	$^{28}Si^{16}O^{+,\clubsuit}$
$^{44}Ca^+$	$^{28}Si^{16}O^+$
$^{47}Ti^+$	$^{29}Si^{18}O^+$
$^{63}Cu^+$	$^{29}Si^{17}O_2^+$
	$^{29}Si^{16}O^{18}O^+$
	$^{28}Si^{17}O^{18}O^+$
$^{65}Cu^+$	$^{29}Si^{18}O_2^+$

Notes: ♣ denotes interfering species that are sufficiently intense that they may overlap measurably onto the adjacent analyte masses.

That these interferences, on masses 27, 43, 44, 63 and 65, are due to the suggested polyatomic species or adjacent peak overlap, is indicated by the unusual element isotope ratios measured and/or by unusually high apparent concentrations of elements that ordinarily only occur at very low concentrations in quartz. Furthermore, these interferences display a down-hole signal attenuation that tracks the source element, Si, in the host, as illustrated by $^{63}Cu^+$ in Figure 2.2.

Although elements such as Al and Ti commonly occur in trace amounts in quartz that could cause molecular interferences such as, $^{27}Al^{16}O^+ = {}^{43}Ca^+$, $^{47}Ti^{16}O^+ = {}^{63}Cu^+$, and $^{49}Ti^{16}O^+$, $^{47}Ti^{18}O^+$, $^{48}Ti^{17}O^+ = {}^{65}Cu^+$, the concentrations implied by the observed apparent isotope intensities are inconsistent with electron microprobe analyses

of the same quartz showing Al, Ca, Ti and Cu to be at concentrations far lower (typically below detection, *i.e.* < ~ 20ppm). This conclusion can also be drawn from the lack of correlation between the LA-ICP-MS measured abundances of the different Ti isotopes and the corresponding intensities at the mass corresponding to the oxide of the same Ti isotope.

No attempt was made to identify all possible interferences arising from the ablation of natural quartz or other inclusion-hosting materials, but it is desirable, nonetheless, to highlight their potential occurrence, and urge care in identifying their source.

At any rate, applying a simple host signal correction to fluid inclusion analyses should reasonably eliminate errors caused by the presence of host-generated interferences.

3.3.2 Inclusion-related analytical interferences

A more problematic interference originates from the inclusion itself. For instance, carbon dioxide, a common component in many geological fluids, potentially gives rise to $^{12}C^{16}O_2^+$, inferring with the measurement of $^{44}Ca^+$, as observed by Günther *et al.* (2001). Similarly, high-Na concentrations and use of an Ar-rich carrier gas can result in the formation of $^{40}Ar^{23}Na^+$ in the plasma that interferes with the determination of $^{63}Cu^+$. Such interferences are difficult to correct and require measurement of alternate masses and/or tuning the instrument to minimise their occurrence.

4. Quantification of element ratios and absolute concentrations in fluid inclusions

After the necessary total background, down-hole fractionation and instrument drift corrections are made, fluid inclusion signals may be quantified. Element ratios are readily calculated by using the bracketing standard analyses to provide an external calibration of instrument sensitivity. The general expression used for determining quantitative concentration ratios is,

$$\frac{C_a^{unk}}{C_b^{unk}} = \left(\frac{C_a^{std} \cdot I_a^{unk}}{I_a^{std}} \right) \cdot \left(\frac{I_b^{std}}{C_b^{std} \cdot I_b^{unk}} \right) \qquad [2.4]$$

where, C_a^{unk} and C_b^{unk} are the concentration of elements *a* and *b* in the unknown sample, as indicated by the subscript, I_a^{unk} and I_b^{unk} are the measured signal intensity of elements *a* and *b* in the unknown, C_a^{std} and C_b^{std} are the concentrations of elements *a* and *b* in the standard, and I_a^{std} and I_b^{std} are the measured signal intensity of elements *a* and *b* in the standard.

To convert element ratios into concentrations, an internal standard is required. This means that an absolute concentration of one (or more) element in the fluid inclusion must be independently measured. This provides the means of correcting for the variation in the analytical sensitivity (*i.e.* cps/μg/g) between the unknown and the standard. Differences in the relative sensitivity are primarily related to the ablation and ionisation efficiencies of the standard and unknown materials. It is assumed that all elements are affected in the same way such that the relative sensitivity factor is treated as a constant that applies to all elements in a given analysis. The expression for obtaining the absolute concentration of an element, is then a simple substitution of an internal standard concentration and rearrangement of Equation [2.4], to yield,

$$C_i^{unk} = \left(\frac{C_i^{std} \cdot I_i^{unk}}{I_i^{std}} \right) \cdot \left(\frac{I_{int,std}^{std} \cdot C_{int,std}^{unk}}{C_{int,std}^{std} \cdot I_{int,std}^{unk}} \right) \qquad [2.5]$$

It is worth re-emphasising that even if there is no independently known internal standard in a sample, *i.e.* the relative sensitivity coefficient goes unmeasured, concentration ratios are still quantitatively determined.

5. Results and discussion

5.1 Calibration effects related to using unknowns and reference standards with different physical properties and different compositions

The extent to which matrix-related calibration effects are significant in LA-ICP-MS fluid inclusion analysis remains uncertain, despite a number of investigations (Moisette *et al.* 1996; Ghazi *et al.* 1996; Günther *et al.* 1997,1998).

Moisette *et al.* (1996) used silicate glass NIST SRM 611 to quantify natural halite-hosted fluid inclusions and film-covered microwells (large volume, 3x3x2 mm^3) of solution using a Nd:YAG (266 nm) laser combined with ICP quadrupole MS. From their data they concluded that direct ablation of silicate glasses and microwells of solution was a satisfactory method for calibration of natural fluid inclusions hosted in halite. No attempt was made to determine absolute concentrations in the fluid inclusions, however, the relative standard deviation of concentration ratios was generally 25% or better for 20–100 μm sized inclusions up to 80 μm deep.

Ghazi *et al.* (1996), on the other hand, produced a signal intensity calibration curve (counts/volume/concentration) by ablating known volumes of standard solution in glass microcapillaries, using a Nd:YAG (266 nm) and ICP quadrupole MS instrument, to quantitatively determine individual natural fluid inclusion compositions in halite. The analytical reproducibility of this technique ranged from 5 to 31% relative, while accuracy was determined to be approximately 5% relative.

Günther *et al.* (1997) also investigated direct liquid ablation as a calibration method by analysing trace element standard solutions, with and without NaCl, contained in 150 μL vessels covered with parafilm using an ArF excimer (193 nm) laser and ICP quadrupole MS. They showed that most trace elements in NIST SRM 610 and 612 silicate glasses could be determined with better than 15% accuracy with a relative standard deviation of better than 10% using direct liquid ablation for calibration. It was also shown that a NaCl (2.5 wt.%) solution matrix does not significantly effect the calibration. In a further study describing a general procedure for fluid inclusion analysis, Günther *et al.* (1998) used direct liquid and NIST SRM 612 silicate glass ablation to calibrate natural- and synthetic quartz-hosted fluid inclusion analyses. For synthetic fluid inclusions they retrieve nominal fluid compositions with good (most

elements better than 60% relative) but variable accuracy (0.6 to 95.6% relative). This bias may be due to two factors; they acknowledge loss of the initial fluid components during the experimental synthesis through fluid reaction with the capsule, but do not consider matrix-related effects arising from the combined ablation of the quartz host and fluid in the inclusion.

Consequently, epoxy- and natural quartz analogue fluid inclusions were used to investigate possible matrix and inclusion ablation-related calibration effects. Since the analogue inclusions were filled with solutions that were not subjected to the uncertainties associated with fluid inclusion synthesis the results allow differentiation between a matrix-related calibration error and that associated with experimental synthesis.

Epoxy- and quartz-hosted analogue inclusions were sampled using a larger laser beam diameter than the sealed pit containing the fluid so that both the host matrix and fluid were ablated simultaneously, as occurs during the analysis of real (natural and experimentally produced) inclusions. Certified silicate glass NIST SRM 610 was used for calibration[9]. At the time of this work, a Fisons PQ2+ STE ICP-quadrupole MS was used to measure ablation signals. Nominal fluid composition and measured epoxy- and quartz-hosted fluid inclusion data are presented in Table 2.2 and plotted in Figure 2.3.

It can be seen from Figure 2.3 that all elements in both host materials were accurately determined, to within the reproducibility of the analytical technique. Also, little difference in precision is observed between the two sample materials. Apparently, the ablation behaviour of quartz (and epoxy) is sufficiently similar to the NIST silicate glass that matrix-effects related to the physical properties of the host cannot be distinguished. These results validate the use of silicate glasses as an external calibration material for LA-ICP-MS analysis of quartz-hosted fluid inclusions. Additionally, the data support the interpretation made by Günther *et al.* (1998), that the apparent biases in their quantitative determination of synthetic fluid inclusion compositions are due to reaction between the experimental fluid and capsule material causing the loss of some solutes.

---

[9] Concentrations for the NIST series of silicate glass standards used for external calibration of unknowns were taken from Pearce *et al.* (1997).

Table 2.2 LA-ICP-MS analysis data for epoxy- and quartz-hosted analogue fluid inclusions and composition of the standard used, NIST612

	Nominal	$\bar{x}$	σ	RSD %	NIST612 (Pearce *et al.* 1997)
Epoxy, $n = 49$					
Na	4200	4421	1657	40	13.8 (wt.%)
^{63}Cu	83	66	3	3.5	37
Sr	77	72	15	19	76
Ba	77	70	16	21	38
La	157	148	59	38	36
Pb	126	121	61	49	39
Th	78	62	13	17	37
U	12	19	5	39	37
Quartz, $n = 34$					
^{63}Cu	100	85	17	20	
Zn	100	124	21	17	38
Sr	99	102	38	37	
Cd	108	117	24	21	28
Ba	99	100	34	34	
La	114	134	45	34	
Au	99	58	43	74	35
Th	100	95	29	31	
U	110	117	43	37	

Notes: Concentrations in parts per million by weight (ppm), unless indicated otherwise. Nominal refers to the starting solution composition of the experiment, $\bar{x}$ is the mean composition determined from n individual analyses, σ is the standard deviation, and RSD % is relative standard deviation expressed as a percentage of the mean. Nominal copper, ^{65}Cu, was used as the internal standard for absolute quantification.

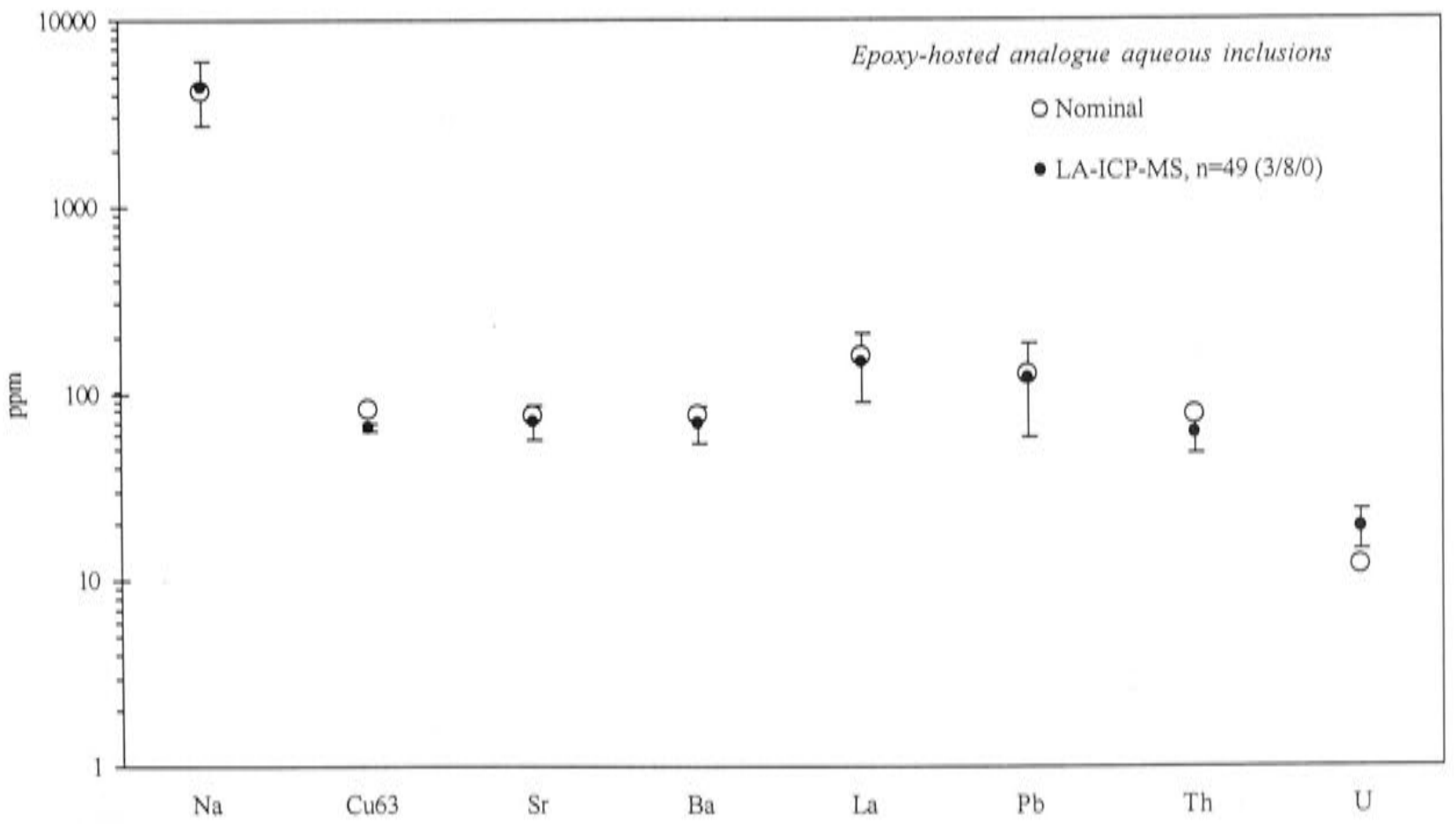

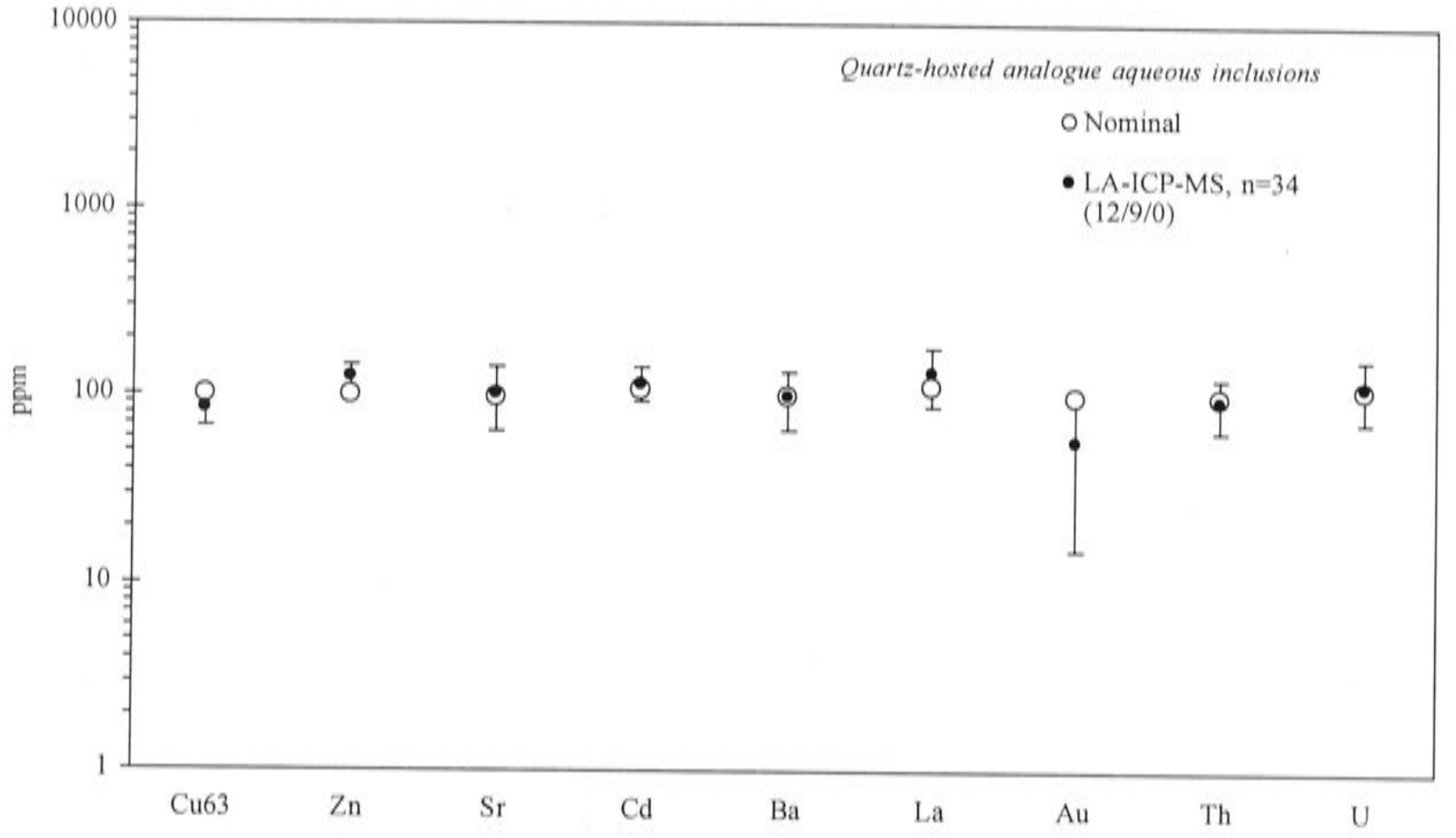

Figure 2.3 Comparison of LA-ICP-MS analysis data for analogue epoxy- and quartz-hosted aqueous inclusions and the nominal fluid concentration. Two different standard trace element solutions were used. Nominal ^{65}Cu concentration was used as the internal standard in both cases. Error bars correspond to one standard deviation.

Despite the apparent absence of any significant physical matrix-related calibration problems, composition effects caused by differences in the inclusion and standard chemical compositions are observed. For example the measured $^{63}Cu/^{65}Cu$ concentration ratios can display large deviations from the natural abundance ratio, up to ~ 25% (*e.g.* Table 2.2, Figure 2.3). These discrepancies in $^{63}Cu/^{65}Cu$ apparently originate in a calibration bias caused by differences in $^{23}Na^{40}Ar^{+}$ production between the standard and unknowns, which is due to their differing compositions. This species interferes only with measurement of $^{63}Cu^{+}$. For instance, the solution used in the analogue quartz-hosted experiment was nominally Na-free, eliminating $^{23}Na^{40}Ar^{+}$ formation, whereas an additional mass 63 component, in the form of $^{23}Na^{40}Ar^{+}$, is produced during analysis of the silicate glass reference material, which contains ~ 13.8 wt.% Na_2O (or ~ 10.2 wt.% Na). For these conditions an apparent excess of ^{63}Cu is indicated by the Cu isotope concentration ratio. The abundance of such molecular species is a function of both the sample/standard composition ratio and the analytical conditions of the session and thus, difficult to control. Furthermore, this calibration bias for $^{63}Cu/^{65}Cu$ has been observed in most synthetic- and natural fluid inclusion LA-ICP-MS experiments to date. In general, it is found in the synthetic fluid inclusion

experiments, which have a much lower Na/Cu concentration ratio than the calibration standard, an apparent $^{65}Cu^{+}$ excess is measured, while in high-salinity, natural brine inclusions which, usually, have a considerably higher Na/Cu concentration ratio than the NIST calibration standard, an apparent $^{63}Cu^{+}$ excess is observed. However, because the available data have been collected under different analytical conditions this general relation cannot be demonstrated more clearly.

Though the pragmatist analysing natural inclusions would suggest measuring only $^{65}Cu^{+}$, and ignoring $^{63}Cu^{+}$, there is a broader significance to the $^{23}Na^{40}Ar^{+}$ interference because it is distinctly composition dependent. Because fluid inclusion compositions are less constrained than most geological materials (*e.g.* silicate minerals and glasses) they may differ greatly from that of the standard. In such circumstances so-called "unusual" interference species are a likely potential analytical complication. Indeed, $^{23}Na^{40}Ar^{+}$ on $^{63}Cu^{+}$ is not normally considered a major interference (Moisette *et al.* 1996; Günther *et al.* 1997), most probably because samples and standards are usually closely matched in composition, but clearly, this is not always the case.

5.2 On the limit of signal quantification in LA-ICP-MS fluid inclusion analysis

An important aspect of any analytical technique is defining the level of uncertainty that can be attributed to a measured signal at the limit of detection. Typically detection limits are defined as three times the standard deviation of the background signal. A signal at this level has a 99.87% probability of not being background, assuming a normal error distribution. This statistic is referred to as the Lower Limit of Detection ($\bar{x}_{LLD}$; Equation [2.6]), and defined as,

$$\bar{x}_{LLD} = \bar{x}_B + 3\sigma_B \qquad [2.6]$$

where, $\bar{x}_B$ is the mean measured background signal and σ_B is the standard deviation of measured background signal. The $\bar{x}_{LLD}$ defines the threshold of qualitative analysis, that is, the minimum signal intensity at which an analyte may be identified. What is not often appreciated is that, quantitative determinations *cannot* be made at this level, as counting errors tend to infinity as the signal approaches $\bar{x}_{LLD}$ (Potts 1987). Put simply, errors intrinsic to quantifying signals at or near this level can lead to a wrong impression of the extent of the true compositional variation in a sample.

It is generally more meaningful to consider the minimum signal that can be measured quantitatively. Potts (1987) argues that the smallest signal that can be confidently measured quantitatively, the Limit of Determination ($\bar{x}_{LoD}$;Equation [2.7]), actually occurs at six times the standard deviation of background signal distribution,

$$\bar{x}_{LoD} = \bar{x}_B + 6\sigma_B \qquad [2.7]$$

Defined on the basis of 3 sigma errors, only the lowermost 0.13% tail of the $\bar{x}_{LoD}$ distribution falls below the $\bar{x}_{LLD}$, which is the minimum level of qualitative signal observation. This means that, 99.87% of all measurements at the $\bar{x}_{LoD}$ level are distinguishably above the background, compared with only 50% of measurements at the $\bar{x}_{LLD}$ level. Accordingly, only LA-ICP-MS fluid inclusion signals above the $\bar{x}_{LoD}$ level have been quantitatively determined in this work.

The limit of detection/quantification requires determination of background measurement statistics which, for fluid inclusion analysis, is not calculated from the

gas/instrument background signal, *i.e.* $\bar{x}_B^{gas/instrument}$ and $\sigma_B^{gas/instrument}$, but rather from the ablation intervals used to determine the host background model, *i.e.* $\bar{x}_B^{host_A}$, $\sigma_B^{host_A}$ and $\bar{x}_B^{host_B}$, $\sigma_B^{host_B}$ (Figure 2.2). Typically, the propagation of errors in calculating a host background correction model from two relatively short host-only ablation intervals, *i.e.* $\left(\sigma_B^{host_A}\right)^2 + \left(\sigma_B^{host_B}\right)^2$, results in a higher limit of detection than using statistics derived from extended measurements of the gas/instrument background.

To summarise, the ideal error in signals occurring at the $\bar{x}_{LoD}$ level is 16.7% relative at one sigma, whereas the error at $\bar{x}_{LLD}$, the most commonly cited form of detection limit, is infinite. Understanding this is important when dealing with near background level signals. Although alternative schemes for determining detection capabilities are available (*e.g.* Longerich *et al.* 1996) they tend not to be as conservative as the approach recommended by Potts (1987) and so leave open the possibility for low signal biasing of the data.

Definitions aside, it has been pointed out by Moissette *et al.* (1996) that detection limits for fluid inclusions are directly proportional to the absolute mass of an analyte in the inclusion. This is determined by the inclusion size and the analyte concentration, and so can vary significantly between inclusions. In the absence of an absolute element concentration within an inclusion, *i.e.* an internal standard, it is not possible to specify a detection limit in the form of a concentration. This, however, has no bearing on the identification of detection limits for determining element concentration ratios. In the event that an internal standard is available, signal detection limits can be converted into concentration units via,

$$C_{\mu g.g^{-1}}^{limit} = I_{cps}^{limit} \cdot \left(\frac{C_i^{std}}{I_i^{std}}\right) \cdot \left(\frac{C_{int.std}^{unk} \cdot I_{int.std}^{std}}{I_{int.std}^{unk} \cdot C_{int.std}^{std}}\right) \qquad [2.9]$$

where, $C_{\mu g.g^{-1}}^{limit}$ is the calculated "detection limit" signal (*e.g.* $\bar{x}_{LoD}$) converted into appropriate concentration units (in this case, μg/g), I_{cps}^{limit} is the signal intensity "detection limit" given in the counts per second.

5.3 Surface contamination

Surface-related contamination can have a deleterious effect on the reliability of quantitative analysis of near-surface fluid inclusions. This is because very shallow inclusions are often measured synchronously with surface-related contamination and analyses cannot be resolved into their respective components.

Although careful cleaning of the sample surface (*e.g.* with clean dilute acid) reduces surface contamination by minimising external sources, in practice most surface contamination results from repeated ablation of inclusions in the sample. This is because a significant portion of the ablated inclusion material condenses onto the pit sidewalls and substrate immediately surrounding the target site (Eggins *et al.* 1998a; Günther and Heinrich 1999). Similar surface contamination features result if shallow inclusions pre-empt ablation by decrepitating. Commonly LA-ICP-MS analysis of a fluid inclusion population requires extended ablation at closely spaced locations on the sample and results in the accumulation of extensive and relatively thick layers of condensate material on the surface (even with the use of He background gas). Samples containing very shallow inclusions or laser optics which are limited to such inclusions are most susceptible to surface contamination bias.

To examine the extent to which surface contamination affects fluid inclusion analyses, the measured composition of shallow fluid inclusions was compared to deeper inclusions in the sample. Shallow inclusions are defined as those that cannot be resolved from the surface of the sample, as distinct from inclusions located deeper in the sample whose signal is clearly separable from the start of ablation.

Surface-related contamination effects were examined using synthetic quartz-hosted fluid inclusions from the series of non-buffered experiments. The nominal potassium concentration in each sample, measured as $^{39}K^{+}$, was used to quantify other solute concentrations.

These fluid inclusions span a wide range of compositional space, from under-saturation to multiple daughter phase saturation at ambient conditions (Figure 2.5 and Table 2.3). This provides a means of testing if the step-wise opening of inclusions, as advocated by Günther *et al.* (1998), is required to achieve comparable analytical precision between daughter-free and solute-saturated fluid inclusions using the instrument at RSES.

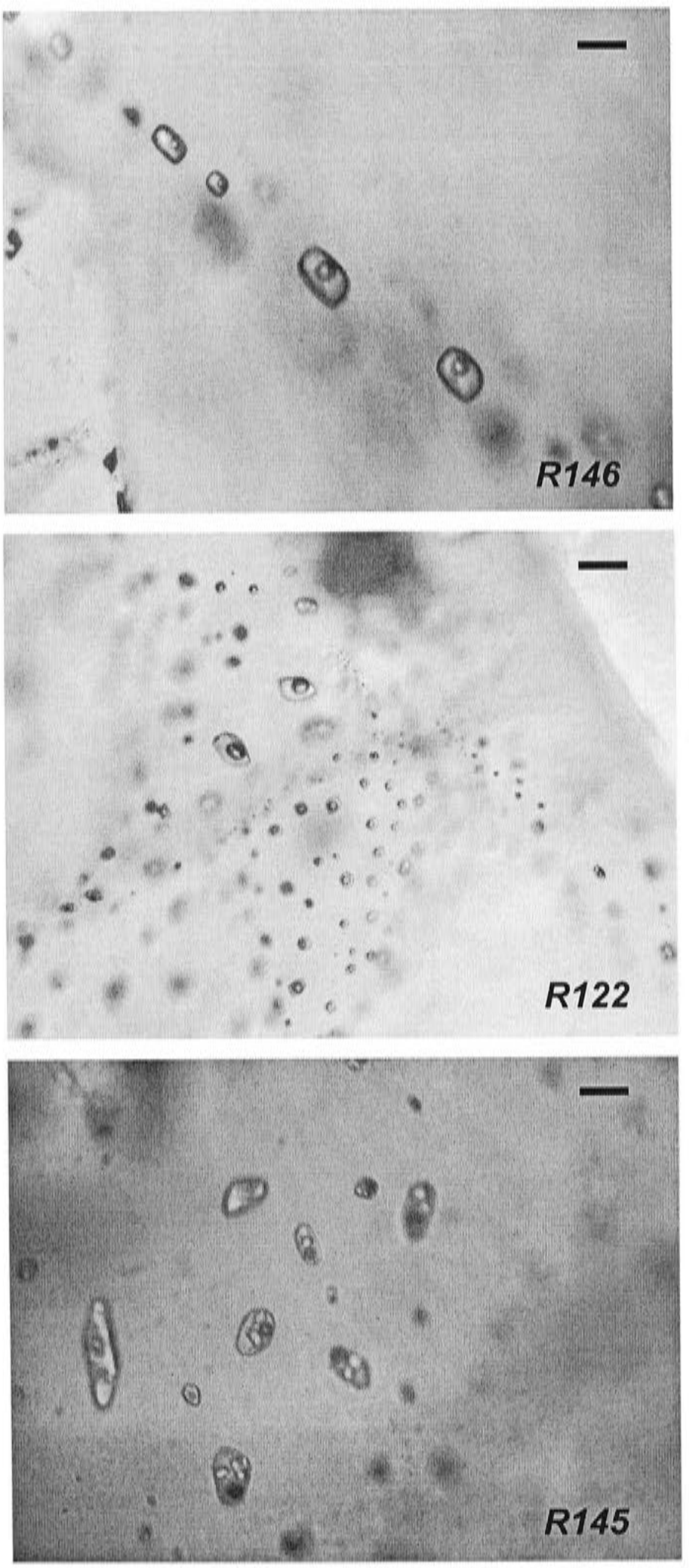

Figure 2.5 Examples of synthetic quartz-hosted fluid inclusions from simple chloride salt-water experiments R146, R122 and R145. Scale bar is 25 μm.

Table 2.3 Comparison of average quantitative LA-ICP-MS major and trace element concentrations and selected statistics measured for deep and shallow from different quartz-hosted, synthetic fluid inclusion experiments

		"Deep" fluid inclusions				"Shallow" fluid inclusions			
Mass	Nominal	$\bar{x}$	σ	RSD%	n	$\bar{x}$	σ	RSD%	n
R146									
^{39}K	0.522 %	Internal standard			18	Internal standard			25
^{23}Na	0.485 %	0.573	0.048	8.4	11	0.653	0.084	12.9	10
^{43}Ca	0.564 %	0.804	0.423	52.7	6	2.060	1.530	74.2	13
^{63}Cu	– (%)	0.510	0.339	66.4	16	0.982	0.933	95.0	25
^{65}Cu	– (%)	0.525	0.361	68.7	16	0.952	0.851	89.4	25
R122									
^{39}K	4.771 %	Internal standard			37	Internal standard			24
^{63}Cu	– (%)	10873	4155	38.2	33	10907	4664	42.8	20
^{65}Cu	– (%)	10943	4280	39.1	33	12428	5545	44.6	21
^{88}Sr	87 ppm	51.0	18.2	35.6	31	63.2	43.7	69.2	21
^{137}Ba	88 ppm	60.9	23.3	38.2	21	64.3	34.0	52.8	11
^{138}Ba	88 ppm	57.7	21.3	36.9	30	77.9	62.1	79.7	21
^{139}La*	86 ppm	5.3	4.5	85.5	21	39.9	95.5	239.2	13
^{169}Tm*	100 ppm	10.6	11.1	104.4	21	95.3	237.0	248.8	15
^{175}Lu*	90 ppm	11.1	11.3	101.8	18	36.9	31.8	86.1	14
^{197}Au*	98 ppm	–	–	–	0	38.9	26.9	69.2	8
^{232}Th	96 ppm	3.5	3.1	89.6	10	10.2	10.0	98.7	8
^{238}U	97 ppm	49.1	42.8	87.3	25	173.2	237.9	137.4	18
R145									
^{39}K	12.255 %	Internal standard			23	Internal standard			17
^{23}Na	7.023 %	7.867	2.184	27.8	21	8.875	2.228	25.1	15
^{43}Ca	5.386 %	6.418	3.623	56.5	20	6.208	4.233	68.2	11
^{63}Cu	– (%)	10.350	5.694	55.0	21	8.132	3.573	43.9	16
^{65}Cu	– (%)	10.362	5.585	53.9	21	9.114	3.785	41.5	16
^{24}Mg	69 ppm	53.4	25.7	48.2	17	392.9	685.3	174.4	16
^{25}Mg	69 ppm	59.4	39.9	67.1	11	495.1	685.5	138.5	12
^{26}Mg*	69 ppm	249.3	347.7	150.3	6	1253.8	2090.6	166.7	9
^{45}Sc	62 ppm	22.8	5.2	22.8	3	138.6	187.5	135.2	10
^{89}Y	61 ppm	17.6	8.5	48.5	18	28.1	50.2	178.5	8

Notes: Initial/nominal K concentration used as an internal standard for quantitative determination of the other dissolved and saturated fluid inclusion components. Concentration units indicated. Correction of measured concentrations for dilution effect on nominal K concentration, by addition of Cu to the solution composition during the run was not applied in the above table, however these corrections for deep inclusion data, based on measured ^{65}Cu, are –0.53%, –1.54%, –3.49% for R146, R122, and R145 respectively. n varies due to elimination of below $\bar{x}_{LoD}$ signals for some analytes. * Marks analyte signals that are characteristically near-background level.

The variation of n between elements in Table 2.3 is because inclusion size varies, as do signal intensities and $\bar{x}_{LoD}$ between inclusions. Analytical outliers, defined as concentrations greater than two standard deviations from the mean, were also rejected. In practice few outliers were identified, indicating the discrimination of significant data from the limit of detection determination was adequate.

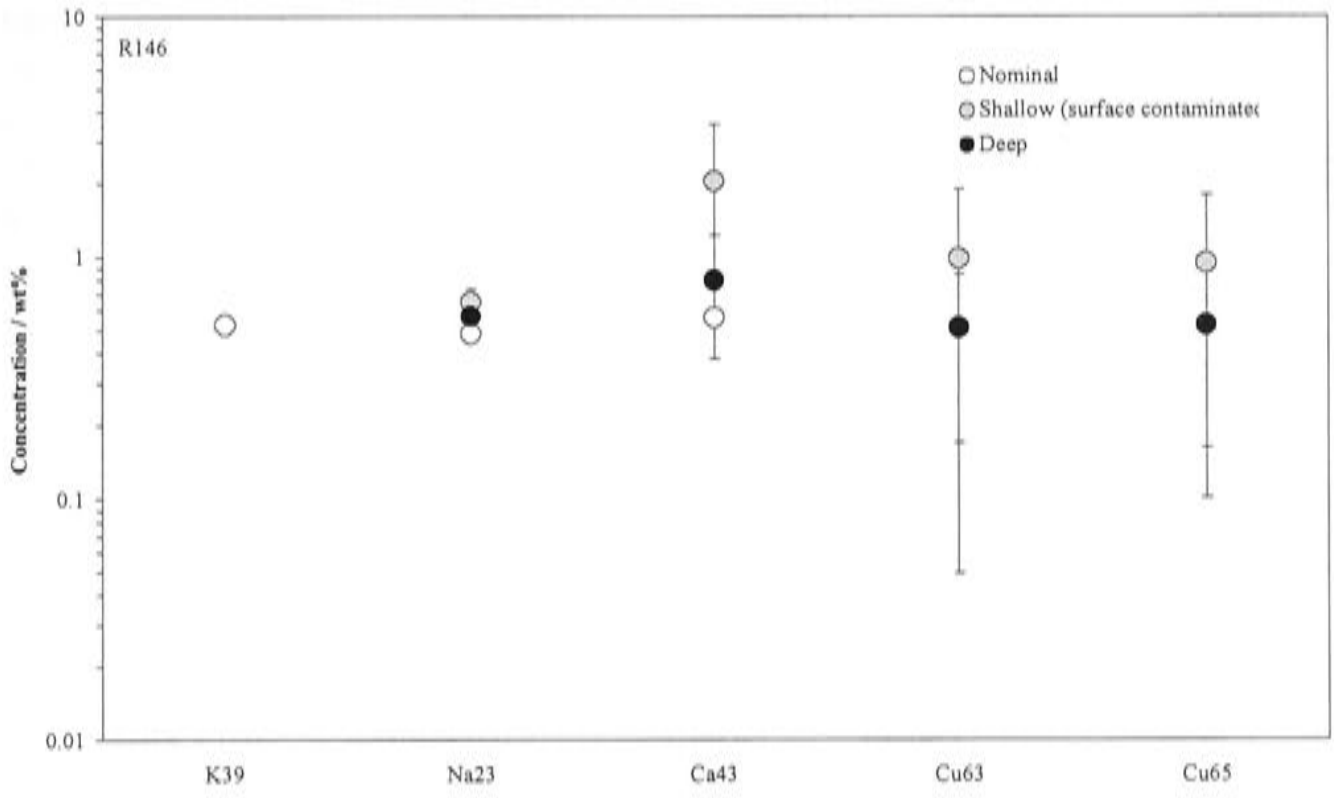
R146
Nominal
Shallow (surface contaminate
Deep
Concentration / wt%
10
1
0.1
0.01
K39
Na23
Ca43
Cu63
Cu65

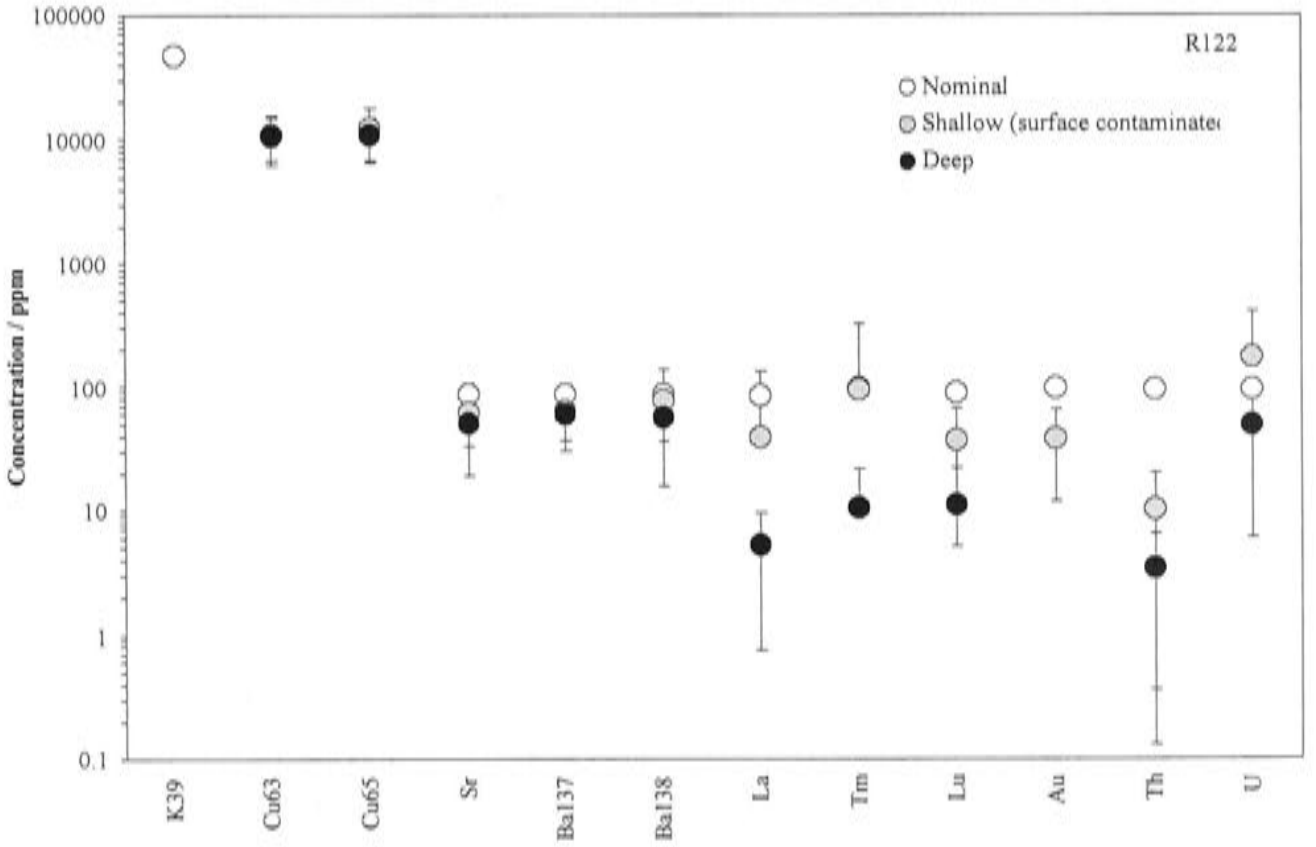
R122
Nominal
Shallow (surface contaminate
Deep
Concentration / ppm
100000
10000
1000
100
10
1
0.1
K39
Cu63
Cu65
Sr
Ba137
Ba138
La
Tm
Lu
Au
Th
U

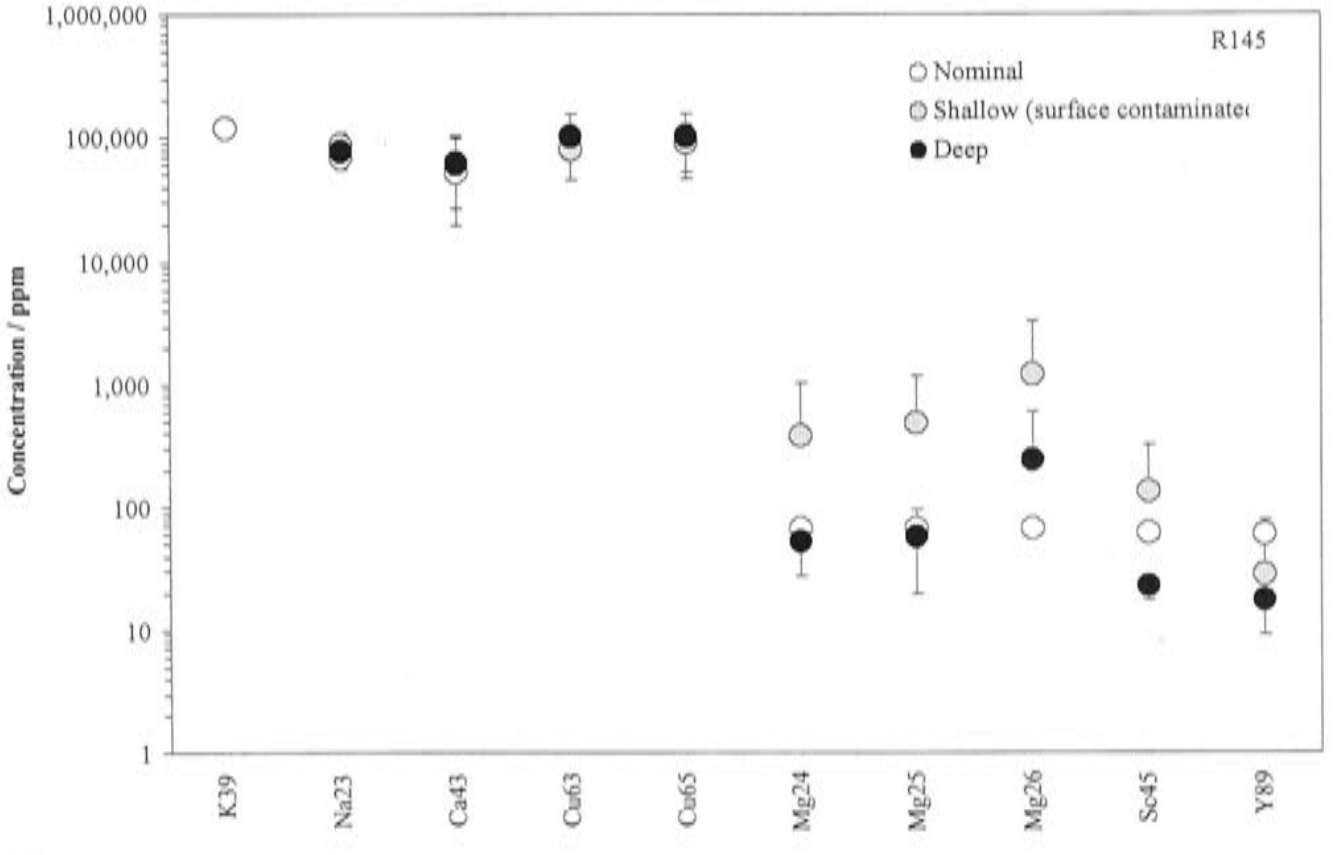
R145
Nominal
Shallow (surface contaminate
Deep
Concentration / ppm
1,000,000
100,000
10,000
1,000
100
10
1
K39
Na23
Ca43
Cu63
Cu65
Mg24
Mg25
Mg26
Sc45
Y89

Figure 2.6 (*opposite*) Comparison of quantitative LA-ICP-MS data for near-surface and deep synthetic fluid inclusions hosted in natural quartz and the nominal fluid composition as determined prior to synthesis. Since data is plotted on a logarithmic scale, lower error bars are not shown where RSD > 100%. Nominal K concentration was used for internal standardisation (large open circle).

While the accuracy of fluid inclusion analysis by LA-ICP-MS may appear poor when the initial/nominal fluid composition is compared with the measured composition, this is explained in part by the inevitability of fluid-capsule reactions in hydrothermal experiments (*PART 2, §5.10*). Such reactions tend to remove initial solutes from the fluid while at the same time dissolving part of the capsule material, in this case Cu, and other buffering phases when present, until the equilibrium fluid-capsule composition is attained.

Comparing replicate measurements of synthetic fluid inclusions is a robust approach to assessing the analytical precision of the LA-ICP-MS technique. The compositional variation observed (*e.g.* Table 2.6) suggests the average precision is about ± 60% relative to the mean at one sigma. It is of course possible that some compositional heterogeneity exists between individual inclusions which contributes to the overall analytical uncertainty. Thus these are estimates of the minimum analytical precision.

No systematic variation in analytical precision between daughter phase-bearing inclusions and fluid-only inclusions was observed when using a single, constant-diameter beam throughout the ablation procedure. This indicates that the use of multistage fluid inclusion ablation procedures (*e.g.* Günther *et al.* 1998) are not warranted. Furthermore, as pointed out by Schäfer *et al.* (1999), the use of multistage inclusion opening methods makes separation of inclusion and host components of the ablation signal much more complicated than ablation using a constant beam diameter.

Recognition of ablation condensate surface contamination led Günther *et al.* (1998) to use a single 80 μm diameter, low-energy pulse to pre-clean the surface above each inclusion prior to analysis. The effectiveness of this procedure was explored by ablating a surface region, devoid of deeper inclusions, and measuring the persistence and intensities of signals for elements characteristic of the ablation condensate contaminant produced by the analysis of three nearby fluid inclusions. Data was acquired using consecutive, single 80 mJ laser pulses using an 88 μm diameter beam under manual control (Figure 2.7).

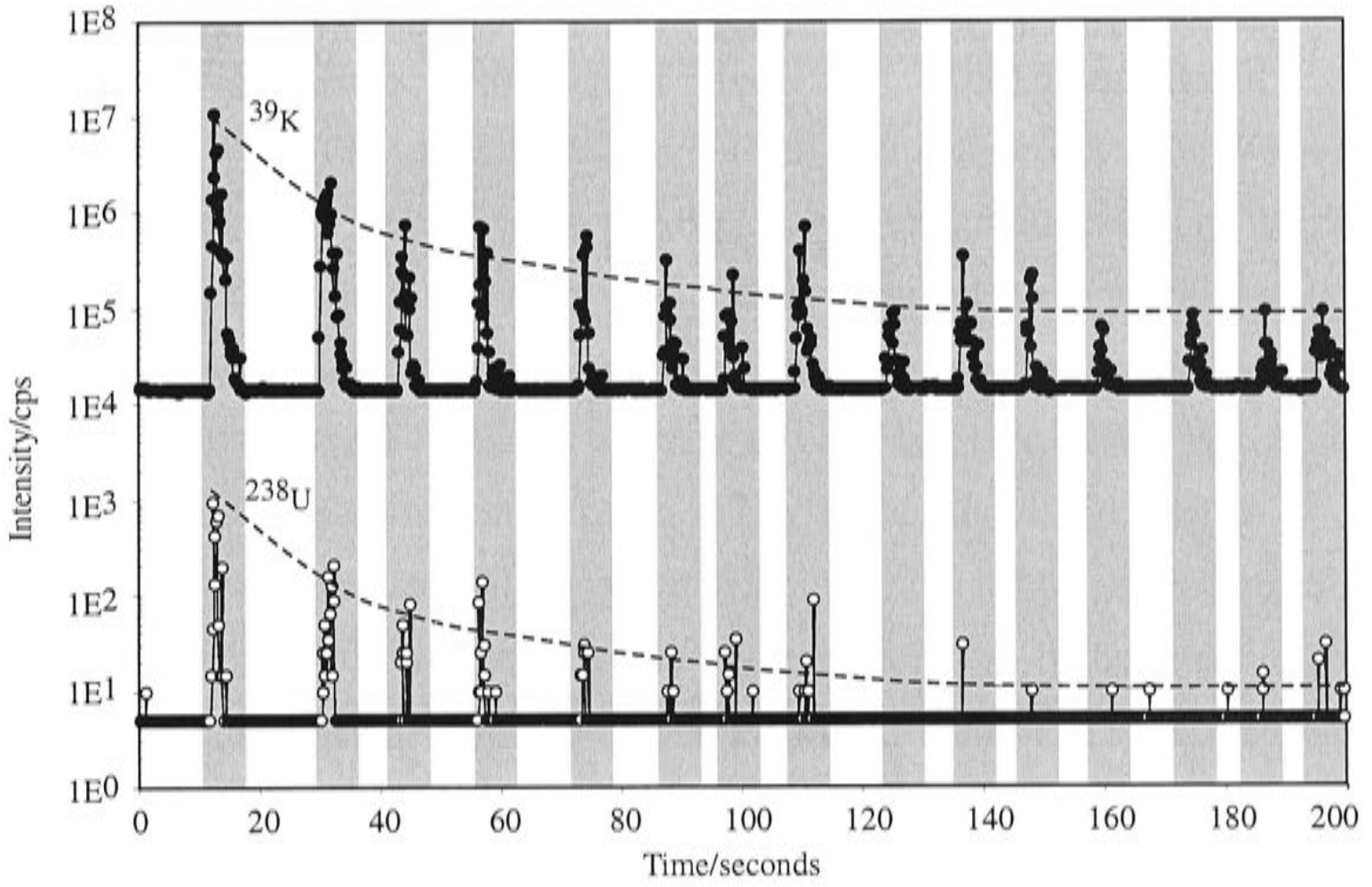

Figure 2.7 LA-ICP-MS signal single pulse ^{39}K and ^{238}U data from a typical ablation condensate blanketed area on R122, after three nearby fluid inclusion analyses, illustrating the persistence of surface contamination despite pre-ablation cleaning. Grey bands indicate the signal interval resulting from individual light pulses. Dashed lines indicate the diminishing effectiveness of the ablation pulses to clean the surface.

These single pulse data suggest that previous ablation-related surface contamination may be more difficult to eliminate than previously acknowledged. Although pre-ablating the surface directly above an inclusion with high-intensity light will be more efficient, there is an increased chance of heating and decrepitating shallow fluid inclusions, especially since quartz is largely transparent to 193 nm light. Experience indicates that poor surface polish or low-energy light increases the probability of erratic ablation.

While a single, large area, low-energy pulse can be used to help reduce the effect of surface-contamination, complete cleaning of the surface does not occur. Accordingly, data derived from inclusions deeper in the sample are more likely to provide reliable trace element data.

5.4 The effect of using different ICP-torch types and carrier gas compositions

Initial LA-ICP-MS experiments suggested an analytical bias might be associated with the carrier gas and ICP-torch configuration, as they seemed to affect sensitivity and background levels. Accordingly a series of experiments were undertaken utilising synthetic quartz-hosted fluid inclusions from R122 (because of the abundance of inclusions present) as a fluid inclusion standard against which to assess instrument configuration-related bias and inter-session analytical precision.

At least two replicate analysis sessions were carried out at each analytical condition and during which multiple individual inclusion measurements were made. In addition to the standard Ar–He mixture, a number of other carrier gas conditions were investigated. These included the addition of hydrogen (Ar–He–H_2) and humidifying the standard Ar–He carrier gas by flowing it over water (Ar–He–H_2O). Both hydrogen gas and water vapour were mixed into the Ar supply prior to entry in to the ablation cell (Figure 2.1). Sample and standards were analysed under the same conditions. Results are presented in Table 2.4.

The total variation of mean compositions measured under different carrier gas and ICP-torch configurations occurs within a factor of 1.70 ± 0.25 (one sigma, excluding Au). This configuration-associated variability is also about the same as the maximum variation observed using the same carrier gas and ICP-torch configuration on different analytical sessions (Figure 2.8). Thus, no systematic bias between the different analytical configurations can be discerned. However, the addition of H_2O vapour to the carrier gas resulted in a significantly elevated background for all masses and reduced sensitivity, and therefore reduced the percentage of usable inclusion analyses from the total.

Table 2.4 LA-ICP-MS data summary for quartz-hosted synthetic fluid inclusions (R122) obtained under different ICP-torch/carrier gas composition instrument conditions

	^{39}K wt.%	^{63}Cu ppm	^{65}Cu ppm	^{88}Sr ppm	^{137}Ba ppm	^{138}Ba ppm	^{139}La ppm	^{169}Tm ppm	^{175}Lu ppm	^{197}Au ppm	^{232}Th ppm	^{238}U ppm
Initial/nominal composition												
	4.77	–	–	87	88	88	86	100	90	98	96	97
Standard/Ar–He												
$\bar{x}$	4.77	21847	22311	54.3	72.4	60.6	7.6	11.6	12.8	4.3	5.9	47.9
s	–	17292	17482	16.4	30.7	21.5	4.6	6.1	8.6	3.3	2.2	29.4
RSD%	–	79.1	78.4	30.2	42.4	35.4	60.6	52.7	66.7	76.2	37	61.4
n	41	39	39	35	22	37	25	27	24	4	6	30
Standard/Ar–H_2–He												
$\bar{x}$	4.77	11120	11270	54.3	64	58.8	9.4	17.4	18.9	1.2	6.4	55.5
σ	–	4427	4509	23.9	25.4	22.2	9.8	19	21.6	1.7	6	48.7
RSD%	–	39.8	40.0	43.9	39.6	37.8	104.7	109.6	114.2	139.7	94	87.8
n	48	43	43	41	30	40	31	30	27	7	17	36
Standard/Ar–H_2O–He												
$\bar{x}$	4.77	17463	17907	61.7	79.1	80.5	9.1	18.4	22.7	–	–	88.2
σ	–	6789	7084	15.8	15.1	10.7	4	17.5	21.8	–	–	66.5
RSD%	–	38.9	39.6	25.7	19	13.2	44.1	95	95.9	–	–	75.4
n	15	14	13	11	5	6	3	10	9	0	0	11
Shield/Ar–He												
$\bar{x}$	4.77	14621	15415	64.2	75.3	71.1	13.8	22.1	22.5	1.7	7.6	79.7
σ	–	13514	15816	32.3	29.3	28.2	17.5	24	27.1	1.4	7.9	66.6
RSD%	–	92.4	102.6	50.3	38.9	39.6	126.5	108.5	120.3	84.4	104.4	83.6
n	57	48	48	50	35	45	28	32	34	16	19	34
Shield/Ar–H_2–He												
$\bar{x}$	4.77	12757	12751	44.5	59.8	54.8	8.8	14.3	18.9	0.6	8.6	47.1
σ	–	8957	8730	18.6	20.9	19.9	10.3	15.9	23.2	0.4	12.5	40.4
RSD%	–	70.2	68.5	41.8	34.9	36.3	116.9	111.2	122.5	71.2	145.8	85.9
n	36	33	33	35	28	33	30	30	30	10	20	28

Notes: Nominal K concentration, given in wt.%, was used as the internal standard for quantification of absolute element abundances. Concentrations in parts per million by weight, measured element masses indicated. LA-ICP-MS determined concentrations not corrected for the dilution effect on the nominal internal standard concentration caused by addition of copper during the experiment. $\bar{x}$ is the mean of *n* replicate analyses, σ is the standard deviation of the sample analyses. RSD% is the relative standard deviation expressed as a percentage of the mean. All analyses that were potentially compromised by surface-related contamination were excluded, as were signals $< \bar{x}_{LoD}$.

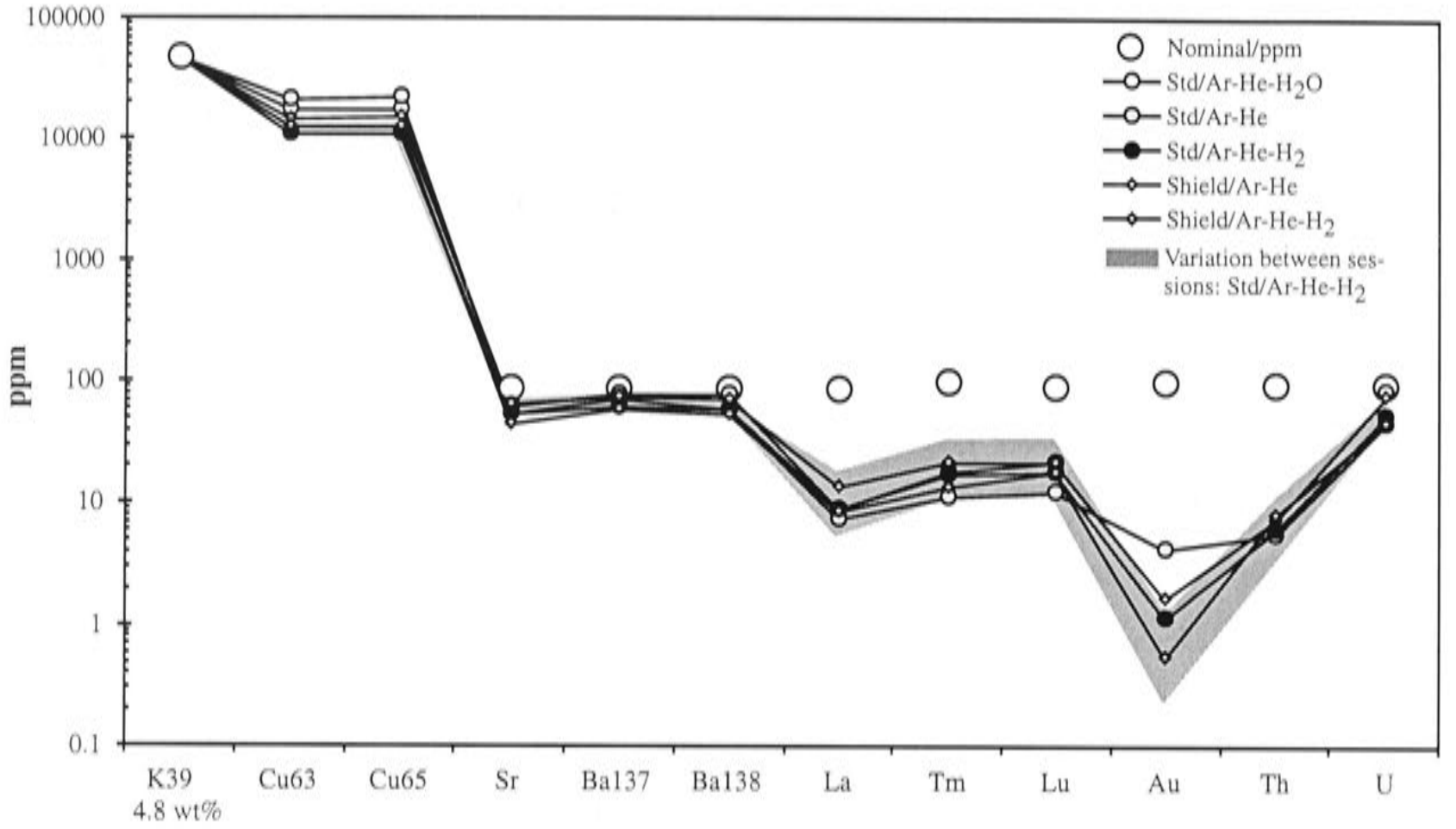

Figure 2.8 Comparison of mean composition determined from replicate analyses of individual synthetic quartz-hosted fluid inclusions in sample R122 measured under different carrier gas and ICP-torch instrument configurations. Initial/nominal experimental fluid composition and an example of the inter-session mean composition variation for analyses made using the same instrument set up shown for reference.

Note that low La, Tm, Lu, Au, and Th concentrations are not an analytical artefact but rather reflect their loss from solution during synthesis.

Different carrier gas and ICP-torch configurations do not bias the measurement of quartz-hosted fluid inclusion compositions provided both the unknown and bracketing standards are analysed under the same conditions.

5.5 Effect of different ablation conditions

Preliminary experiments also revealed significant differences in the form and intensity of fluid inclusion signals measured by the ICP-MS as the laser pulse frequency was varied. Synthetic quartz-hosted fluid inclusions, again from experiment R122, were employed to provide a source of standard composition against which the analytical performance could be assessed as a function of the ablation sampling conditions. Samples and standards were analysed under the same conditions. Data for these experiments are presented in Table 2.5 and Figure 2.9.

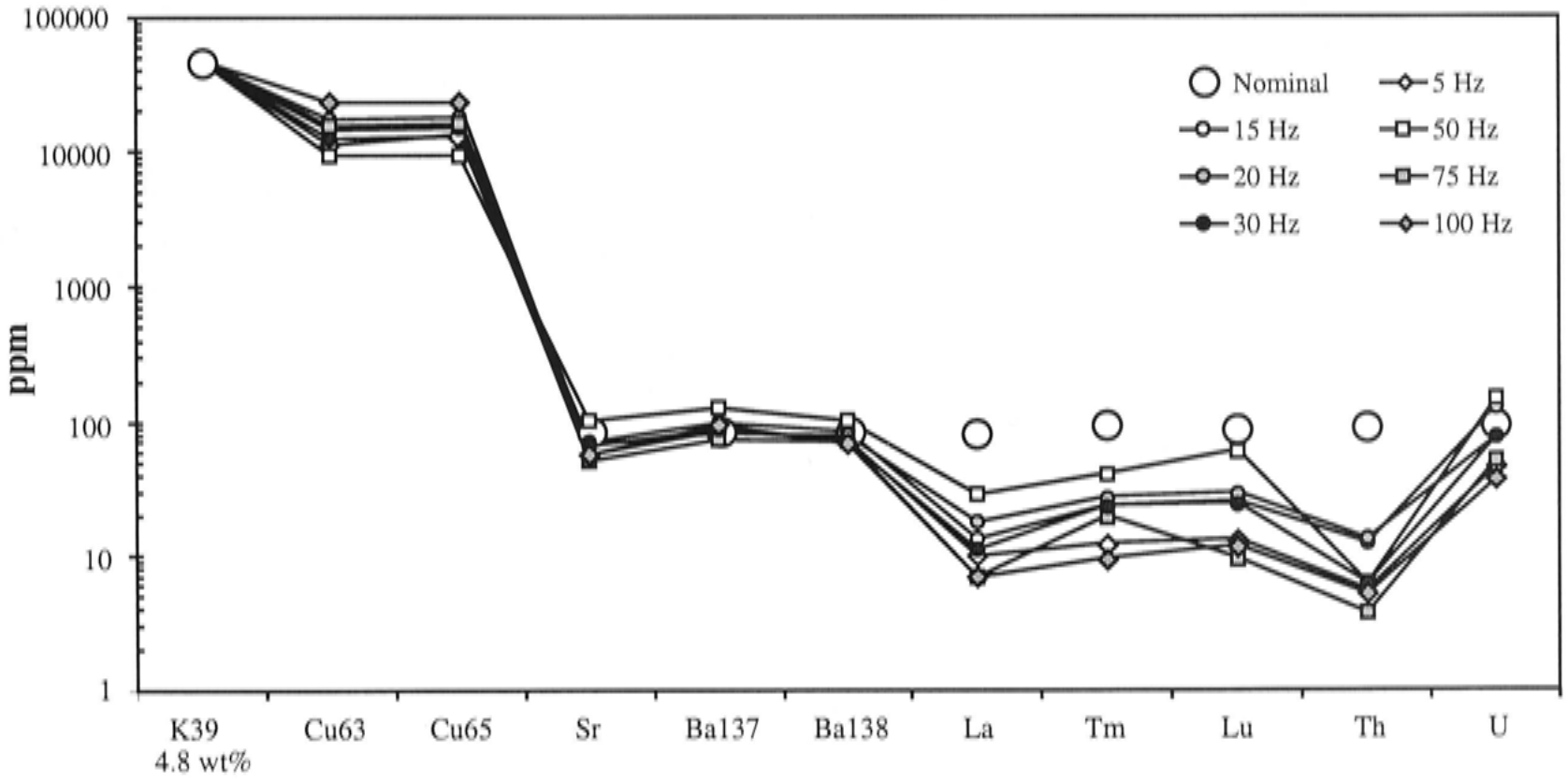

Figure 2.9 Comparison of the mean composition determined for quartz-hosted synthetic fluid inclusions from experiment R122 by LA-ICP-MS as a function of ablation frequency. Initial/nominal solution composition plotted for reference. Low inclusion La, Tm, Lu, Th, and U concentrations reflect their loss from solution during inclusion synthesis at elevated *T* and *P*. It is not an analytical artefact associated with these elements.

At all ablation rates, similar inclusion composition patterns were measured and no systematic bias was observed, but the mean concentrations, for the same element, vary by a factor of 3.25 ± 1.52 (one sigma) between 5 and 100 Hz. This is considerably greater variation than observed when Ar-carrier gas composition and ICP torch configuration were varied and beyond what can be considered reasonable for the technique.

Table 2.5 Quantitative LA-ICP-MS data for quartz-hosted synthetic fluid inclusions from experiment R122 acquired as a function of the ablation frequency in hertz (Hz, laser pulses per second)

	^{39}K	^{63}Cu	^{65}Cu	^{88}Sr	^{137}Ba	^{138}Ba	^{139}La	^{169}Tm	^{175}Lu	^{232}Th	^{238}U
5 Hz											
$\bar{x}$	47711	11399	13716	58	85	74	10	12	13	6	46
σ	–	4455	4405	23	32	28	5	8	9	2	35
RSD%	–	39	32	41	38	38	49	67	65	43	76
n	9	9	9	9	9	9	8	9	8	6	9
15 Hz											
$\bar{x}$	47711	14433	14936	71	99	87	13	23	25	12	125
σ	–	1379	1417	27	36	26	8	13	15	14	60
RSD%	–	10	9	38	36	30	63	54	59	115	48
n	9	8	8	9	9	8	9	8	8	8	8
20 Hz											
$\bar{x}$	47711	17374	17936	67	83	79	18	28	30	13	77
σ	–	17193	17718	30	34	35	24	31	36	20	61
RSD%	–	99	99	44	41	45	132	110	119	153	79
n	40	38	38	37	38	38	38	37	37	36	37
30 Hz											
$\bar{x}$	47711	12323	12916	67	88	70	11	24	24	6	76
σ	–	9749	10233	23	20	25	8	15	15	4	51
RSD%	–	79	79	34	23	35	72	66	62	64	67
n	14	13	13	13	12	14	12	11	11	12	13
50 Hz											
$\bar{x}$	47711	9364	9490	101	125	103	29	42	62	6	148
σ	–	3900	3923	88	103	84	38	61	85	5	122
RSD%	–	42	41	87	83	81	130	148	136	75	83
n	4	4	4	4	4	4	3	4	3	3	4
75 Hz											
$\bar{x}$	47711	15478	15998	51	73	72	7	20	10	4	51
σ	–	1393	1667	21	16	17	3	20	4	2	31
RSD%	–	9	10	42	22	23	49	103	43	41	60
n	4	4	4	4	4	4	4	4	4	4	4
100 Hz											
$\bar{x}$	47711	23467	22940	57	96	68	7	10	12	5	37
σ	–	29323	31130	18	32	22	6	9	11	5	39
RSD%	–	125	136	32	34	32	85	91	94	98	108
n	7	7	7	7	7	7	7	6	6	4	7

Notes: Concentrations are in parts per million by weight, analyte mass for each element indicated. Initial/nominal solution K concentration used as an internal standard for quantification purposes. All signals < $\bar{x}_{LoD}$ excluded.

The most consistent mean composition measurements were acquired over a relatively narrow range of ablation rates, from about 15 to 30 Hz for an average 40 μm diameter beam. These conditions appear to give the optimum compromise between the ablation frequency dependence of signal-to-background ratios, and separation of surface and inclusion signals, and minimise the complexities associated with sampling from extreme aspect ratio ablation sites. Typical fluid inclusion ablation profiles obtained at 5 and 75 Hz are shown in Figure 2.10.

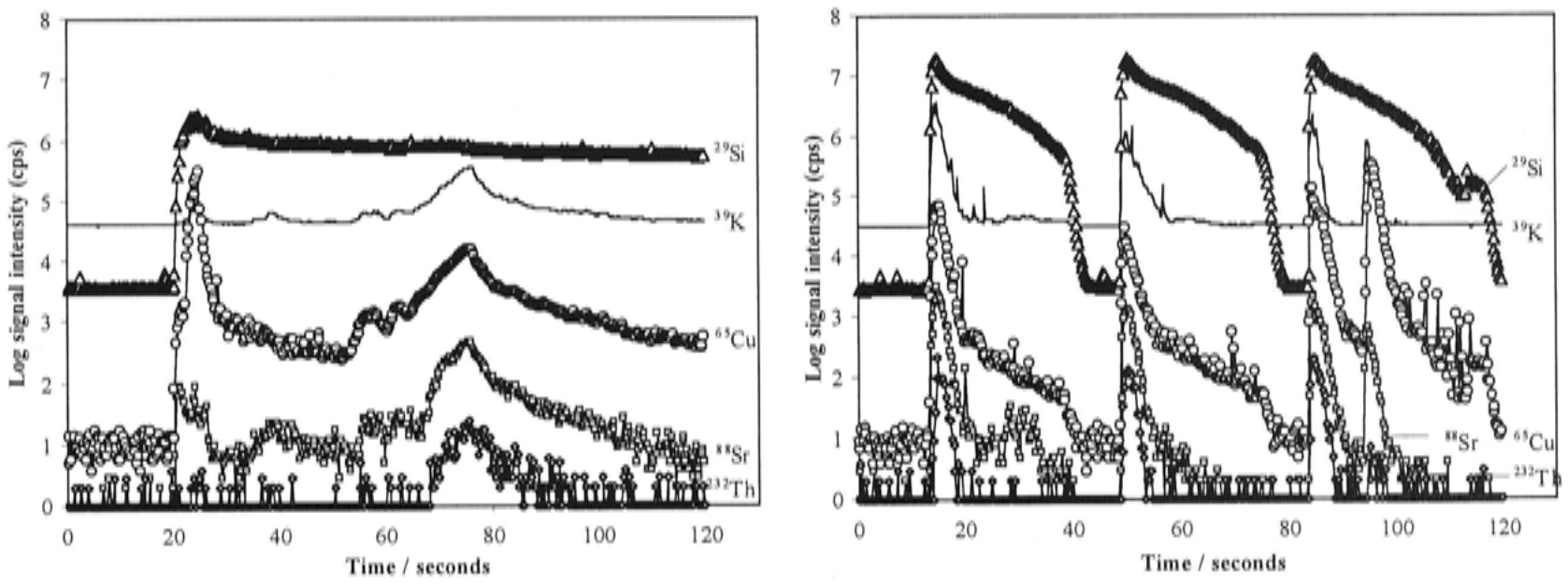

Figure 2.10 Comparison of typical fluid inclusion LA-ICP-MS ablation profiles at 5 Hz (*left*) and 75 Hz (*right*) for synthetic sample R122. Three separate inclusion sites were ablated at 75 Hz. Note the separation of surface contamination and fluid inclusion signals at 5 Hz, but not at 75 Hz (except for the third location at which a second very deep inclusion was encountered).

At ablation rates less than 10 Hz fluid inclusions take longer to sample, leading to signals that are notably drawn out (*e.g.* > 20 seconds) and have relatively low peak intensities, compared with data acquired at higher ablation rates. Under these conditions the signal-to-background ratio is relatively low, potentially explaining the lower precision of such analyses. It is also possible that the fluid inclusion sampling efficiency varies because of splashing (Günther *et al.* 1998) and/or re-sampling of inclusion material within the ablation site. However, surface phenomena are clearly resolved from inclusions at low ablation rates.

Signal intensities (*e.g.* cps) tend to increase with laser pulse rate and pulse energy, as does the inclusion signal-to-background ratio (Günther *et al.* 1998). However, inclusion data obtained at relatively high ablation rates (> ~ 30 Hz) becomes less consistent. The degraded reproducibility appears to result from a loss of depth resolution (smearing) in the sample signal with increasing ablation rate. This is related

to the response time of the ablation cell and transport system. Under very rapid ablation, signals from nearby individual inclusions or surface contamination may not be resolvable, a potential issue for samples containing inclusions of different composition. Also, because of the lower depth resolution inclusions must be analysed from much deeper in the sample to avoid surface contamination. This, however, means inclusions are being sampled from extreme aspect ratio pits, which is associated with data reduction uncertainties.

To summarise, the main factors determining the optimum ablation rate appear to be the degree to which the sample signal is smoothed between the ablation cell and the ICP-MS, the light pulse energy and the beam size and inclusion depth. For this system and ablation rate of 15 to 25 Hz ablation is considered optimal.

5.6 Ablation behaviour of quartz and its potential bearing on analytical precision

Another aspect bearing on the analytical precision of fluid inclusion analysis, but so far neglected in this discussion, is the ablation behaviour of the quartz-host and its effect on inclusion sampling. In particular, the ablation behaviour of quartz is sometimes erratic and causes an incomplete inclusion yield during the sampling process. For example, cracks have been occasionally observed to propagate from some fluid inclusions prior to being breached during the ablation process. Under these circumstances it is common for fluids to migrate and even appear to boil along these fractures. This clearly results in incomplete sampling of the inclusion and potential measurement of fractionated inter-element concentration ratios. Such behaviour can be observed, however, so suspect analyses may be removed from consideration.

Experience suggests that erratic ablation processes are a significant source of the total measurement uncertainty in fluid inclusion LA-ICP-MS analysis. Laser sampling ideally occurs through photo-thermal ablation, *i.e.* where the irradiated surface is evaporated. This is usually achieved in materials that absorb the laser efficiently. Quartz, however, known for its high transmission in the UV range (it is used in UV optics), couples poorly with 193 nm light and requires multi-photon absorption for photo-thermal ablation. This is because the Si–O bond energy gap is about 9 eV whereas ArF laser light photons are 6.4 eV (Fiebig *et al.* 1999). Consequently, quartz usually undergoes photo-mechanical ablation, which is determined largely by the presence of surface defects and so is essentially uncontrolled surface fragmentation (Ihlemann 1992). Figures 2.11 and 2.12 illustrate a variety of features typical of ablated quartz surfaces.

Fiebig *et al.* (1999) argue that quartz ablation is improved by increasing laser fluence when using an 193 nm excimer ArF laser. It is possible that the use of shorter wavelength light sources, for which radiation absorption by quartz should be considerably higher, in the future may improve ablation behaviour and hence the reproducibility of quartz-hosted fluid inclusion measurements.

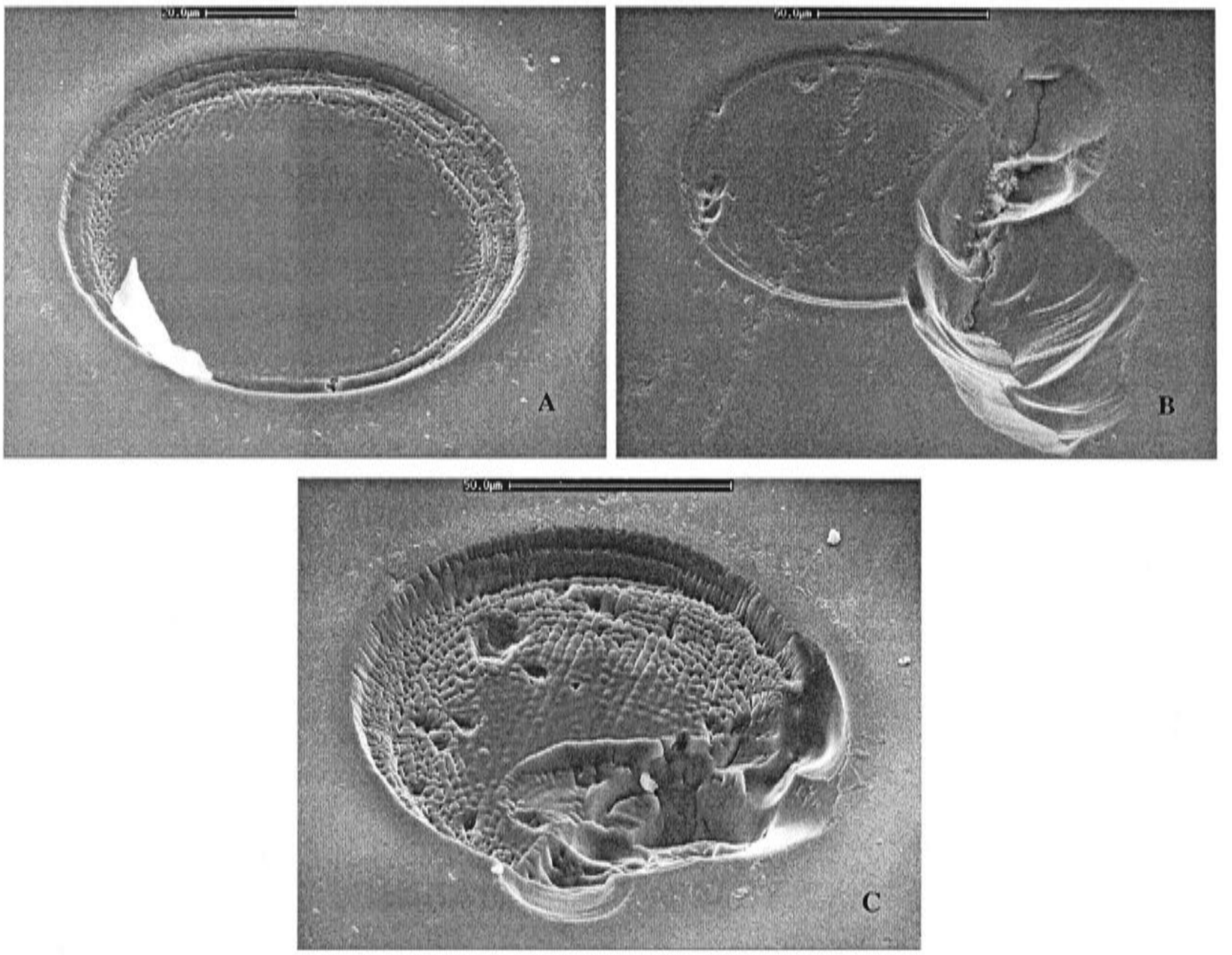

Figure 2.11 Examples of quartz surfaces ablated by ArF excimer laser (193 nm). A) Controlled photothermal ablation of quartz. The bright object is debris unrelated to ablation. B and C) are examples of the surface fragmentation that are typical of uncontrolled photomechanical ablation. Also, there appears to be melt developed of on the base of the pits in A and C.

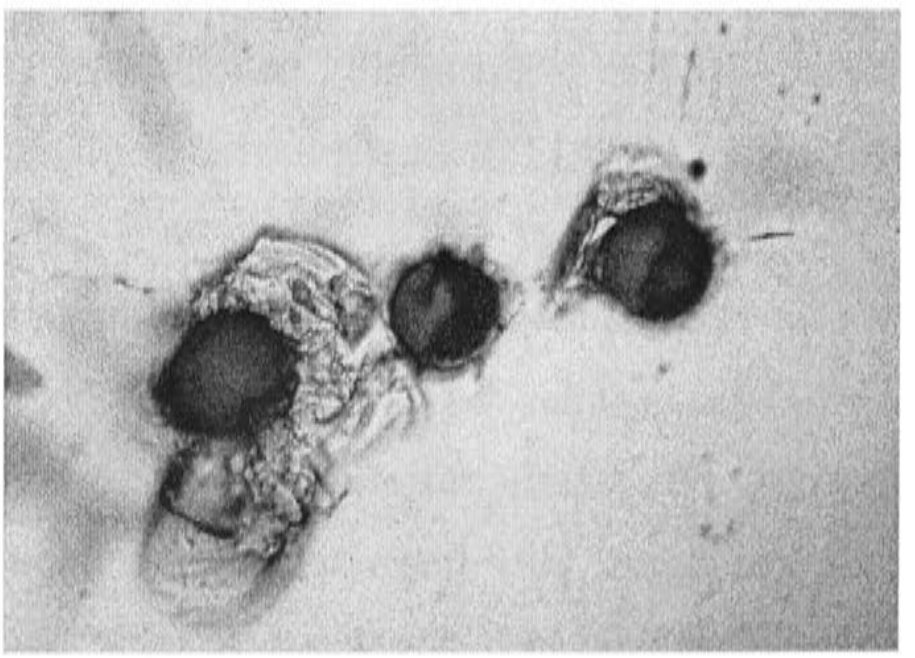

Figure 2.12 Photomicrograph of fluid inclusion ablation pits in quartz produced under the same laser conditions. Pit diameter is 35 μm. Note extent of near-surface fracturing varies significantly between pits.

5.7 Comparison of synthetic fluid inclusion and quenched solution compositions: another look at the accuracy of LA-ICP-MS measurements

Non-buffered capsule solutions, in which the synthetic fluid inclusions were grown, were extracted shortly after quenching of the experiments and analysed[10]. This facilitated a direct comparison of the starting solution composition[11], the fluid inclusion composition determined by LA-ICP-MS and the quenched experimental fluid (Table 2.6, Figure 2.13).

Table 2.6 Comparison of quench solution and loss corrected synthetic fluid inclusion compositions

	Quench solution/ Starting solution		Fluid inclusions SN-ICP-AES		LA-ICP-MS♥		Comments
	Mass	Nominal	$\bar{x}$	$\sigma^{\blacklozenge}$	$\bar{x}$	$\sigma^{\ddagger}$	
R146							
	^{39}K	5220 ppm	4973	41	4973	41	• Quench K concentration used to correct fluid inclusion composition.
	^{23}Na	4850 ppm	4463	45	5459	457	
	^{43}Ca	5640 ppm	3497	27	7652	4031	
	^{63}Cu	– (ppm)	917	7	4858	3224	
	^{65}Cu	– (ppm)	NA		5002	3436	
R122							
	^{39}K	47710 ppm	37343	265	37343	265	• Quench K concentration used to correct fluid inclusion composition. • Au not measured in quench solution, below detection by LA-ICP-MS in fluid inclusions. • A small copper-chloride daughter phase present in all fluid inclusions.
	^{63}Cu	– (ppm)	7047	32	8510	3252	
	^{65}Cu	– (ppm)	NA		8565	3350	
	^{88}Sr	87 ppm	BD		48	18	
	^{137}Ba	88 ppm	BD		45	17	
	^{138}Ba	88 ppm	NA		40	14	
	^{139}La	86 ppm	0.05	0.01	4	4	
	^{169}Tm	100 ppm	0.17	0.01	8	9	
	^{175}Lu	90 ppm	0.13	0.12	9	9	
	^{232}Th	96 ppm	BD		3	2	
	^{238}U	97 ppm	1.06	0.24	38	33	
R145							
	^{39}K	12.255 %	5.231	0.011	9.94	0.90	• Quench Mg concentration and ^{24}Mg used to correct fluid inclusion composition.
	^{23}Na	7.023 %	3.961	0.087	6.4	1.8	
	^{43}Ca	5.386 %	5.790	0.039	5.21	2.9	

[10] After the run, capsules were cleaned, pierced and the remaining free fluid sampled by syringe, weighed and diluted with a solution of high-purity 2% distilled HNO_3 to provide a useful analytical volume and stabilise the dissolved components until analysis. Indium was also added to the diluted quench solutions as an internal standard for analytical purposes. This diluted experimental quench solution was then analysed by solution nebulization-inductively coupled plasma-atomic emission spectrometry (SN-ICP-AES) using a Varian instrument operating at the Department of Geology, Australian National University. Quench solution analyses were calibrated against known standard solutions.

[11] Starting solution compositions used in the synthetic fluid inclusion experiments were independently confirmed by SN-ICP-AES analysis after preparation.

Starting solution		Quench solution/ SN-ICP-AES		Fluid inclusions LA-ICP-MS♥		Comments
Mass	Nominal	$\bar{x}$	σ♦	$\bar{x}$	σ‡	
^{63}Cu	– (%)	2.955	0.012	8.4	4.6	• Sylvite (KCl), halite (NaCl) and copper-chloride daughter phases present in all fluid inclusions.
^{65}Cu	– (%)	NA		8.4	4.5	
^{24}Mg	69 ppm	43	3.9	43	21	
^{25}Mg	69 ppm	NA		48	32	
^{45}Sc	62 ppm	1.5	0.1	19	4	
^{89}Y	61 ppm	1.1	0.3	15	7	
R148						
^{39}K	24823 ppm	25190	11	25190	11	• Quench K concentration used to correct fluid inclusion composition. • Minor unknown amount NaCl lost on loading capsule – nominal Na concentration is in error • No daughter phases appear to be precipitated in fluid inclusions.
^{23}Na	50295 ppm	20626	120	16187	4791	
^{43}Ca	14299 ppm	14023	60.2	12576	1769	
^{63}Cu	– (ppm)	21479	58.7	31179	11635	
^{65}Cu	– (ppm)	NA		29789	9007	
^{139}La	28 ppm	28	0.1	21	8	
^{238}Cs	30 ppm	ND				
^{238}U	27 ppm	21	2	17	11	

Notes: ♦ Analytical uncertainty for SN-ICP-AES concentrations is calculated from the standard deviation of three replicate intensity measurements taken for each sample. LA-ICP-MS data were reduced using the concentration determined of an element not saturated in the quench solution. This internal standard element is indicated in the comments. ♥ "Original" data, including the number of individual fluid inclusion analyses, is located in Table 2.3. ‡ Uncertainty on the internal standard element is taken directly from the SN-ICP-AES data. NA refers to the fact that individual isotopes cannot be measured using ICP-AES, only the total elemental abundance. ND indicates elements not analysed for. BD refers to elements that were analysed, but have concentrations below detectable levels.

The concentrations of all components are significantly lower in quench solutions than in the starting solutions. Because certain components are known to be highly soluble at ambient conditions they are expected to remain unmodified upon quenching (*e.g.* NaCl, KCl, $MgCl_2$ solubilities in water at 20 °C are 26.7 wt.%, 25.4 wt.% and 35.2 wt.%, respectively). However, that these "quenchable" solutes are not in the quench solution at the same concentration as before the inclusion synthesis, is clear evidence that the fluid composition changed during the run.

Petrographic and spectroscopic techniques can be used to identify precipitated daughter phases in the fluid inclusions. For synthetic inclusions, the composition of these phases will indicate which major components were lost from solution by precipitation on cooling (Table 2.6).

Solute losses during experiments probably occur through diffusion and exchange processes with the copper capsule (and mineral phases, if present). Such processes must, however, occur relatively rapidly in these simple un-buffered experiments, as elemental ratios between the quench stable components in the fluid

inclusions and the post-run solution are indistinguishable. Figure 2.13 compares fluid inclusion and quench solution compositions.

When the fluid inclusion compositions are corrected for the partial loss of the internal standard element during the run by using an internal standard from the post-run capsule fluid, both the fluid inclusion and quenched solution compositions are identical for those elements not affected by precipitation on quenching. This implies that the synthetic fluid inclusion LA-ICP-MS technique can be accurate if the correct procedure is followed.

All composition deviations between quench solutions (SN-ICP-AES) and the fluid inclusions (LA-ICP-MS) are consistent with solute precipitation on quenching of the experiment. The close correspondence of the fluid inclusion and quench solution composition in R148 is consistent with it being the only experiment in the series in which the inclusions contain no saturated phases at room temperature.

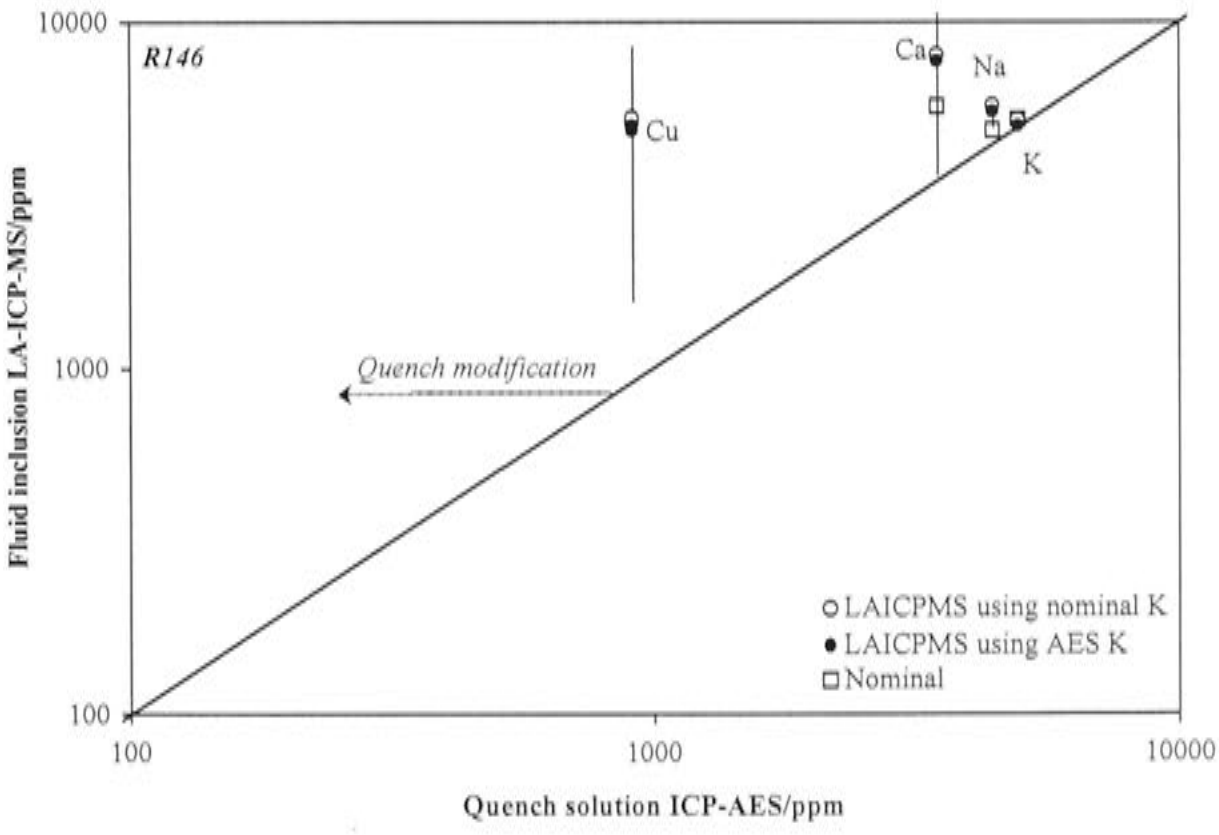

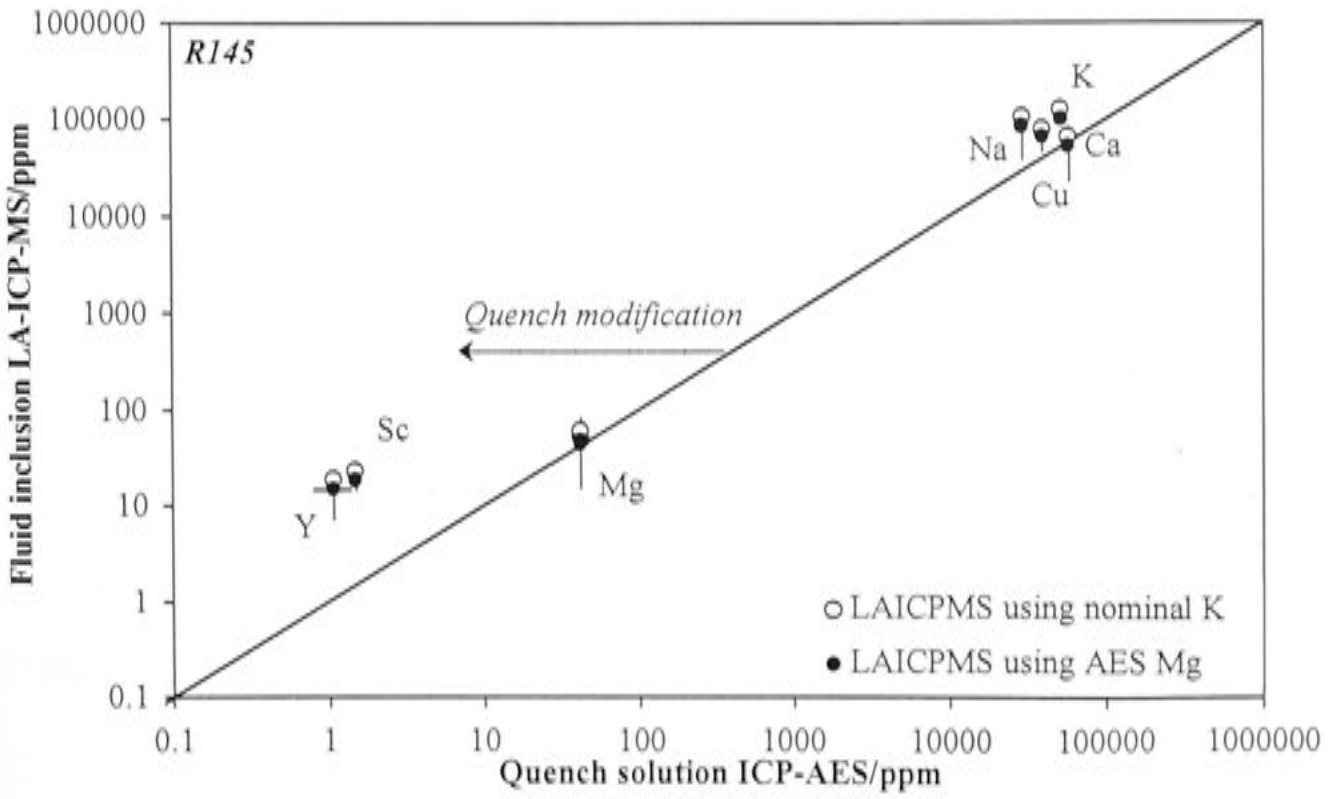

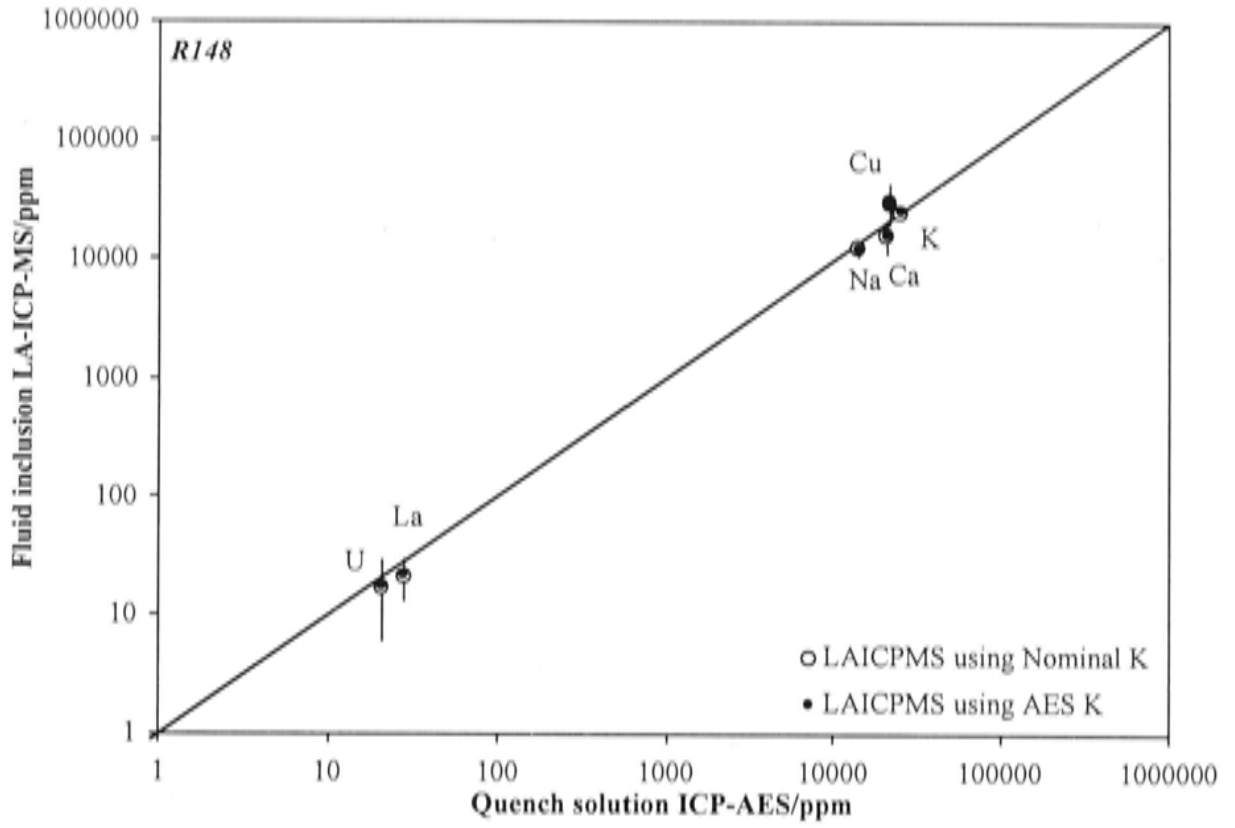

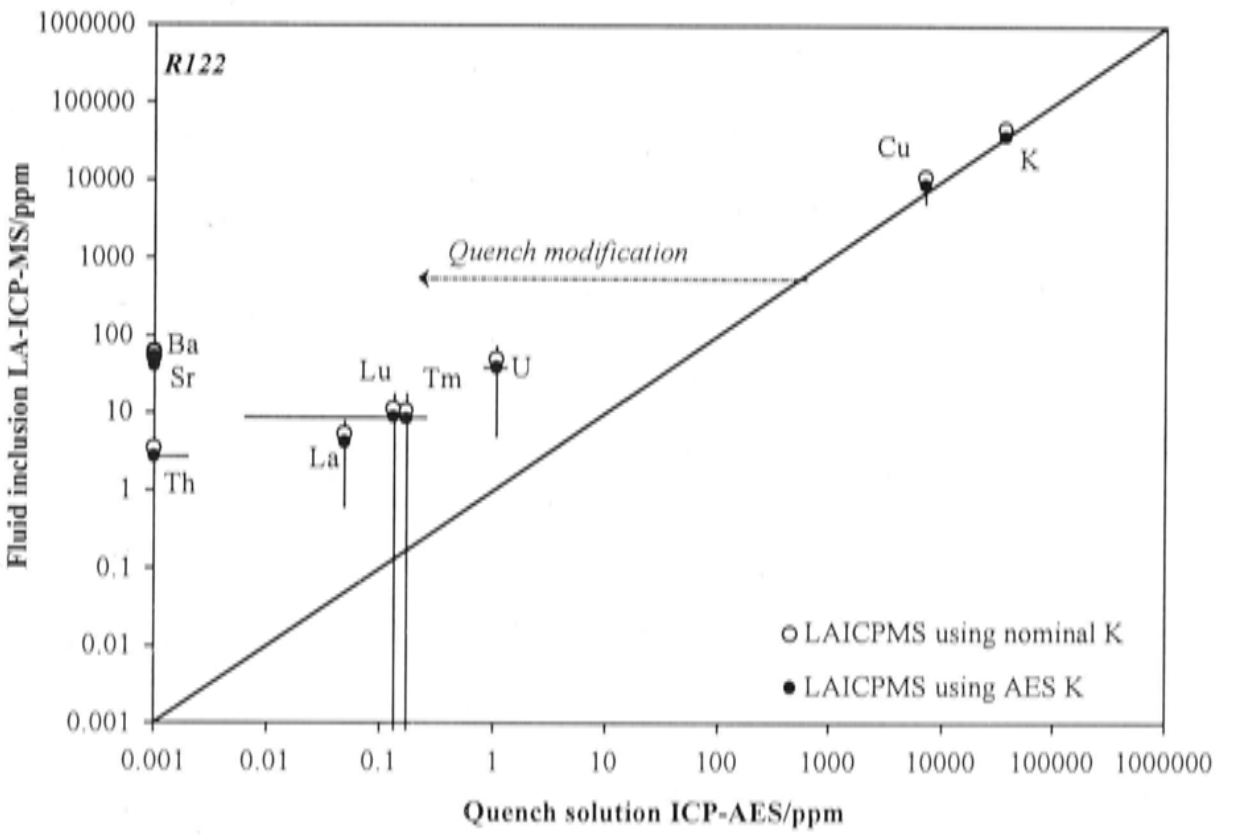

Figure 2.13 Comparison of fluid inclusion and quench solution composition for runs R146, R145, R148, and R122. The effect of quench modification (*i.e.* precipitation) is indicated. LA-ICP-MS compositions calculated using both the quench (ICP-AES determined internal standard) and starting (nominal) solution K (or Mg) concentration as the internal standard are shown. For R146, the starting/nominal solution is also plotted against the quench fluid composition for reference.

It is concluded that few solution components can be assumed to maintain an unmodified concentration from the beginning to the end of the experiment (*cf.* Loucks and Mavrogenes 1999). That point made, it is a simple matter to extract the experimental solution after the run and measure the concentration of an element not likely to be affected by quenching. This quench solution measurement can then be used to obtain reliable absolute concentrations for the quench-modified components from the fluid inclusion LA-ICP-MS measurements.

5.8 Comparison of LA-ICP-MS and PIXE fluid inclusion analysis techniques

As a further test of the accuracy of quantitative fluid inclusion LA-ICP-MS and fluid inclusion mineral-solubility experimental methods, a series of mineral-buffered, synthetic quartz-hosted fluid inclusions, of essentially unknown composition but doped initially with a range of trace elements were prepared and analysed by LA-ICP-MS. This same population was also analysed by proton induced X-ray emission (PIXE), another quantitative fluid inclusion analysis technique (Anderson *et al.* 1989; Heinrich *et al.* 1992; Ryan *et al.* 1995, 2001)

PIXE analysis of fluid inclusions was undertaken at the Heavy Ion Analytical Facility at CSIRO, North Ryde, Sydney, Australia. This sensitive microprobe technique employs MeV accelerated protons to excite fluorescence of characteristic X-rays to measure in situ and non-destructively the composition of intact fluid inclusions. Analyses were made in scanning mode and are possible because the high-energy protons have a large penetration depth and can be focussed with high spatial resolution (Ryan *et al.* 2001). PIXE yields from fluid inclusions were calculated from a layered model and corrected for the geometry and overlap of the proton beam with the inclusion and its host mineral using the GeoPIXE software package (Heinrich *et al.* 1992; Ryan *et al.* 1995). Quantification of the proton induced X-ray yield, like synchrotron X-ray fluorescence, is notionally "standardless" but requires accurate knowledge of the inclusion depth, its three-dimensional geometry and host mineral properties.

PIXE was used to measure Cu, K, Fe and Cl concentrations in single inclusions from four different mineral-buffered synthesis experiments. The potassium concentration measurement by PIXE was used as the internal standard for quantification of LA-ICP-MS signals since the trace element spiking-method for quantifying of the experiments was found to be unreliable (*PART 2, §5.6,5.10*). Major element concentrations in these fluid inclusions calculated from initial trace element concentrations were unrealistically high - in some cases, impossibly so (> 100 wt.%).

Comparison of the absolute concentrations measured by PIXE and LA-ICP-MS shows that the two techniques produce the same quantitative elemental concentrations within their respective analytical uncertainties, with the exception of Fe (Table 2.7; Figure 2.14). The measurement of Fe by LA-ICP-MS was suspected to be unreliable due to isobaric molecular interferences (*e.g.* $^{40}ArO^{+}$), a well known problem

in conventional ICP-MS analysis (Günther *et al.* 2001). Trace element concentrations in the synthetic fluid inclusions were not measurable by PIXE.

Table 2.7 Comparison of PIXE and LA-ICP-MS data for mineral-buffered synthetic fluid inclusions

	PIXE / wt.%			LA-ICP-MS / wt.%		
	$\bar{x}$	σ	n	$\bar{x}$	σ	n
AH87						
K	20.60	1.16	4	*Internal standard-PIXE*		47
Cu	8.45	4.02	4	9.33	2.57	47
Fe	0.07	0.03	4	1.22	2.19	21
Cl	29.3	1.05	2	*33.4 wt.%*		
AH88						
K	7.36	1.08	2	*Internal standard-PIXE*		17
Cu	10.40	5.67	2	8.41	3.67	17
Fe	0.06	0.04	1	< LoD		
Cl	14.60	0.75	1	*12.8 wt.%*		
AH89						
K	0.83	0.26	2	*Internal standard-PIXE*		16
Cu	2.22	0.03	2	1.63	1.54	16
Fe	0.02	0.00	2	0.37	0.64	4
Cl	3.26	0.37	1	*6.2 wt.%*		

Notes: Concentrations in weight percent. Cl concentration tabulated in LA-ICP-MS column (*italicised*) refers to the nominal concentration in the starting solution, Cl could not be measured by LA-ICP-MS.

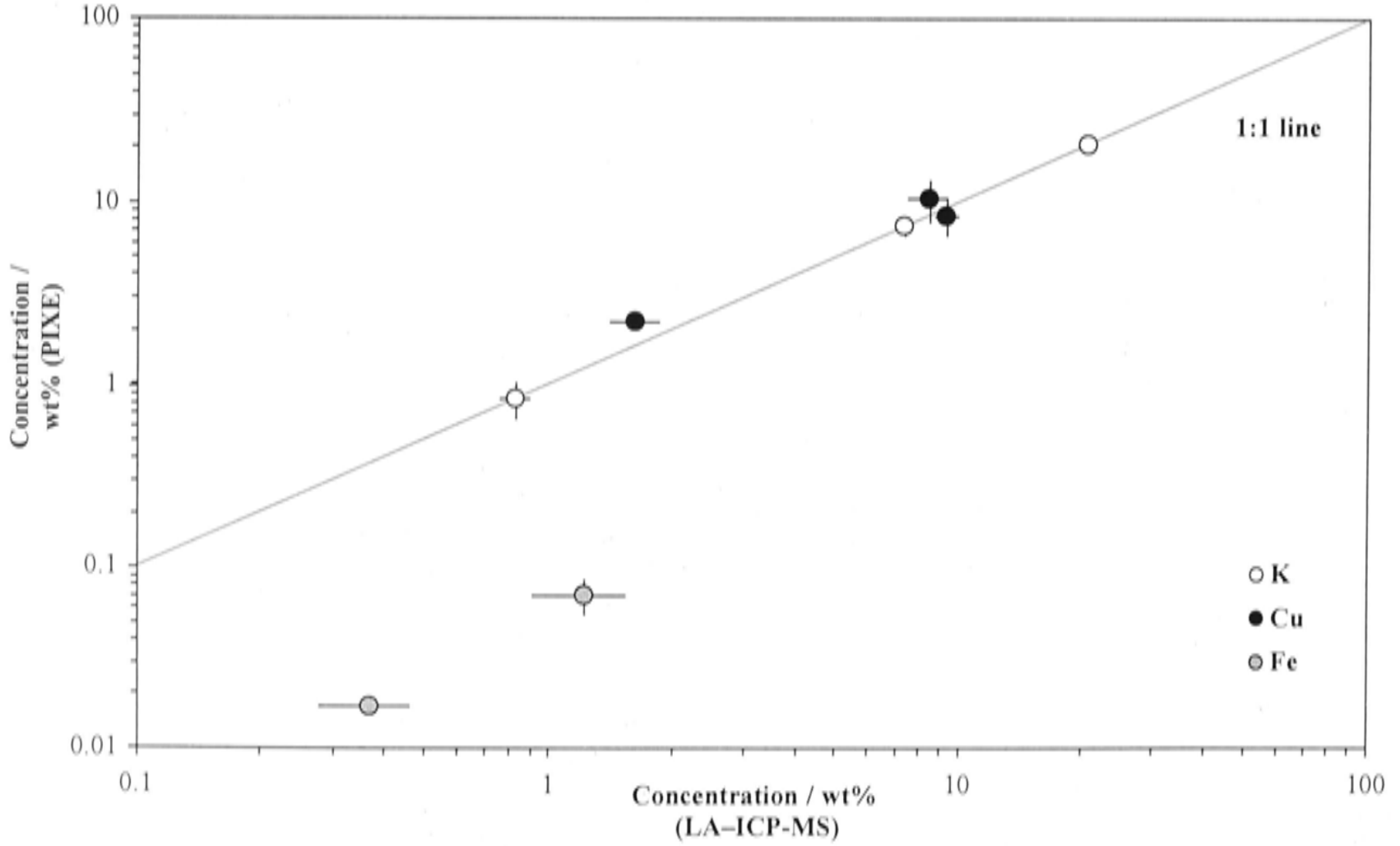

Figure 2.14 Comparison of LA-ICP-MS and PIXE synthetic fluid inclusion data from AH87, AH88 and AH89 for Cu, K, and Fe. LA-ICP-MS data were quantified by using the K concentration determined by PIXE as an internal standard and NIST 612 silicate glass as the external calibration standard. Bars indicate standard error of the mean $\left(\sigma/\sqrt{n}\right)$.

5.9 Another note on synthetic fluid inclusions and the attainment of fluid-mineral equilibrium in multi-component systems: Trace elements

Given the consistency of quantitative fluid inclusion measurements by the two different techniques, the LA-ICP-MS trace element data was recalculated using the mean potassium concentration measured by PIXE. As expected, the measured fluid inclusion trace element composition was consistently lower, by one or more orders of magnitude, than the composition of the starting solution. However, there is significant compositional variation among the trace elements (Figure 2.15). Assuming that individual fluid inclusions are isolated at different times, the pattern of variation suggests fluid-mineral reaction kinetics are element specific. The relatively constant Ba/Cu and Sr/Cu are interpreted, like major element ratios that are constant, *e.g.* K/Cu and Na/K (Figure 1.8), as indicative of approaching fluid-mineral equilibrium on the time-scale of fluid inclusion entrapment. The erratic distribution of other element ratios, *e.g.* Th/Cu and Lu/Cu, is consistent with real compositional heterogeneity within the inclusion population for these elements and suggests their equilibration with the coexisting minerals is much slower.

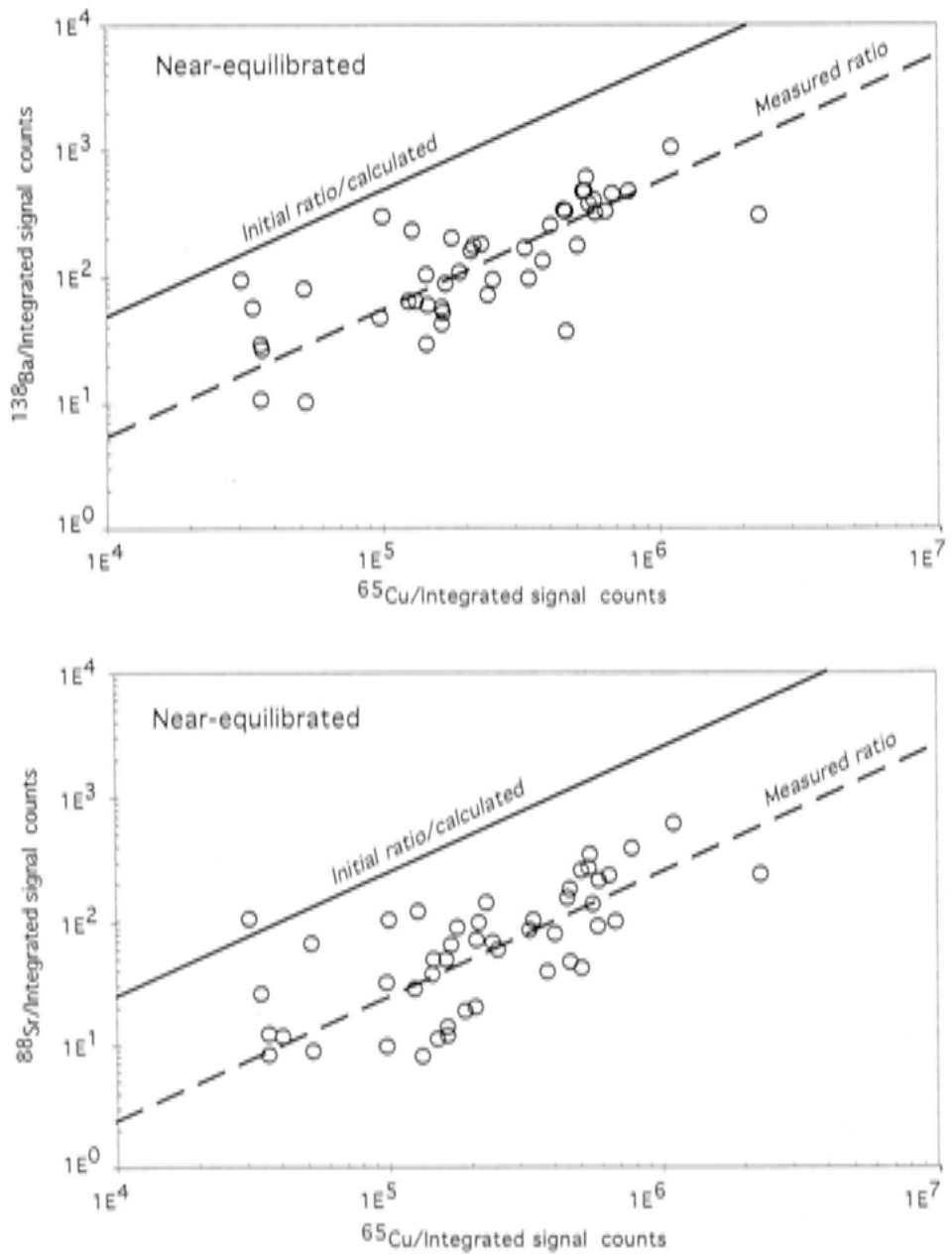

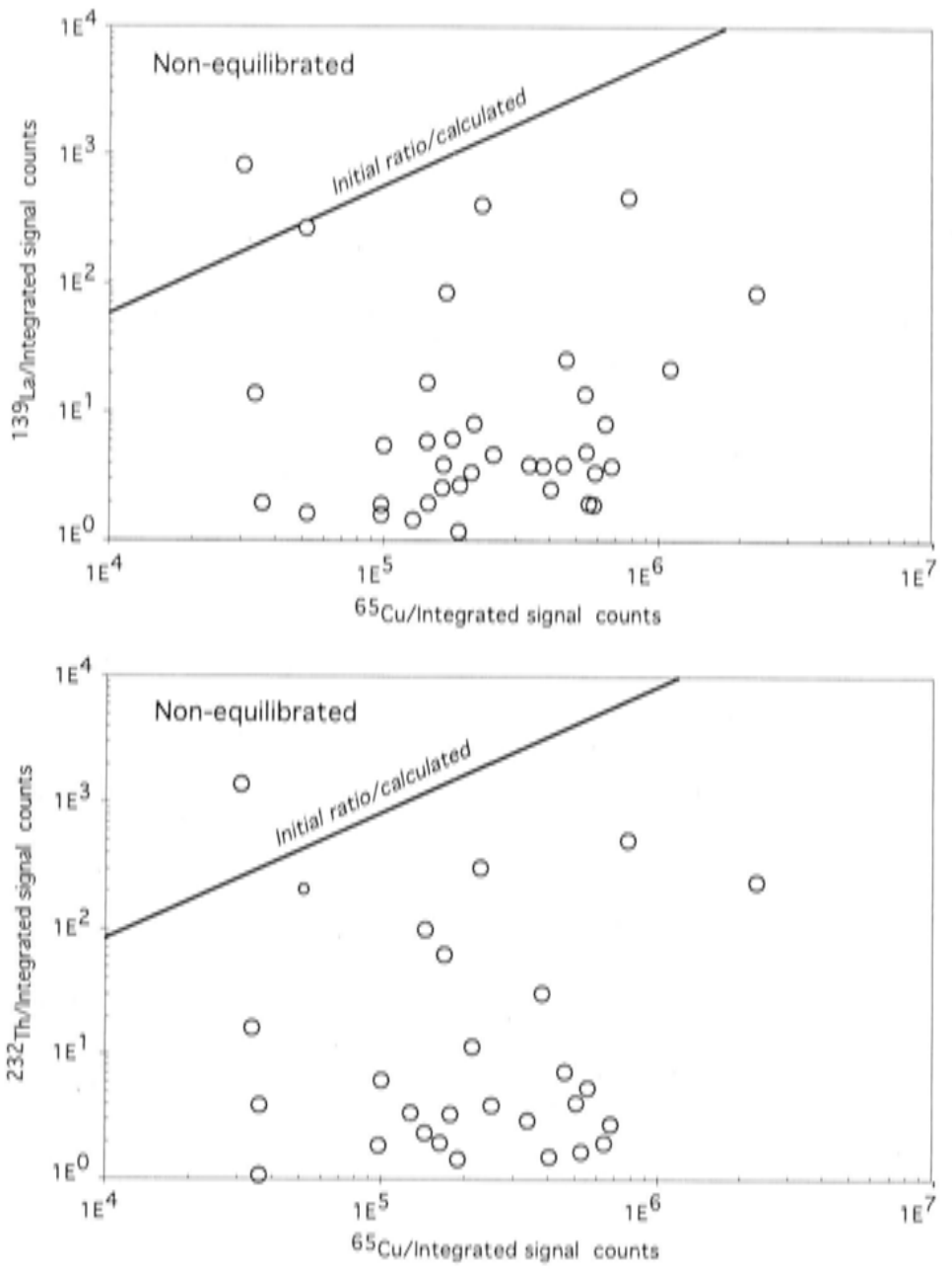

Figure 2.15 Comparison of trace element behaviour with respect to copper in individual fluid inclusions from AH87, buffered by Qz–Kf–Sil–Mt–Hm–Cu, as total integrated signals, in counts. Signal counts are fully corrected for background etc. Signal intensity is a proxy for absolute inclusion mass/volume, while the signal intensity ratio specifies the composition. The expected trace element signal intensity was calculated as a function of the measured Cu signal assuming the initial trace element composition of the fluid is preserved in the inclusions. Measured signal intensity ratio shown for reference in the first two plots.

Despite the evidence for disequilibrium among some trace solutes, those elements, typically major components, with simple fluid-mineral reaction relations do attain equilibrium. Major element data for AH87 is plotted in Figure 1.8 for comparison. Therefore, it is presumably the mineral-fluid reaction kinetics of the major elements, since these may significantly affect dissolved silica concentrations, which influences the rate that fluid inclusions form. In contrast, trace element exchange reactions appear to exert little influence on the overall behaviour of the system (also see *PART 1, §3*).

5.10 A discussion of methods for obtaining absolute concentrations from natural and synthetic fluid inclusions by LA-ICP-MS

To convert LA-ICP-MS measured ratios into concentrations an independently known internal standard is required. Since it is a destructive technique the internal standard must be determined prior to ablation. Because intact fluid inclusions are buried below the surface, conventional means (*e.g.* electron microprobe) of obtaining composition data for use as an internal standard are not available. Currently, various approaches are used to obtain internal standard data for natural and synthetic inclusion fluid inclusions.

5.10.1 Natural fluid inclusions

Deriving basic compositional information for natural and synthetic inclusions from microthermometry measurements on observed phase changes is a well-established technique (Roedder 1984), but relies on the assumption that the behaviour of complex multi-component fluids can be approximated by a simple experimentally calibrated system. Consequently, the accuracy to which concentrations can be determined in this manner is dependant on the analyst choosing the most appropriate model system, which is clearly not always the case (*cf.* Hedenquist and Henley 1985). Günther *et al.* (1998) presented a general algorithm for calculating an approximate Na concentration from microthermometric measurements made on complex natural inclusions, based largely on the simple NaCl–H_2O model system. Subsequently, this algorithm has been widely applied in quantitative LA-ICP-MS studies of natural inclusions (Audétat *et al.* 1998; Ulrich *et al.* 1999; Heinrich *et al.* 1999; Audétat *et al.* 2000a,b; Ulrich *et al.* 2001). It must be recognised that such general treatments are approximations and as such have the potential to induce large errors.

At the current time, given the intrinsic precision of the LA-ICP-MS fluid inclusion technique and the undeterminable error associated with the approaches such as those recommended by Günther *et al.* (1998), it is unreasonable to assume that absolute concentrations can be known more accurately than ± 50% for individual inclusions in natural samples (better compositional constraint is achieved if multiple measurements can be made on a homogeneous population of inclusions). This can be

acceptable, however, because mineral solubilities, and hydrothermal fluid compositions generally, vary over several orders of magnitude.

5.10.2 Synthetic fluid inclusions

The results of this study clearly document that trace element doping of experimental solutions for subsequent quantitative determination by LA-ICP-MS or other techniques, in both simple un-buffered and complex mineral-buffered fluid inclusion synthesis experiments, is fraught with significant uncertainty and so is not suitable for quantifying solute concentrations in most mineral-buffered solubility experiments. This is because trace elements, intended as inert internal standards, do react with the buffering minerals and so approach new equilibrium concentrations. In a sense, this is reassuring since it indirectly demonstrates that the mineral-fluid system is reactive which is an essential experimental requirement.

An alternative means of quantifying mineral-buffered solubility experiments is to conduct experiments in which one of the buffered fluid components is known to be extremely soluble at room temperature. Such soluble salts, for example NaCl, KCl, $CaCl_2$, LiCl, and $MgCl_2$ are readily mineral-buffered and can be independently measured in the quenched experimental solution. Combined with LA-ICP-MS, the quench concentration can be used as the internal standard for the quantification of absolute concentrations of the non-quenchable components from the fluid inclusions. The components of a solution that are quench modified are usually easily recognised through standard petrographic identification of the presence of daughter phase precipitates. Should all solute components appear saturated, quench fluid analyses will be of little use and absolute concentrations will have to be obtained by alternative methods (§5.10.1, 5.10.3 and 5.10.4). Noting, of course, that reliable concentration ratios in the inclusions can always be determined by LA-ICP-MS.

Like other techniques, all errors in the determination of the concentration of an internal standard element are propagated into the calculated absolute concentrations.

5.10.3 Independent complementary techniques

A measurement by any technique (*e.g.* PIXE and SXRF) that provides the absolute concentration of an element in a fluid inclusion, that can also be measured using LA-ICP-MS, has the potential to be used as an internal standard for the quantification of absolute composition of the trapped fluid (*PART 2, §5.8*). Another advantage of using a combination of techniques is that the variety of chemical composition data can be extended considerably. With careful petrographic correlation of inclusion populations the LA-ICP-MS technique has few limitations other than the propagation of error from the internal standard measurement.

5.10.4 An alternative, "internal standard-less" method for quantitative fluid inclusion LA-ICP-MS

The data from this study show that for the analytical conditions used during this study there is effectively no difference in the relative analytical volume versus signal yield between ablation of the NIST silicate glass standard and fluid inclusions. Otherwise a calibration error would have been observed. Since this is the case, internal standard-less quantification of inclusions by LA-ICP-MS should be possible provided the volume of any given inclusion can be accurately determined.

Indeed an equivalent expression to Equation [2.3] can be derived using the inclusion volume, instead of a concentration, as the internal standard for quantitative determination of absolute concentrations by LA-ICP-MS. It takes the form,

$$C_{i\,(by\ volume)}^{inclusion} = \left(\frac{I_i^{inclusion}}{V_{I_i^{unk}}^{inclusion}} \right) \cdot S_{\mu g\,/\,count}^{Absolute\ std} \cdot S^{Relative\ unk/std} \qquad [2.10]$$

where, $C_{i\,(by\ volume)}^{inclusion}$ is the concentration of element *i* in the inclusion in weight.volume^{-1} units (*e.g.* μg/cm^3), $I_i^{inclusion}$ is the integrated signal counts for *i* in the inclusion, $V_{I_i^{unk}}^{inclusion}$ is the measured inclusion volume in μm^3, and $S_{\mu g\,/\,count}^{Absolute}$ is the absolute sensitivity, as determined from the calibration standard, in μg of *i* per count. $S^{Relative\ unk/std}$ is

analogous to the coefficient used to correct for relative differences in the analytical sensitivity between the standard and unknown in the standard expression, but defined,

$$S^{Relative\ unk/std} = \left(\frac{C^{HOST}_{int.std} \cdot I^{std}_{int.std} \cdot \rho^{HOST}_{g/cm^3}}{I^{HOST}_{int.std} \cdot C^{std}_{int.std} \cdot \rho^{std}_{g/cm^3}} \right) \qquad [2.11]$$

where, ρ^{HOST}_{g/cm^3} and ρ^{std}_{g/cm^3} are the density of the inclusion host material and calibration standard, respectively, in g/cm^3. $C^{HOST}_{int.std}$ and $I^{HOST}_{int.std}$ are, respectively, the concentration and measured signal intensity of an internal standard element in the inclusion host material (*N.B.* this does not, in anyway, relate to the inclusion composition). Other symbols previously defined. Continuing,

$$S^{Absolute}_{\mu g/count} = \left(\frac{C^{std}_i \cdot \rho^{std}_{g/cm^3} \cdot 10^{12}}{I^{std}_i} \right) \cdot V^{standard}_{I^{std}_i} \qquad [2.12]$$

where, C^{std}_i is in μg/g concentration units and $V^{standard}_{I^{std}_i}$ is the volume of standard ablated in μm^3 that yields I^{std}_i counts and given by,

$$V^{standard}_{I^{std}_i} = 0.1^{depth/pulse}_{\mu m} \cdot \left(0.5 \varnothing^{beam}_{\mu m}\right)^2 \cdot \pi \cdot Hz^{ablation} \cdot t^{I^{std}_i}_{seconds} \qquad [2.13]$$

where, $0.1^{depth/pulse}_{\mu m}$ is the average depth per pulse in μm (here taken from Eggins *et al.* 1998a), $\varnothing^{beam}_{\mu m}$ is the beam diameter in μm, $Hz^{ablation}$ is the ablation frequency in light pulses per second, $t^{I^{std}_i}_{seconds}$ is time in seconds over which I^{std}_i counts were measured on the standard.

Inclusion volumes are readily determined by optical measurement using a microscope and fitting these, where appropriate, to a hypothetical ellipsoid (*cf.* Heinrich *et al.* 1992, Anderson and Bodnar 1993). For fluid inclusions with irregular geometries other techniques may provide better results (Bodnar 1983).

Quantitative determination of fluid inclusion compositions by LA-ICP-MS in this way is entirely analogous to X-ray techniques (*e.g.* PIXE and SXRF) and so suffers from the same difficulties. As indicated by Mavrogenes *et al.* (1995), the principle

source of measurement error with this type of technique is in the inclusion volume determination. The procedure for LA-ICP-MS, however, is slightly simplified since the inclusion depth measurement, required for X-ray absorption calculations, is not required since the depth versus ablation yield and fractionation is automatically accounted for by proper use of the calibration standards (*e.g. PART 2, §3.2*).

It is important to realise that fluid inclusion signal quantification via this expression leads to absolute concentrations being expressed in mass by volume units, rather than the usual mass/mass units. Excluding instrument-related measurement errors, all uncertainty in such absolute concentrations originates in the accuracy of the inclusion volume measurement. To convert inclusion concentrations from mass/volume to mass/mass units requires knowledge of the bulk fluid inclusion density. Although such densities could be estimated from experimental measurements on appropriate simple model systems, bulk fluid densities are poorly understood as a function of composition, P and T, and any errors in the density approximation will be propagated.

PART 3

Copper(I) solubility and speciation in mineral-buffered supercritical fluids: A synthetic fluid inclusion study

Abstract

Mineral-buffered solubility and copper(I) speciation in the quartz-saturated part of the Cu–Cu_2O–MgO–SiO_2–HCl–H_2O system was determined using synthetic fluid inclusions. Fluid inclusions were synthesised in the piston-cylinder apparatus over a wide range of salinity (0.29–11.3 mol/kg Cl), T (525–850 °C) and P (0.3–1.7 GPa). Quench solution Mg compositions (unmodified by quenching), determined independently by SN-ICP-AES, were used to quantify the composition of individual fluid inclusions (representative high P–T fluid samples) measured by LA-ICP-MS. Fluid inclusions from numerous experiments were independently analysed by PIXE. X-ray absorption spectroscopy was undertaken to further characterise copper(I) speciation in the supercritical fluids. Solubility data was regressed independently to obtain speciation details and selected thermodynamic parameters.

The solubility of the assemblage native copper-cuprite-quartz-talc (Cu–Cpr–Tc–Qz) increases with salinity at constant T and P (in highest T experiments enstatite (Ens; instead of Tc) was the stable Mg-bearing mineral, so Cu–Cpr–Ens–Qz). Hydroxide copper(I) complexes and polynuclear species are negligible in these fluids and chlorocopper(I) complexes predominate over the entire range of Cl concentrations investigated. Similarly, chloromagnesium(II) complexes predominate over all experimental conditions investigated. Theoretical solubility calculations using data derived at much lower T and P are in variable agreement with the experimental data of this study. The total Cu/Cl concentration ratio of the buffered fluid decreases with increasing Cl and T at constant P. Low Cu:Cl (*e.g.* ~ 1:4) suggests chlorocopper(I) complexing is important but cannot be explained by models containing conventional $CuCl_n^{1-n}$ complexes. This is because positively ionised magnesium(II) species and H^+ are minor components in the fluid, whereas Cu and Cl dominate the solute mass and charge balance. Consequently, the formation of $CuCl_n^{1-n}$ complexes with $n > \sim 1$ results

in an apparent net charge imbalance, violating the neutrality constraint for these fluids. Two solutions to this problem were identified.

Cu solubilities are consistent with progressive formation of neutral higher-order chlorocopper(I) complexes ($CuCl(HCl)^0_{n-1\,(aq)}$) with increasing salinity and T at constant P. A least squares fit to both the Cl and T series solubility data is best satisfied by complexes with up to $n = 4$. Equilibrium constants for complex formation were determined. For $CuCl^0_{(aq)}$, the log K value differs up to approximately one log unit from estimates calculated from the low T-P literature; for higher-order complexes no comparisons may be made.

Alternatively, because activity-composition relations of even simple multi-component supercritical fluids are essentially unknown at high-P, it is equally plausible that $HCl^0_{(aq)}$ becomes disproportionately stable relative to $CuCl^0_{(aq)}$ at high salinities and with increasing T at fixed P. In this case, the experimental data could be fit using a conventional speciation model where activity coefficients (γ_i) for neutral species (i) vary independently, such that $\gamma_{HCl^0_{(aq)}} / \gamma_{CuCl^0_{(aq)}}$ becomes less than unity at high Cl concentrations and with increasing T at constant P.

At 710 °C Cu–Cpr–Tc–Qz solubility in aqueous fluid containing 1 mol/kg Cl increases with P to at least 1.7 GPa. Conspicuously, with increasing P (> ~ 0.5 GPa) Tc solubility increases and molal Cu concentrations exceed those of Cl. The isothermal Cu solubility isopleth parallels that of quartz solubility in the simple SiO_2–H_2O system. Solubilities increase with P and suggest that the stability of copper(I) hydroxide complexes (*e.g.* $CuOH^0_{(aq)}$) shifts to higher salinities such that H_2O may become an effective ligand at high-P.

High-T, in situ X-ray absorption near edge structure (XANES) spectroscopy experiments were undertaken on single homogenised synthetic fluid inclusions to further characterise chlorocopper(I) coordination environment in supercritical fluids as a function of salinity, T and mineral-buffer assemblage. Cu K-edge XANES spectra indicate that highly coordinated chlorocopper(I) complexes (*e.g.* Cu:Cl, 1:3–4) predominate at high salinity whereas lower order, linear Cu–Cl coordination predominates at lower salinities in fluids buffered by native copper-cuprite-talc-quartz. This is consistent with the interpretation of the solubility data. At equivalent salinity, T and P conditions fluids buffered by native copper-orthoclase-sillimanite-quartz-

magnetite-hematite show no evidence of higher-order chlorocopper(I) complexes. Preliminary extended X-ray absorption fine structure (EXAFS) data for these latter inclusions indicates that $CuCl_2^-$ predominates. The stability of higher-order complexes is strongly coupled to HCl concentrations, which at constant P and T is determined by both the specific mineral assemblage and total salinity.

This is the first spectroscopic evidence for highly coordinated chlorocopper(I) complexes in supercritical fluids. This is also the first in situ spectroscopic data to show the supercritical fluid speciation dependence on the coexisting mineral-buffer assemblage. Similarly, this is the first experimental confirmation that copper concentrations in mineral-buffered fluids can be extremely high, *e.g.* ~10 wt.%, something which until now was only speculated.

The results were applied to mineral transport and deposition in porphyry copper deposits. More generally the results provide insight into hydrous mineral solubilities at high-pressure and the potential bearing this has on the origin of the subduction zone geochemical signature observed in arc magmas.

1. Introduction

The vast majority of economic copper deposits are hydrothermal in origin and often display an intimate spatial and temporal association with shallow igneous rocks at the deposit- and regional-scales (*e.g.* Gustafson and Hunt 1975; Dilles 1987; Stoffregen 1987; Ulrich *et al.* 1999, 2001). These are commonly referred to as porphyry or epithermal deposits depending upon the depth of formation.

Numerous petrological, isotopic and geochemical studies have documented convincing evidence that suggests that the ore-bearing hydrothermal component in porphyry-epithermal systems is essentially magma-derived, being librated on volatile saturation of the silicate melt (*e.g.* Sheppard *et al.* 1969,1971; Holland 1972; Henley and McNabb 1978; Burnham 1979; Titley and Beane 1981; Hayba *et al.* 1985; Dilles *et al.* 1992; Giggenbach 1992a, b, 1997; Hedenquist and Lowenstern 1994). Such fossilised magmatic-hydrothermal ore-bearing (and barren) systems, and what appear to be their active analogues, are common to most subduction-related magmatic arc settings (Sawkins 1972, 1984; Henley and Ellis 1983; Sillitoe 1972, 1973, 1975, 1994).

Though field relations are well documented, the hydrothermal chemistry of ore elements in these environments is poorly constrained. This is simply because the thermodynamic properties of most aqueous complexes are inadequately known at near-magmatic hydrothermal conditions. It is the stability of metal-ligand complexes that determines the transport and deposition of hydrothermal ores. In nature, ore deposition is controlled by the interaction of a number of factors. These include T and P gradients, the permeability of the fracture network or inter-grain porosity, ligand availability, pH, redox, the reactivity of the fluid with the coexisting mineral phases and the occurrence of phenomena such as liquid-vapour phase separation and fluid mixing (*e.g.* Henley *et al.* 1984; Brimhall and Crerar 1987; Henley and Berger 2000; Hezarkhani *et al.* 1999). Hence, without a rigorous understanding of the properties of aqueous complexes, our ability to quantitatively explain and predict the geological processes responsible for the formation of intrusive porphyry-type and related hydrothermal ore systems at higher levels in the crust (*e.g.* epithermal) will remain rudimentary.

The general paucity of solubility and speciation data for minerals in high-T and P fluids is due in part to the limitations of traditional experimental techniques. For instance, in situ spectroscopic methods are usually restricted to subcritical, vapour-saturated conditions, while studies that rely on post-quench chemical analysis of high-T

solutions can suffer from the effects of solute precipitation on cooling and decompression to ambient conditions (quench modification). As already alluded to in *PARTS 1* and *2*, such experimental difficulties can be avoided if high *P–T* fluids are isolated as inclusions at the conditions of interest. Applying the experimental fluid inclusion approach, in conjunction with sensitive microanalysis techniques suitable for the study of individual inclusions, such as LA-ICP-MS, PIXE, Raman and synchrotron X-ray absorption spectroscopy, makes direct investigation of mineral solubilities, trace element behaviour and speciation in supercritical fluids at near-magmatic and high-grade metamorphic environments, all possible.

The oxidation potential of most geological fluids is sufficiently low that dissolved copper occurs predominantly in its univalent state, Cu^+. In magmatic hydrothermal fluids, chloride, along with bisulfide, constitute by far the most abundant potential ligand species for copper (*e.g.* Heinrich *et al.* 1992; Seward and Barnes 1997; Audétat *et al.* 1998; Ulrich *et al.* 1999). Bisulfide is known to form stable copper(I) complexes under reduced, near-neutral to alkaline conditions where total sulfur concentrations are high (*e.g.* Shea and Helz 1988, 1989; Helz *et al.* 1993; Thompson and Helz 1994; Mountain and Seward 1999). The importance of bisulfide complexes, however, is probably minor in high-*T* fluids that are acidic and in which sulfur occurs as both H_2S and SO_2, as is typical of fluids exsolved from volcanic arc magmas (*e.g.* Hedenquist *et al.* 1993, 1998; Giggenbach 1987, 1992a, b, 1997). Under such conditions copper(I)-chloride complexes may be more important. The purpose of this study was therefore to gain some insight into the nature of copper-chloride species and their solubilities in supercritical hydrothermal fluids.

1.2 Previous investigations of copper(I)-chloride speciation and solubility

1.2.1 Summary

Numerous studies of cuprous-chloride speciation have been made at low T using solubility, potentiometric and spectrophotometric measurement techniques (< 100 °C, *e.g.*, Noyes and Chow 1918; Glasner and Avinur 1961; Hurlen 1961; Sukhova *et al.* 1969; Ahrland and Rawsthorne 1970; Hikita *et al.* 1973; Sugasaka and Fujii 1976; Davis *et al.* 1978; Fritz 1980, 1981, 1982, 1984; Sharma and Millero 1990; Ciavatta and Iuliano 1998). These investigations, mainly undertaken at ambient conditions, generally agree. It appears that for aqueous solutions containing up to 1 mol/kg dissolved Cl, mononuclear copper(I)-chloride complexes, described by the general formula $CuCl_n^{1-n}$ predominate. With increasing chloride concentrations (*i.e.* [Cl] > ~ 1 mol/kg), however, polynuclear species of the general form $Cu_mCl_n^{m-n}$ may become important (Ahrland and Rawsthorne 1970).

Recent analytical advances allowed Mountain and Seward (1999) to determine the solubility of chalcocite (Cu_2S) at 22 °C and hence the low-T stability of cuprous-hydrosulfide/sulfide complexes. High-T data for sulfide complexes are scarce and uncertain (*e.g.* Romberger and Barnes 1970). Calculations by Mountain and Seward (1999) suggest that chlorocopper(I) complexes predominate over copper(I)-hydrosulfide species at high T (*e.g.* > 250 °C, P_{sat}, orthoclase-muscovite-quartz, 1 mol/kg Cl).

Although a number of experimental studies on copper(I)-chloride solubility and speciation have been undertaken up to 350 °C, most are restricted to vapour-saturated P (*e.g.* Romberger and Barnes 1970; Crerar and Barnes 1976; Var'yash and Rekharskiy 1982; Hemley *et al.* 1992; Var'yash 1992; Seyfried and Ding 1993; Xiao *et al.* 1998; Fulton *et al.* 2000a, b; Liu *et al.* 2001, 2002; Archibald *et al.* 2002).

Perusal of this literature reveals a number of inconsistencies in the early data particularly with regards to the pioneering studies of Romberger and Barnes (1970), and Crerar and Barnes (1976). The deficiencies of these studies are related primarily to poor redox control, which has been noted by the authors themselves and discussed in subsequent investigations (*e.g.* Crerar *et al.* 1978; Xiao *et al* 1998; Mountain and Seward 1999).

More recent determinations of copper(I)-chloride complex stability obtained using solubility and spectroscopic measurement techniques are in relative agreement and indicate that mononuclear $CuCl_n^{1-n}$ species dominate under all chloride concentrations investigated.

1.2.2 Notes on high-temperature studies

Romberger and Barnes (1970)

Romberger and Barnes (1970) measured covellite solubility in hydrosulfide solutions from 20 to 200 °C. Their data indicate both a positive correlation between Cu concentration and T as well as sulfide concentration. Unfortunately, the usefulness of their experiments is limited because they assumed Cu was in the 2+ valence state in both covellite and the hydrothermal solution. It is now known from X-ray photoelectron and EXAFS studies of sulfides that copper is univalent in covellite (CuS), anilite (Cu_7S_4), digenite (Cu_9S_5), chalcocite (Cu_2S), chalcopyrite ($CuFeS_2$) and bornite (Cu_5FeS_4), (Nakai *et al.* 1978; Folmer and Jellinek 1980; van der Laan *et al.* 1992). Consequently, because the redox state in the experiments of Romberger and Barnes (1970) was not controlled their data cannot be properly interpreted.

Crerar and Barnes (1976)

The study of Crerar and Barnes (1976) was the first attempt at measuring Cu solubility in complex NaCl-bearing aqueous solutions buffered by chalcopyrite-pyrite-bornite and native copper-chalcocite assemblages at 200 to 350 °C. From regression of their solubility data they concluded that $CuCl^0_{(aq)}$ was the dominant copper(I)-chloride species in all of their experiments. Unfortunately, their results may be in error, as it is unlikely that the hydrogen/oxygen fugacity was effectively controlled by the buffer employed (graphite-CO_2), because the redox buffer probably did not fully equilibrate at such low T. This is suggested by mineral solubilities that are approximately one order of magnitude lower than the experiments of Var'yash and Rekharskiy (1982), Var'yash (1992), Xiao *et al.* (1998) and Liu *et al.* (2001a).

Var'yash (1990)

Var'yash (1990) investigated the solubility of cuprite (Cu_2O) from 150 to 450 °C at vapour-saturated *P* in neutral to alkaline conditions in the system Cu_2O–HCl–NaOH–H_2O in which the redox potential of the fluids was buffered by the coexistence of Cu_2O–Cu. Hydrolysis of cuprite at low *p*H conditions was also investigated in the system Cu–HCl–H_2O at 300 to 450 °C at 0.5 and 100 MPa. Redox conditions in these experiments were controlled using aluminium metal, which reacted with the H_2O to produce hydrogen during the experiment. Thermodynamic data were derived for the species Cu^+, $Cu(OH)^0$ and $Cu(OH)_2^-$. The experiments indicate that for the *T* range investigated only the ion, Cu^+, is important under acidic conditions. Cuprous-hydroxy complexes become more dominant with increasing *p*H to neutral and alkaline conditions, at least in the absence of other ligands.

Xiao *et al.* (1998)

Xiao *et al.* (1998), experimentally investigated copper(I)-chloride complexing between 40 and 300 °C at water-saturated vapour pressure. They interpreted their data in terms of Cu dissolving as four aqueous species, Cu^+, $CuCl^0_{(aq)}$, $CuCl_2^-$ and $CuCl_3^{2-}$ and calculated stepwise formation constants for these species. From this Xiao *et al.* (1998) concluded that $CuCl_2^-$ was the dominant species over a wide range of conditions. Var'yash (1992) suggested that $CuCl_2^-$ was the only important species between 300 and 500 °C at 50 MPa (500 bar). Above 150 °C, the data of Xiao *et al.* (1998) show variable agreement with other researchers (*e.g.* Var'yash 1992). Their lower *T* data, however, is consistent with previous work (*e.g.* Fritz 1980, 1981, 1982; Sharma and Millero 1990; Var'yash and Rekharskiy 1981). Xiao *et al.* (1998) also found that below 250 °C copper(I)-chloride complexes are not capable of transporting significant Cu in reduced solutions.

Mountain and Seward (1999)

Although no high-*T* experiments were undertaken by Mountain and Seward (1999), they reassessed the data of Crerar and Barnes (1976) in the light of their own $CuHS^0$ + $Cu(HS)_2^-$ + $Cu_2S(HS)_2^{2-}$ speciation model, developed from room *T* solubility experiments. They argued that hydrogen fugacity in Crerar and Barnes (1976) could be interpreted, if the activity of H_2S was known, as it may have been fixed by the sulfide

buffers employed and not by graphite-CO_2 equilibria as thought in the original study. Thus, Mountain and Seward (1999) refit the Crerar and Barnes (1976) data and calculated the relative stabilities of copper(I) hydrosulfide and chloride species for a "typical" hydrothermal fluid at 300 °C. The predicted relations are consistent with observed low-sulfidation geothermal systems such as Ohaaki-Broadlands where negligible Cu, but substantial Au is measured. Only at high-sulfur concentrations and alkaline *p*H conditions do reduced-sulfur complexes make a significant contribution to total copper(I) solubility. Chlorocopper complexes were expected to predominate under acidic, relatively oxidised conditions and with increasing *T* and Cl concentrations.

Fulton *et al.* (2000a, b)

Fulton *et al.* (2000a, b) used in situ extended X-ray absorption fine structure (EXAFS) spectroscopy to determine the detailed Cl^- and H_2O coordination structure around Cu^+ in H_2O–HCl solutions up to 325 °C. The effect of adding NaCl to the solutions, up to 2.0 mol/kg, on cuprous-chloride speciation was also investigated. These experiments indicate that even in 2.0 mol/kg NaCl solutions, the linearly coordinated dichlorocopper(I) species, $CuCl_2^-$, is especially stable from 100 to 325 °C. The analysis found that there are no tightly bound H_2O molecules in the first solvation shell of $CuCl_2^-$, which also excludes the possibility of hydrolysis species (OH^-) in these experiments. In the NaCl-free solutions, where Cu≈Cl, another linear complex, H_2O–CuCl, dominates the Cu^+ speciation. Despite consideration of higher-order Cl^-complexing or polynuclear speciation, no evidence for such behaviour was observed in any of the experiments.

Liu *et al.* (2001a, 2002)

Liu *et al.* (2001a) conducted cuprite (Cu_2O) solubility experiments up to 250 °C along the vapour-saturation curve, where *p*H was buffered by acetate solution equilibria and derived stepwise formation constants for the species, $CuCl^0_{(aq)}$, $CuCl_2^-$ and $CuCl_3^{2-}$. Copper(II) concentrations were negligible in all experiments considered successful. This argument was based on the lack of colour and spectroscopy in the UV–visible range (sensitive to Cu^{2+}) of the quench solutions (*e.g.* Brugger *et al.* 2001). Copper(I)-chloride speciation was investigated by varying sodium chloride and sodium acetate concentrations up to 2.0 mol/kg. Stepwise formation constants for cuprous-

acetate species were also derived from a series of chloride-free experiments. They concluded that copper(I) acetate complexes are unimportant in chloride-dominated fluids. The stability of the species $CuCl_2^-$ increases at higher T, at the expense of others such as $CuCl^0_{(aq)}$ and $CuCl_3^{2-}$, even at the highest chloride concentrations of their experiments. The experimental results are essentially in agreement with those of Var'yash (1992), Xiao *et al.* (1998) and Fulton (2000a,b). No evidence indicating the presence of polynuclear species was observed.

Liu *et al.* (2002) undertook in situ, ultraviolet (UV) spectroscopy of copper-bearing LiCl solutions (up to 9.1 mol/kg LiCl) to 250 °C. These solutions contained 11 to 25 ppm copper. This study reported, for the first time, an equilibrium formation constant for $CuCl_4^{3-}$ at T above ambient. Moreover, their interpretation of the spectra indicates that $CuCl_4^{3-}$ becomes the predominant copper species at lithium chloride concentrations above 5 mol/kg. The equilibrium formation constants for species with lower Cl^- coordination, namely $CuCl_2^-$ and $CuCl_3^{2-}$, which were also obtained, agree well with other experimental studies (Xiao *et al.* 1998; Liu *et al.* 2001a) and, in the case of $CuCl_3^{2-}$, also with theoretical estimates (Sverjensky *et al.* 1997).

Hemley *et al.* (1992) and Seyfried and Ding (1993)

Only two experimental solubility studies are available for Cu above 350 °C (Hemley *et al.* 1992; Seyfried and Ding 1993). Unfortunately, however, these studies are difficult to interpret, as the data is not sufficiently extensive (total Cl was not varied) to extract reliable thermodynamic information. Nonetheless, because these are the only available published data for Cu solubility in supercritical sulfide- and chloride-bearing fluids they deserve a short discussion as they provide points against which to assess relevant thermodynamic data.

Hemley *et al.* (1992) measured Cu solubility in sulfide-bearing systems from 300 to 500 °C and 50 to 200 MPa and total chloride up to 1 mol/kg; *p*H was constrained by the potassium feldspar-quartz-muscovite assemblage. Digenite (Cu_2S) solubility in an Fe-free system, where sulfur fugacity was unbuffered, and Cu solubility in the assemblage chalcopyrite-magnetite-pyrite-pyrrhotite were investigated. From their results, Hemley *et al.* (1992), concluded: 1) increasing Cl is likely to result in an increase in Cu solubility due to a shift to lower *p*H conditions via silicate buffer reactions; 2) metal solubility is primarily a reflection of the relative stability of the

individual metal-chloride complexes, that must compete with hydrogen and the alkali ions for Cl; 3) sulfide mineral solubilities increase with decreasing *P*; and, 4) increasing sulfur fugacity (*i.e.* bisulfide concentrations) decreases Cu solubility. Because few reliable experimental data existed, $CuCl^0$ was the only Cu-species considered in the interpretation of their data and those of Seyfried and Ding (1993). The results of Hemley *et al.* (1992) suggest Cu solubility at 650 to 700 °C could reach several weight percent in mineral-buffered supercritical fluids.

Helgeson (1969), Ruaya (1988) and Sverjensky *et al.* (1997)

Published theoretical estimates of the formation constants for copper(I) chloride complexes (Helgeson 1969; Ruaya 1988; Sverjensky *et al.* 1997) deviate significantly from the experimental results of Var'yash (1992), Xiao *et al.* (1998) and Liu *et al.* (2001a, 2002), especially approaching 350 °C. At higher *P* and *T*, theoretical estimates are essentially unconstrained due to an absence of experimental data. Thermodynamic properties derived in more recent studies that include high-*T* experimental data are considered more reliable (*e.g.* Liu 2001a, 2002).

Archibald *et al.* (2002)

In a novel experimental study by Archibald *et al.* (2002), nantokite (CuCl) solubility was investigated in *liquid-undersaturated* $HCl–H_2O$ vapour from 280 to 320 °C and up to 10.3 MPa. From their data they concluded a single hydrated cuprous-chloride gaseous species, $Cu_3Cl_3^0 \cdot (H_2O)_n$ where $n = 6\pm1$, was responsible for the observed solubility. This is the only high-*T* study in which polynuclear species have been postulated as important. The argument forwarded for the prevalence of polynuclear species in their experiments was based on some transpiration mass spectrometry experiments, found in the literature, suggesting that polynuclear complexes were stable in very low-*P* environments. However, they acknowledge also, because only the Cu:Cl ratio of the complex is determinable from solubility measurements, a simpler and more conventional mononuclear species, $CuCl^0 \cdot (H_2O)_{6(\pm1)}$ would fit the data equally well. Such a species would potentially also be more in accord with the recent in situ, high-*T*, X-ray absorption spectroscopy study of quartz-hosted, natural vapour phase fluid inclusions by Mavrogenes *et al.* (2002). This study indicated that the copper was predominantly dissolved as a simple linear species, $CuCl_2^-$ in the vapour phase, although it should be noted that vapours

studied by Archibald *et al.* (2002) contained ~200 ppm Cu, whereas Mavrogenes *et al.* (2002) do not report the Cu concentration in the studied fluid inclusions. This is important because the extent of polynuclear complexes, if it occurs, should depend on composition. Interestingly this same species, $CuCl_2^-$, was identified by Fulton *et al.* (2000a, b) as important in the liquid phase, and using his spectroscopic data was able to exclude the possibility of polynuclear species being significant in those experiments. Although the direct relevance of these latter two studies to the interpretation of Archibald *et al.* (2002) data may be questionable, the point being made is the balance of available observations, do not yet provide a compelling case for (or against) multinuclear species predominating in high-T fluids.

The need to acquire mineral solubility data at higher T and P is exemplified, by no means exclusively, by porphyry-type hydrothermal systems in which fluid-mineral interactions up to magmatic T are diagnostic. Specifically, the primary copper ore minerals in these systems are commonly deposited in the interval 500–250 °C from vapour-saturated and supercritical fluids and, as evident from the preceding discussion, almost no experimental data for the stability of cuprous-chloride complexes above 350 °C and none above 500 °C or higher than 150 MPa exist.

2. Background theory: Solubility, speciation and multi-component solution equilibria

For solubility experiments to be of general utility, the chemical system in which they are conducted must be completely defined thermodynamically (Crerar *et al.* 1978; Barnes 1981). In doing so, the solubility measurements may be interpreted in terms of the aqueous speciation and the thermodynamic properties of the solutes may also be derived. Such information can then be used to assess mineral solubility relations quantitatively outside of the simple system in which the measurements were originally made.

Any number of arbitrary independent constraints can be used to describe the chemical system, the minimum number for a complete definition, however, depends on the number of unknowns, which in most cases means the number of aqueous species in the solution that are to be considered.

Independent constraints for calculating the equilibrium concentrations or activities of species may take the form of simple mass balance equations, though any extensive or conservative property (*e.g.* energy) of a closed system can be used, as well as known equilibrium constants. A charge balance equation may also be specified, given that solutions are electrically neutral and it is reasonable to assume that this remains true at high P–T. These equations may be combined with another expression specifying the activity-composition relations in the solution. This complete set of non-linear equations may then be simultaneously solved for the concentration and the activity of each aqueous species using simple numerical techniques (*e.g.* Crerar 1975, Wood and Crerar 1985; Ziegler *et al.* 1999). In detail, this usually means making an initial guess of the ionic strength or of the concentrations of all the species in the fluid and then iteratively solving the equation matrix. A solution is reached when successively calculated concentrations have converged to a constant value at the required precision.

This general approach is applied in most experimental solubility and spectroscopic studies where extraction of quantitative aqueous species data is the primary aim (*e.g.* Helgeson 1964; Garrels and Christ 1965; Crerar and Anderson 1971; Seward 1976; Crerar and Barnes 1976; Crerar *et al.* 1978; Wood *et al.* 1987; Fein *et al.* 1992; Xiao *et al.* 1998; Loucks and Mavrogenes 1999; Ziegler *et al.* 1999; Walther

1997a, b, 2001; Liu *et al.* 2001a; Müller and Seward 2001). It is the method by which solubility data of this study are interpreted.

3. Experimental

3.1 Mineral-buffered fluid inclusion synthesis and analysis

The mineral solubility method was combined with the synthetic fluid inclusion technique to investigate copper(I) complexing in supercritical fluids as a function of Cl concentration, *P* and *T*. Experiments were conducted in pure copper metal capsules using the piston-cylinder technique[12]. Mineral-assemblages were employed to control the redox potential and *p*H conditions of the fluid. Details of the specific assemblages are discussed as appropriate.

The chemical composition of individual fluid inclusions was measured using excimer ArF (193 nm) laser ablation-inductively coupled plasma-mass spectrometry (LA-ICP-MS) in conjunction with solution nebulization-inductively coupled plasma-atomic emission spectrometric (SN-ICP-AES) analysis of the quench solution from the capsule. The concentration of soluble, non-quench modified components in the solutions extracted from the capsule after the run were used as an internal standard for quantification of absolute concentrations from the LA-ICP-MS data.

Capsule materials were loaded gravimetrically. Crystalline buffering materials were ground relatively fine prior to loading. The ratio of the buffering mineral-assemblage to fluid (excluding the copper capsule) in these experiments was about 5 ± 2 (mineral/fluid by mass). The relatively high mineral/fluid ratio reduced the likelihood of any buffering phase completely dissolving, which would result in an

---

[12] Although, conventional experiments using pure copper metal capsules in cold-seal hydrothermal apparatus were attempted, a number of experimental difficulties were encountered. For example, because water was employed as the *P* medium in the apparatus used (Department of Geology, ANU) copper capsules would become heavily corroded externally. At high *T* this was a major problem as it leads to rapid failure of capsules. Use of other metals, like platinum and gold, for containing experiments suffered from alloying with Cu, frustrating attempts to control the activity of copper in the system - a requirement of these experiments. Although, the *a*–*X* relations for a number of binary Cu alloys are well known (*e.g.* Cu–Au) and could be used to serve the dual purposes of capsule material and controlling metal activities, this topic was not pursued. Electrolytically plating Cu capsules with Ni prior to running and increasing the capsule wall thickness to ≥ 1 mm was found to provide substantial resistance to external corrosion. This experimental approach to fluid inclusion synthesis in cold-seal hydrothermal apparatus, however, was abandoned in favour of the piston-cylinder apparatus technique that was being developed simultaneously.

indeterminate experimental condition. Additionally it produces a large surface area for fluid-mineral interactions ensuring efficient buffering and rapid equilibration. This is supported by the systematic behaviour of the solubility data and replicate analysis of individual inclusions (*PART 1, §3*).

The principal mineral assemblages employed to buffer the fluid composition were talc-quartz-cuprite-native copper and enstatite-quartz-cuprite-native copper.

Pure laboratory reagents as well as synthesised and natural minerals, confirmed by XRD, were used to buffer the experimental conditions. Chlorine was added to the experiments in the form of dried analytical-grade $CuCl_2$, the amount added determined the total Cl concentration in the experimental fluid. After all solid phases and salts were weighed into the capsule deionised water was added to give the desired total chloride concentration in the fluid and approximate bulk charge density appropriate to the conditions of the experiment. The amount of H_2O added was pre-calculated from the known internal volume of the undeformed capsule, an EOS (or steam tables) for pure water, and the masses and densities of the solid phases added. It was assumed that the initial total Cl concentration remained constant from start to end of experiment.

After the run, capsules were cleaned, pierced and the remaining free fluid sampled using a syringe, weighed and diluted with a solution of high-purity 2% distilled HNO_3 to provide a useful analytical volume and stabilise the dissolved components until analysis. Some capsule solutions were lost on piercing, as the significant strength of the capsules allows internal over-pressure at ambient conditions, so that on opening they rapidly expelled the quench fluid. After sampling the quench solution, indium was added as an internal standard for analytical purposes. This diluted quench solution was subsequently analysed by SN-ICP-AES using a Varian instrument operating at the Department of Geology, ANU. Quench solution analyses were calibrated against known, matrix-matched standard solutions.

Fresh quench solutions were always colourless, though often cloudy. This was taken as evidence that Cu^{2+} concentrations were negligible and was subsequently confirmed by X-ray absorption spectroscopy of the synthesised fluid inclusions. The small amounts of capsule solution that could not be extracted invariably turned greenish-blue after exposure to air. This is interpreted as oxidation of the dissolved copper.

Following extraction of the quench solution, capsules were opened fully and solid phases carefully removed for examination. If the complete mineral buffer assemblage was identified by optical microscopy, and in some cases by powder X-ray diffraction, in the run products, then the experiment was considered successful. Only results from successful experiments are presented. Although re-crystallisation and grain size coarsening of the initial buffering phases was common during the experiments, especially for cuprite (Cu_2O), no new phases were identified in the post run products. It was not unusual to find large (up to millimetre scale) deep red crystals of cuprite inter-grown with native copper.

Invariably, experimental solution compositions were modified on quenching. This could be confirmed on petrographic examination of the synthetic fluid inclusions, as quench modified components (*e.g.* Cu) are identifiable as daughter phases at room *T*.

Fluid inclusion samples were analysed by LA-ICP-MS to determine the fluid composition. Precipitated phases within the inclusions were included in the analysis, ensuring that compositions are representative of the experimental conditions. Precipitated phases in inclusions are readily identified by their ability to completely dissolve on heating the sample, this same behaviour is not observed for mineral grains accidentally trapped in inclusion at the run *PT*. Absolute concentrations were obtained using quenched solution SN-ICP-AES data to internally standardise fluid inclusion analyses. LA-ICP-MS conditions were optimised for each analytical session.

Fluid inclusions from numerous experiments were also independently analysed for Cu concentration by PIXE using the methods described by Heinrich *et al.* (1992) and Ryan *et al.* (1995). These data are in good agreement with LA-ICP-MS results (see *PART 2, §5.11*). Although the Mg γ-ray emission produced from nuclear interactions with the proton beam (also known as proton induced gamma-ray emission; PIGE) was recorded and, in principle, could be used to calculate the Mg concentrations in fluid inclusions, the necessary γ-ray attenuation and data reduction procedures are not currently available.

Further details regarding experimental, sample preparation, analytical and data reduction procedures are described elsewhere in *PARTS 1* and *2*.

3.2 Fluid inclusion petrography

At ambient T (~ 20 °C), fluid inclusions from individual experiments are characterised by a vapour bubble, condensed liquid and a distinctive colourless to brown, tetrahedral daughter crystal (Figure 3.1). Phase proportions are uniform for individual experiments and vary systematically with P–T–X conditions. Systematic variation in phase proportions at room T include, the relative volume of vapour bubbles in inclusions increasing systematically with increasing T (at constant P and constant salinity) consistent with the expected decrease in the fluid density, similarly the relative volume of the precipitated Cu daughter phase increases systematically with Cl concentration (at constant T and P), consistent with a salinity dependence for Cu solubility. Inclusions completely homogenise on heating. Such characteristics are indicative of fluid-mineral equilibrium.

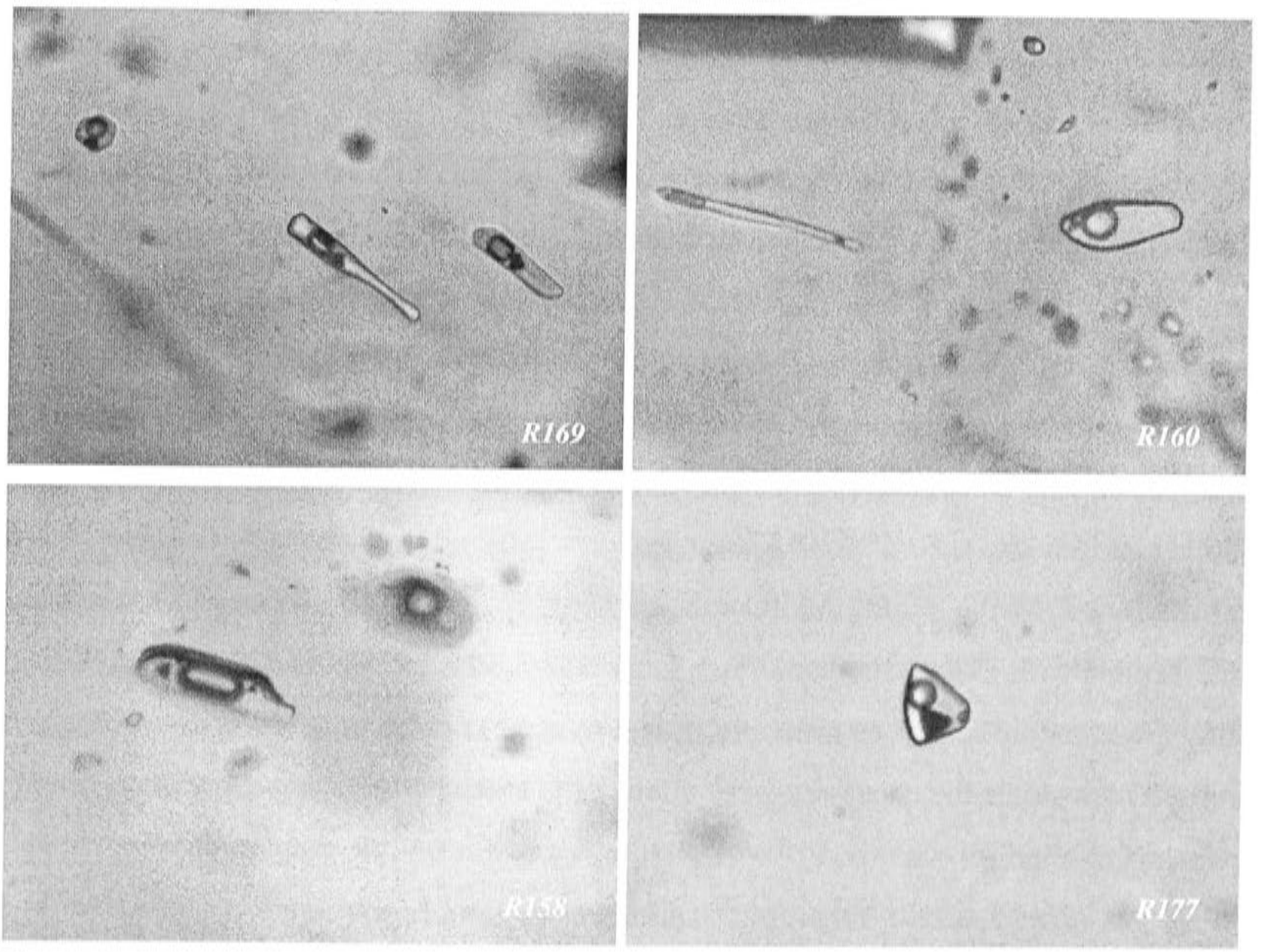

Figure 3.1 Photomicrographs taken at 25 °C of typical quartz-hosted aqueous fluid inclusions synthesised at various P–T–X conditions and buffered by the mineral assemblage Cu–Cpr–Tc–Qz. Experimental runs referenced. Inclusions in these images are approximately 20-50 μm in size.

The fluid density of inclusions formed above ~ 1.5 GPa at 710 °C is sufficiently high that no bubble nucleates on cooling (Figure 3.2). Such high-density fluid inclusions are internally over-pressured at room conditions. Accordingly, intact natural inclusions from similar *P–T* regimes are rare as they usually decrepitate during decompression. The distinctive tetrahedral daughter crystal appears to be the same mineral phase observed in all of the Cl-bearing experiments (Figure 3.1). Various attempts to identify the precipitated mineral phase using PIXE and laser Raman spectroscopy were unsuccessful because it invariably decomposed under the incident beam. However, the general appearance, morphology, and the conspicuous absence of this daughter mineral from Cl-free fluid inclusions formed under similar buffering and *P–T* conditions, are consistent with it being the cubic cuprous halide mineral, nantokite (CuCl; Figure 3.2).

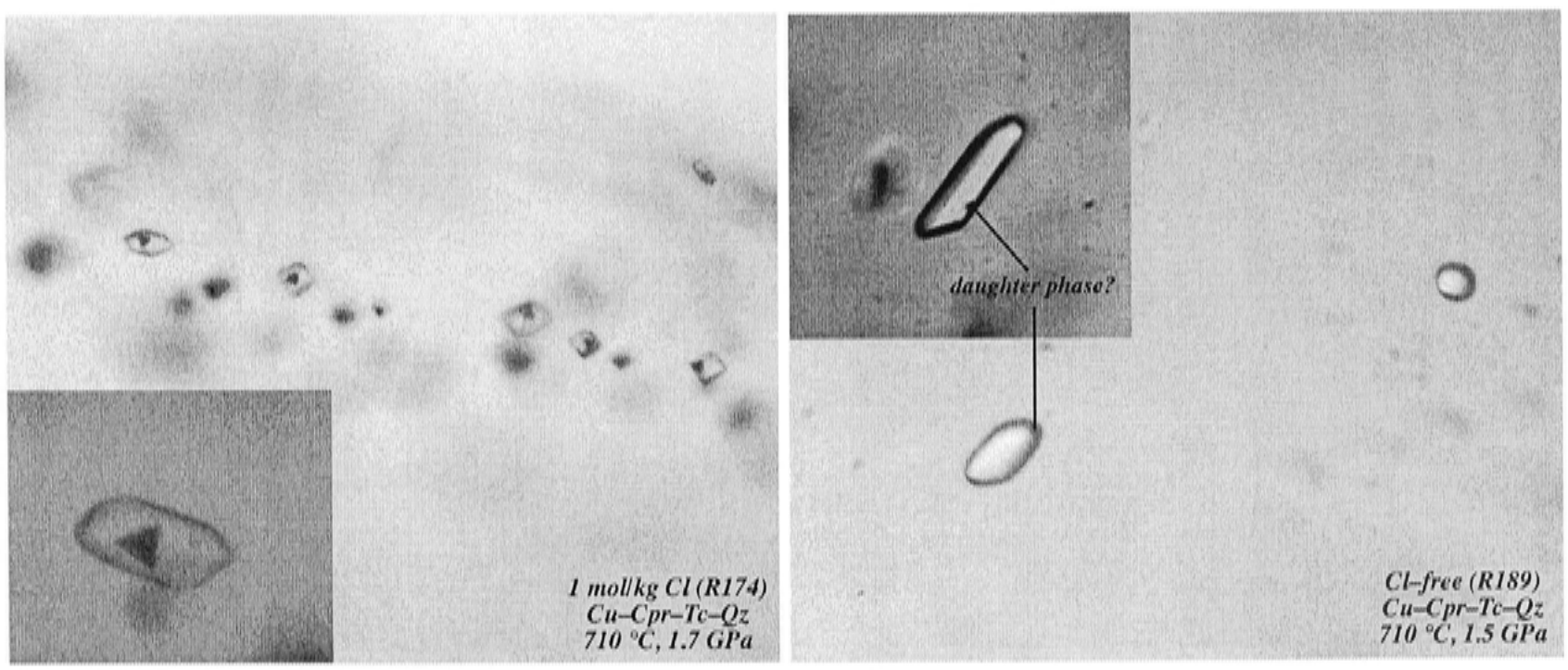

Figure 3.2 Photomicrographs taken at 25 °C of high-density quartz-hosted fluid inclusions synthesised at 710 °C and 1.7 GPa (R174) and 1.5 GPa (R189) in 1 mol/kg Cl and Cl-free aqueous fluid respectively. Both experimental fluids were buffered by the mineral assemblage native copper-cuprite-talc-quartz (Cu–Cpr–Tc–Qz). Inclusions in these images are 10 to 35 μm. Inset: enlarged view of a typical fluid inclusion. Note daughter phase petrography differs significantly between Cl-bearing (nantokite, CuCl) and Cl-free fluid inclusions. The quench precipitated phase in Cl-free inclusions is too small to positively identify optically (perhaps cuprite, Cu_2O).

3.3 Precision and accuracy of the solubility data

The intrinsic accuracy and precision of quartz-hosted fluid inclusion analysis by LA-ICP-MS was extensively investigated (details given in *PART 2*). These studies revealed that the inherent precision, under the optimum analytical conditions, is at best ± 50% at one standard deviation (σ). Nonetheless, the technique is accurate, that is the mean composition ($\bar{x}$) obtained from multiple analyses of a homogeneous fluid population is reliable. Consequently, it is the uncertainty of the mean that is important and this is related to the number of individual measurements (n), not just the analytical precision. The uncertainty of the mean can be assessed using confidence interval statistics (Devore and Peck 1995). The confidence interval represents the range of plausible values for the mean at a given probability, based on the sample statistics,

$$\bar{x} \pm (z \text{ critical value}) \frac{\sigma}{\sqrt{n}}$$

For a 95% confidence interval, which is generally considered to represent a reasonable compromise between reliability and precision (*e.g.* Loucks and Mavrogenes 1999), the z critical value is 1.96 (this gives a central area of 0.95 under the standard normal probability curve).

4. Mineral solubility: Effect of chloride and speciation

4.1 Experimental data

A series of isothermal-isobaric solubility experiments were undertaken to examine the effect of varying chloride concentration and hence the stability of copper(I)-chloride species. These experiments were buffered using a single mineral assemblage, native copper-cuprite-talc-quartz (Cu–Cpr–Tc–Qz), at 629 °C and ~340 MPa. Under these conditions, solubility may be interpreted in terms of cuprite dissolution,

$$1/2\,Cu_2O_{(Cuprite)} + H^+_{(aq)} + nCl^-_{(aq)} = CuCl^{1-n}_{n\,(aq)} + 1/2\,H_2O_{(liq)} \qquad [3.1]$$

Ascertaining the stoichiometry of this reaction, n, as a function of chloride activity is the first step towards a quantitative understanding of the stability of the aqueous chlorocopper(I) complexes. Equilibrium [3.1] is sensitive to changes in acidity (pH), although not redox sensitive, the oxidation potential must still be controlled such that Cu^{2+} concentrations are negligible under the experimental conditions. Thus, these parameters, redox potential and pH, were fixed experimentally. The redox potential of the system is controlled via the coexistence of native copper and cuprite,

$$2Cu^0_{(Native)} + H_2O_{(liq)} = Cu_2O_{(Cuprite)} + H_{2\,(g)} \qquad [3.2]$$

Acidity is controlled (through the $Mg^{2+}_{(aq)}/H^{+2}_{(aq)}$ ratio) by the equilibria describing the coexistence of talc and quartz, which can be given as,

$$1/3Mg_3Si_4O_{10}(OH)_{2\,(Talc)} + 2H^+_{(aq)} = 4/3SiO_{2\,(Quartz)} + Mg^{+2}_{(aq)} + 4/3H_2O_{(liq)} \qquad [3.3]$$

Experimental details and measured solubilities are reported in Table 3.1. Figure 3.3 shows the relation between total Cl and the solubility of Cu and Mg in supercritical aqueous fluid in equilibrium with Cu–Cpr–Tc–Qz at constant P and T.

Table 3.1 Experimental details and dissolved element concentrations for the Cu–Cpr–Tc–Qz assemblage as a function of chloride concentration at 629 °C and ~334 MPa

Run	R159	R160	R161	R162	R163	R164	R169	R173	R178	R176	R177
Temperature/ °C	629	629	629	629	629	629	629	629	629	629	629
Pressure/ MPa	330 (6)	330 (3)	334 (3)	370 (6)	334 (3)	331 (6)	341 (1)	334 (3)	334 (3)	364 (5)	338 (6)
Duration (hours)	289	265	355	353	380	307	264	141	162	137	171
Mineral/Fluid	2.5	2.9	2.8	3.5	4.7	4.5	3.1	2.6	3.4	3.2	4.4
$m_{Cl}^{total(1)}$	**0.285**	**0.576**	**0.876**	**1.175**	**1.485**	**2.132**	**2.705**	**3.826**	**5.666**	**7.323**	**11.283**
$m_{Cu}^{total(2)}$	0.21	0.58	0.72	0.89	1.01	–	0.76	2.81	1.12	1.85	2.82
$\pm 95\%\ C.L._{Cu,mol/kg}^{LA-ICP-MS}$	0.05	0.14	0.13	0.18	0.34	–	0.36	0.54	0.17	0.45	0.47
$n_{Cu}^{LA-ICP-MS}$	22	12	12	36	16	–	10	15	13	44	48
$m_{Cu}^{total(3)}$	–	–	–	–	–	2.45	1.46	–	–	–	–
$\pm 95\%\ C.L._{Cu,mol/kg}^{PIXE}$	–	–	–	–	–	0.49	0.47	–	–	–	–
n_{Cu}^{PIXE}	–	–	–	–	–	4	4	–	–	–	–
$m_{Mg}^{total(4)}$	0.005	0.008	0.008269	0.017	0.0212	0.02963	0.02172	0.03525	0.02358	0.028	0.0457
$\pm 95\%\ C.L._{Mg,mol/kg}^{SN-ICP-AES}$	0.0001	0.0057	0.000078	0.01	0.0013	0.00082	0.00092	0.00083	0.00039	0.018	0.0098

Notes: Concentrations in molality (moles per kilogram of solvent). P variation during the experiment given in parentheses. Confidence limits (C.L) about the mean determined from n replicate measurements were calculated as $\pm 1.96/\sqrt{n}$. Sub- and superscripts on n indicate element and analytical method. Mineral/Fluid is the mass ratio of the buffer minerals to fluid weighed into the capsule initially, excluding the Cu capsule and initial salt. The parameter varied is indicated in bold.

1) Total Cl concentration added to the capsule.
2) Total Cu concentration determined from individual fluid inclusions by LA-ICP-MS analysis.
3) Total Cu concentration determined from individual fluid inclusions by PIXE analysis.
4) Total Mg concentration obtained by SN-ICP-AES analysis of the quench solution, which was also used for quantification of LA-ICP-MS data (see text).

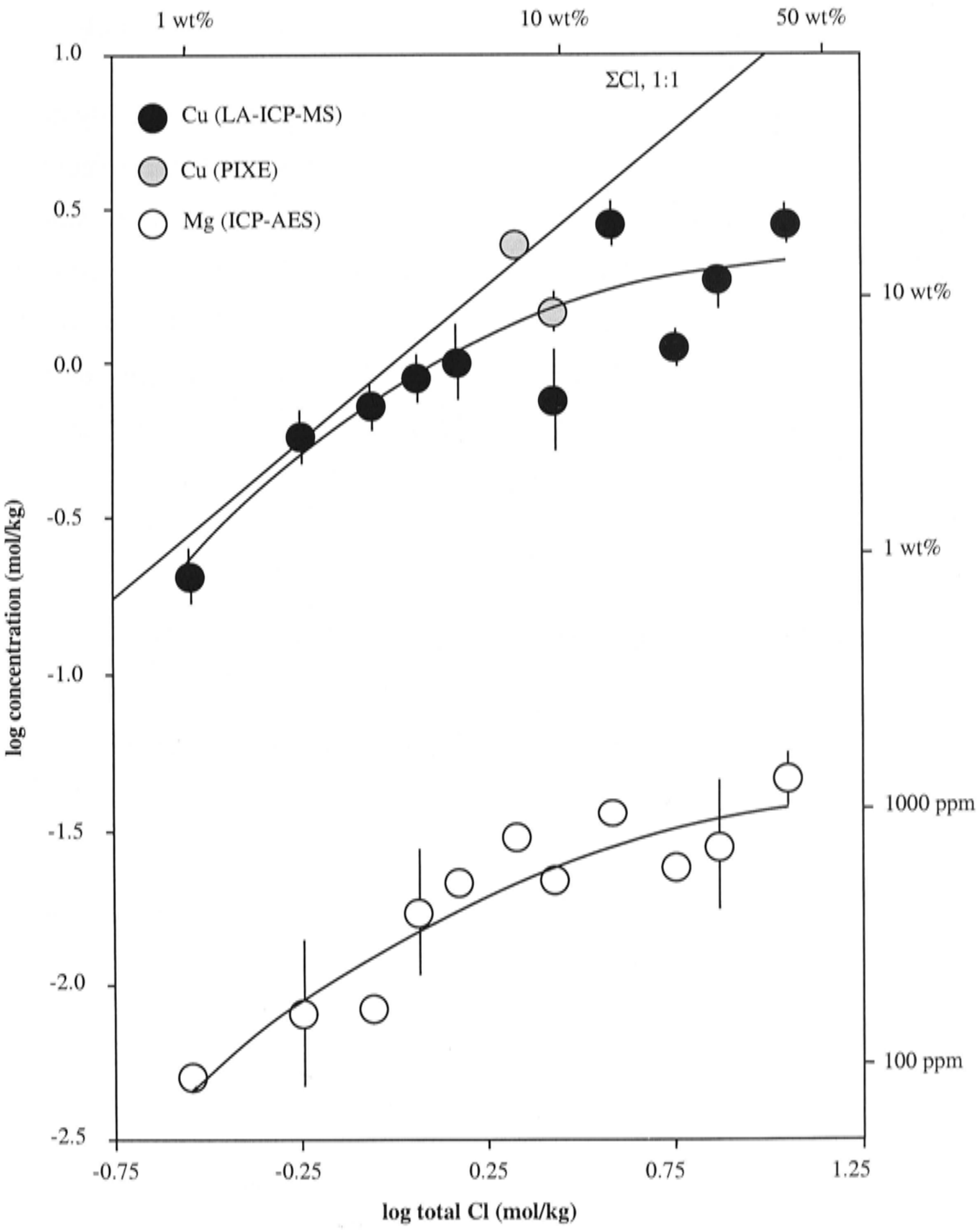

Figure 3.3 Solubility of Cu and Mg in aqueous fluid as a function of total Cl concentration buffered by the mineral assemblage Cu–Cpr–Tc–Qz at 629 °C and ~ 334 MPa. Concentration in log molality (log moles/kg), measurement uncertainty (± 95% *C.L.*) indicated where larger than the symbol, 1 to 1 total Cl, also shown for reference; Concentration by mass (ppm, wt.%) shown on alternate axes. Analytical technique used to measure each element is indicated. Solid lines are second order polynomial least square fits to the data.

4.2 Data Interpretation

This section describes the procedure used to interpret the solubility data and the results. Initially, a solubility model was defined, containing what were considered to be the most likely species. Extrapolated thermodynamic data from the literature were then used to calculate the theoretical mineral solubility. These predicted solubilities were compared directly with the experimental measurements. Finally, the solubility data were used to identify the chlorocopper(I) species and obtain their equilibrium formation constants using a non-linear optimisation routine to eliminate the residual difference between model and experimental data.

4.2.1 Calculation of mineral solubility and Cu–Mg–H–Cl speciation

Mineral solubility in the experiments can be described by the following equilibria,

$$1/3Mg_3Si_4O_{10}(OH)_{2\,(Talc)} + 2H^+_{(aq)} = 4/3SiO_{2\,(Quartz)} + Mg^{2+}_{(aq)} + 4/3H_2O_{(liq)}$$

$$H^+_{(aq)} + OH^-_{(aq)} = H_2O_{(liq)}$$

$$H^+_{(aq)} + Cl^-_{(aq)} = HCl^0_{(aq)}$$

$$Mg^{2+}_{(aq)} + Cl^-_{(aq)} = MgCl^+_{(aq)}$$

$$MgCl^+_{(aq)} + Cl^-_{(aq)} = MgCl^0_{2\,(aq)}$$

$$Mg^{2+}_{(aq)} + OH^-_{(aq)} = MgOH^+_{(aq)}$$

$$1/2\,Cu_2O_{(Cuprite)} + H^+_{(aq)} + nCl^-_{(aq)} = CuCl^{1-n}_{n\,(aq)} + 1/2\,H_2O_{(liq)} \qquad [3.1]$$

Within this scheme $CuCl^{1-n}_{n\,(aq)}$ does not represent an actual species and n refers to the average ligand number of the chlorocopper (I) complex. For individual copper species, n has an integer value. All copper(I) species are assumed to be mononuclear.

Equilibrium constants for these reactions may be written,

$$K_{talc-qz} = \frac{a_{Mg^{2+}} \cdot a_{H_2O}{}^{4/3}}{a_{H^+}{}^{2}} \qquad [3.4]$$

$$K_{H_2O} = \frac{a_{H_2O}}{a_{H^+} \cdot a_{OH^-}} \qquad [3.5]$$

$$K_{HCl} = \frac{a_{HCl^0}}{a_{H^+} \cdot a_{Cl^-}} \qquad [3.6]$$

$$K_{MgCl^+} = \frac{a_{MgCl^+}}{a_{Mg^{2+}} \cdot a_{Cl^-}} \qquad [3.7]$$

$$K_{MgCl_2^0} = \frac{a_{MgCl_2^0}}{a_{MgCl^+} \cdot a_{Cl^-}} \qquad [3.8]$$

$$K_{MgOH^+} = \frac{a_{MgOH^+}}{a_{Mg^{2+}} \cdot a_{OH^-}} \qquad [3.9]$$

$$\beta_n = \prod_0^n K_n = \frac{a_{CuCl_n^{1-n}} \cdot a_{H_2O}{}^{1/2}}{a_{H^+} \cdot a_{Cl^-}{}^{n}} \qquad [3.10]$$

where β_n is the cumulative equilibrium constant product describing cuprite dissolution [3.1] in terms of the stepwise formation of n chloride coordinated copper(I) species. The solubility product, K_0, of cuprite is equal to $n = 0$. a is the thermodynamic activity, for the ith aqueous species, which is defined as $a_i = \gamma_i \cdot m_i$, where γ and m refer to the activity coefficient and molal concentration, respectively.

Despite the acidic conditions imposed by the Tc–Qz buffer (*e.g.* calculated pH = 3.9 at 1 mol/kg Cl, 630 °C and 340 MPa), hydroxide complexes of Mg in these experiments may not be negligible, on the basis of the value of the first hydrolysis reaction[13] constant calculated from published thermodynamic data for Mg^{2+} (*e.g.* $\log K^{25°C,1\,bar}_{Mg(OH)^+_{(aq)}} = -11.68$, and $\log K^{630°C,334\,MPa}_{Mg(OH)^+_{(aq)}} = -3.87$; Shock *et al.* 1997). Interestingly,

[13] General representation of the cation hydrolysis reaction,

$$M^z_{(aq)} + nH_2O = M(OH)^{z-1}_{n\,(aq)} + nH^+_{(aq)}$$

where, M refers to the ion of interest, n defines the hydroxide species

most previous studies of Tc–Qz solubility have not considered magnesium(II) hydroxide complexes (*e.g.* Frantz and Popp 1979; Luce *et al.* 1985; Grabman and Popp 1991; Walther 1997a). Similarly, theoretical estimates of the first copper(I) hydrolysis constant also suggest that hydroxide complexes may not be negligible in these experiments (*e.g.* $\log K^{25°C,1\ bar}_{CuOH^0_{(aq)}} = -10.01$, and $\log K^{630°C,334\ MPa}_{CuOH^0_{(aq)}} = -2.46$; Akinfiev and Zotov 2001). Accordingly, the following reaction may also be required to interpret Cpr dissolution,

$$Cu^+_{(aq)} + OH^-_{(aq)} = CuOH^0_{(aq)}$$

For which the equilibrium constant is

$$K_{CuOH^0_{(aq)}} = \frac{a_{CuOH^0_{(aq)}}}{a_{Cu^+} \cdot a_{OH^-}} \qquad [3.11]$$

The standard states used in this study are defined as the pure mineral and liquid at the T and P of concern for solid phases and H_2O. For aqueous species the conventional, hypothetical ideal one molal solution referenced to infinite dilution at the T and P of interest was used. Since essentially pure mineral phases were used to buffer the experiments their activities are taken as unity. The activity of H_2O was assumed equal to its mole fraction, $a_{H_2O} = X_{H_2O}$, so as to account for the effect of solutes in the more concentrated solutions. The assumption that the dissolved components result in ideal dilution of the solvent at low-P is supported by the experimental work of Aranovich and Newton (1996, 1997). An extended-term Debye-Hückel equation was used to calculate the molal activity coefficients of individual charged species ($\gamma_i^{+/-}$; Helgeson *et al.* 1981),

$$\log\left(\gamma_i^{+/-}\right) = -\frac{A_\gamma z_i^2 \sqrt{\bar{I}}}{1 + B_\gamma \mathring{a}_i \sqrt{\bar{I}}} + \dot{B}_\gamma \bar{I} + \Gamma_\gamma \qquad [3.12]$$

where the subscript *i*, refers to the *i*th individual species, A_γ and B_γ are conventional Debye-Hückel solvent coefficients, calculated for high-P and T using the expressions defined by Helgeson and Kirkham (1974),

$$A_\gamma = \frac{1.8248\times10^6\sqrt{\rho}}{(\varepsilon T)^{3/2}} \qquad [3.13]$$

$$B_\gamma = \frac{50.291\times10^8\sqrt{\rho}}{\sqrt{\varepsilon T}} \qquad [3.14]$$

The dielectric constant (ε) and density of H_2O (ρ) required in the calculation of A_γ and B_γ, were determined using the algorithms reported by Haar *et al.* (1984). z_i is the formal valence of the species. $\mathring{a}_i$ is the ion size parameter in angstroms (10^{-10} m; Å), which by reference to the values of Kielland (1937), monovalent ions were assigned a value of 4, except for H^+ which was 9, divalent and higher-charged species were taken as 5. $\dot{B}_\gamma$ is an empirical solute-solvent interaction term for electrolyte-bearing aqueous solutions, dependent on the P–T–X conditions of the fluid. As a first approximation, $\dot{B}_\gamma$ was taken as equal to $\dot{B}_{\gamma,NaCl}$, at all P and T, as no data more directly applicable to Cu–Mg–H–Cl solutions are available. This is also reasonable for solutions dominated by 1:1 electrolytes (Helgeson *et al.* 1981). Mg is a trace component in the solutions studied. The value of $\dot{B}_{\gamma,NaCl}$ was calculated from the parameters and equations given by Oelkers and Helgeson (1990). On the other hand, it was found that, by arbitrarily changing the value of the $\dot{B}_\gamma$ parameter, the calculated copper concentration is relatively insensitive to choice of $\dot{B}_\gamma$. $\bar{I}$ is the ionic strength of the solution, defined as,

$$\bar{I} = \frac{1}{2}\sum_{i=1}^{N} z_i^2 m_i \qquad [3.15]$$

where m_i is the molal concentration of the *i*th species and the summation is taken over all, N, species in the solution. Γ_γ is the mole fraction to molality conversion factor,

$$\Gamma_\gamma = -\log\left(1 + 0.0180153 m^*\right) \qquad [3.16]$$

where m^* is the total molality of all the species in solution.

The behaviour of activity coefficients of neutral species $\left(\gamma_i^0\right)$ in supercritical fluids can be successfully treated using a Setchénow-type expression (Setchénow 1892),

$$\log\left(\gamma_i^0\right) = b_{\gamma^0} \bar{I} + \Gamma_\gamma \qquad [3.17]$$

Various approaches to the calculation of Setchénow coefficients (b_{γ^0}) have been advocated (*e.g.* Oelkers and Helgeson 1991; Walther 1997a). Although these models are consistent with the data on which they were demonstrated, they produce very different interpretations of the speciation. For example, Oelkers and Helgeson (1991) suggest that with increasing concentration and T and decreasing P, γ_i^0 values become greater than 1, requiring the formation of polynuclear species. Whereas, Reardon and Langmuir (1976) and Walther (1997a) argued that in fact the reverse was potentially more likely, *i.e.* $\gamma_i^0 < 1$, such that neutral species become increasingly stable under supercritical conditions. General resolution of this problem is beyond the intent of this investigation and awaits further experimental study. Regardless, in the first instance the usual conservative approach was taken and neutral species were arbitrarily assigned unit value activity coefficients.

Equilibrium constants must be calculated at the P and T of interest in order to solve the speciation model. This usually requires extrapolation of species properties from experimental data obtained under different conditions. Numerous empirical and theoretical techniques have been developed for extrapolating the thermodynamic properties of aqueous species to elevated P–T conditions. They include isocoulombic methods (*e.g.* Lindsay 1980; Ruaya 1988; Gu *et al.* 1994), empirical correlation equations based on H_2O density (*e.g.* Marshall and Franck 1981), theoretical density models (Mesmer *et al.* 1988; Anderson *et al.* 1991) and various approaches based on electrostatic theory (*e.g.* Helgeson 1969; Helgeson and Kirkham 1974; Helgeson *et al.* 1981; Shock and Helgeson 1988; Tanger and Helgeson 1988; Walther and Schott 1988; Brady and Walther 1990; Walther 1991). These models are not discussed in detail. However, it should be remarked that several means were used for the practical purpose

of obtaining the necessary equilibrium constants at the conditions of these experiments. For most reactions, the revised Helgeson-Kirkham-Flowers (HKF) EOS (*e.g.* Helgeson *et al.* 1981; Tanger and Helgeson 1988) was used to extrapolate the thermodynamic properties of aqueous species up to 1000 °C and 500 MPa, using literature HKF parameters and the SUPCRT92 program (Johnson *et al.* 1992). Whereas, for the ionisation constants of the Mg–Cl complexes, extrapolation of low-T data was not required as empirical equations describing the experimental measurements, which cover the P and T range of interest, are available (Frantz and Marshall 1982). Table 3.2 lists the equilibrium constants and sources used in the calculations.

Table 3.2 Equilibrium constants used in the Cu–Cpr–Tc–Qz speciation calculations at 629 °C and 334 MPa

Reaction	$\log K^{630°C,334\,MPa}$	Source
$1/3Mg_3Si_4O_{10}(OH)_{2\,(Talc)} + 2H^+_{(aq)} = 4/3SiO_{2\,(Quartz)} + Mg^{2+}_{(aq)} + 4/3H_2O_{(liq)}$	2.93	Helgeson *et al.* (1978; minerals) Shock *et al.* (1997; aqueous species)
$H^+_{(aq)} + Cl^-_{(aq)} = HCl^0_{(aq)}$	3.30	Tagirov *et al.* (1997; $HCl^0_{(aq)}$) Shock *et al.* (1997; $Cl^-_{(aq)}$)
$H^+_{(aq)} + OH^-_{(aq)} = H_2O_{(liq)}$	10.1	Shock *et al.* (1997)
$Mg^{2+}_{(aq)} + Cl^-_{(aq)} = MgCl^+_{(aq)}$	4.03	Frantz and Marshall (1982)
$MgCl^+_{(aq)} + Cl^-_{(aq)} = MgCl^0_{2\,(aq)}$	2.20	Frantz and Marshall (1982)
$Mg^{2+}_{(aq)} + OH^-_{(aq)} = MgOH^+_{(aq)}$	6.26	Shock *et al.* (1997)

The solution model is further constrained using mass balance equations for Cl, Cu, Mg and electrical charge,

$$m_{\mathrm{Cl}}^{total} = \overline{n}\left(\sum_{0}^{n} m_{\mathrm{CuCl}_n^{1-n}}\right) + m_{\mathrm{HCl}^0_{(aq)}} + m_{\mathrm{Cl}^-} + 2m_{\mathrm{MgCl}^0_{2\,(aq)}} + m_{\mathrm{MgCl}^+} \qquad [3.18]$$

$$m_{\mathrm{Cu}}^{total} = \sum_{0}^{n} m_{\mathrm{CuCl}_n^{1-n}} + m_{\mathrm{CuOH}^0_{(aq)}} \qquad [3.19]$$

$$m_{\mathrm{Mg}}^{total} = m_{\mathrm{MgCl}^0_{2\,(aq)}} + m_{\mathrm{MgCl}^+} + m_{\mathrm{MgOH}^+} + m_{\mathrm{Mg}^{2+}} \qquad [3.20]$$

$$0 = (1 - \overline{n})\left(\sum_{0}^{n} m_{\mathrm{CuCl}_n^{1-n}}\right) + m_{\mathrm{MgCl}^+} + m_{\mathrm{MgOH}^+} + 2m_{\mathrm{Mg}^{2+}} + m_{\mathrm{H}^+} - m_{\mathrm{Cl}^-} - m_{\mathrm{OH}^-} \qquad [3.21]$$

where m_j^{total} refers to the total molal concentration (moles per 1000 g H_2O) of element j (*i.e.* Cl, Cu and Mg) and m_i refers the molal concentration of the ith aqueous species. $\bar{n}$ refers the average number of Cl coordinated with the dissolved copper. The relation between the total dissolved copper and the stability of the complexes as a function of chloride concentration is clearer when the equilibrium constant and mass balance expressions are combined, Equations [3.10], [3.11] and [3.19] respectively,

$$m_{Cu}^{total} = \frac{K_0 a_{H^+}}{a_{H_2O}^{1/2}} \left(\left(\frac{1}{\gamma_{Cu^+_{(aq)}}} + \frac{K_1 a_{Cl^-}}{\gamma_{CuCl^0_{(aq)}}} + \cdots + \frac{K_n a_{Cl^-}{}^n}{\gamma_{CuCl_n^{1-n}{}_{(aq)}}} \right) + \left(\frac{K_{CuOH^0_{(aq)}} a_{H_2O}}{\gamma_{CuOH^0_{(aq)}} K_{H_2O}} \right) \right) \qquad [3.22]$$

Hence, the speciation may be calculated at any given P–T–X by simultaneous solution of Equations [3.4] to [3.21].

4.2.2 Data regression method

The speciation calculation was treated as a constrained optimisation problem. Framed in this way, Equations [3.4] to [3.21] were not used to eliminate variables but rather as constraints on the solution. A non-linear Generalised Reduced Gradient (GRG) algorithm was employed to iterate species concentrations until an optimal solution was reached, *i.e.* all constraints were satisfied (Lasdon *et al.* 1978; Smith and Lasdon 1992). Calculations were performed using the built-in Solver function in the Microsoft Excel 2001 software. Infeasible solutions were avoided by converging on the same solution from a number of different starting compositions. Furthermore, numerical upper and lower bounds were imposed on all variables to restrict them to physically meaningful values during the iterations. A similar approach to solving speciation in supercritical solutions was taken by Ziegler *et al.* (1999).

The experimental data were regressed to obtain a simple empirical least square fit (*e.g.* as in Figure 3.3). A residual function, representing the difference between the experimental (the least square fit), and the calculated mineral solubility was then optimised. The cumulative residual is defined,

$$S^2_{Residual} = \sum \left[\log\left(m^{total}_{Cu,\ experimental}\right) - \log\left(m^{total}_{Cu,\ calculated}\right) \right]^2 \qquad [3.23]$$

where m is the total concentration of Cu in mol/kg as measured and calculated. Minimisation of the residual directly yields values for the log equilibrium formation constants of each copper species considered, *e.g.* Equation [3.22]. Because optimised log K values were regressed simultaneously for individual experiments it was possible to analyse their variation to estimate their uncertainty. The value of $S^2_{Residual}$ was used to compare the apparent accuracy with which the different speciation models describe the data, thus acting as a guide to the identity and number of copper species present.

4.2.3 Mg–O–H–Cl speciation: Further discussion of the thermodynamic data required from the literature

To interpret the experimental data quantitatively, the speciation for all components is needed. For those experiments buffered by Cu–Cpr–Tc–Qz, this requires that thermodynamic properties of the species in the Mg–O–H–Cl sub-system be known or estimated reliably as any errors will be propagated in the Cu(I)–Cl species and their derived properties. This necessitates a brief review of the literature data used for the speciation calculations.

The thermodynamic properties of Qz and Tc used in this study were taken from Berman (1988) as they are consistent with a large number of experimental studies.

The thermodynamic properties of magnesium(II) chloride aqueous species $\left(Mg^{2+}, MgCl^{+}, MgCl^{0}_{2\,(aq)}\right)$ at elevated T and P have been the subject of numerous investigations. Although most such studies have approached this problem by examining the solubility relations of the Tc–Qz equilibrium (Frantz and Popp 1979; Luce *et al.* 1985; Saccocia and Seyfried 1990; Grabman and Popp 1991), other methods have also been applied, such as measuring the electrical conductance of supercritical $MgCl_2$–H_2O solutions (Frantz and Marshall 1982).

Saccocia and Seyfried (1990) recently investigated Mg–Cl speciation in $MgCl_2$–NaCl solutions buffered by the Tc–Qz equilibrium at 300 to 400 °C and 50 MPa. Since only dilute solutions were investigated (< 1 mol/kg total Cl) no evidence for $MgCl^{0}_{2\,(aq)}$ was observed. The entire observed Mg solubility was explained by the species Mg^{2+} and $MgCl^{+}$. Consequently, thermodynamic properties for $MgCl^{+}$ were derived by D.A. Sverjensky (*personal communication,* cited in Saccocia and Seyfried, 1990) from their experimental data.

The first and second ionisation constants of $MgCl^{0}_{2\,(aq)}$ have been obtained by electrical conductance measurement to 600 °C and 400 MPa ([3.7] and [3.8]; Frantz and Marshall 1982). In the light of these measurements, Frantz and Popp (1981) revised their own previously reported (Frantz and Popp 1979) ionisation constants for $MgCl_2$ that were based on Tc–Qz solubility measurements. The electrical conductance results are in reasonable agreement with the mineral solubility experiments of Luce *et al.* (1985) and Saccocia and Seyfried (1990). Eugster and Baumgartner (1987) independently assessed the existing data (part of which is contained within an

unpublished Ph.D thesis, Wilson 1986). They identified no major inconsistencies between studies and reported fit parameters for empirical expressions describing the stepwise ionisation constants for $MgCl^0_{2\,(aq)}$ at high *P–T*.

Grabman and Popp (1991) revisited the Tc–Qz equilibrium, studying solubility relations in $MgCl_2$–NaCl–HCl solutions up to about 6 mol/kg total Cl at 200 MPa from 500 to 700 °C. This investigation suggested that, not only were the species Mg^{2+}, $MgCl^+$ and $MgCl^0_{2\,(aq)}$ required, but additional higher-order Mg–Cl or Mg–Na–Cl species were also necessary to explain the measurements in concentrated solutions. Such species, however, could not be identified unambiguously. Walther (1997a) revaluated the solubility data of Grabman and Popp (1991). He found that should the activity coefficients of the neutral species, $HCl^0_{(aq)}$, $NaCl^0_{(aq)}$ and $MgCl^0_{2\,(aq)}$, deviate from unity, as might be expected, then higher-order or polynuclear complexes were not needed to explain the data. Additionally, it was noted by Grabman and Popp (1991) and Walther (1997a) that the existing thermodynamic properties for Mg^{2+} are relatively uncertain. Inaccuracies related to the reported species properties (and thermodynamic model) represent, of course, an alternative explanation as to why calculations fail to reproduce experimentally determined Mg solubilities in equilibrium with Tc–Qz (*e.g.* Grabman and Popp 1991).

Shock *et al.* (1997) reported properties for $MgOH^+$ which are in close agreement with potentiometric measurements of the first hydrolysis constant for magnesium(II) made by Palmer and Wesolowski (1997) to 250°C in NaCl aqueous solutions (up to 5 molal ionic strength). There are, however, no experimental data to verify the stability of magnesium(II) hydroxide complexes at higher *P–T*.

Regardless of the apparent complexities associated with the interpretation of aqueous Mg–Cl speciation in mineral solubility studies, a critical appraisal of the literature data suggests that it is appropriate to treat only the species Mg^{2+}, $MgOH^+$, $MgCl^+$ and $MgCl^0_{2\,(aq)}$ in this work. Thermodynamic properties for Mg^{2+} and $MgOH^+$ are taken from Shock *et al.* (1997), along with the equilibrium dissociation constant data of Frantz and Marshall (1982) for $MgCl^+$ and $MgCl^0_{2\,(aq)}$.

Not only because of its importance in hydrothermal systems the dissociation of HCl has received much experimental attention, via a variety of techniques (*e.g.*

electrical conductance, calorimetry and solubility), over a wide range of T and P (*e.g.* Franck 1956; Robinson and Bates 1971; Bach *et al.* 1977; Frantz and Marshall 1984; Ruaya and Seward 1987; Holmes *et al.* 1987; Sverjensky *et al.* 1991; Sretenskaya 1992; Tagirov *et al.* 1997; Pokrovskii 1999; Ho *et al.* 2001). Despite this, there remains some uncertainty in the thermodynamic properties of HCl, as there are significant discrepancies between many of these studies. For instance, the electrical conductance measurements of Frantz and Marshall (1984) are inconsistent with the phase equilibrium solubility data of Zotov *et al.* (1990) and Sverjensky *et al.* (1991).

The most severe discrepancies are apparent in the near-critical and low-density supercritical regions. Recognising this, Tagirov *et al.* (1997) conducted a series of experiments, in which the solubility of $AgCl_{(s)}$ in KCl and NaCl solutions and $Ag_{(s)}$ solubility in HCl+NaCl solutions was measured, to help resolve these problems. These experimental results were combined with all of the available data on HCl^0 dissociation to obtain an internally consistent set of thermodynamic properties for HCl, which can be extrapolated (*e.g.* the HCl^0 dissociation constant) to at least 700 °C and 500 MPa. The standard state properties and revised HKF parameters (Tanger and Helgeson 1988) for HCl^0 derived by Tagirov *et al.* (1997) represent an optimum fit to the various datasets available in the literature. The difference between the HCl^0 dissociation constants calculated using the parameters of Tagirov *et al.* (1997) and Pokrovskii (1999), who refit only the conductance data of Frantz and Marshall (1984), is generally less than 0.1 log units. Hence, the properties of Tagirov *et al.* (1997) were adopted in this study.

4.2.4 Comparison with extrapolations of previous "low-temperature" (< 350 °C) copper(I) species data

Previous studies have determined thermodynamic properties for aqueous copper(I) species from comparatively low-T and P experimental data and using theoretical approaches. Recent sources include Sverjensky *et al.* (1997), Liu (2001b), and Akinfiev and Zotov (2001). Extrapolation of such data enables calculation of mineral solubilities at higher T and P. The thermodynamic properties extracted from low-T experiments fit those conditions, but when extrapolated to high-T the different model calculations diverge significantly. Before deriving an independent speciation model from the present work it is insightful to compare the various theoretical solubilities calculated from the literature with the present experimental data.

Sverjensky *et al.* (1997) estimated HKF parameters for $CuCl^0_{(aq)}$, $CuCl_2^-$, $CuCl_3^{2-}$ based on correlations between standard partial molal properties at 25 °C and 1 bar and the revised HKF equations of Tanger and Helgeson (1988). Since no high-P and -T experimental data were used by Sverjensky *et al.* (1997), the reliability is uncertain as it depends heavily on the validity of correlating properties determined at 25 °C. More importantly, log K values for the formation of chlorocopper(I) complexes predicted by Sverjensky *et al.* (1997) at elevated conditions are in disagreement with recent solubility and spectroscopy measurements (Varyash 1992; Xiao *et al.* 1988; Liu 2001a, 2002). Consequently, the thermodynamic properties for chlorocopper(I) complexes determined by Sverjensky *et al.* (1997) are not considered reliable.

Akinfiev and Zotov (2001) analysed the experimental data of Var'yash (1990, 1992) and Xiao *et al.* (1998) to obtain HKF EOS parameters for the species Cu^+, $CuOH^0_{(aq)}$, $Cu(OH)_2^-$, $CuCl^0_{(aq)}$, and $CuCl_2^-$. These represent the only data available for aqueous copper(I) hydroxide complexes.

Liu (2001b) details unpublished HKF parameters for the species $CuCl^0_{(aq)}$, $CuCl_2^-$, $CuCl_3^{2-}$ and $CuCl_4^{3-}$, obtained by regression of his solubility and UV–visible spectroscopic data (Liu *et al.* 2001a, 2002).

The equilibrium formation constants for chlorocopper(I) complexes calculated at 630 °C and 334 MPa using the data of Liu (2001b) and Akinfiev and Zotov (2001) are reported in Table 3.3 – values predicted by Sverjensky *et al.* (1997) are included for completeness.

Table 3.3 Extrapolated equilibrium constants of formation for chloro- and hydroxy-copper(I) complexes at 629 °C and 334 MPa

Reaction	$\log K^{630°C,334\,MPa}$		
	Liu (2001b)	Akinfiev & Zotov (2001)	Sverjensky *et al.* (1997)
$1/2Cu_2O_{(Cuprite)} + H^+_{(aq)} = Cu^+_{(aq)} + 1/2H_2O_{(liq)}$	–	2.48	2.20*
$Cu^+_{(aq)} + Cl^-_{(aq)} = CuCl^0_{(aq)}$	3.76	2.32	2.75
$CuCl^0_{(aq)} + Cl^-_{(aq)} = CuCl^-_{2\,(aq)}$	0.99	3.57	2.37
$CuCl^-_{2\,(aq)} + Cl^-_{(aq)} = CuCl^{2-}_{3\,(aq)}$	-1.89	–	0.73
$CuCl^{2-}_{3\,(aq)} + Cl^-_{(aq)} = CuCl^{3-}_{4\,(aq)}$	0.52	–	–
$Cu^+_{(aq)} + OH^-_{(aq)} = CuOH^0_{(aq)}$	–	7.67	–
$CuOH^0_{(aq)} + OH^-_{(aq)} = Cu(OH)^-_{2\,(aq)}$	–	-3.69	–

Notes: * Cu^+ and Cl^- properties taken from Shock *et al.* (1997), except for Akinfiev and Zotov (2001) who report alternative HKF parameters for Cu^+, and these were used in the calculation of their log K values. Cuprite properties taken from Helgeson *et al.* (1978).

Though not apparent from examination of the log K values in Table 3.3 the different datasets regressed by Liu (2001b) and Akinfiev and Zotov (2001) are in reasonable agreement (Liu *et al.* 2001a; Liu *et al.* 2002). Thus, it is not obvious why these two studies predict markedly different chlorocopper(I) complex formation constants, most notably for $CuCl^-_{2\,(aq)}$, at elevated conditions.

The solubility of the mineral assemblage Cu–Cpr–Tc–Qz was calculated at 630 °C, 334 MPa as a function of salinity. Three separate calculations were made for comparative purposes:

I. Cu solubility as determined by chlorocopper(I) complexes using the data of Liu (2001b; and log K_0 = 2.20, calculated from Shock *et al.* 1997). Copper(I) hydroxide species were not included (Figure 3.4A);
II. Cu solubility calculated with both hydroxide and chloride complexes using the data of Akinfiev and Zotov (2001; Figure 3.4B); and,
III. Solubility was calculated using the chlorocopper(I) complex data of Liu (2001b) and $CuOH^0_{(aq)}$ data of Akinfiev and Zotov (2001; Figure 3.4A).

For these calculations, only the total Cl concentration was specified, and Equations [3.4] to [3.18] were solved simultaneously, while assuming $a_{H_2O} = X_{H_2O}$, to determine the total Mg and Cu concentrations. The results are compared with the experimentally measured values in Figure 3.4. Solubility could not be calculated over

the full range of the experiments (successive iterations would not converge at high salinity).

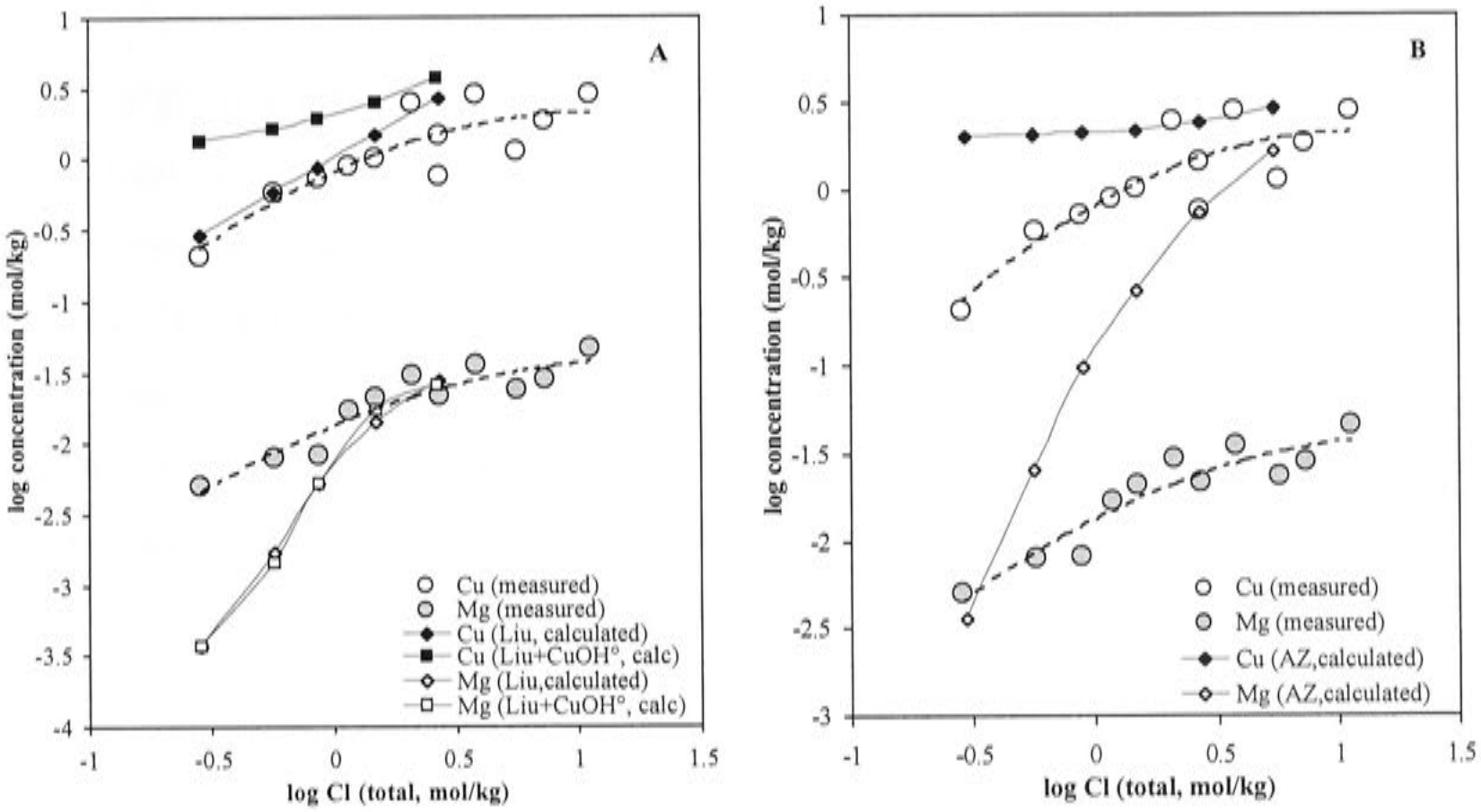

Figure 3.4 Experimental and predicted Mg and Cu concentrations as a function of total Cl at 629 °C, 334 MPa saturated with the mineral assemblage Cu–Cpr–Tc–Qz. A) Chlorocopper(I) species of Liu (2001b) with and without $CuOH^0_{(aq)}$ (squares = model I, and diamonds = model III, respectively); and, B) Mixed copper(I) chloride and -hydroxide complexes, Akinfiev and Zotov (2001). Dashed lines are least square second order polynomial fits to the experimental data.

The thermodynamic data for $CuOH^0_{(aq)}$ (Akinfiev and Zotov 2001) significantly overestimate its stability at the conditions of these experiments. Both theoretical models (II and III) containing this species predict solubilities that are up to an order of magnitude too high at low salinities. Over the range of salinities covered by the experimental data there is no indication that copper(I) hydroxide complexes are significant. Experimental data suggest that dissolved copper(I) is predominantly chloride complexes.

The existing thermodynamic data for $CuCl^-_{2\,(aq)}$ are in significant disagreement. Akinfiev and Zotov (2001) predict $CuCl^-_{2\,(aq)}$ to be the predominant complex at these conditions. Consequently, their model predicts a rapid increase in total Mg with increasing chloride in correspondence with the increasing $CuCl^-_{2\,(aq)}$ concentration. This is because positively charged Mg species (and H^+) are required to satisfy the charge balance constraint, which is dominated by the aqueous copper

species. Thus, the speciation predicted by the Akinfiev and Zotov (2001) thermodynamic model is inconsistent with the measurements. Liu (2001b), however, predicts $CuCl^0_{(aq)}$ to predominate in these solutions and so a rapid rise in Mg, to preserve electrical neutrality in the solution, is not anticipated.

The data of Liu (2001b; model I), predicts the observed Cu and Mg solubility pattern more closely, suggesting it is the more reliable of the available thermodynamic data. However, the trend to lower total Cu/Cl ratios at high salinity is not reproduced, despite the inclusion of highly coordinated chlorocopper(I) species. Calculation convergence becomes a problem with increasing salinities, most likely because of the stability of the higher-order charged complexes and the neutrality constraint imposed on the model. Alternatively there is a deficiency (likely) in the activity coefficient model over the salinity range of the measurements, such that the concentration of charged species are underestimated.

Although the preceding discussion focuses on the Cu species, it obvious that the predicted Mg concentrations also disagree with those measured (Figure 3.4), regardless of the data used. This discrepancy is a further clue that something is amiss, though not necessarily with the data for the Mg species.

4.2.5 Copper(I) speciation, derived equilibrium constants and discussion

The number and identity of copper species necessary to describe the data was assessed by fitting various models and minimising the difference between the calculated and measured fluid compositions, *i.e.* $S^2_{Residual}$ (*PART 3, §4.2.2*). The type and distribution of copper (I) complexes in the experiments can be gauged, to a first approximation, from the overall shape and slope of measured log *m*Cu versus log *m*Cl (Figure 3.3). Since a non-linear relation is apparent, it suggests that several complexes are required to explain the experimental data, as a single species is unlikely to produce the observed trend. Because the data indicate hydroxide species are negligible over the range of salinity investigated (the slope remains positive at low Cl), only chlorocopper(I) complexes were considered. Note however, hydroxide complexes could be expected to become important at this *P–T* at lower salinities than those covered by the present experiments.

Several speciation models incorporating conventional charged species (*i.e.* $CuCl_n^{1-n}$; Equation [3.1]) were tested. These models essentially represent various refined forms of the existing speciation data (*e.g.* Liu 2001b). The results of these models, which included the following species Cu^+, $CuCl^0_{(aq)}$ and $CuCl_2^-$, are presented in Table 3.4 and Figure 3.5. In model 1 all three species were considered variables, whereas, in model 2, the properties of Cu^+, were calculated using the HKF parameters reported by Shock *et al.* (1997) and only $CuCl^0_{(aq)}$ and $CuCl_2^-$ were fitted. Additional model details are specified in the Table notes. The species distributions predicted by each model are shown in Figures 3.6 and 3.7.

Though these conventional three species models provide a reasonable fit to the relatively dilute solution measurements, they invariably diverge considerably from the measurements at high salinities (*i.e.* [Cl] > 1mol/kg), resulting in unacceptable model residuals ($S^2_{Residual} > 1$). Both models suggest that $CuCl^0_{(aq)}$ is the predominant species and that Cu^+ and $CuCl_2^-$ are relatively unimportant. Although a reasonable case could be made that the experiments do not extend to sufficiently low total chloride to adequately define K_0, the value of the cuprite solubility product determined using model 1 is in reasonable agreement with that calculated from published data (Shock *et al.* 1997), as incorporated in model 2. Not surprisingly then, there are no substantial differences in the speciation or data fit quality between these models (*e.g.* Figure 3.6).

In fact, the fit of both models is little better than that predicted using the data of Liu (2001b). However, both models 1 and 2 do represent an improvement over the existing Cu data as they yield a better fit to the Mg data over the full range of concentration.

Table 3.4 Formation constants for conventional $CuCl_n^{1-n}$ complexes derived (and the residual to the fit) from mineral solubility experiments at 629 °C and 334 MPa

Reaction	$\log K^{630°C,334MPa}$	$S^2_{Residual}$
Model 1, n=0,1,2		***1.096***
$1/2Cu_2O_{(Cuprite)} + H^+_{(aq)} = Cu^+_{(aq)} + 1/2H_2O_{(liq)}$	1.71 ± 0.33	
$Cu^+_{(aq)} + Cl^-_{(aq)} = CuCl^0_{(aq)}$	4.16 ± 0.51	
$CuCl^0_{(aq)} + Cl^-_{(aq)} = CuCl^-_{2\,(aq)}$	-2.8 ± 1.1	
Model 2, n=1,2		***1.269***
$Cu^+_{(aq)} + Cl^-_{(aq)} = CuCl^0_{(aq)}$	3.37 ± 0.20	
$CuCl^0_{(aq)} + Cl^-_{(aq)} = CuCl^-_{2\,(aq)}$	-4.05 ± 0.31	

Notes: Both models constrained using Equations [3.4] to [3.21], and the relation $a_{H_2O} = X_{H_2O}$.
Uncertainties are ± 1σ.
Model details:
Model 1. Three species, $Cu^+_{(aq)}$, $CuCl^0_{(aq)}$ and $CuCl^-_{2\,(aq)}$ used in the fitting, all varied.
Model 2. Two complexes varied, $CuCl^0_{(aq)}$ and $CuCl^-_{2\,(aq)}$; the ion was fixed using the equilibrium constant for $n = 0$ (*i.e.* $1/2Cu_2O_{(Cuprite)} + H^+_{(aq)} = Cu^+_{(aq)} + 1/2H_2O_{(liq)}$; $\log K_0^{630°C,334MPa} = 2.20$) calculated from published thermodynamic values for Cu^+ (Shock *et al.* 1997) and Cu_2O (Helgeson *et al.* 1978).

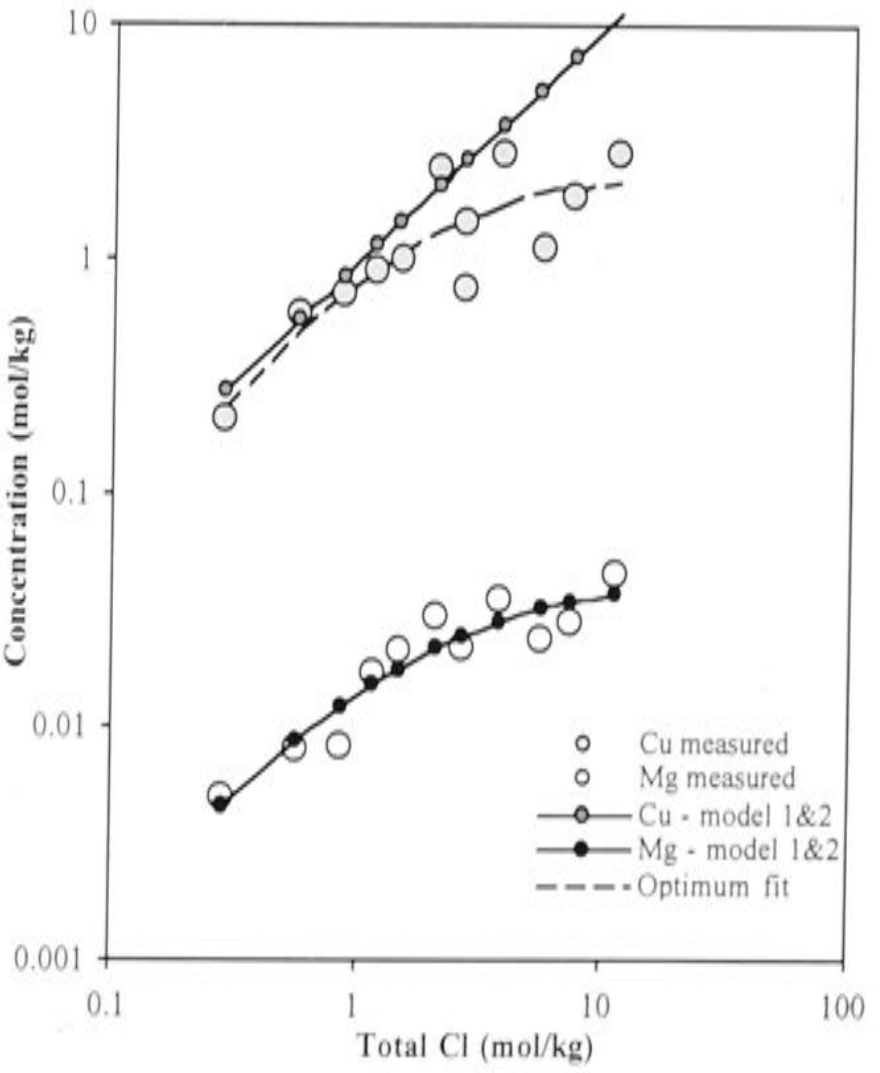

Figure 3.5 Comparison of the experimentally measured solubility of the assemblage Cu–Cpr–Tc–Qz at 629 °C and 334 MPa as a function of total Cl and the best fits achievable using conventional chlorocopper(I) species of the form $CuCl_n^{1-n}$, where n = 0,1,2. Models 1 & 2 are indistinguishable on this plot. The optimum (least squares) fit is shown for reference. Note these fits are not really optimal.

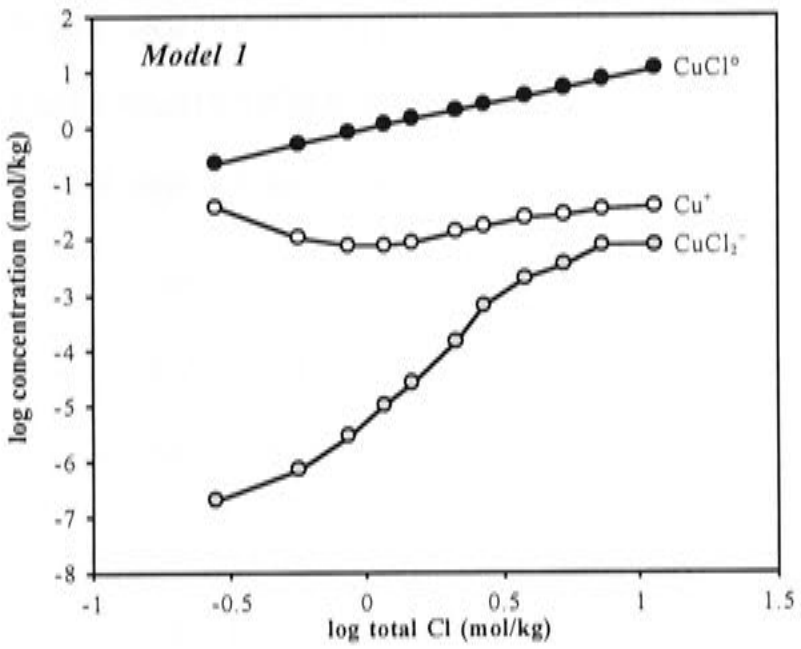

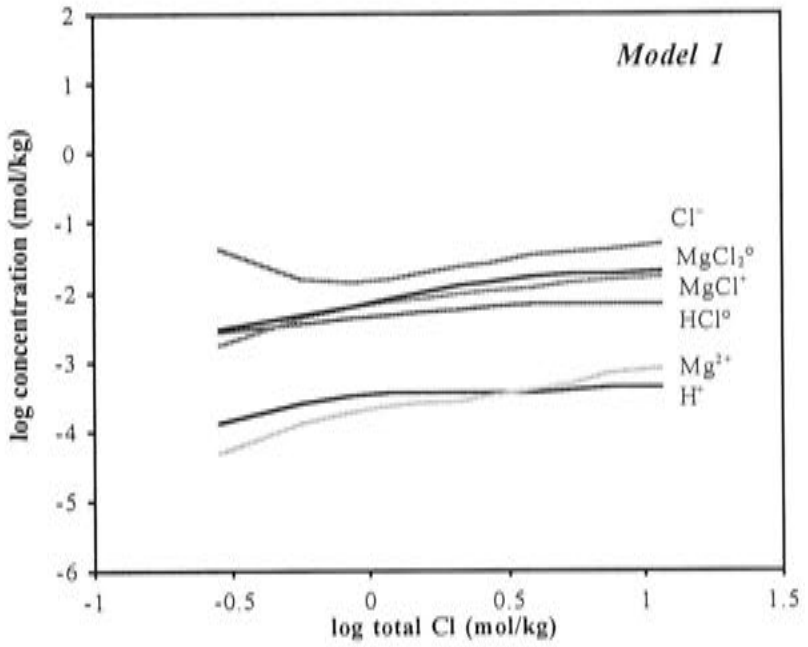

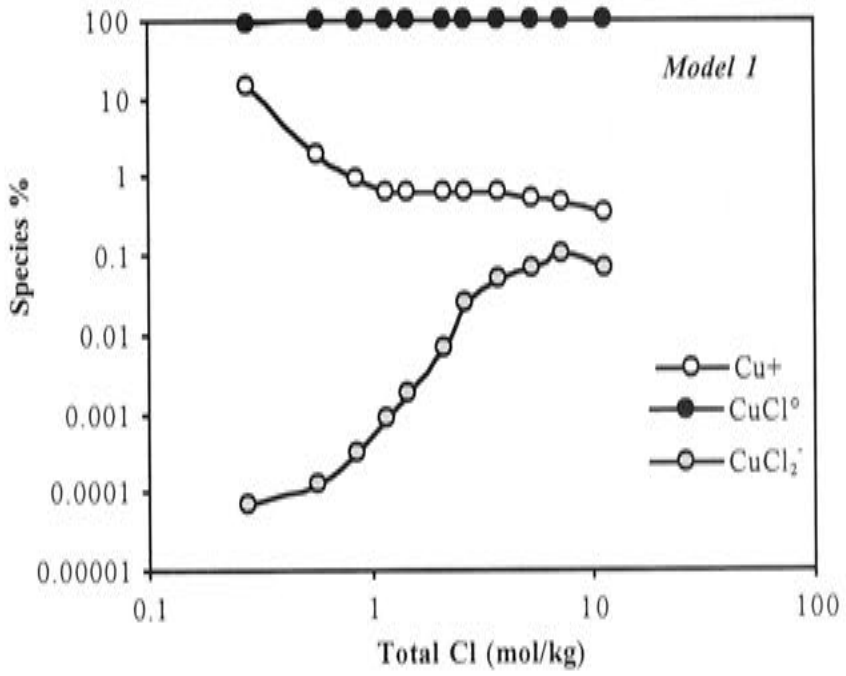

Figure 3.6 Distribution of species predicted by model 1. *Above*: the concentration of individual species as a function of total Cl; and, *Right*: the percentage distribution of aqueous copper species as a function of total Cl.

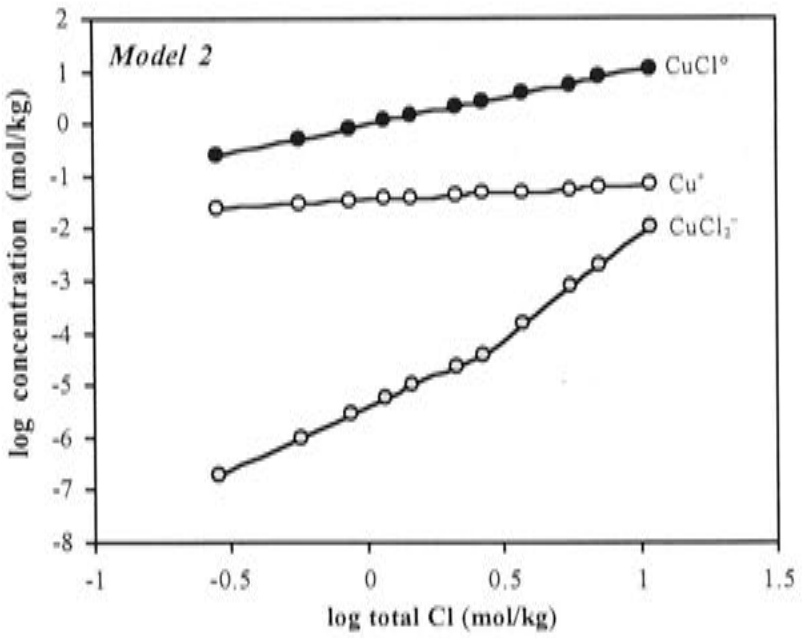

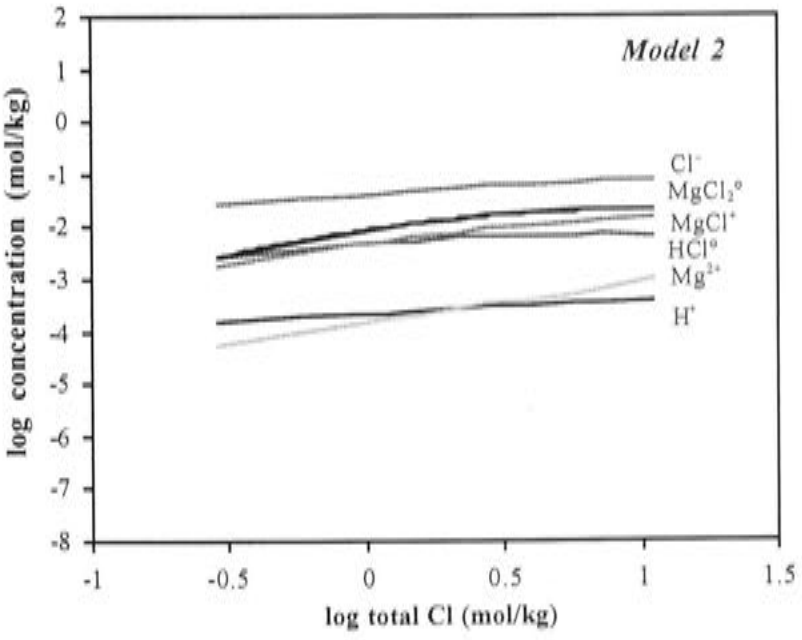

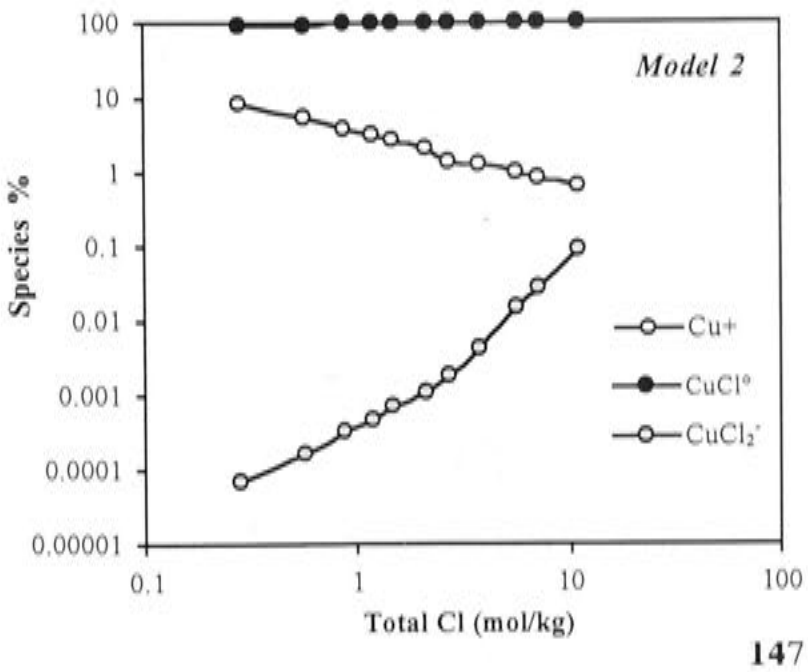

Figure 3.7 Distribution of species predicted by model 2. *Left*: the concentration of individual species as a function of total Cl; and, *Right*: the percentage distribution of aqueous copper species as a function of total Cl.

The model speciation is relatively insensitive to uncertainty in the Mg–Cl speciation. This was tested by arbitrarily varying the ionisation equilibrium constants, log K_{MgCl^+} and log $K_{MgCl^0_{2(aq)}}$ (Equations [3.7] and [3.8]), and recalculating the species distribution.

Additional models including higher-order complexes or polynuclear species were considered in an attempt to improve $S^2_{Residual}$. Conventional higher-order species (*i.e.* $CuCl_n^{1-n}$), however, do not significantly improve the fit. Alternatively, the inclusion of polynuclear complexes (*i.e.* $Cu_mCl_n^{m-n}$) in the model resulted in a considerably poorer fit to the data, as indicated by substantially increased residuals. This suggests that such species can be considered negligible in these experiments. Highly charged chlorocopper(I) and polynuclear complexes do not explain the high salinity experimental data. But firstly, why is the formation of conventional higher-order chlorocopper(I) species unfavourable, despite the high $m_{Cl}^{total} : m_{Cu}^{total}$ (~ 4:1) of the fluid?

It appears that the solute charge balance is a major constraint with regard to the viability of forming higher-order $CuCl_n^{1-n}$-type species in these experiments. This simply relates to the fact that Cu and Cl are major elements in the solutions whereas the total Mg (and H^+) are present at essentially trace concentrations. Thus charge balance of the stepwise formation of negatively charged chlorocopper(I) complexes at high salinity is because the Mg concentration, which determines the quantity of positively ionised species (*i.e.* Mg^{2+} and $MgCl^+$), is small and so limits the concentration of negative chlorocopper(I) complexes, noting that the concentration of H^+ is also small. This also explains the relative insensitivity of the chlorocopper(I) speciation to uncertainty in the properties of the Mg–Cl complexes. Increasing Cu^+ concentrations with salinity to balance the formation of negatively charged species would buffer the ratio $m_{Cl}^{total}/m_{Cu}^{total}$ at unity, as would the formation of neutral $Cu_nCl_n^0$ complexes (*e.g.* $Cu_3Cl_3^0$) but this is not observed at high salinities. Clearly an alternative to the formation of $CuCl_n^{1-n}$-type species for the miscreant high $m_{Cl}^{total}/m_{Cu}^{total}$ ratio must be sought.

The inability of conventional speciation models to describe the data at high salinity suggests: 1) higher-order chlorocopper(I) complexes must be uncharged; and/or, 2) the assumption of unit activity coefficients for neutral species is inappropriate.

The inference that, if present, higher-order chlorocopper(I) complexes have a neutral configuration was investigated. The simplest general stoichiometry of such complexes can be assumed to be $CuCl(HCl)^0_{n-1\,(aq)}$. In this case, cuprite solubility may be described by the reactions,

$$1/2\,Cu_2O_{(Cuprite)} + H^+_{(aq)} = Cu^+_{(aq)} + 1/2\,H_2O_{(liq)}$$

$$1/2\,Cu_2O_{(Cuprite)} + n\,HCl^0_{(aq)} = CuCl(HCl)^0_{n-1\,(aq)} + 1/2\,H_2O_{(liq)}$$

As with the conventional charged species, n is the ligand coordination number of the chlorocopper(I) complex, *e.g.* n = 1 defines $CuCl^0_{(aq)}$. These reactions were substituted into the conventional speciation model, replacing Equation [3.10] with the equilibrium constants,

$$K_0 = \frac{a_{Cu^+} \cdot a_{H_2O}{}^{1/2}}{a_{H^+}} \qquad [3.25]$$

$$\prod_1^n K_n = \frac{a_{CuCl(HCl)^0_{n-1}} \cdot a_{H_2O}{}^{1/2}}{a_{HCl}{}^n} \qquad [3.26]$$

and adjusting the charge balance and other relevant equations accordingly. No changes were made to the treatment of Mg–H–Cl speciation, activity coefficients for ionised species were still calculated using the B_γ Equation [3.12] and all neutral species were arbitrarily assigned unit value activity coefficients. The activity of the minerals remained set equal to 1 and $a_{H_2O} = X_{H_2O}$. Two models which incorporated Cu^+ plus two (n = 1 and 2; model 3) and four (n =1 to 4; model 4) neutral $CuCl(HCl)^0_{n-1\,(aq)}$ complexes are presented. Table 3.5 lists fit quality and derived formation constant details for models 3 and 4. The calculated mineral solubilities and the species distributions are illustrated, respectively, in Figures 3.8 & 3.9 (model 3) and Figures 3.10 & 3.11 (model 4).

Table 3.5 Formation constants for $CuCl(HCl)^0_{n-1}$ complexes derived (and the residual to the fit) from mineral solubility experiments at 629 °C and 334 MPa

Reaction	$\log K^{630°C,334\,MPa}$	$S^2_{Residual}$
Model 3, n=1,2		***0.270***
$Cu^+_{(aq)} + Cl^-_{(aq)} = CuCl^0_{(aq)}$	3.05 ± 0.17	
$CuCl^0_{(aq)} + HCl^0_{(aq)} = CuCl(HCl)^0_{(aq)}$	2.04 ± 0.42	
Model 4, n=1,2,3,4		***0.017***
$Cu^+_{(aq)} + Cl^-_{(aq)} = CuCl^0_{(aq)}$	3.01 ± 0.21	
$CuCl^0_{(aq)} + HCl^0_{(aq)} = CuCl(HCl)^0_{(aq)}$	1.85 ± 0.36	
$CuCl^0_{(aq)} + 2HCl^0_{(aq)} = CuCl(HCl)^0_{2\,(aq)}$	3.03 ± 0.97	
$CuCl^0_{(aq)} + 3HCl^0_{(aq)} = CuCl(HCl)^0_{3\,(aq)}$	5.2 ± 1.3	

Notes: Uncertainties are ± 1 σ.

Model 3. Three aqueous copper species model. Two complexes varied in the fitting, $CuCl^0_{(aq)}$ and $CuCl(HCl)^0_{(aq)}$; the ion was fixed using the equilibrium constant for n = 0 (*i.e.* $1/2Cu_2O_{(Cuprite)} + H^+_{(aq)} = Cu^+_{(aq)} + 1/2H_2O_{(liq)}$; $\log K_0^{630°C,334\,MPa}$ = 2.20) which was calculated from published thermodynamic properties for Cu^+ (Shock *et al.* 1997) and Cu_2O (Helgeson *et al.* 1978). This model produced the optimum least squares fit for conditions up to about 2.7 mol/kg total Cl; reported equilibrium constants were taken from the fit to this region. $S^2_{Residual}$ reflects the misfit at > 2.7 mol/kg Cl.

Model 4. Five aqueous copper species model. Complexes $\left(CuCl(HCl)^0_{n-1\,(aq)}\right)$ n = 1 to 4 were varied in the fitting. Cu^+ was determined via the solubility product, $\log K_0^{630°C,334\,MPa}$, and calculated as for model 3. This model gives the optimum least squares fit for all but the highest salinity experiment, thus $S^2_{Residual}$ is the misfit on that experiment.

Both models containing neutral species result in substantially improved fits to the experimental data, relative to models based on conventional charged complexes. Although the simple two complex model (model 3) reproduces the data with the least squares fit up to moderate salinities, the divergence apparent at higher Cl concentrations (*i.e.* Cl:Cu > ~ 2) remains almost within the analytical uncertainty at ± ~ 1 σ. Coupled with the scatter in the mean solubility results at high salinities, there is sufficient ambiguity that it is difficult to differentiate between the two and four neutral chlorocopper(I) complex models. Perhaps, however, it is sufficient to note that the experimentally observed solubility trend is far better explained by the stepwise formation of neutral chloride complexes, and that this was not anticipated by extrapolations of data from lower T and P studies.

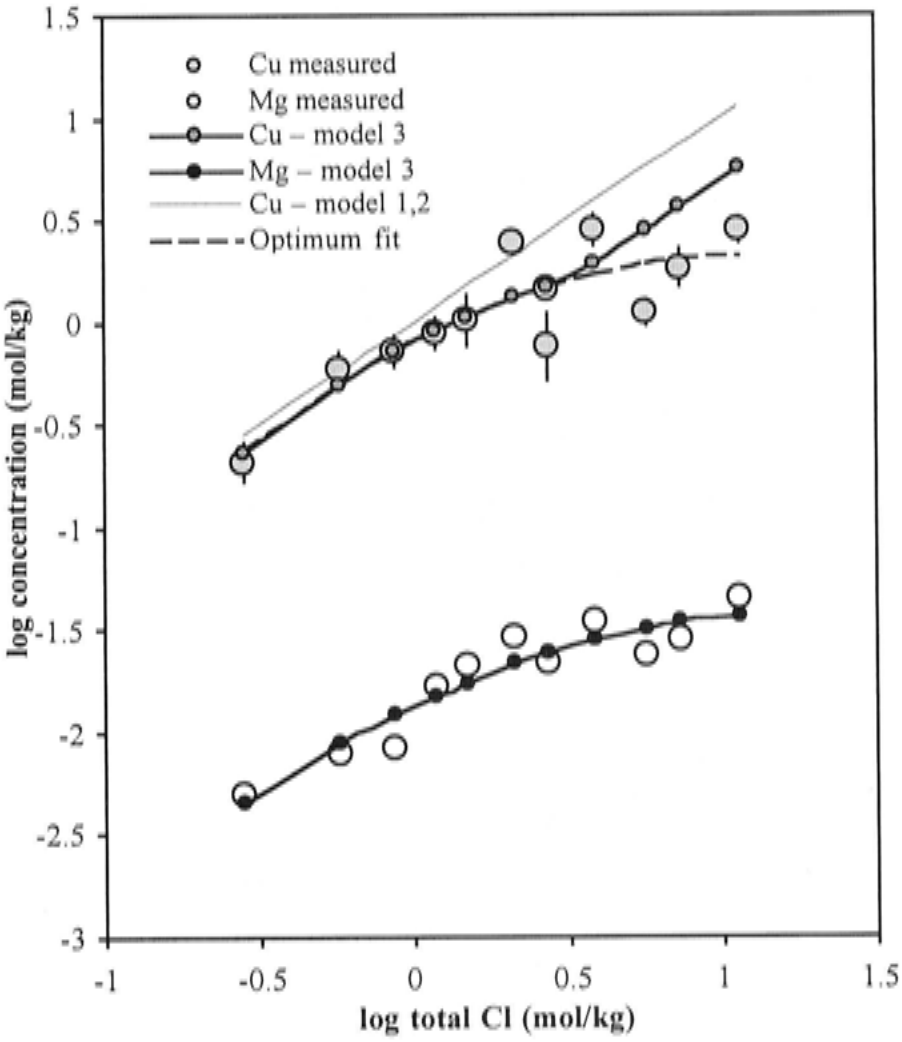

Figure 3.8 Comparison of the experimentally measured solubility of the assemblage Cu–Cpr–Tc–Qz at 629 °C and 334 MPa as a function of total Cl and the fit for model 3 using neutral chlorocopper(I) species of the form $CuCl(HCl)^0_{n-1}$, n = 1,2. Conventional species models (1 & 2) are shown for comparison. The optimum (least squares) fit is shown for reference. Note these fits are not really optimal at the highest salinities measured.

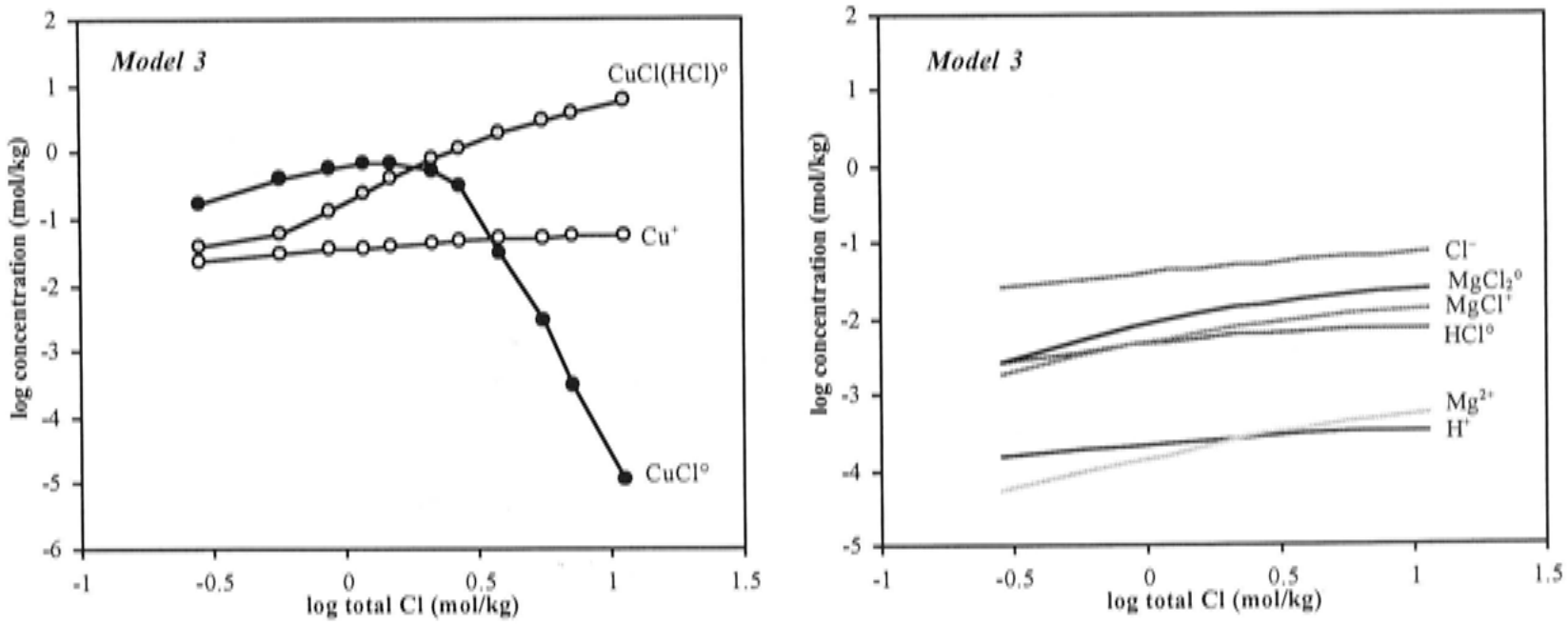

Figure 3.9 Comparison of the speciation predicted by model 3 for the assemblage Cu–Cpr–Tc–Qz at 629 °C and 334 MPa. *Left*: the concentration of individual species as a function of total Cl; and, *Right*: the percentage distribution of aqueous copper species as a function of total Cl.

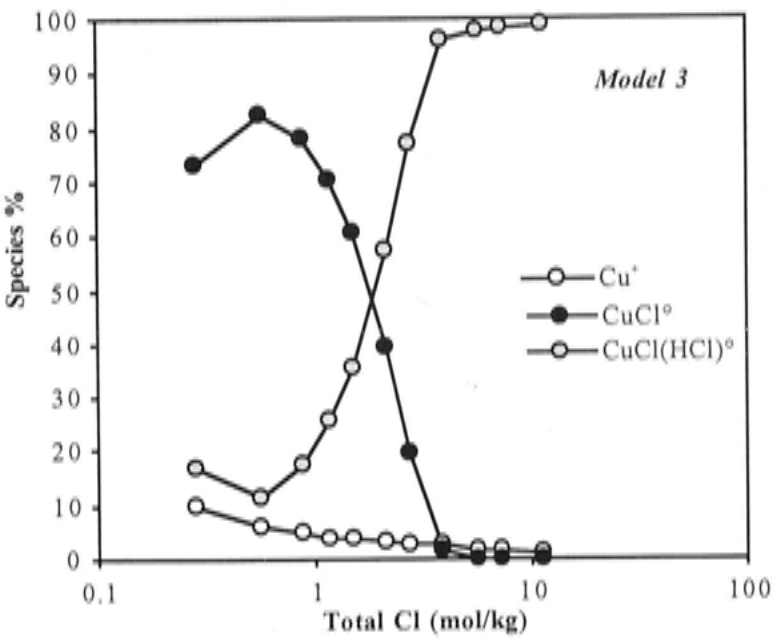

Figure 3.10 Comparison of the experimentally measured solubility of the assemblage Cu–Cpr–Tc–Qz at 629 °C and 334 MPa as a function of total Cl and the fitting for model 4 using neutral chlorocopper(I) species of the form $CuCl(HCl)^0_{n-1}$, n=1,2,3,4. Conventional speciation models (1 & 2) are shown for comparison. The optimum (least squares) fit is shown for reference.

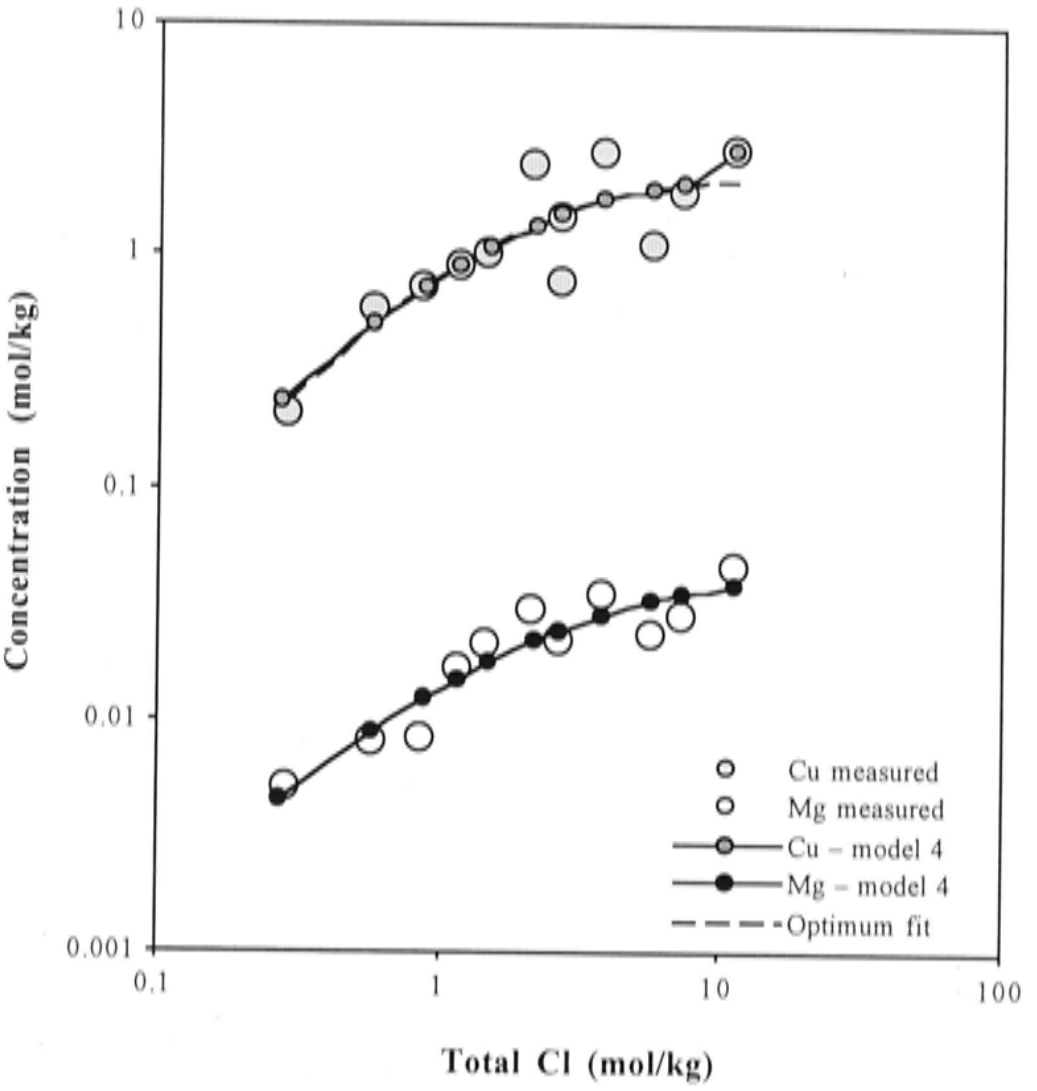

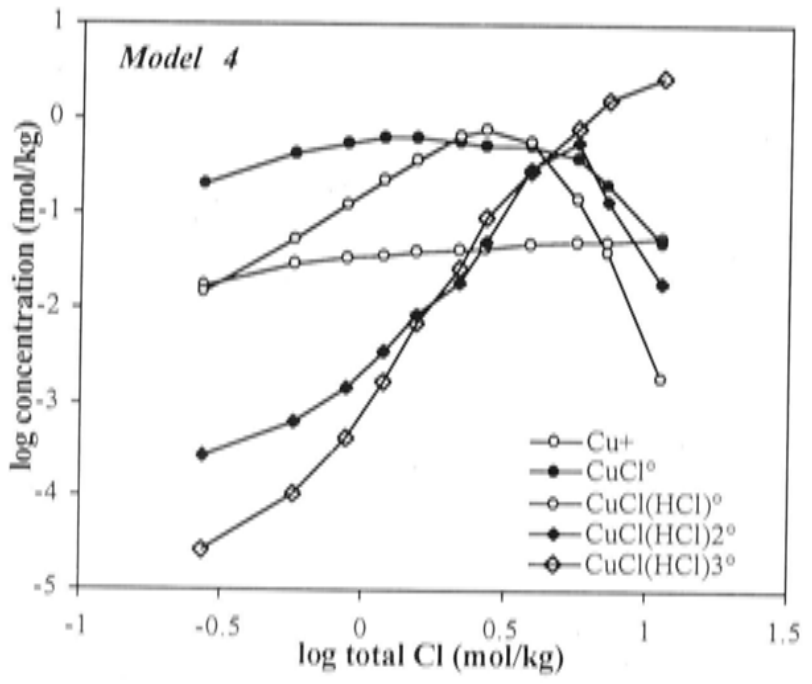

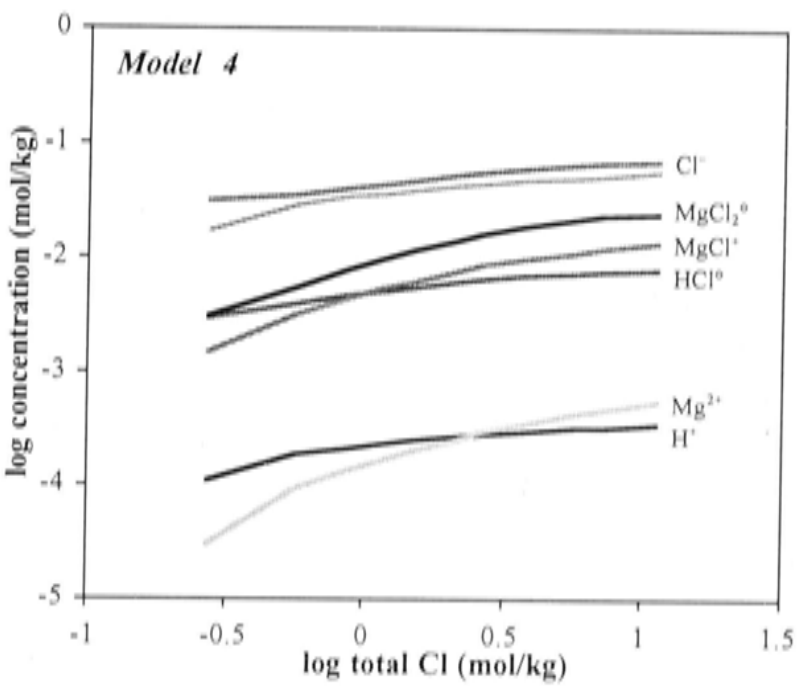

Figure 3.11 Comparison of the speciation predicted by model 4 for the assemblage Cu–Cpr–Tc–Qz at 629 °C and 334 MPa. *Above (left and right)*: the concentration of individual species as a function of total Cl; and, *Right*: the percentage distribution of aqueous copper species as a function of total Cl

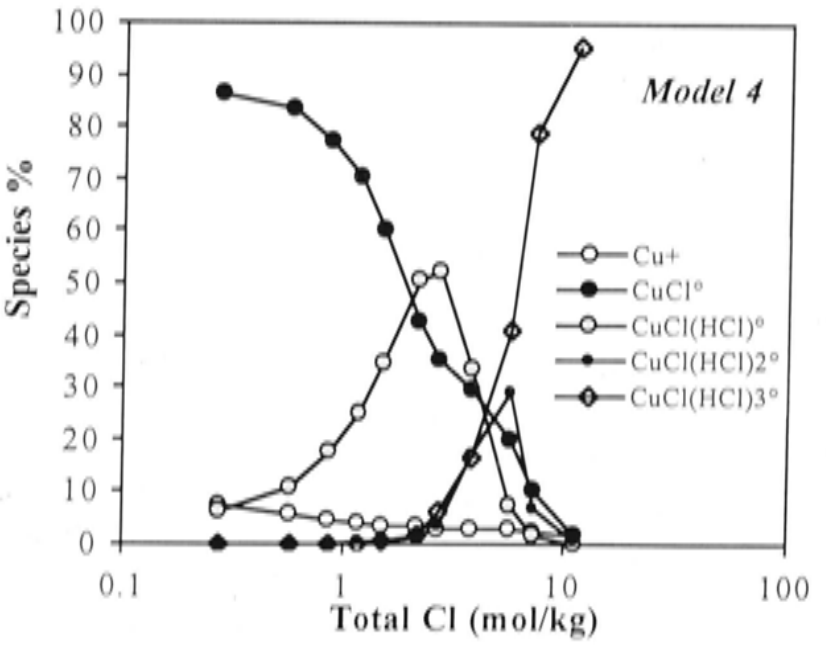

On the other hand, if the constraint of unit activity coefficients for neutral species (*e.g.* $HCl^0_{(aq)}$ and $CuCl^0_{(aq)}$) is relaxed, the data might be reconciled within a conventional speciation model. This would require that $HCl^0_{(aq)}$ becomes increasingly stable relative to $CuCl^0_{(aq)}$ at high salinity (*i.e.* $\gamma_{HCl^0_{(aq)}} / \gamma_{CuCl^0_{(aq)}} < 1$). The formation of higher-order charged species, and hence their importance remains negligible, as the charge balance constraint combined with low Mg solubility is unchanged.

Since these experiments may well be considered simple CuCl–HCl mixtures and given that the effective electrostatic radii of Cu^+ and Na^+ are similar (1.90 and 1.91 Å, respectively; Helgeson *et al.* 1981), it could be assumed simply that the behaviour of NaCl–HCl solutions might be a good proxy. The activity coefficients of neutral ion pairs in supercritical NaCl–HCl fluids have been estimated using Setchénow coefficients (b_{γ^0}) calculated using different techniques by Oelkers and Helgeson (1991) and Walther (1997a).

Oelkers and Helgeson (1991) reinterpreted experimental electrical conductance data to derive expressions for calculating Setchénow coefficients for the neutral ion pairs of a number of electrolytes, including NaCl and HCl.

Given the approximating assumption that the behaviour of $CuCl^0_{(aq)}$ will resemble that of $NaCl^0_{(aq)}$ under supercritical conditions, the Cu–Cpr–Tc–Qz solubility data was re-examined. For this, model 2 was modified to include Setchénow-type activity coefficients, Equation [3.14], using b_{γ,HCl^0} and $b_{\gamma,NaCl^0}$ values calculated from Oelkers and Helgeson (1991), $CuCl^-_{2\,(aq)}$ was also excluded due to the charge balance problem. The speciation and activity coefficients calculated by this model are shown in Figure 3.12.

It is interesting to note that at these conditions $\gamma_{HCl^0_{(aq)}}$ is predicted to undergo rapid change ($b^{O\&H(1991)}_{\gamma,HCl^0} = 38.1$), whereas, $CuCl^0_{(aq)}$ can be more or less treated as behaving ideally ($b^{O\&H(1991)}_{\gamma,NaCl^0} = 0.75$; Figure 3.12) over the range of composition investigated. This model, however, inevitably predicts $\gamma_{HCl^0_{(aq)}} / \gamma_{CuCl^0_{(aq)}} > 1$, resulting in lower $HCl^0_{(aq)}$ concentrations compared with other models, further exacerbating the need for higher-order neutral chlorocopper complexes at high salinity. $S^2_{Residual}$ for this model

is 1.282, which is essentially no better than assuming unit value activity coefficients for the neutral species in any conventional species model.

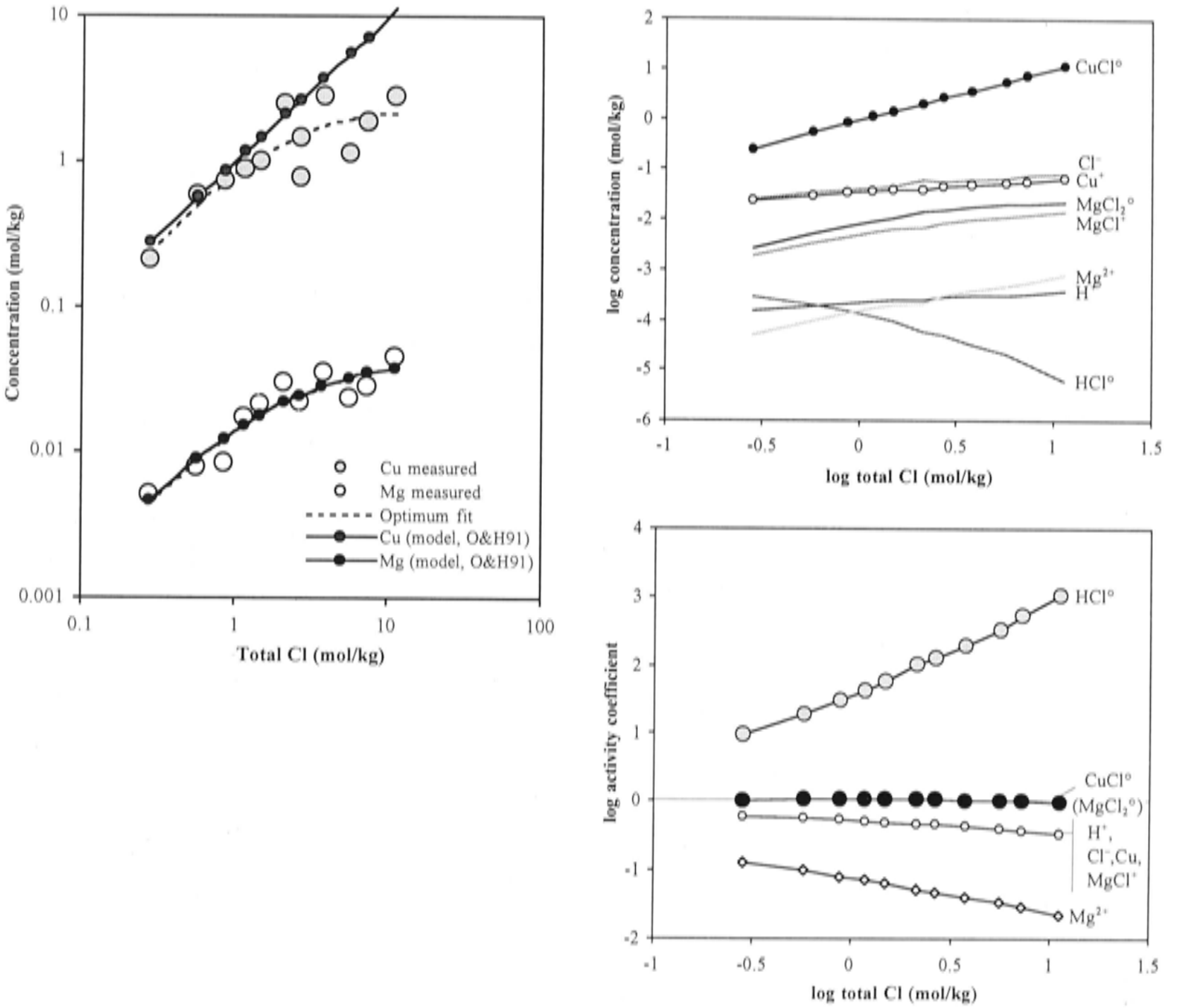

Figure 3.12 ***Above*****: Comparison of the experimental data and a conventional solubility model incorporating Setchénow coefficients calculated using the equations of Oelkers and Helgeson (1991; O&H91) and the $\dot{B}_\gamma$ equation for charged species. Model speciation (*above right*) and activity coefficients (*lower right*) also shown. Refer to text for further model details.**

A different approach to the calculation of neutral species activity coefficients was taken by Walther (1997a), who criticised the methods of Oelkers and Helgeson (1991). Walther (1997a) argued that the available data suggested neutral molecules may be generally more stable in supercritical fluids than conventionally assumed, if the interactions of neutral species are accounted for via their activity coefficients. The main consequence of this approach is, that otherwise undocumented species (*e.g.* polynuclear or similarly exotic species) are not required to explain the existing experimental data. To demonstrate, Walther (1997a) reinterpreted the Tc–Qz solubility measurements in

concentrated NaCl fluids of Grabman and Popp (1991; discussed in *PART 3, §4.2.3*) using a conventional species model and Setchénow coefficients for neutral species. In the analysis, Walther (1997a) determined at each T an average b_{γ^0} that was assigned to all neutral species in order to fit the data.

The average Setchénow coefficient approach taken by Walther (1997a), however, is not applicable to the present data as it will not change the activity coefficient of $HCl^0_{(aq)}$ relative to $CuCl^0_{(aq)}$, as required by the measurements. A more comprehensive treatment that considers each neutral species with an individual Setchénow parameter is necessary. That the activity coefficients should vary between neutral species is not unexpected (*e.g.* Long and Devit 1952). But it is not possible with the current data to simultaneously derive individual activity coefficients for the neutral species and log K values for the copper speciation. Nonetheless, it remains theoretically feasible that non-ideal interactions among neutral species, rather than the formation of new complexes, are responsible for the observed solubility trends.

4.2.6 Summary: Solubility and chlorocopper(I) complexing at constant pressure and temperature

The solubility of the assemblage Cu–Cpr–Tc–Qz increases as a function of salinity at constant T and P. Copper(I) hydroxide complexes and polynuclear species are negligible in these fluids and chlorocopper(I) complexes predominant over the entire range of Cl concentration investigated. Theoretical solubility calculations using data derived at much lower T and P are in variable agreement with the experimental data of this study (*e.g.* Liu 2001b and Akinfiev and Zotov 2001). It is clear that low $m_{\mathrm{Cu}}^{total}/m_{\mathrm{Cl}}^{total}$ fluid compositions as observed with increasing Cl in these experiments cannot be explained by models containing conventional CuCl_n^{1-n} complexes (which includes existing theoretical models). This is because charge balance requirements combined with low Mg (and H^+) concentrations inhibit the viability of high-order conventional charged species in these experiments.

Because the activity-composition relations of even simple neutral ion pairs in multi-component, high-P supercritical fluids are essentially unknown, the possibility that $\mathrm{HCl}_{(aq)}^0$ becomes disproportionately stable relative to $\mathrm{CuCl}_{(aq)}^0$ at high salinities cannot be excluded. Though it is worth noting that the experimental data are not reconciled using existing treatments of neutral species (*e.g.* Oelkers and Helgeson 1991). Regardless, a conventional species model may be made consistent with the observations, provided that the activity coefficient ratio, $\gamma_{\mathrm{HCl}_{(aq)}^0}/\gamma_{\mathrm{CuCl}_{(aq)}^0}$, becomes less than unity at high-Cl concentrations.

An alternate explanation also consistent with the mineral solubility data is the progressive formation of neutral higher-order chlorocopper(I) complexes ($\mathrm{CuCl(HCl)}_{n-1\,(aq)}^0$) with increasing salinity. A least squares fit to all the data is best satisfied by complexes with up to $n = 4$ at least. Equilibrium constants for complex formation were determined from the data. For $\mathrm{CuCl}_{(aq)}^0$, the log K value compares well with that estimated by the HKF parameters of Liu (2001b); for higher-order complexes no comparisons may be made. Assessing the reliability of the log K values derived for the higher order species is difficult because the identities of these complexes are not unequivocally defined by the measurements and therefore the log K values depend on the chosen thermodynamic model.

5. Mineral solubility: Effect of temperature (524 to 850 °C) on high-pressure supercritical fluids

5.1 Experimental data

Mineral solubility relations in the quartz-saturated portion of the system Cu_2O–MgO–SiO_2–HCl–H_2O were investigated from 524 to 850 °C, at ~ 335 MPa using synthetic fluid inclusions. Because solubility is also determined by salinity, the total Cl concentration of the fluid was controlled for this isobaric series.

For most experiments the solubility of the assemblage Cu–Cpr–Tc–Qz in 2 mol/kg Cl was measured. However, since talc dehydrates at approximately 755 °C at 335 MPa (Hemley *et al.* 1977; Johnson *et al.* 1992) to enstatite (Ens) plus Qz plus H_2O by the reaction,

$$Mg_3Si_4O_{10}(OH)_{2\,(Talc)} = SiO_{2\,(Quartz)} + 3MgSiO_{3\,(Enstatite)} + H_2O$$

the solubility of the assemblage Cu–Cpr–Ens–Qz in 1 mol/kg Cl fluid was measured above 755 °C. Like the Tc-bearing assemblage, the redox potential and *p*H conditions of the fluid are buffered. Cu–Cpr define the redox conditions Equation [3.2], while Ens–Qz fix the fluid acidity through the equilibrium,

$$MgSiO_{3\,(Enstatite)} + 2H^+_{(aq)} = SiO_{2\,(Quartz)} + Mg^{2+}_{(aq)} + H_2O \qquad [3.25]$$

The results of this series of experiments are presented in Table 3.6 and Figure 3.13.

Table 3.6 Experimental details and dissolved element concentration measurements for Cu–Cpr–Tc–Qz and Cu–Cpr–Ens–Qz assemblages in 2 mol/kg Cl aqueous fluid from 524 to 850 °C at constant *P* (~ 335 MPa)

Run	R153	R156	R164	R157	R158	R179	R180
Mineral assemblage(5)	**Tc–Qz**	**Tc–Qz**	**Tc–Qz**	**Tc–Qz**	**Tc–Qz**	**Ens–Qz**	**Ens–Qz**
Temperature/ °C	**524**	**599**	**629**	**650**	**725**	**771**	**850**
1000/K	1.255	1.146	1.108	1.084	1.002	0.958	0.890
Pressure/ MPa	334 (3)	390 (7)	331 (6)	334 (3)	335 (6)	338 (6)	327 (12)
Duration (hours)	454	336	307	263	188	160	109
Mineral/Fluid	3.2	4.0	4.5	3.0	3.3	3.8	4.2
$m_{Cl}^{total(1)}$	2.117	1.929	2.132	1.926	1.926	0.998	0.998
$m_{Cu}^{total(2)}$	1.35	1.7	–	0.94	0.35	2.3	0.86
$\pm 95\%\ C.L._{Cu,\ mol/kg}^{LA-ICP-MS}$	0.19	0.65	–	0.24	0.09	1.0	0.18
$n_{Cu}^{LA-ICP-MS}$	43	13	–	12	19	8	25
$m_{Cu}^{total(3)}$	2.21	4.0	2.45	0.94	0.57	–	–
$\pm 95\%\ C.L._{Cu,\ mol/kg}^{PIXE}$	0.70	1.8	0.50	0.42	0.57	–	–
n_{Cu}^{PIXE}	4	9	4	6	2	–	–
$m_{Mg}^{total(4)}$	0.07818	0.028	0.0296	0.0210	0.00412	0.036	0.00444
$\pm 95\%\ C.L._{Mg,\ mol/kg}^{SN-ICP-AES}$	0.00079	0.011	0.0056	0.0025	0.00064	0.023	0.00047

Notes: Concentrations in molality (moles per kilogram of solvent). K is *T* in kelvin.

(1) to (4) *see Table 3.1 for details*

(5) All mineral assemblages also include Cu and Cpr.

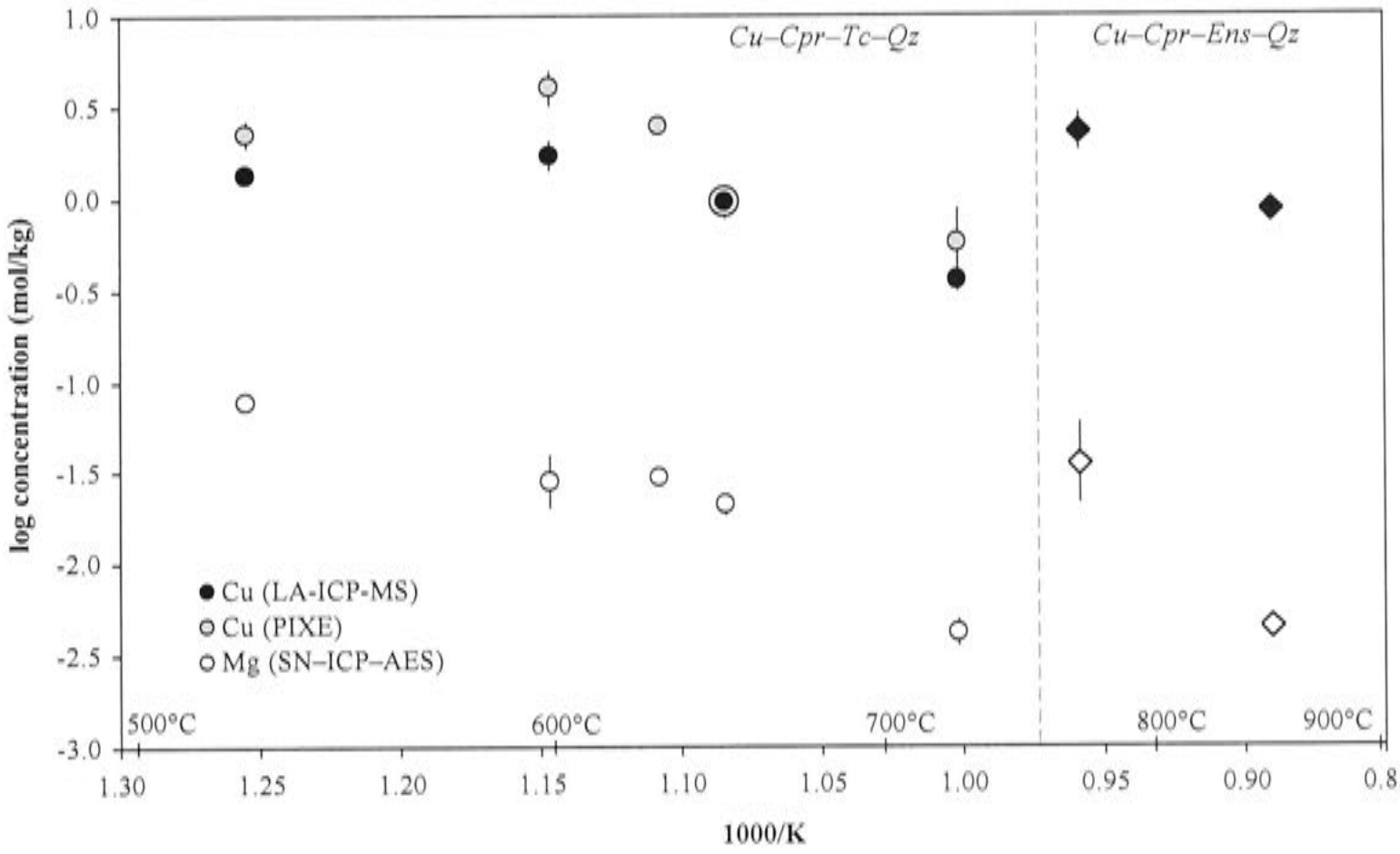

Figure 3.13 Solubility in the system Cu_2O–MgO–SiO_2–HCl–H_2O buffered by the assemblages Cu–Cpr–Tc–Qz (circles; 2 mol/kg total Cl) and Cu–Cpr–Ens–Qz (diamonds; 1 mol/kg total Cl) as a function of *T* (K) at constant *P* (~ 335 MPa). Concentrations, in log molal (mol/kg) units. Different analytical techniques indicated by shading, 95% *C.L.* shown where larger than the symbol. Independent LA-ICP-MS and PIXE Cu data at 650 °C (R157) are identical. Vertical dashed line separates Tc and Ens stability fields (755 °C, 335 MPa).

5.2 Data Interpretation

5.2.1 Cu–Mg–O–H–Cl speciation and solubility: Comparison with existing thermodynamic predictions

The experimental data were initially compared to the solubilities predicted by existing theory to gauge the extent of agreement. Predicted Cu–Cpr–Tc–Qz solubility was calculated using the method outlined in *PART 3, §4.2.1* and substituting equilibrium constants predicted from existing data for minerals (Helgeson *et al.* 1978), Mg–O–H–Cl species (Frantz and Marshall 1982; Shock *et al.* 1997) and Cu–Cl complexes (Liu 2001b). Equilibrium constants and relevant notes on the calculations are given in Table 3.7. The calculated solubilities in 2 mol/kg Cl fluid are compared with the experimental measurements in Figure 3.14.

Table 3.7 Extrapolated equilibrium constants (log *K*) from the literature* used to calculate Cu–Cpr–Tc–Qz solubility in aqueous fluid at 524 to 725 °C and 335 MPa (Figure 3.14)

Reaction	log *K* (calculated)				
T/ °C	524	599	629	650	725
1000/K	1.254	1.147	1.108	1.083	1.002
$1/3Mg_3Si_4O_{10}(OH)_{2\,(Talc)} + 2H^+_{(aq)} = 4/3SiO_{2\,(Quartz)} + Mg^{2+}_{(aq)} + 4/3H_2O_{(liq)}$	3.51	3.09	2.93	2.83	2.49
$Mg^{2+}_{(aq)} + Cl^-_{(aq)} = MgCl^+_{(aq)}$	2.63	3.62	4.01	4.28	5.21
$MgCl^+_{(aq)} + Cl^-_{(aq)} = MgCl^0_{2\,(aq)}$	1.36	1.96	2.20	2.358	2.91
$Mg^{2+}_{(aq)} + OH^-_{(aq)} = MgOH^+_{(aq)}$	5.40	6.00	6.25	6.42	7.05
$H^+_{(aq)} + Cl^-_{(aq)} = HCl^0_{(aq)}$	2.07	2.94	3.29	3.56	4.41
$H^+_{(aq)} + OH^-_{(aq)} = H_2O_{(liq)}$	9.85	10.0	10.1	10.2	10.5
$1/2Cu_2O_{(Cuprite)} + H^+_{(aq)} = Cu^+_{(aq)} + 1/2H_2O_{(liq)}$	1.89	2.12	2.20	2.26	2.44
$Cu^+_{(aq)} + Cl^-_{(aq)} = CuCl^0_{(aq)}$	3.50	3.67	3.76	3.82	4.07
$CuCl^0_{(aq)} + Cl^-_{(aq)} = CuCl^-_{2\,(aq)}$	0.96	0.98	0.99	1.00	1.04
$CuCl^-_{2\,(aq)} + Cl^-_{(aq)} = CuCl^{2-}_{3\,(aq)}$	-1.87	-1.88	-1.89	-1.89	-1.90
$CuCl^{2-}_{3\,(aq)} + Cl^-_{(aq)} = CuCl^{3-}_{4\,(aq)}$	-0.27	0.30	0.52	0.68	1.21

Notes: *Shock *et al.* (1997), Tagirov *et al.* (1997), Frantz and Marshall (1982), Liu (2001b), Helgeson *et al.* (1978).

All speciation calculations using the above data in the specified solubility model produce a minor convergence error at 2 mol/kg Cl. This means there is some uncertainty in the calculated solubilities, though they do appear to be sufficiently well constrained not to render them meaningless. (*N.B.* non-italised K refers to *T* in kelvin, whereas italised *K* refers to the equilibrium constant).

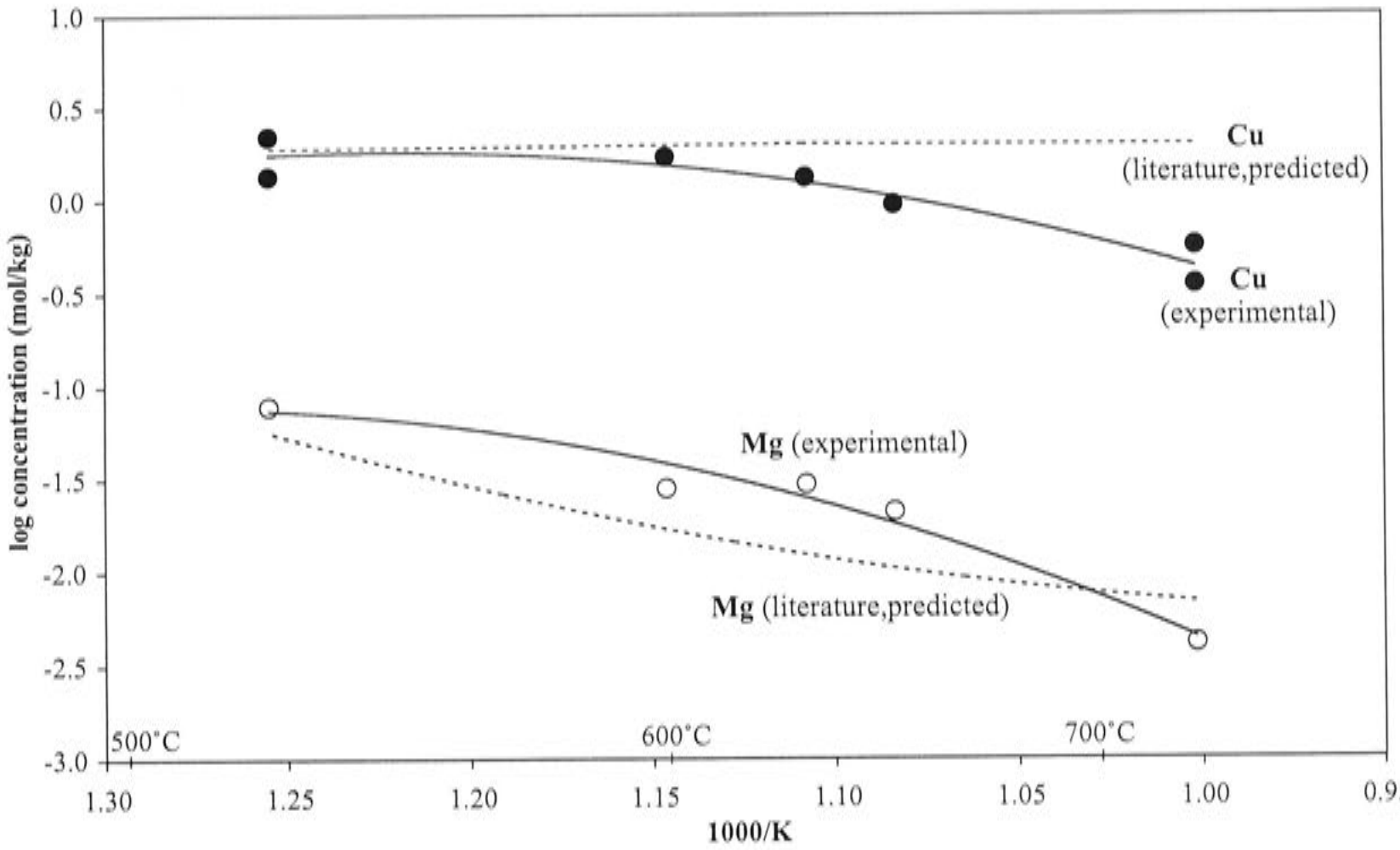

Figure 3.14 Predicted (dashed line) and experimental (continuous line) solubility trends of Cu–Cpr–Tc–Qz in aqueous fluid containing 2 mol/kg Cl as a function of inverse *T* (K) at 335 MPa. Experimental solubility is regressed from selected data (see *PART 3, § 5.2.2*).

There appears to be reasonable agreement between predicted and measured solubilities. However, comparison of the theoretical solubility with previous experimental data as a function of salinity agreed well only at 2 mol/kg Cl. Considering these calculations are also for 2 mol/kg Cl solutions, this may be fortuitous or, more likely, is an artefact related to the convergence error associated with these calculations. Nonetheless, existing models fail to predict the observed decline in Cu solubility with increasing *T* (*e.g.* Liu 2001b) at constant *P* and chloride concentration. The distribution of copper(I) species predicted using existing thermodynamic data (*e.g.* Liu 2001b) remains relatively constant over the *T* interval with $CuCl^0_{(aq)}$ occurring as the predominant species and higher-order complexes contributing negligibly to the overall solubility.

In general, ion association and complex formation is favoured by increasing *T* at constant *P* (Helgeson 1964; Oelkers and Helgeson 1990). This seems counter-intuitive, but the formation of new complexes usually results in an entropy gain related to a decrease in the total coordination number of the associated species due to the liberation of H_2O molecules from solvation shells (Helgeson 1964). Given that complex formation is likely to be favoured with increasing *T*, the deficiencies in the

literature models and the insights already made regarding higher-order complex formation at similar conditions, an alternate speciation analysis of the data was attempted.

5.2.2 Cu–Cpr–Tc–Qz solubility (I): Data selection and empirical regression

This isobaric series of experiments provides information on the solubility of the mineral assemblage and can also be regressed to determine the stability of the individual chlorocopper(I) complexes at each *T*.

PIXE and LA-ICP-MS analyses were obtained for the same fluid inclusions, allowing direct comparison of techniques. Although the PIXE and LA-ICP-MS results are similar in some instances, *e.g.* overlapping ± 1 σ uncertainties in the case of KCl-rich fluid inclusions (*e.g.* Figure 2.14), PIXE usually gives a significantly higher concentration than the corresponding mean LA-ICP-MS measurement (*i.e.* ± 2 σ uncertainties do not overlap) for these essentially CuCl–H_2O only fluid inclusions. This difference is almost certainly an analytical artefact related to the considerable and unavoidable uncertainties in the fluid inclusion model input parameters required for quantifying PIXE yields. The largest of these potential sources of PIXE error are: 1) the accuracy to which the bulk inclusion density can be estimated; and 2) the accuracy to which the average depth and to which a simple ellipsoid (based on a couple of axial width and length measurements) approximates the real three-dimensional geometry and position of the analysed inclusion. For estimating bulk inclusion densities *PVTX* for NaCl–H_2O fluids were used (as is the usual case, Heinrich *et al.* 1992). The extent to which this approximation is valid for these essentially CuCl–H_2O fluids is unknown but is no doubt somewhat in error. As for inclusion position and geometry, the amount of error associated with the measurements and the ellipsoid approximations can be substantial (*e.g.* for irregular shaped inclusions this may be > 50 %, for further discussion on inclusion volume measurement and associated uncertainties see, Bodnar 1983; Heinrich *et al.* 1992; Anderson and Bodnar 1993; Mavrogenes *et al.* 1995). These factors combine such that the PIXE data are not considered to be as accurate as LA-ICP-MS data that has been quantified using an accurately determined internal standard element, as is the case for these experiments.

In particular, there are several PIXE data (experiments: R153, R56, R164) that appear to be unreliable, presumably due to due to errors associated with input parameters for the PIXE inclusion model. Specifically, PIXE measurements that imply a fluid $m_{\mathrm{Cl}}^{total}/m_{\mathrm{Cu}}^{total}$ much less than 1 are probably erroneous as such "excess Cu" measurements are not consistent with the charge balance constraint on the fluid - the

concentration of Cl or other anionic components (*e.g.* $OH^-_{(aq)}$) are insufficient to balance the implied copper(I) dissolved in the fluid. In contrast, LA-ICP-MS measurements for the same inclusion populations yield reasonable bulk fluid compositions (*e.g.* $m_{Cl}^{total}/m_{Cu}^{total} > 1$), and so are generally considered more reliable. Therefore, anomalously high-Cu analyses by PIXE were excluded from empirical data regressions.

The previous series of experiments on the effect of salinity (*PART 3, §4*) overlaps the conditions of this isobaric series. These former experiments provide a reliable independent estimate of fluid composition and speciation at the coincident condition. The regressed concentrations for the *T* at which the PIXE results are anomalous (R164) was included in the empirical treatment of the *T*–*X* data.

The regressed empirical solubility for Cu–Cpr–Tc–Qz is shown in Figure 3.15. The fit regression parameters and the 2 mol/kg total Cl line are also given for reference.

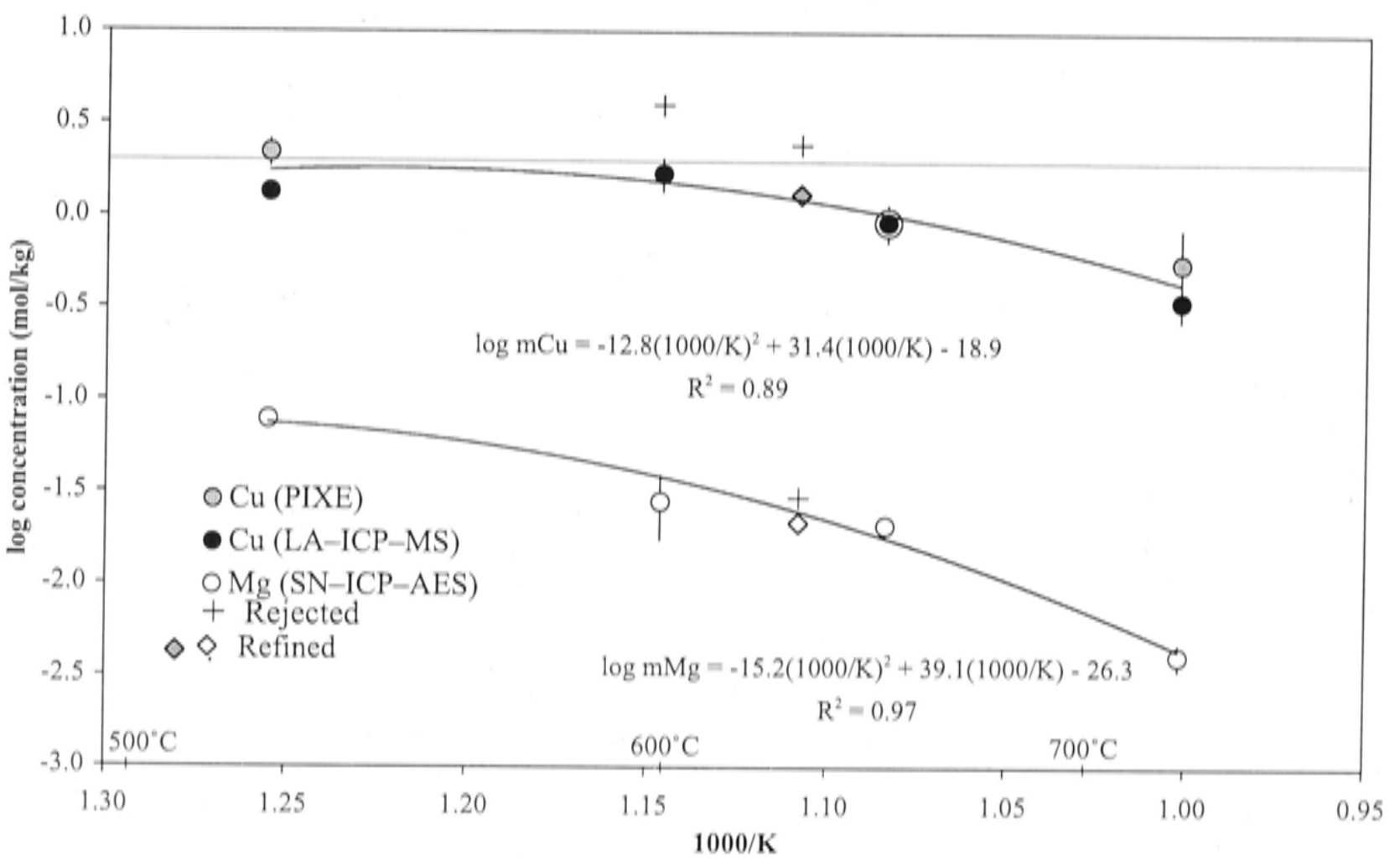

Figure 3.15 Regression of selected solubility data (PIXE and LA-ICP-MS; circles) for Cu–Cpr–Tc–Qz as a function of *T*. Selected ("refined") data were derived from the salinity series (diamonds). Concentrations in log molal (mol/kg) units, error bars indicate 95% *C.L.*, 2 mol/kg (total Cl concentration) plotted for comparison.

The independent estimate from the salinity series fits exactly on the trend of these experiments. Because this result provides an independent test of the quality of the isobaric series, these data are considered robust.

Having obtained empirical expressions describing the solubility measurements as a function of T, the experimental data were analysed within a thermodynamic framework to derive information regarding the copper(I) speciation and the relevant equilibrium constant data. The results are presented in the following section.

5.2.3 Cu–Cpr–Tc–Qz solubility (II): Speciation, derivation of equilibrium constants, and other thermodynamic properties as a function of temperature

The stabilities of the chlorocopper(I) complexes can be determined as a function of T, and other useful thermodynamic properties also derived, by regressing the isobaric data series within a thermodynamic framework that has some theoretical justification.

The equilibrium constant is related to the Gibbs free energy of a reaction ($\Delta_r G^\circ$) by,

$$\Delta_r G^\circ = -RT\ln K, \quad \text{(alternatively } \Delta_r G^\circ = -2.303RT\log K) \qquad [3.26]$$

Here, T refers to the temperature in kelvin (K) and R is the gas constant. The standard state enthalpy ($\Delta_r H^\circ$) and entropy ($\Delta_r S^\circ$) are related to $\Delta_r G^\circ$ through,

$$\Delta_r G^\circ = \Delta_r H^\circ - T\Delta_r S^\circ \qquad [3.27]$$

hence, substitution and rearrangement of Equations [3.26] and [3.27] gives,

$$\ln K = -\frac{\Delta_r H^\circ}{RT} + \frac{\Delta_r S^\circ}{R} \qquad [3.28]$$

Equation [3.28] may be rewritten,

$$\ln K = \frac{A}{T} + B \qquad [3.29]$$

Implicit in this expression is that $\Delta_r S^\circ$ and $\Delta_r H^\circ$ are independent of T, which is equivalent to assuming that the heat capacity terms for products and reactants cancel ($\Delta_r C_P = 0$). This assumption can be erroneous under some conditions (Nordstrom and Munoz 1994). Lindsay (1980), however, noticed that for reactions arranged with an isocoulombic form, *i.e.* equal numbers of like-charged reactants and products, the heat

capacity change of the reaction is constant and close to zero. The underlying reason for such an observation is thought to be that species with the same charge respond similarly to changes in T. According, the isobaric data series was regressed assuming that the equilibrium constants for the formation of neutral chlorocopper(I) complexes (provided reaction are represented appropriately) have a linear dependence on T (*i.e.* it is assumed the relation given by Equation [3.29] applies).

Because the $m_{Cu}^{total} : m_{Cl}^{total}$ of the fluid increases above 1:4 at the highest T, the isobaric Cu–Cpr–Tc–Qz solubility experiments were interpreted using model 4 (*i.e.* Cu^+ and $CuCl(HCl)^0_{n-1\,(aq)}$, where n = 1, 2, 3 and 4). The chlorocopper(I) complex forming reactions considered and regression results are given in Table 3.8, footnotes to this table give further details and assumptions relevant to the regression. Preliminary calculations indicated that the data could not be explained by a more conventional speciation. Furthermore, this is consistent with the behaviour identified by this study at similar P–T–X conditions. Regression results for log equilibrium constants for individual complex forming reactions are plotted in Figure 3.16 as is, for comparison, the data obtained from varying salinity experiments at 629 °C, 334 MPa.

Table 3.8 Formation constants for $CuCl(HCl)^0_{n-1}$ complexes obtained (and the residual to log$K$ fitting) from regression of isobaric (335 MPa) mineral solubility experiments as a function of T (524 to 725 °C) and assuming a linear dependence (Equation [3.29]).

			$\log K_n^{T,335MPa}$				
		T/ °C	524	599	629	650	725
n	Reaction	1000/K	1.254	1.147	1.108	1.083	1.002
	Model 4						
1	$Cu^+_{(aq)} + Cl^-_{(aq)} = CuCl^0_{(aq)}$		3.14	2.76	3.08	3.01	2.31
2	$CuCl^0_{(aq)} + HCl^0_{(aq)} = CuCl(HCl)^0_{(aq)}$		1.84	2.02	2.09	2.13	2.27
3	$CuCl^0_{(aq)} + 2HCl^0_{(aq)} = CuCl(HCl)^0_{2\,(aq)}$		1.26	1.99	2.25	2.42	2.97
4	$CuCl^0_{(aq)} + 3HCl^0_{(aq)} = CuCl(HCl)^0_{3\,(aq)}$		2.62	4.84	5.62	6.14	7.81
		$S^2_{Residual}$	0.0001	0.0018	0.0000	0.0004	0.0045

Notes: *Model 4*. Simultaneously and for each experiment T the concentration of complexes $\left(CuCl(HCl)^0_{n-1\,(aq)}\right)$ n = 1 to 4 were varied independently until the least squares solubility for the measured dissolved element concentrations was fitted; ion properties were determined using the equilibrium constant for n = 0 (*i.e.* $1/2Cu_2O_{(Cuprite)} + H^+_{(aq)} = Cu^+_{(aq)} + 1/2H_2O_{(liq)}$) calculated using the data of Shock *et al.* (1997) and Helgeson *et al.* (1978). It was also assumed in the regression that the stepwise formation of higher-order complexes was preferred with increasing T. Log equilibrium constants used to constrain the speciation are given in Table 3.7, concentrations for mass balance constraints are given in Table 3.6.

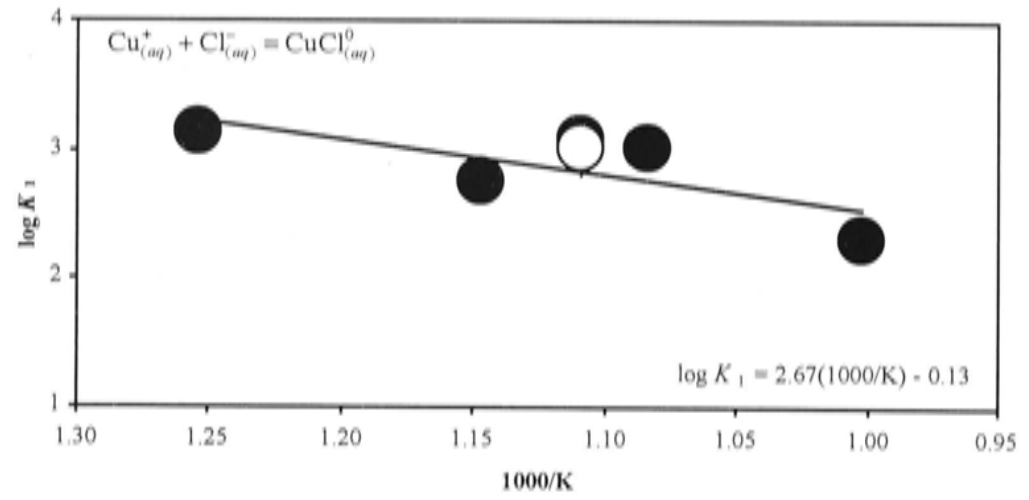

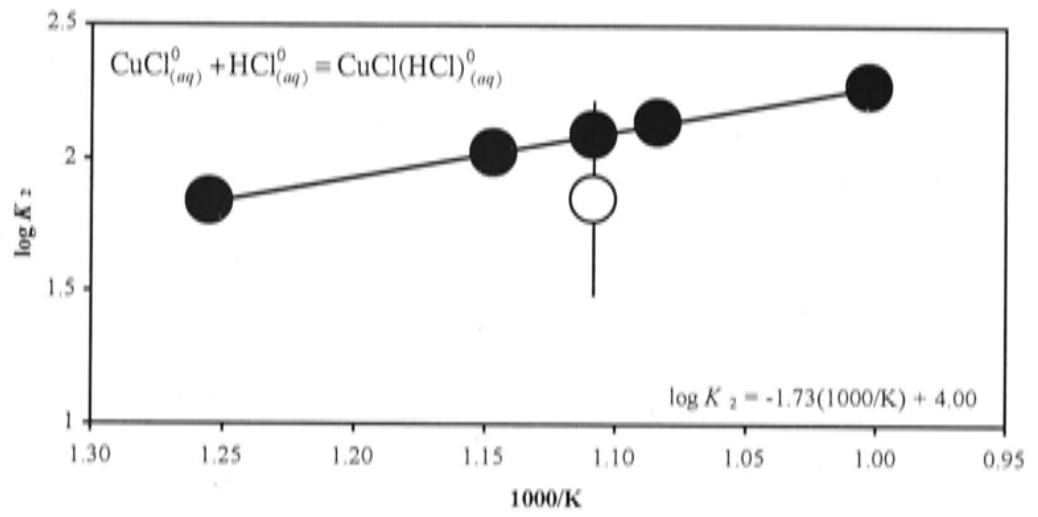

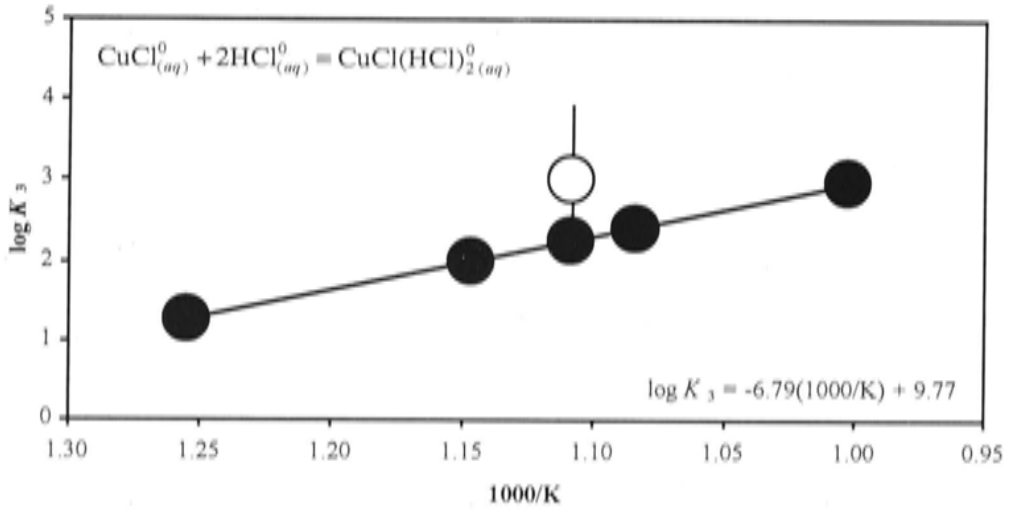

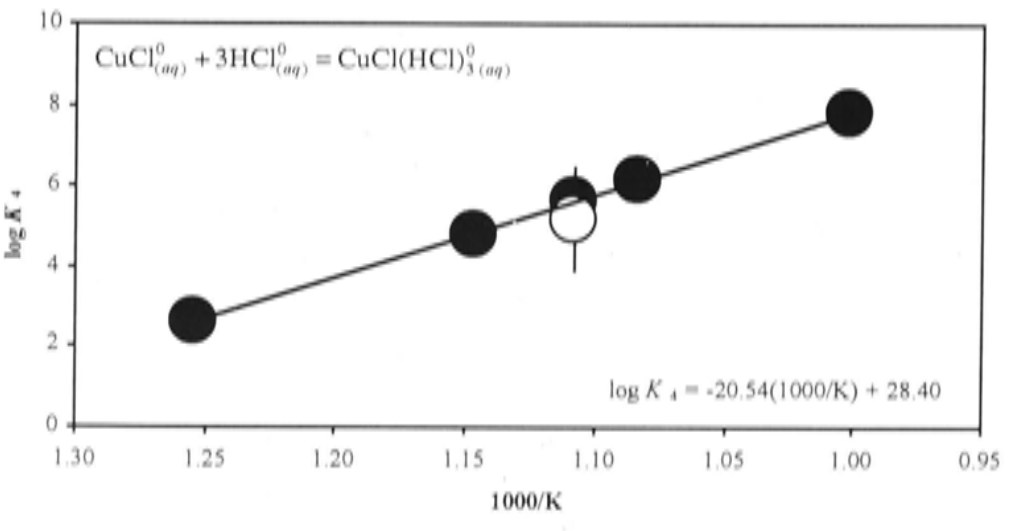

Figure 3.16 Log equilibrium constants for chlorocopper(I) complex forming reactions as a function of T (K) from regression of the isobaric data series (335 MPa; filled circles) and comparison with data obtained from the varying salinity experiments at 629 °C, 334 MPa (uncertainties are ± 1 σ; open circles) (open circles). Reactions and linear least squares fit (line) and equation parameters are specified on their respective plot.

The misfit of the regression is minor as indicated by $S^2_{Residual}$ values (Table 3.8) but does suggests that additional higher-order species may be present (*e.g.* > ~725 °C the fluid $m_{Cu}^{total}/m_{Cl}^{total}$ > 1:4, which exceeds the highest-coordinated chlorocopper(I) complex considered) and/or the assumption of unit value activity coefficients for neutral species is not valid.

It will be noted that the neutral chlorocopper(I) complex forming reactions were not arranged in a strictly isocoulombic form, as equal numbers of species must also occur on both sides of the reaction. Nonetheless, the regressions can be considered to yield at least a first approximation of the reaction properties, and in any case provides a reference position to test against with future data. A more complex fit is not justified given the sparsity of measurements and further assumptions that would be required.

From the derivation of Equation [3.29] it can seen (Equation [3.28]) that the enthalpy and entropy change of each neutral chlorocopper(I) complex forming reaction can also be obtained. Table 3.9 gives the enthalpy and entropy of reaction derived from the linear least squares regression of the equilibrium constants fitted to the isobaric data series.

Table 3.9 Changes in enthalpy ($\Delta_r H^\circ$) and entropy ($\Delta_r S^\circ$) for $CuCl(HCl)^0_{n-1}$ complex forming reactions (where, $\Delta_r C_P$ = 0) determined from isobaric (335 MPa) mineral solubility experiments from 524 to 725 °C

Reaction	$\Delta_r H^\circ$ (kJ/mol)	$\Delta_r S^\circ$ (J/K/mol)
$Cu^+_{(aq)} + Cl^-_{(aq)} = CuCl^0_{(aq)}$	-51 (±28)	-3 (±30)
$CuCl^0_{(aq)} + HCl^0_{(aq)} = CuCl(HCl)^0_{(aq)}$	+33	+76
$CuCl^0_{(aq)} + 2HCl^0_{(aq)} = CuCl(HCl)^0_{2(aq)}$	+130	+187
$CuCl^0_{(aq)} + 3HCl^0_{(aq)} = CuCl(HCl)^0_{3(aq)}$	+393	+544

The experimental and calculated solubility determined using regressed parameters for Equation [3.28] for Cu–Cpr–Tc–Qz from 500 to 750 °C at 335 MPa in a Cl-bearing (2 mol/kg) supercritical fluid, is illustrated in Figure 3.17. The equilibrium Cu–H–Cl speciation calculated for this fluid is shown in Figure 3.18.

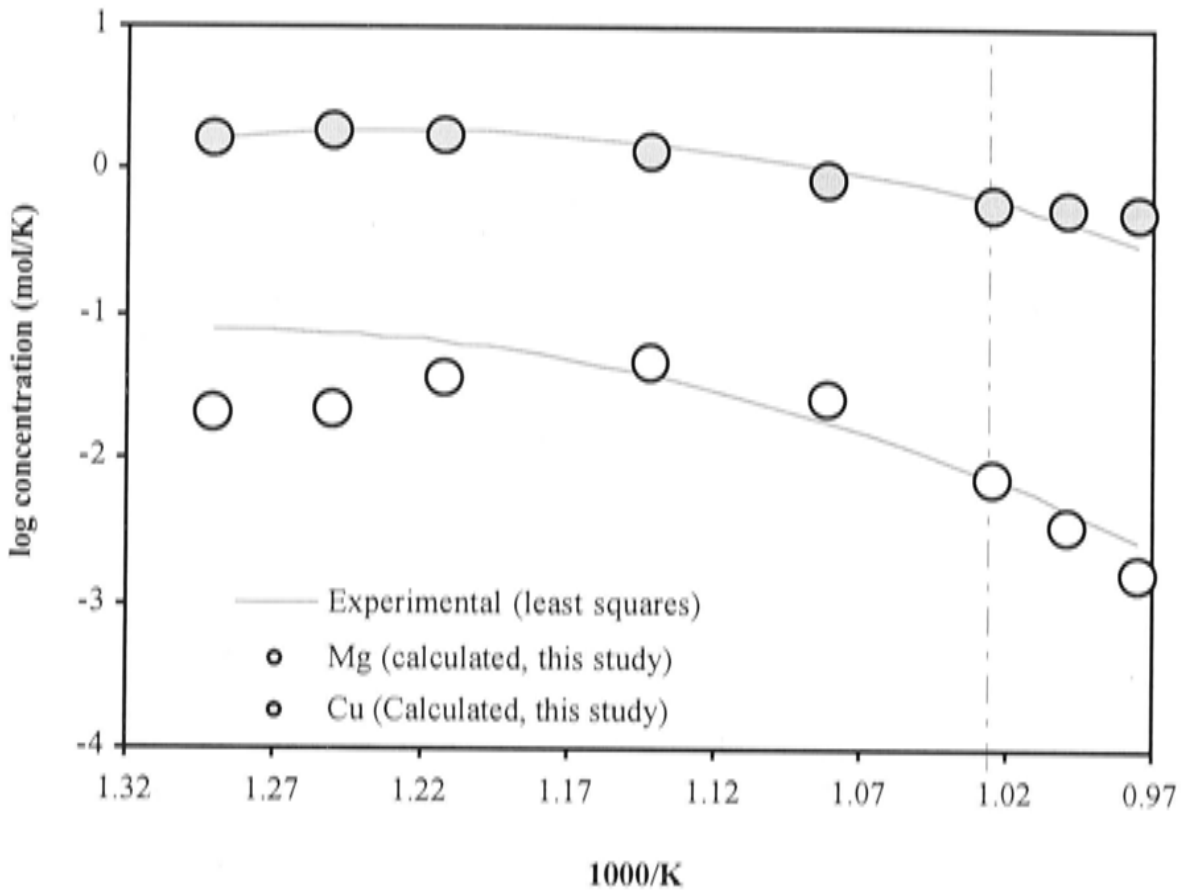

Figure 3.17 Comparison of the experimental and predicted solubility of Cu–Cpr–Tc–Qz from 500 to 750 °C at 335 MPa in 2 mol/kg Cl aqueous fluid using the data of this study. The high-*T* side of the plot terminates at 755 °C (= Tc dehydration). Vertical dashed line denotes the *T* at which the $m_{Cu}^{total}/m_{Cl}^{total}$ of the fluid is 1:4 (*i.e.* equal to the stoichiometry of the highest chlorocopper(I) complex in the model).

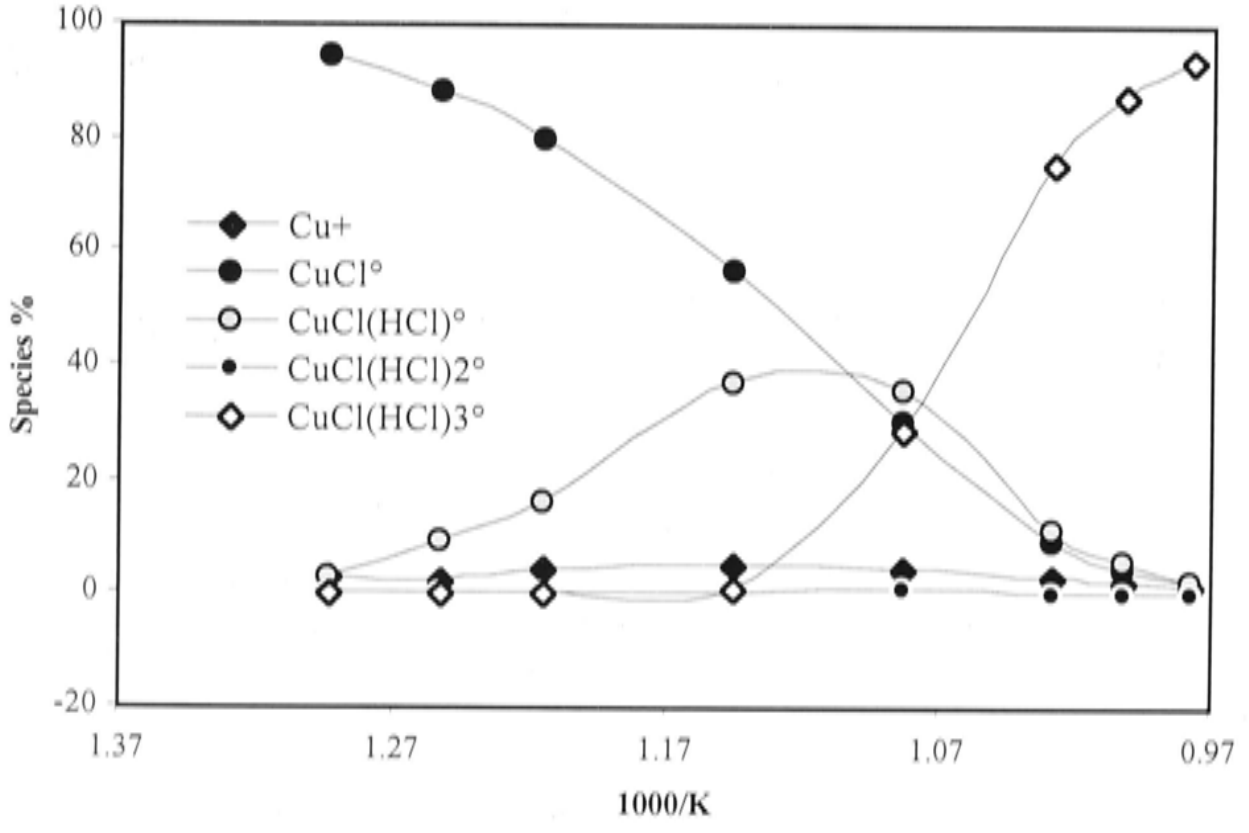

Figure 3.18 Distribution of copper(I) species calculated for a fluid containing 2 mol/kg Cl in equilibrium with Cu–Cpr–Tc–Qz from 500 to 750 °C at 335 MPa. Points correlate with calculated solubility points on Figure 3.17. Other features as described for Figure 3.17.

It has been shown that dissolved element concentrations observed for the isobaric series of experiments can be explained by the prevalence of neutral $CuCl(HCl)^{0}_{n-1\ (aq)}$ type complexes with increasing T at constant P and salinity.

Although the data has been interpreted in terms of neutral chlorocopper(I) complexes, $a-X$ relations for such species are poorly known, and the arbitrary assignment of an ideal solution model is possibly inadequate. Recognising this, a key feature of the experimental data, independent of interpretation of speciation interpretations, is the apparent increase in the stability of the HCl component with increasing T, be it involved in complex formation or otherwise, in these supercritical high-P fluids.

5.2.4 Cu–Cpr–Ens–Qz solubility: Limitations imposed by analytical uncertainty and comparison with extrapolated equilibrium constants obtained from this study

Above the *T*–*P* stability of Tc, Cu–Cpr–Ens–Qz solubility in aqueous fluid containing 1 mol/kg total Cl was determined (Figure 3.13). It is desirable to extract fluid speciation details from these experiments and combine them with the Tc-assemblage results. However, unlike the previous experimental series, empirical regression cannot be employed to more robustly constrain the solubility, as too few data were collected.

In the absence of more comprehensive data, the question becomes, can the Cu–Cpr–Ens–Qz experimental data be considered to give the correct general trend and magnitude of solubility and thus provide a preliminary opportunity to test the extrapolation reliability of the new copper(I) species data?

Ignoring the difference in Cl concentration between the Tc- and Ens-bearing experiments, the apparent rapid increase in Cu and Mg solubility across the Tc dehydration boundary, implied primarily by R179 (771°C), is erroneous. A discontinuity (not just a break in slope) in the solubility curve across the Tc–Ens transition is inconsistent with thermodynamic equilibrium, as the assemblage Tc–Ens–Qz–H_2O is isothermally and isobarically invariant, *i.e.* the fluid composition is fixed by the coexistence of all three minerals (Figure 3.19). The break is most clearly indicated by Mg. Although Cl varies between Tc (2 mol/kg) and Ens (1 mol/kg) experiments, potentially explaining the anomaly, experimental solubilities do not positively correlate with Cl (which could be expected to a first order). Accordingly, it is concluded that R179 is unreliable and should be rejected. The cause of its aberrance is uncertain but is thought to be due to Mg contamination (Ens?) of the quench solution during sampling. This may also explain the large uncertainty on the Mg measurement and unacceptable mean fluid $m_{\mathrm{Cu}}^{total} : m_{\mathrm{Cl}}^{total}$ of ~ 2.3:1, as quench concentration Mg is used to quantify Cu. Although the absolute concentrations are in error, the Cu/Mg ratio (measured by LA-ICP-MS) of R179 should be reliable.

The Cu and Mg solubilities reported for R180 (850 °C) are considered reliable, as reasons to the contrary are not obvious.

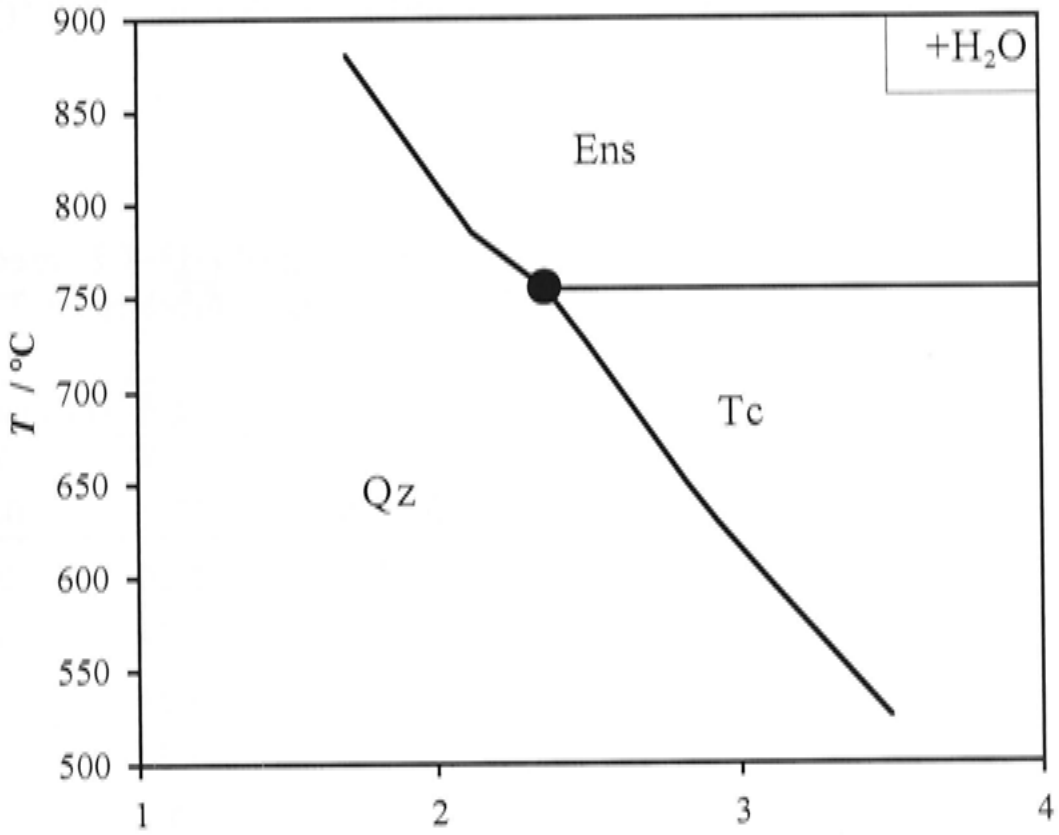

Figure 3.19 Calculated mineral stability fields in a portion of the system $MgO–SiO_2–H_2O$ and their equilibrium (or *p*H buffering) relation with the fluid at 335 MPa, as used to interpret the data of this study. The isothermal-isobaric invariant point is indicted (circle).

The experimental mineral solubility and that predicted from the Tc-assemblage data of this study for 1 mol/kg Cl (total) fluid is plotted in Figure 3.20. Equilibrium constants for the Mg–O–H–Cl species, predicted from existing data in the literature for 770 and 850 °C at 335 MPa, are given in Table 3.10. In the Tc stability field the Cu solubility predicted by this study mimics the general trend of the experimental data measured in 2 mol/kg Cl up to the Tc dehydration *T*, without the distinct Cu plateau (*cf.* Figure 3.17). This is because the predicted $m_{Cu}^{total} : m_{Cl}^{total}$ of the fluid remains < 1:4 up to at least 725 °C. However, above the Tc–Ens transition, predicted solubilities are clearly limited by the stoichiometry of the chlorocopper(I) (and possibly Mg) complexes considered (Figure 3.21).

The reliability of the solubility calculation in the Tc field at 1 mol/kg total can be independently assessed using data from the salinity series (629 °C) and a single measurement at 710 °C from the *P* series at 1 mol/kg total (Figure 3.21; *PART 3, §6*). The calculated solubility is in very good agreement with the salinity series data, however, at 710 °C the experimental solubility is slightly higher. For Cu, this discrepancy may be analytical, as the concentration is higher than that expected for a fluid containing 2 mol/kg Cl at the same conditions (*cf.* Figure 3.15). The experimental data for Mg is consistent with the other empirical trends, so rather it is ability of this

simple speciation model to correctly predict solubilities above ~ 700 °C that is in doubt (*e.g.* Figure 3.15).

Table 3.10 Extrapolated equilibrium constants for Mg–H–O–Cl speciation from the literature* used to calculate Cu–Cpr–Ens–Qz solubility at 770 and 850 °C at 335 MPa (Figure 3.20)

Reaction	log *K* (calculated)	
T/ °C	770	850
1000/K	0.959	0.890
$MgSiO_{3\,(Enstatite)} + 2H^+_{(aq)} = SiO_{2\,(Quartz)} + Mg^{2+}_{(aq)} + H_2O_{(liq)}$	2.20	2.03
$Mg^{2+}_{(aq)} + Cl^-_{(aq)} = MgCl^+_{(aq)}$	5.74	6.64
$MgCl^+_{(aq)} + Cl^-_{(aq)} = MgCl^0_{2\,(aq)}$	3.23	3.76
$Mg^{2+}_{(aq)} + OH^-_{(aq)} = MgOH^+_{(aq)}$	7.44	8.11
$H^+_{(aq)} + OH^-_{(aq)} = H_2O_{(liq)}$	10.7	11.0
$H^+_{(aq)} + Cl^-_{(aq)} = HCl^0_{(aq)}$	4.93	5.83
$1/2Cu_2O_{(Cuprite)} + H^+_{(aq)} = Cu^+_{(aq)} + 1/2H_2O_{(liq)}$	2.54	2.70

Notes: *Shock *et al.* 1997, Helgeson *et al* .1978, Tagirov *et al.* 1997, Frantz and Marshall 1982; see Table 3.2 for further reference details. Required chlorocopper(I) speciation data from (*this study*) given in Table 3.9.

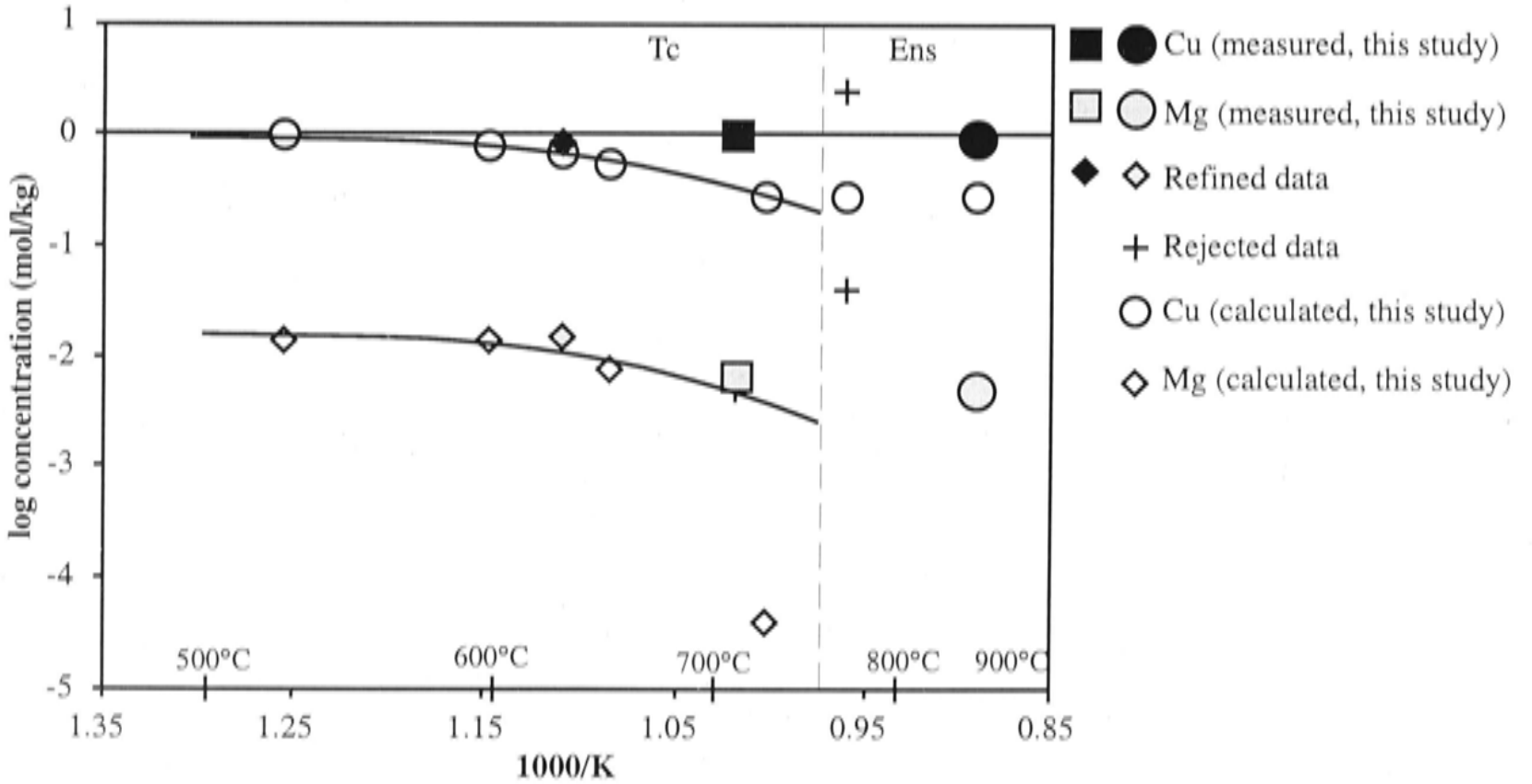

Figure 3.20 Comparison of experimental and calculated solubilities (using chlorocopper(I) data from this study; Table 3.9) in 1 mol/kg total Cl for Cu–Cpr–Qz–(Tc±Ens) at 500 to 850 °C at 335 MPa. Dashed line separates Tc and Ens stability fields. Measured solubilities are circles above the transition and squares below. Coincident *P* series data (squares) and refined data taken from the salinity series (shaded diamonds), both 1 mol/kg Cl, plotted for comparison with the predicted solubility in the Tc field. Solid line through predicted Mg is approximate, indicating the general trend as suggested by the available measurements at 1 mol/kg total Cl, which is also shown for reference. Experimental 95% *C.L.* plotted, but may be smaller than the size of the symbol. Calculated Mg in the Ens stability field is not shown as it grossly underestimates the experimental data, *i.e.* $\log m\mathrm{Mg}^{this\ study}_{calculated}$ = -6.0 and -8.3 at 770 and 850 °C respectively.

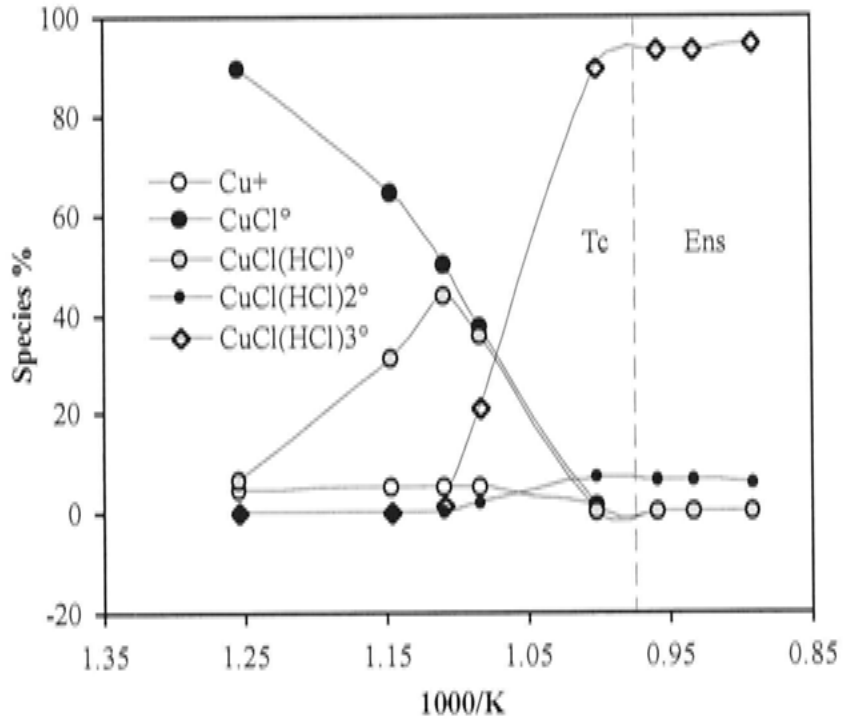

Figure 3.21 The distribution of chlorocopper(I) species in 1 mol/kg Cl aqueous fluid from 500 to 850 °C at 335 MPa buffered by Cu–Cpr–Qz–(Tc±Ens). The calculation utilised Cu–H–Cl species properties derived in this study. Solubility details are presented in the previous Figure (3.20).

Despite the shortcomings of the calculations, the experimental data indicate a change in the solubility trend at the breakdown of Tc. A change is expected because of the difference in the T-dependant properties of Ens relative to Tc, and hence the T dependence of the acidity buffering reactions, *i.e.* $\partial \log\left(a_{Mg^{2+}} / a_{H^+}{}^2\right) / \partial T$. Because the relative slopes of the Tc–Qz and Ens–Qz buffers are similar, the change in solubility trend should not be large (Figure 3.19). Whether this is sufficient to explain the slight inflection to prograde solubility implied by the experimental data remains to be demonstrated.

6. Mineral solubility: Effect of pressure to 1.7 GPa

6.1 Experimental data

Synthetic fluid inclusions were employed to determine the solubility of the assemblage Cu–Cpr–Tc–Qz from 0.3 to 1.7 GPa at 710 °C. Fluid salinity in this isothermal series of experiments was kept constant at 1 mol/kg total Cl, except for a single experiment which contained no Cl. These data, given in Table 3.11 and Figure 3.22, represent the first multi-component solubility measurements for a complex mineral assemblage to upper mantle *P–T* conditions.

Table 3.11 Experimental details and dissolved element concentration measurements for the Cu–Cpr–Tc–Qz assemblage as a function of pressure at 710 °C in 1 mol/kg total Cl and Cl-free aqueous fluid

Run	R183	R171	R172	R174	R189*
Temperature/ °C	710	710	710	710	710
Pressure/ GPa	**0.313** (0.014)	**0.662** (0.005)	**0.991** (0.003)	**1.703** (0.007)	**1.494** (0.012)
Duration (hours)	138	235	168	158	146
Mineral/Fluid	2.2	2.4	2.2	3.1	4.8
$m_{Cl}^{total(1)}$	0.998	0.998	0.998	0.998	–
$m_{Cu}^{total(2)}$	0.89	1.26	2.2	3.7	0.0753
$\pm 95\%\ C.L.\ {}^{LA-ICP-MS}_{Cu,\ mol/kg}$	0.14	0.34	0.76	0.62	0.0090
$n_{Cu}^{LA-ICP-MS}$	54	13	8	49	24
$m_{Cu}^{total(3)}$	–	1.5	–	–	–
$\pm 95\%\ C.L.\ {}^{PIXE}_{Cu,\ mol/kg}$	–	1.0	–	–	–
n_{Cu}^{PIXE}	–	7	–	–	–
$m_{Mg}^{total(4)}$	0.0060	0.01720	0.142	0.205	0.0060
$\pm 95\%\ C.L.\ {}^{SN-ICP-AES}_{Mg,\ mol/kg}$	0.0023	0.00052	0.058	0.012	–

Notes: Concentrations in molality (moles per kilogram of solvent).
* R189 contains no Cl
(1) to (4), see Table 3.1 for details.

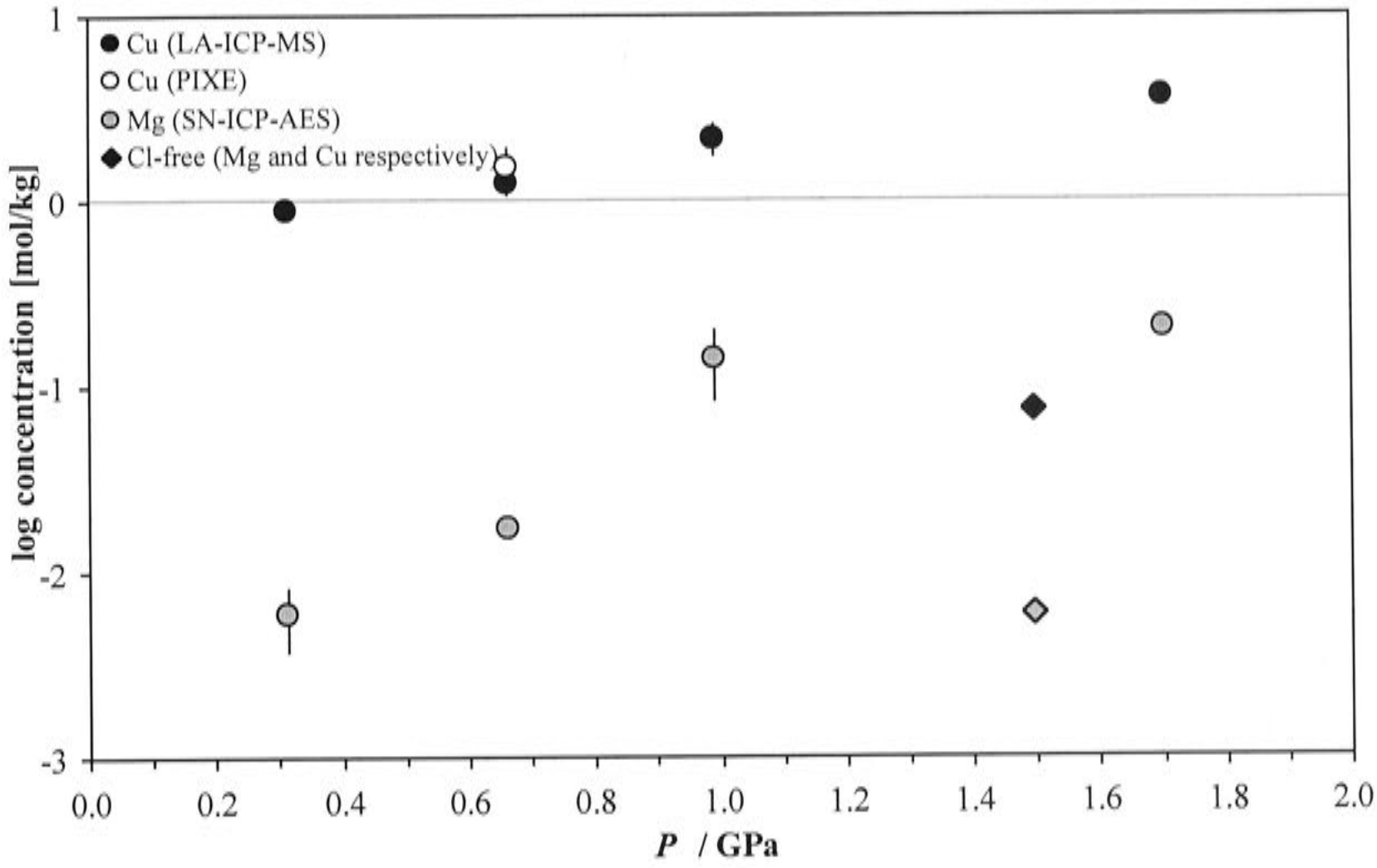

Figure 3.22 Solubility (mol/kg) of the Cu–Cpr–Tc–Qz assemblage as a function of *P* (GPa) in aqueous fluid. Analytical technique used to acquire the individual data is indicated. Error bars indicate the 95% confidence interval for the mean.

A single Cl-free fluid inclusion synthesis experiment was undertaken at 710 °C, 1.5 GPa buffered by Cu–Cpr–Tc–Qz (R189). Fluid inclusions from this Cl-free experiment are petrographically distinct; they do not contain a conspicuous tetrahedral daughter mineral (Figure 3.2). By inference, the tetrahedral daughter mineral in all Cl-bearing experiments is a copper(I) halide, its occurrence and morphology are consistent with it being nantokite (CuCl).

6.2 Data Interpretation

6.2.1 Cu–Mg–O–H–Cl speciation and solubility: Comparison with and limitations of existing thermodynamic models

Extrapolation using the HFK model to high P–T is limited by knowledge of the dielectric constant of water (ε), for which experimental measurements exist only to 0.5 GPa (Heger *et al.* 1980). Although, there is evidence suggesting simulated values of ε for pure H_2O can be used to extend the HKF approach to at least 2.0 GPa (*e.g.* Wasserman *et al.* 1995), the appropriate EOS parameters are not available for most species (in fact, only $SiO^0_{2\,(aq)}$). Furthermore, the general reliability of such calculations is yet to be verified experimentally. Accordingly, HKF-type extrapolation is restricted to 0.5 GPa and 1000 °C (Johnson *et al.* 1992).

Cu–Cpr–Tc–Qz solubility in 1 mol/kg aqueous fluid was predicted to 0.5 GPa at 710 °C using the same data as for comparisons of previous experimental series (Helgeson *et al.* 1978`; Frantz and Marshall 1982; Liu 2001b; Shock *et al.* 1997). The equilibrium constants used in the calculations are given in Table 3.12. The experimental and predicted solubilities are plotted for comparison in Figure 3.24.

Table 3.12 Literature data* used to calculate Cu–Cpr–Tc–Qz solubility in 1 mol/kg Cl aqueous fluid at 710 °C and 0.2 to 0.5 GPa

Reaction	log K (calculated)			
P / GPa	0.2	0.3	0.4	0.5
$1/3Mg_3Si_4O_{10}(OH)_{2\,(Talc)} + 2H^+_{(aq)}$				
$= 4/3SiO_{2\,(Quartz)} + Mg^{2+}_{(aq)} + 4/3H_2O_{(liq)}$	2.43	2.49	2.70	2.87
$Mg^{2+}_{(aq)} + Cl^-_{(aq)} = MgCl^+_{(aq)}$	7.24	5.43	4.42	3.73
$MgCl^+_{(aq)} + Cl^-_{(aq)} = MgCl^0_{2\,(aq)}$	4.03	3.03	2.47	2.09
$H^+_{(aq)} + Cl^-_{(aq)} = HCl^0_{(aq)}$	5.43	4.48	3.85	3.37
$1/2Cu_2O_{(Cuprite)} + H^+_{(aq)} = Cu^+_{(aq)} + 1/2H_2O_{(liq)}$	2.29	2.38	2.46	2.52
$Cu^+_{(aq)} + Cl^-_{(aq)} = CuCl^0_{(aq)}$	5.13	4.23	3.70	3.35
$CuCl^0_{(aq)} + Cl^-_{(aq)} = CuCl^-_{2\,(aq)}$	1.13	1.07	0.95	0.84
$CuCl^-_{2\,(aq)} + Cl^-_{(aq)} = CuCl^{2-}_{3\,(aq)}$	-2.47	-1.96	-1.84	-1.81
$CuCl^{2-}_{3\,(aq)} + Cl^-_{(aq)} = CuCl^{3-}_{4\,(aq)}$	0.26	1.00	1.21	1.28

Notes: * Shock *et al.* (1997), Tagirov *et al.* (1997), Frantz and Marshall (1982), Liu (2001b), Helgeson *et al.* (1978).

At 1 mol/kg Cl, all speciation calculations converged to a satisfactory solution; all mass action, mass balance and neutrality constraints were satisfied.

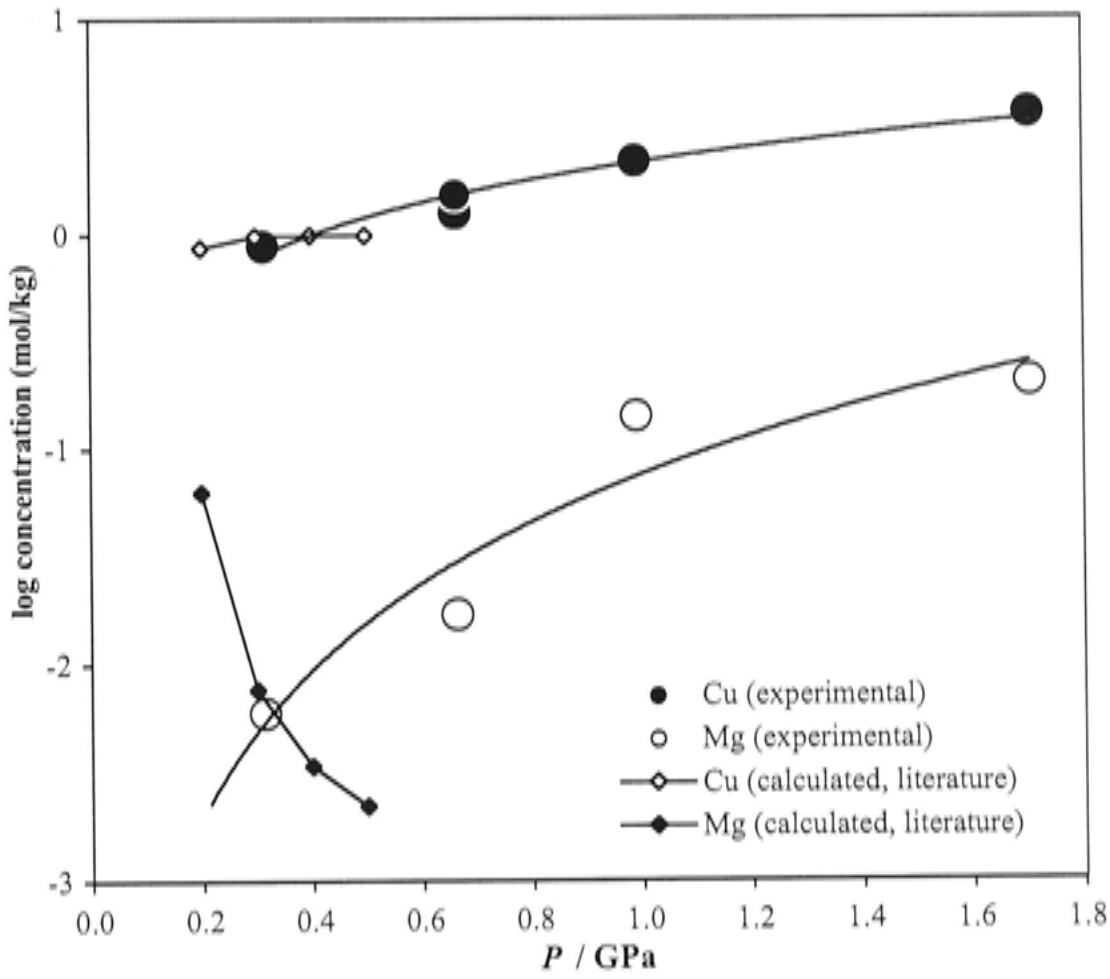

Figure 3.24 Comparison of the experimental Mg and Cu concentrations and that predicted using existing thermodynamic properties as a function of *P* at 710 °C and 1 mol/kg total chloride buffered by the assemblage Cu–Cpr–Tc–Qz. Refer to text for details.

At constant *T*, ionisation constants for aqueous species are usually linearly correlated with the logarithm of H_2O density over a range of *P* (*e.g.* Franck 1956, 1961; Quist 1970; Marshall and Quist 1967; Marshall 1970, 1972; Sweeton *et al.* 1974; Marshall and Franck 1981; Marshall and Mesmer 1984; Mesmer *et al.* 1988, 1989; Anderson *et al.* 1991). Although this simple relation could be utilised to extrapolate the existing thermodynamic data approximately to the *P* of these experiments, it is clear from Figure 3.24 that the existing solubility model does not predict the observed *P* dependence. Seemingly, the agreement at 0.3 MPa is largely fortuitous.

The possible uncertainty in the literature data is considered to be insufficient to significantly alter the copper(I) speciation interpretation already presented. Furthermore, it is argued, that it is the behaviour of Mg, a minor component, that is sensitive to the speciation of the major component, Cu. The failure of the theoretical model implies there is a significant gap in our current understanding of mineral solubility as function of *P*.

6.2.2 Mineral solubility and speciation in supercritical aqueous fluid at very high-pressure

Given the possible uncertainty in the literature data apparent below 0.5 GPa, there seems little point in pursuing the interpretation of copper(I) speciation to higher P in the same detailed manner as for the previous experimental series. Nonetheless the solubility data may be treated with a more general approach to derive speciation trends to high-P.

The most conspicuous feature of the isothermal data is the occurrence with increasing P (> ~ 0.5 GPa) of molal Cu concentrations exceeding those of Cl. In the previous experimental series individual analyses indicating $m_{\mathrm{Cl}}^{total}/m_{\mathrm{Cu}}^{total} < 1$ were rejected as anomalous, however, these were isolated data which were inconsistent with the general solubility trend. Whereas, in the isothermal P series there is no reason to suspect analytical or experimental error being responsible, as the observed $m_{\mathrm{Cl}}^{total}/m_{\mathrm{Cu}}^{total} < 1$ trend is systematic. Accepting the data, it is clear that chlorocopper(I) complexing alone cannot produce the observed mineral solubilities and, correspondingly, cannot be the predominant dissolution mechanism in these high-P experiments.

The only other mineral solubility data available at similar P–T conditions is for silica (see *PART 1*). Qz dissolves congruently in otherwise pure H_2O via the formation of hydroxysilica complexes, suggesting H_2O is a ligand of potential importance for other rock-forming minerals dissolved in high-P supercritical fluids. Although dissolved silica could not be measured in these experiments, because they are Qz-saturated, existing Qz solubility data are directly applicable (*e.g.* Manning 1994); while recalling the possible uncertainty in $a-X$ relations at these P–T conditions (*PART 1*). Accordingly, the isothermal solubility trends of Cu, Mg and silica are shown in Figure 3.25 for comparison. The general similarity in mineral solubility patterns is unmistakable and suggests a switch from chloride-dominated copper(I) complexing at low-P (< ~ 0.5 GPa) to hydroxide species with increasing P.

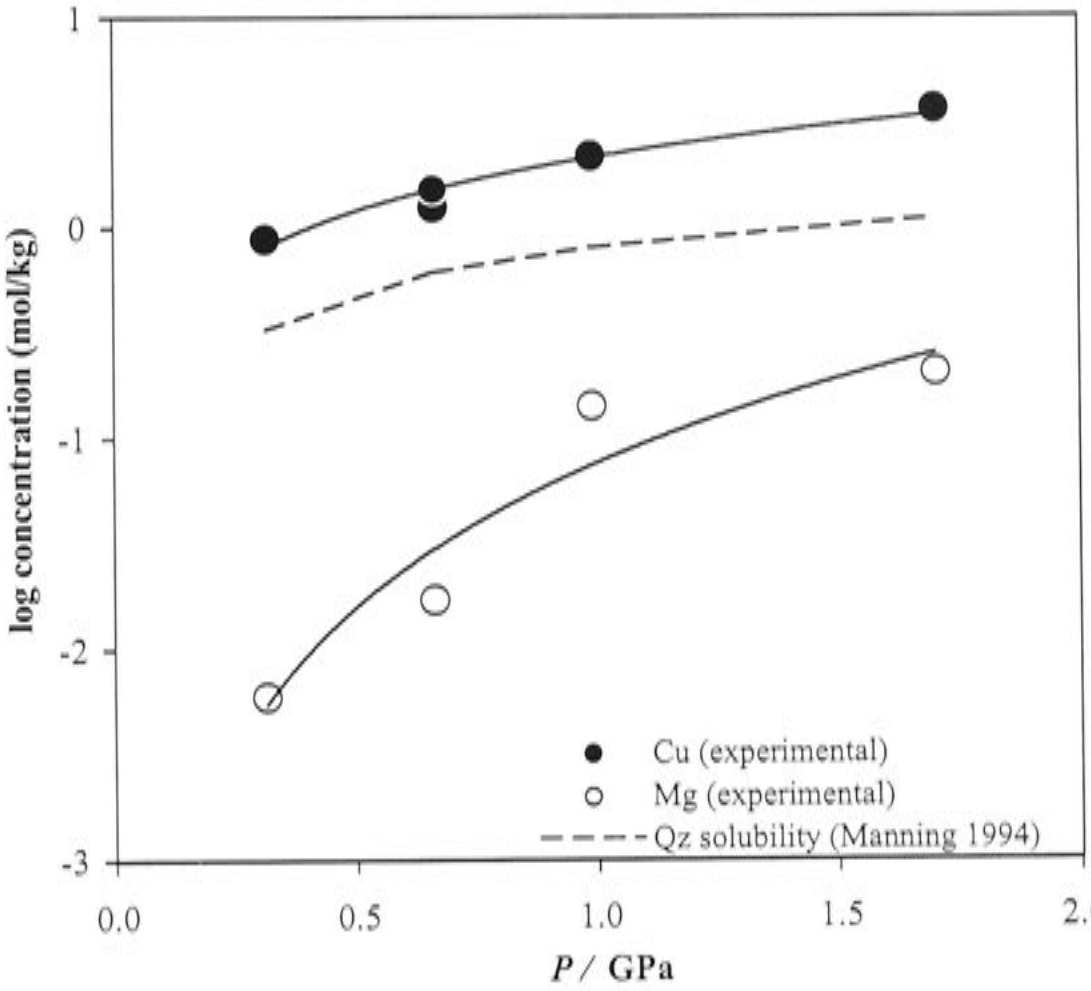

Figure 3.25 Diagram of experimental Cu and Mg solubility for Cu–Cpr–Tc–Qz in 1 mol/kg Cl aqueous fluid at 710 °C from 0.3 to 1.7 GPa and the solubility of quartz in pure H_2O at the same conditions (Manning 1994).

Congruent dissolution of Cpr in H_2O can be described by the general reaction,

$$1/2\,Cu_2O_{(Cuprite)} + nH_2O_{(g)} = CuO^0_{0.5}\cdot(H_2O)_n \qquad [3.30]$$

Wherein, n is the number of H_2O molecules coordinated to the dissolved copper(I). Taking the conventional standard state of the pure gas at 1 bar and the T of interest for H_2O, hence the subscript (g), an apparent equilibrium constant (K') for this reaction can be expressed[14],

$$\log K' = \log mCu - n\log fH_2O \qquad [3.31]$$

where, m is the molal concentration of Cu (mol/kg), which is assumed to behave ideally, and f refers to the fugacity of H_2O. Thus, the stoichiometry of the Cpr

[14] The general expression describing the condition of equilibrium is,

$$\Delta_r G_{T,P} = 0 = \Delta_r G^\circ_{T,1\ bar} + \int_1^P \Delta V_T(P)dP + RT\ln K$$

Thus, the relation [3.31] is simplified.

hydrolysis reaction as a function of P, n, may be determined from the slope given by log mCu versus log fH$_2$O (Figure 3.26).

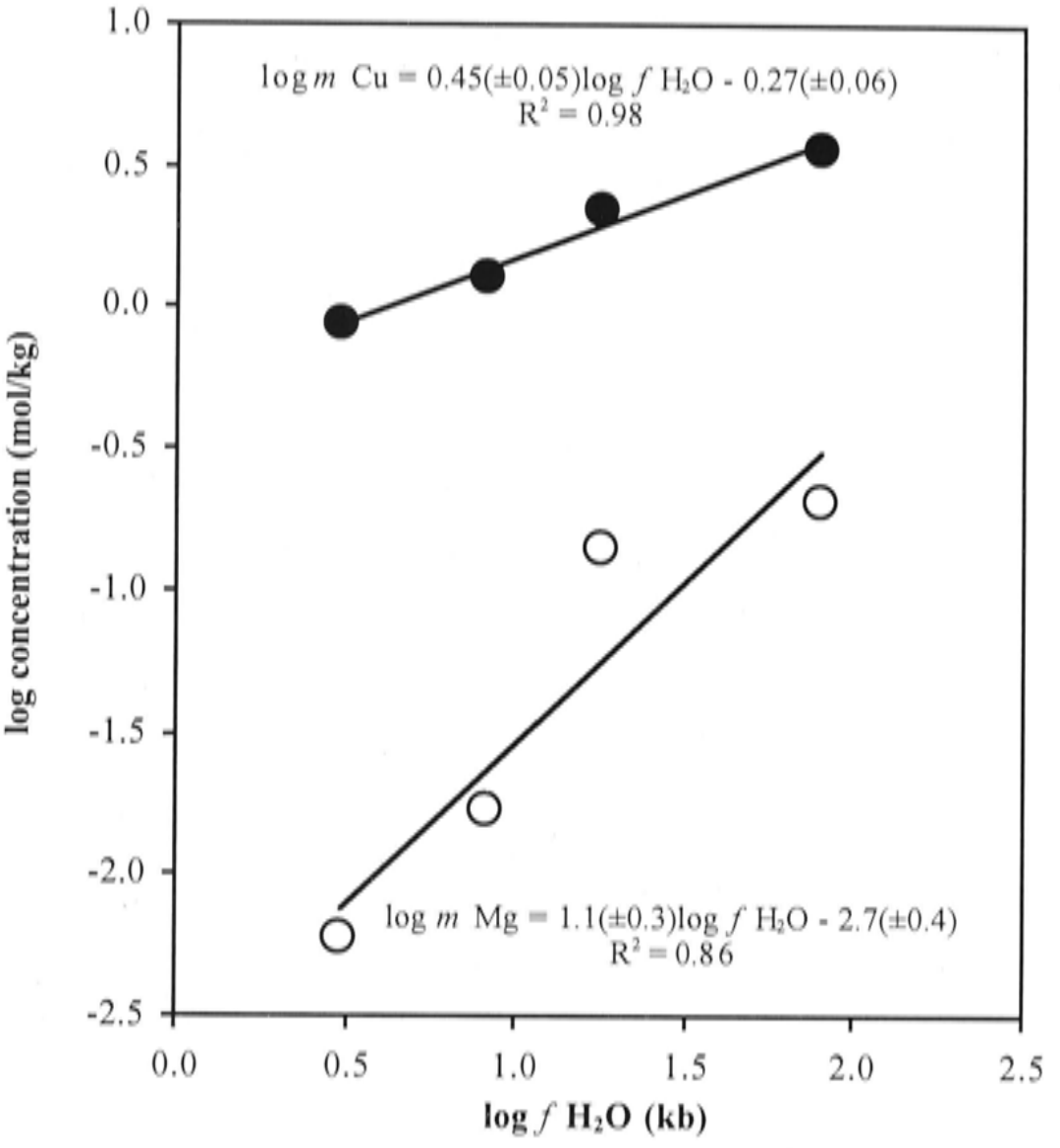

Figure 3.26 Diagram of log molality Cu and Mg (solid and open symbols, respectively) versus log fH$_2$O for Cu–Cpr–Tc–Qz solubility measurements at 710 °C from 0.31 to 1.7 GPa. Regression Equations are rearranged forms of [3.31]; standard errors on fit parameters given. fH$_2$O is in kilobars (1 kb = 0.1 GPa)

The slope, n, given in Figure 3.26 for Cu is ~ 0.5, substituting this value into Equation [3.30] suggests the predominant copper(I) species at high-P is $CuO^0_{0.5} \cdot (H_2O)_{0.5}$, this stoichiometry is equivalent to the simple neutral species, $CuOH^0_{(aq)}$. Although this analysis is somewhat simplistic (*i.e.* cholorocopper(I) complexes, activity coefficients and the volume of the reaction as a function of P have not been explicitly accounted for in determining the slope), the uncomplicated result tentatively suggests that it may be acceptable. That said, the comparatively low solubilities measured in the Cl-free system (a single experiment) suggest the speciation may be more complicated than indicated by this preliminary analysis of the data. To verify the predominant dissolution mechanism and thereby derive valuable information on the reaction volume, the ligand activities (H_2O and Cl) need to be varied independently of P.

A linear relation between log mMg and log fH$_2$O is also apparent. This correlation is equally difficult to interpret, especially given that consideration of Equation [3.3] suggests that Tc solubility should decrease with increasing P (*i.e.* P_{H_2O}), and thus magnesium(II) hydroxide complexes should also decrease in importance. The key to explaining the prograde solubility of Tc is probably related to the release of Cl ligands from chlorocopper(I) complexes with increasing P, for example,

$$CuCl^0_{(aq)} + H_2O_{(liq)} = CuOH^0_{(aq)} + HCl^0_{(aq)} \qquad [3.32]$$

It is suggested that with increasing P (*i.e.* increasing f H$_2$O) equilibrium [3.32] shifts towards the right. Because chlorocopper(I) concentrations are large relative to Mg, so are the potential quantities of HCl that can become available to drive Tc dissolution through magnesium(II) chloride complex formation, which can be summarised by the reaction,

$$1/3Mg_3Si_4O_{10}(OH)_{2\,(Talc)} + 2HCl^0_{(aq)} = 4/3SiO_{2\,(Quartz)} + MgCl^0_{2\,(aq)} + 4/3H_2O_{(liq)} \qquad [3.33]$$

The behaviour of mineral solubilities with increasing P suggests that H$_2$O becomes increasing important as a potential ligand for dissolving anhydrous rock-forming minerals, as indicated by the transition from chloride to hydroxide copper(I) complexing. This is significant as other ligands, like Cl, are effectively liberated to increase the solubility of hydrous phases, which would otherwise to be predicted to become increasingly stable (=insoluble) with P.

7. Mineral solubility: Summary of *P–T–X* solubility data and speciation

The fluid inclusion data are systematic and provide a clear picture of the general *P–T–X* solubility and speciation scheme, which is illustrated in Figure 3.27.

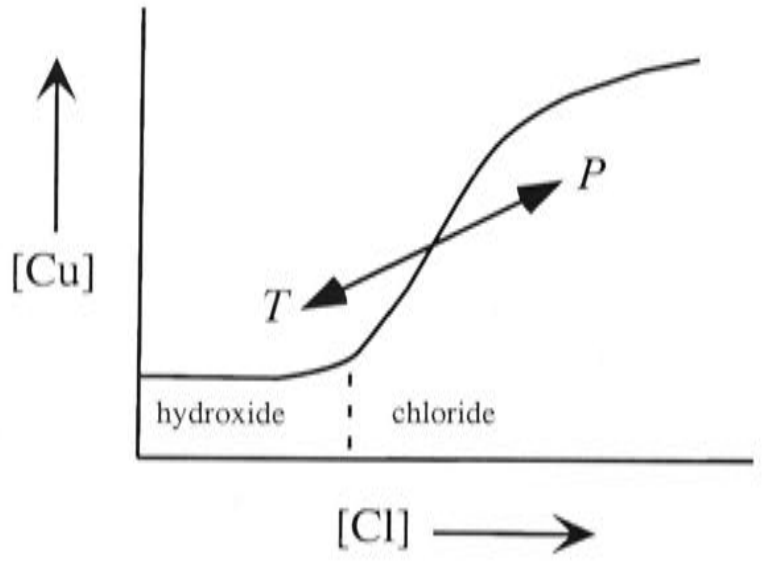

Figure 3.27 Schematic illustration of the relative effects of *P*, *T* and salinity (Cl concentration) on Cu solubility in supercritical aqueous fluid under mineral-buffered conditions. Arrows indicate the relative direction in which the solubility curve moves with increasing *T* or *P* as function of Cl concentration. Salinity regions in which copper(I) chloride or hydroxide complexes predominate are separated by the dashed line.

For a fixed Cl concentration, the relative stabilities of hydroxide and chloride copper(I) complexes changes with *P–T* conditions, which in turn determines the solubility. Chloromagnesium(II) complexes predominate over all experimental conditions investigated. At constant *P–T*, Cpr solubility increases in concert with Cl concentration because chlorocopper(I) complexes predominate. Experimental and theoretical constraints imply chlorocopper(I) complexes have a neutral stoichiometry, most likely $CuCl(HCl)^{0}_{n-1\ (aq)}$. Though non-ideal interactions between CuCl and HCl molecules, reflected by way of individual activity coefficients, would also be consistent with the solubility data. At low-*P* (< ~ 0.5 GPa) mineral solubility is retrograde with increasing *T* between 525 to 850 °C. This appears to be related to a disproportional increase in the stability of the HCl fluid component at low-*P* and high-*T*. With increasing *P* solubility increases and the stability of copper(I) hydroxide complexes (*e.g.* $CuOH^{0}_{(aq)}$) appears to extend to higher salinities, though it should be noted this is not well constrained by the current data.

8. Laser Raman microspectroscopy: Fluid inclusions and minerals from solubility experiments

Experimental samples were analysed by laser Raman microspectroscopy to further characterise the experimental products and also attempt in situ high-T spectroscopy on homogenised individual inclusions to identify copper(I) complexes. Analyses were made using a Dilor Microdil 28 laser Raman microprobe located at Geoscience Australia (formerly AGSO and BMR), in Canberra. The Raman spectra were generated using a Spectra-Physics model 2020 Ar^+ laser excitation source (λ = 514.5 nm). The laser Raman microprobe has been described in detail by Liu and Mernagh (1990).

Fluid inclusions vapour bubbles contain no detectable CO_2, H_2S or other gases, which could potentially affect the mineral solubility and thus fluid speciation (Figure 3.28). The detection limit for CO_2 on this instrument is ~ 0.1 mol % (*personal communication*, T.P. Mernagh, 2003).

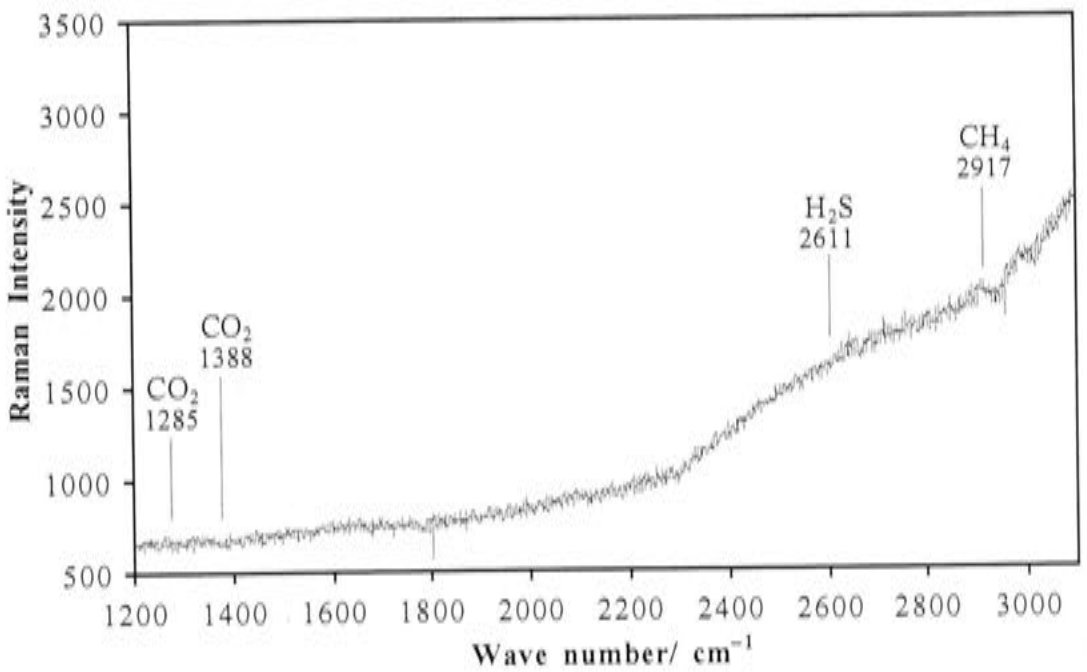

Figure 3.28 Raman microprobe spectra for the vapour bubble in a synthetic aqueous fluid inclusion formed in equilibrium with the assemblage Cu–Cpr–Tc–Qz. Band positions for potential gas contaminants (all below detection) indicated.

The distinctive tetrahedral daughter mineral, nantokite (CuCl), could not be characterised by Raman spectrometry, as it invariably decomposed under the incident beam, even at low laser power. As a point of note, the Raman reference spectra for nantokite reported by Frost (2003) is in fact identical to that of quartz. This suggests a misidentification and is consistent with the comment by Frost, that nantokite "looks exactly like quartz", which was the mineral from which nantokite was claimed to have

been separated in that study. Nantokite may be visually similar in some respects, however, it has a hardness of ~ 2 and readily oxidises in air.

Cpr (Cu_2O) was unambiguously identified in the experimental samples, both attached to quartz surfaces and as accidental occurrences within individual fluid inclusions (Figures 3.29 and 3.30). Unlike nantokite, no problems with Cpr decomposition under the beam were encountered.

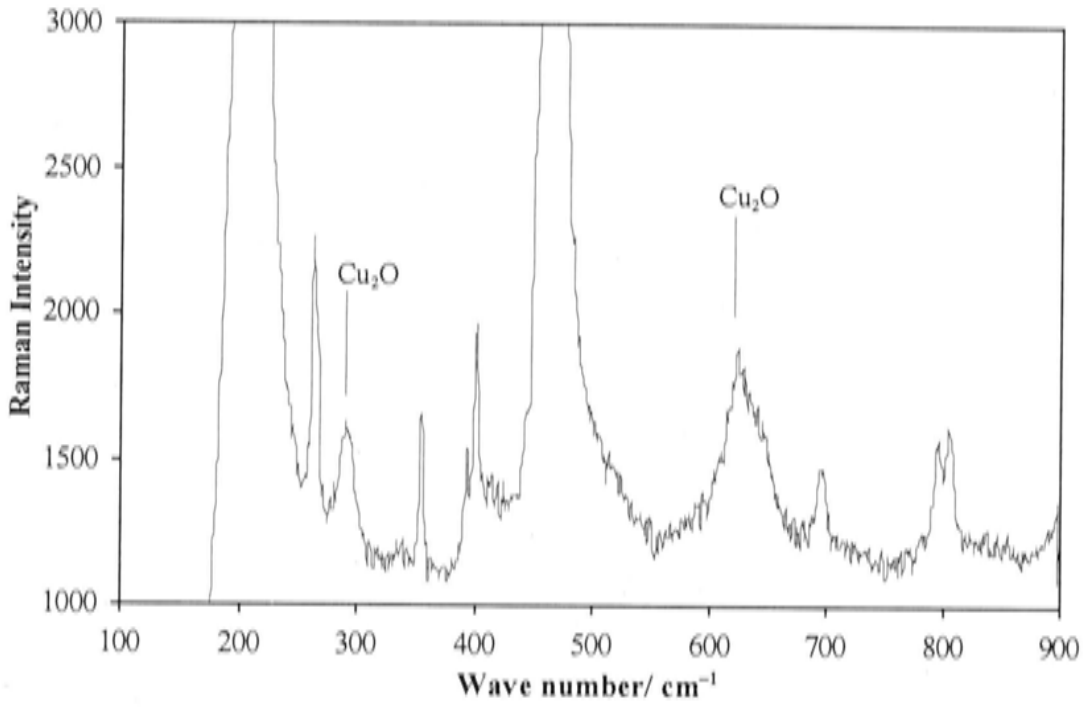

Figure 3.29 Examples of Raman microprobe spectra for Cpr and Qz. Diagnostic Cpr peaks indicated, other bands are characteristic of Qz. Upper: Accidentally trapped Cpr in a Qz-hosted fluid inclusion (*cf.* Figure 3.30). Lower: Cpr on quartz.

In some samples a thin yellow to orange coloured film was observed to coat parts of healed fractures containing fluid inclusions within the Qz. This phase was positively identified by Raman as Cpr, and hence consistent with the primary buffering assemblage and equilibrium. Cpr is petrographically distinct, in colour and morphology, from the precipitated daughter phase, nantokite. Though Cpr occurs in some inclusions along with nantokite, such Cpr occurrences are not systematic and are

interpreted as accidental trappings during inclusion formation; such inclusions do not completely homogenise on heating, in that they remain Cpr-saturated. This represents incontrovertible evidence of the fluids having attained equilibrium with Cpr prior to entrapment as inclusions.

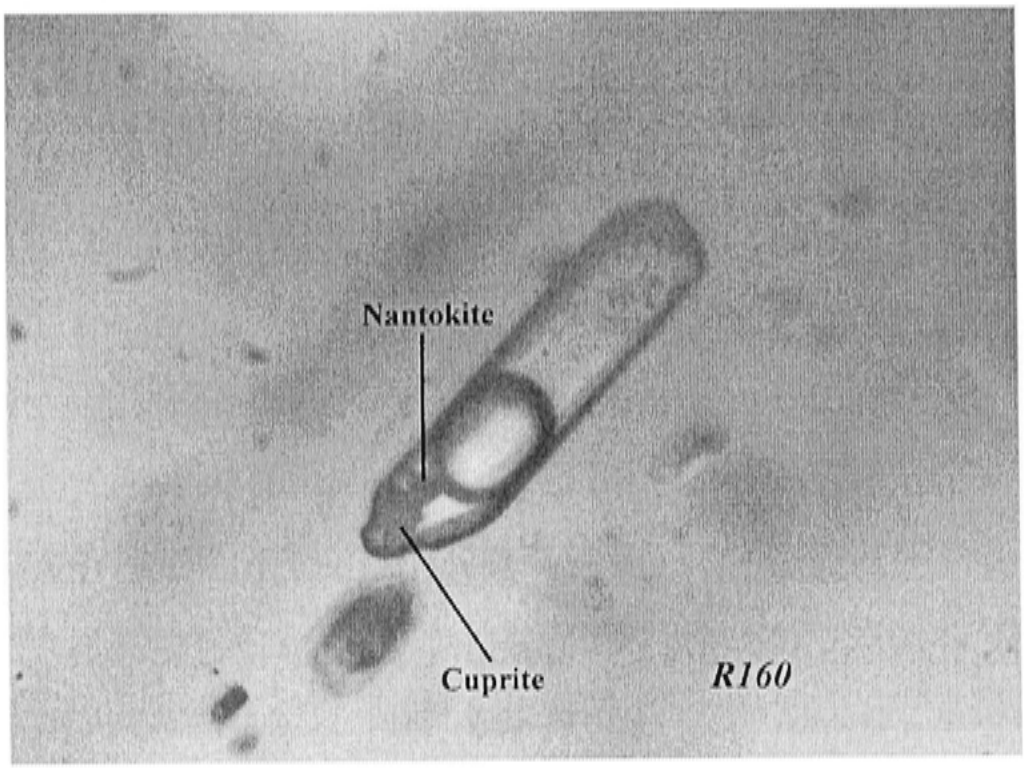

Figure 3.30 An example of a fluid inclusion from experiment R160 containing nantokite (CuCl) and accidentally trapped cuprite (Cu_2O).

Attempts to spectroscopically identify copper(I) complexes in situ at high-T in single homogenised fluid inclusions were unsuccessful, despite some inclusions containing molal concentrations of Cu. With increasing T, no changes were detectable in the Raman spectra.

9. High-temperature, in situ X-ray absorption spectroscopy of individual synthetic fluid inclusions: Further investigation of chlorocopper(I) speciation

Fluid inclusions document the *P–V–T–X* conditions of formation and can be considered, to a first approximation, to be constant volume (isochoric) systems. At T_h, inclusions homogenise to a single fluid phase. Although the fluid composition and density (so *P* also) are fixed for a specified *T*, the system is not actually univariant (even if minor dissolution and volume changes in the host between T_h and *PT* are neglected)[15]. This is because homogeneous aqueous species reactions may vary independently with changes in *T*, albeit under the constraints of constant volume and composition. There is, however, at constant volume a simple linear relation between the log *K* for many homogeneous aqueous reactions and $1/T$ for fluids. Indeed, this is an underlying argument for basing thermodynamic models for aqueous species on solvent density (*e.g.* Mesmer *et al.* 1988; Anderson *et al.* 1991). Nonetheless, the speciation of the fluid in a homogenised inclusion is assumed to approximate that at the conditions of formation. Accordingly, high-*T*, in situ X-ray absorption spectroscopy was undertaken on individual synthetic fluid inclusions to spectroscopically verify the chlorocopper(I) complexes inferred from solubility experiments. The application of X-ray absorption spectroscopy to single fluid inclusions has been demonstrated previously (Anderson *et al.* 1995; Mavrogenes *et al.* 2002).

9.1 X-ray absorption near-edge structure (XANES) spectroscopy: Background and experimental method

K-edge XANES spectra are derived from the excitation of a 1s electron to higher energy bound or delocalised (continuum) excited states. These electronic transitions give rise to an absorption edge. The energy of the transitions and hence absorption edge depend upon the oxidation state. Transitions shift to higher energy with increasing charge (~ 1–2 eV/charge). This behaviour has been used to quantify oxidation state ratios (Wong *et al.* 1984; Sutton *et al.* 1993; Bajt *et al.* 1994; Berry *et al.* 2003).

[15] If univariant, only *T* may vary independently, and would imply speciation in the fluid inclusion is fixed on homogenisation, but this not the case.

For each oxidation state the absorption edge comprises features that can be attributed simplistically to transitions between bound electronic states (*e.g.* 1s → 3d, 1s → 4s, 1s → 4p) (Shulman *et al.* 1976; Waychunas *et al.* 1983). The intensity and energy of these features can be strongly dependent upon the coordination environment due to the effect of symmetry on transitions between different electronic states.

XANES spectra are recorded by monitoring the absorption of X-rays as a function of X-ray energy. In this case X-ray absorption is detected from the intensity of Cu K_α fluorescence, emitted when an outer shell electron falls into the *K*-shell vacancy caused by the absorption process. The experiment requires a tuneable X-ray source and hence can only be undertaken at a synchrotron. For the study of fluid inclusions a high degree of spatial resolution is required in order to not only analyse individual inclusions but also particular regions within an inclusion (*i.e.* avoid crystals and shrinkage bubbles). A broad beam approach is also unsuitable because of the presence of Cu minerals and other precipitates in nearby fractures.

XANES spectra were recorded at beamline 13-ID-C of the Advanced Photon Source (GSECARS), Argonne National Laboratory, USA. The excitation energy of the incident X-ray beam was selected using a Si(111) double crystal monochromator and the beam was focused using Kirkpatrick-Baez mirrors (Eng *et al.* 1998) to a spot size of 2–10 μm. The energy was calibrated by defining the first derivative peak in the spectrum of Cu foil to be 8978.9 eV. Cu K_α fluorescence was recorded using a 16 element Ge fluorescence detector. The polished quartz sections hosting the inclusions were held in a windowless Linkam TS1500 heating stage mounted vertically at 45° to both the X-ray beam and detector. The inclusion *T* was estimated from measurements at the top and bottom surfaces of the sample and is within ±10 °C of the quoted value. Inclusions were located and viewed in situ using a long working distance objective and transmitted light.

XANES spectra were recorded by scanning the energy from 8970 to at least 9075 eV with a step size of 0.5 eV over the absorption edge, and a counting time of 1 second per point. For each condition a number of spectra were recorded sequentially in order to observe any changes with time indicative of beam damage. Spectra were compared after subtraction of a linear baseline and normalisation to the average absorption coefficient above 9050 eV. Most spectra were recorded near T_h, this is simply related to the finite strength of quartz hosting the fluid inclusions, as at higher

PT the probability of fluid inclusions decrepitating significantly increased resulting in fewer data for these more extreme conditions.

9.2 Fluid inclusion samples

Cu *K*-edge X-ray absorption near-edge structure (XANES) spectra were recorded for two separate series of mineral-buffered synthetic quartz-hosted fluid inclusions as a function of Cl concentration and *T*.

Cu–Cpr–Tc–Qz: R169 and R177

Experimentally and compositionally well-defined fluid inclusions from the salinity series (R169 and R177) were analysed. Fluids were buffered by Cu–Cpr–Tc–Qz and further details are given in Table 3.1.

Cu–Kf–Sil–Qz–Mt–Hm: AH87 and AH88

A series of synthetic fluid inclusion mineral solubility experiments were undertaken in which the fluid was buffered by the assemblage native copper-orthoclase-quartz-sillimanite-magnetite-hematite (Cu–Kf–Sil–Qz–Mt–Hm) as a function of Cl concentration at ~ 700 °C and ~ 0.35 GPa. For completeness, a general reaction describing native copper dissolution and complexing as a function of *p*H, redox and salinity can be written,

$$1/2\,Cu_{(Native)} + H^{+}_{(aq)} + nCl^{-}_{(aq)} = CuCl^{1-n}_{n\,(aq)} + 1/2\,H_{2\,(g)}$$

The coexisting silicate and oxide minerals buffer fluid acidity (via $K^{+}_{(aq)}/H^{+}_{(aq)}$ ratio) and redox potential via the equilibria,

$$KAlSi_3O_{8\,(K-feldspar)} + H^{+}_{(aq)} = 1/2\,Al_2SiO_{5\,(Sillimanite)} + 5/2SiO_{2\,(Quartz)} + K^{+}_{(aq)} + 1/2H_2O \qquad [3.34]$$

$$2Fe_3O_{4\,(Magnetite)} + H_2O = 3Fe_2O_{3\,(Hematite)} + H_{2\,(g)}$$

Solubility data are plotted in Figure 3.31. Specifically, spectra were collected for samples AH87 and AH88 of this series (refer to Table 2.7).

This experimental series, however, is ill-suited to regression of solubilities to obtain fluid speciation information. This is because the absolute concentrations and experimental *T* are relatively uncertain, as these experiments were conducted in the

developmental stages of both quantitative LA-ICP-MS fluid inclusion analysis and large volume, piston-cylinder synthesis techniques.

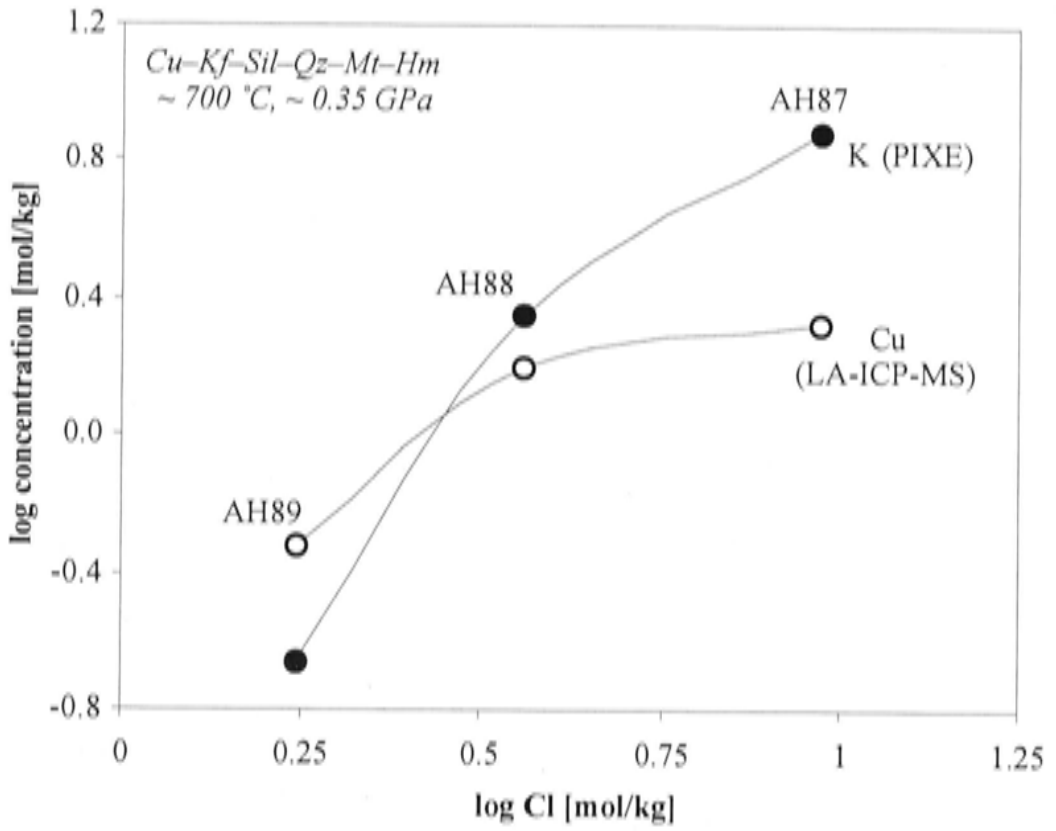

Figure 3.31 Cu and K solubility data for the assemblage Cu–Kf–Sil–Qz–Mt–Hm at ~ 700 °C and ~ 0.35 GPa as function of Cl concentration. Sample and fluid inclusion analytical technique indicated.

Solubilities were obtained from individual fluid inclusions by PIXE and were used to internally standardise LA-ICP-MS data, as quench solutions were not sampled (an initial oversight). PIXE concentrations appear to be too high (and consequently LA-ICP-MS data also) as they are not easily reconciled with the known Cl concentration of the fluid. Similarly, there is significant uncertainty in the *T* of the experiments (perhaps ~ ± 35 °C), as the critical importance of thermocouple position for accurate *T* control was not fully appreciated at this time. Nonetheless, these experiments show every sign of having attained fluid-mineral equilibrium (*e.g. PART 1, §3*) such that the data is still considered to be useful to a first approximation. Furthermore, although the Cu–Kf–Sil–Qz–Mt–Hm solubility data is poorly constrained, the fact that K/Cu (for instance) varies significantly with Cl concentration suggests some complexity in the fluid *a–X* relations, which is related to fluid speciation.

Further pertinent details are discussed in *PART 1, §3* and *PART 2, §5.11,5.12.*

9.3 Results and interpretation

9.3.1 Cu K-edge normalised and derivative XANES features

A number of representative XANES spectra are shown in Figure 3.32a. These show shifts in the energy of the absorption edge and differences in the edge shape. These differences in edge shape can be difficult to interpret since they may result from either different intensities of the transitions which comprise the edge (*e.g.* a change in coordination) or a mixture of oxidation states. The interpretation of the spectra is simplified by taking the derivative as shown in Figure 3.32b. In these spectra, peaks are observed at energies which are characteristic of the oxidation state. The intensity of the peak is related to the concentration of an oxidation state and/or the concentration of a particular coordination geometry for that oxidation state. In principle the intensities could be calibrated to extract quantitative information.

The Cu^0 spectrum in Figure 3.32 is that of Cu foil. The Cu^+ spectrum has previously been interpreted as $CuCl_2^-$ (Fulton *et al.* 2000a; Mavrogenes *et al.* 2002) and was collected for sample AH88 at 500 °C. The presence of Cu^+ is characterised by an intense $1s \rightarrow 4p$ transition at ~ 8983 eV. This is a very intense pre-edge feature which merges with the actual absorption edge to produce a large apparent edge shift between Cu^+ and Cu^{2+}. This transition also varies in intensity with coordination number. Linear Cu^+ complexes have a normalised absorption amplitude for this peak of ~ 1, whereas the intensity is only about 0.5 for tetrahedral complexes (Kau *et al.* 1987). This results from the different effects of bonding on the p orbitals to which the transition occurs. Cu^+ is therefore determined from the energy of the derivative peak, whereas the Cu^+ coordination number is related to the intensity of the $1s \rightarrow 4p$ transition. Cu^{2+} spectra are characterised by two peaks, denoted α and β, which vary in relative intensity and energy. The β peak corresponds to the main absorption edge while the α peak is associated with an absorption edge shoulder and is strongly dependent on the coordination environment. The α_1 and β_1 peaks are for a dilute Cu^{2+} reference solution, while the α_2 and β_2 peaks are for sample R169 at 420 °C after prolonged exposure to the beam. These α and β peaks are entirely consistent with previous studies (Palladino *et al.* 1993; Alcacio *et al.* 2001). For all samples the derivative spectra comprise a combination of the peaks shown in Figure 3.32b.

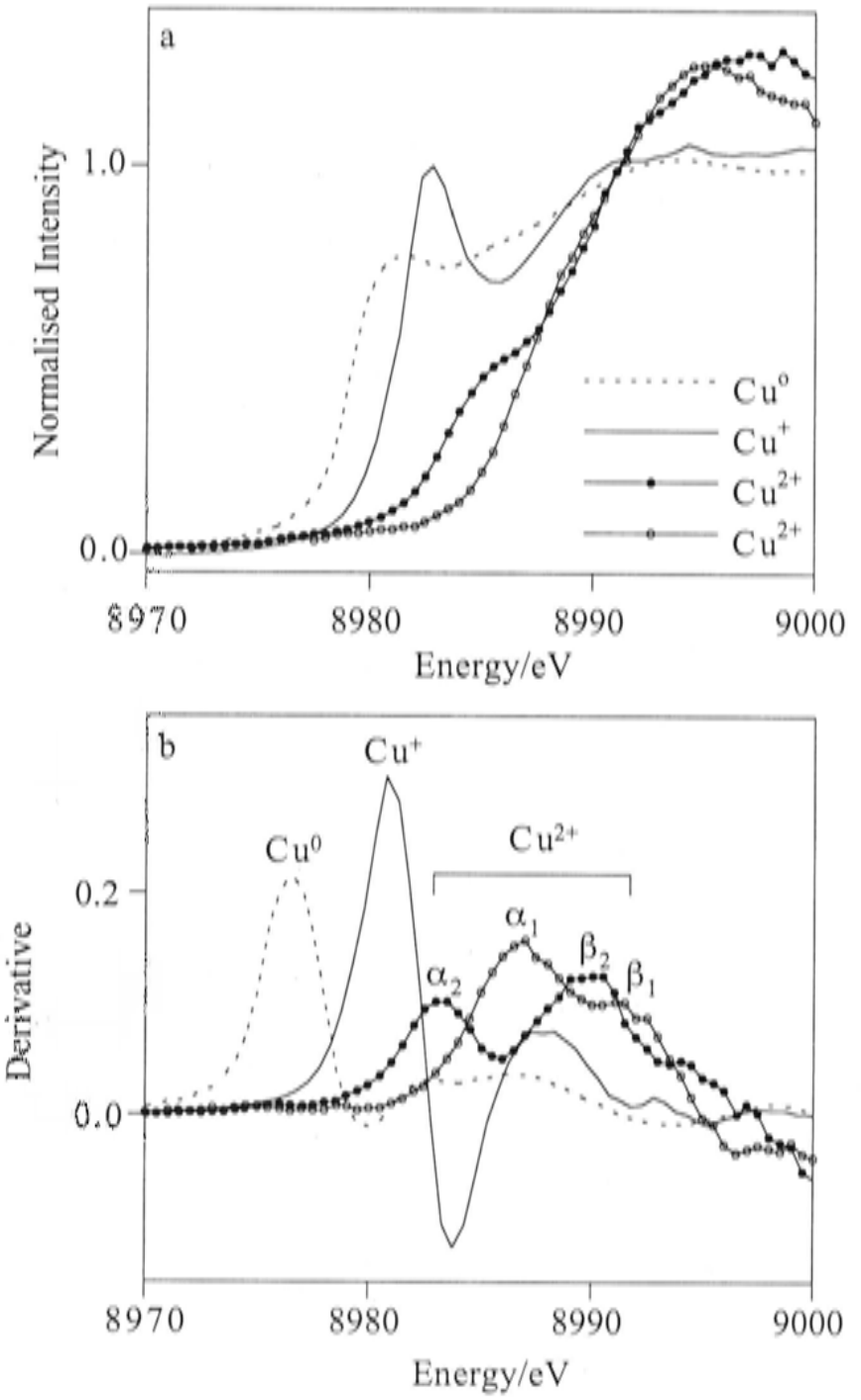

Figure 3.32 Representative Cu *K*-edge (a) normalised XANES and (b) derivative spectra. Differences in edge shape and position reflect the average oxidation state and coordination environment.

9.3.2 Cu^0 and Cu^{2+}: artefacts related to beam-induced damage

As indicated, XANES spectra imply significant variations in the oxidation state between samples. However, in some cases these differences are correlated with beam exposure and do not reflect the original oxidation state (Cu^+) and speciation of the inclusion. As spectra were recorded for all samples as a function of time, beam-induced damage was effectively monitored. Two examples of changes in the Cu oxidation state due to beam exposure are shown in Figure 3.33. In both cases the initial solution only contained Cu^+ but with continued irradiation, and seemingly facilitated by increasing *T*, the oxidation state changed. These are clearly seen from the appearance of shoulders on the Cu^+ derivative peak leading to the eventual replacement of the Cu^+

peak with that of the new oxidation state. In some cases Cu^{2+} is produced and in others Cu^0. This is despite reducing the beam intensity to as low as possible, *i.e.* the minimum photon flux required to collect spectra with adequate signal to noise.

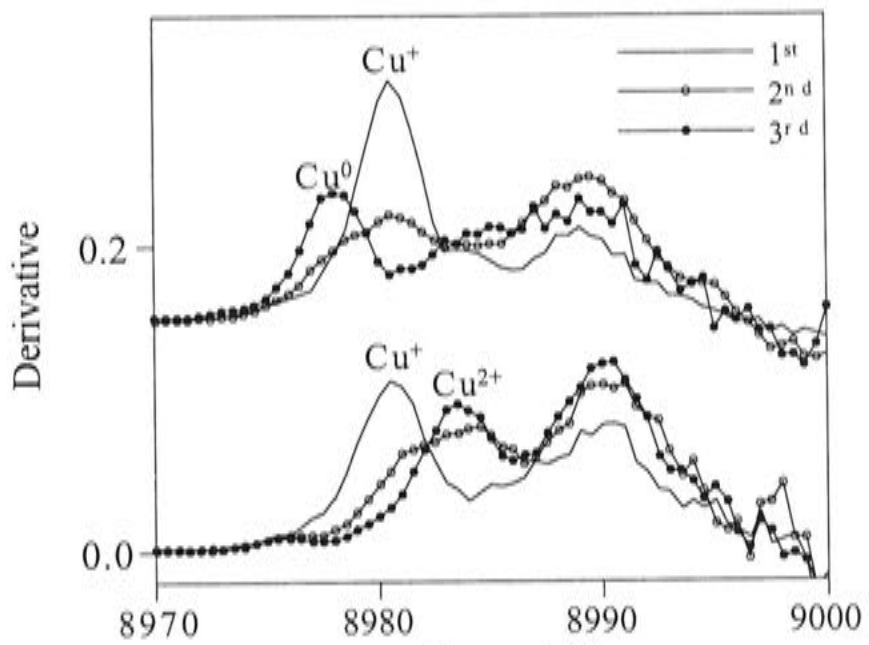

Figure 3.33 Cu *K*-edge XANES derivative spectra illustrating beam-induced reduction and oxidation of Cu^+ in separate inclusions. Spectra acquisition sequence indicated.

Whereas all spectra for samples AH87 and AH88 indicated either Cu^{2+} at low-*T* or linearly coordinated Cu^+ at high-*T*, significant variation is seen in the spectra for samples R169 and R177 (*PART 3, §9.3.3*). Sample R169 also shows oxidation of Cu^+ to Cu^{2+} but Cu^{2+} persists in one case to the highest *T* for which spectra were recorded (~ 400 °C). In another case Cu^+ with a strong 1s → 4p feature (~ 0.8) was observed at ~ 400 °C. There was insufficient time to test the *T* dependence of the oxidation state. In the case where Cu^+ was observed, the inclusion had not previously been exposed to the beam at lower *T*. It is possible that for these samples the beam-induced reaction at room *T* may permanently alter the chemistry of the inclusions (*e.g.* diffusive loss of H_2, produced by reduction of H^+ in solution) such that at higher *T* the expected Cu^+ is not observed.

In summary, beam exposure appears to be capable of either promoting oxidation of what is initially Cu^+ in solution to Cu^{2+} or, at particularly high-*T* (up to 650 °C), reduction to Cu^0. Such effects may permanently damage the inclusion. The processes or mechanisms involved in these reactions are unclear but almost certainly equate to beam damage.

9.3.3 Chlorocopper(I) speciation derived from "undamaged" XANES spectra

Although the potentially damaging effects of the beam on these solutions was noted, it is stressed that such phenomena are readily discernible from spectra that are considered to capture the original chemical state and speciation of the sample. Indeed, initial spectra are reproducible and appear to reliably document the true fluid oxidation state and speciation, unlike data from highly irradiated inclusions.

Cu–Kf–Sil–Qz–Mt–Hm

Spectra were recorded for multiple single fluid inclusions of samples AH87 and AH88 as a function of *T* up to 500 °C. At room *T* Cu^{2+} occurs, while above ~ 200 °C only Cu^{+} is observed. In a number of cases the initial room *T* spectrum indicated Cu^{+} but changed to Cu^{2+} with time. In many cases the inclusion was observed to darken (consistent with the appearance of Cu^{2+} which, unlike Cu^{+}, absorbs visible light). At higher *T*, the spectrum characteristic of linearly coordinated Cu^{+} was observed in all cases, with up to 20 sequentially recorded spectra being identical. On cooling to room *T*, the Cu^{2+} spectrum was again observed, with the Cu^{+}/Cu^{2+} dependence on *T* being completely reversible (Figure 3.34). Accordingly, Cu^{2+} observed at room *T* in these samples is not considered to be related to beam damage.

Cu^{+} is unstable at room *T* in solution and it is suggested that beam exposure promotes oxidation to Cu^{2+} with the concomitant reduction of another species (*e.g.* $2H^{+} + 2e^{-} \rightarrow H_2$) in the solution. At high-*T* where Cu^{+} is more stable than Cu^{2+} and the associated reduced species, the reaction is reversed, ideally returning the system to its original high-*T* state. All spectra recorded at elevated *T* are similar whether the inclusion had or had not been irradiated at room *T*.

There are effectively no differences between the spectra for samples AH87 and AH88 over the *T* range from ~ 250–500 °C. The intensity of the 1s → 4p feature (~ 1.0) is consistent with linear coordination of Cu^{+} by Cl (*i.e.* $CuCl_2^{-}$). For a small number of inclusions this transition is slightly weaker (~ 0.8) which would be expected for an increase in the Cl coordination number, or possibly the replacement of Cl by O (*i.e.* H_2O) as a ligand (the 1s → 4p transition for the linear O coordination of Cu^{+} in cuprite has an intensity of ~ 0.65).

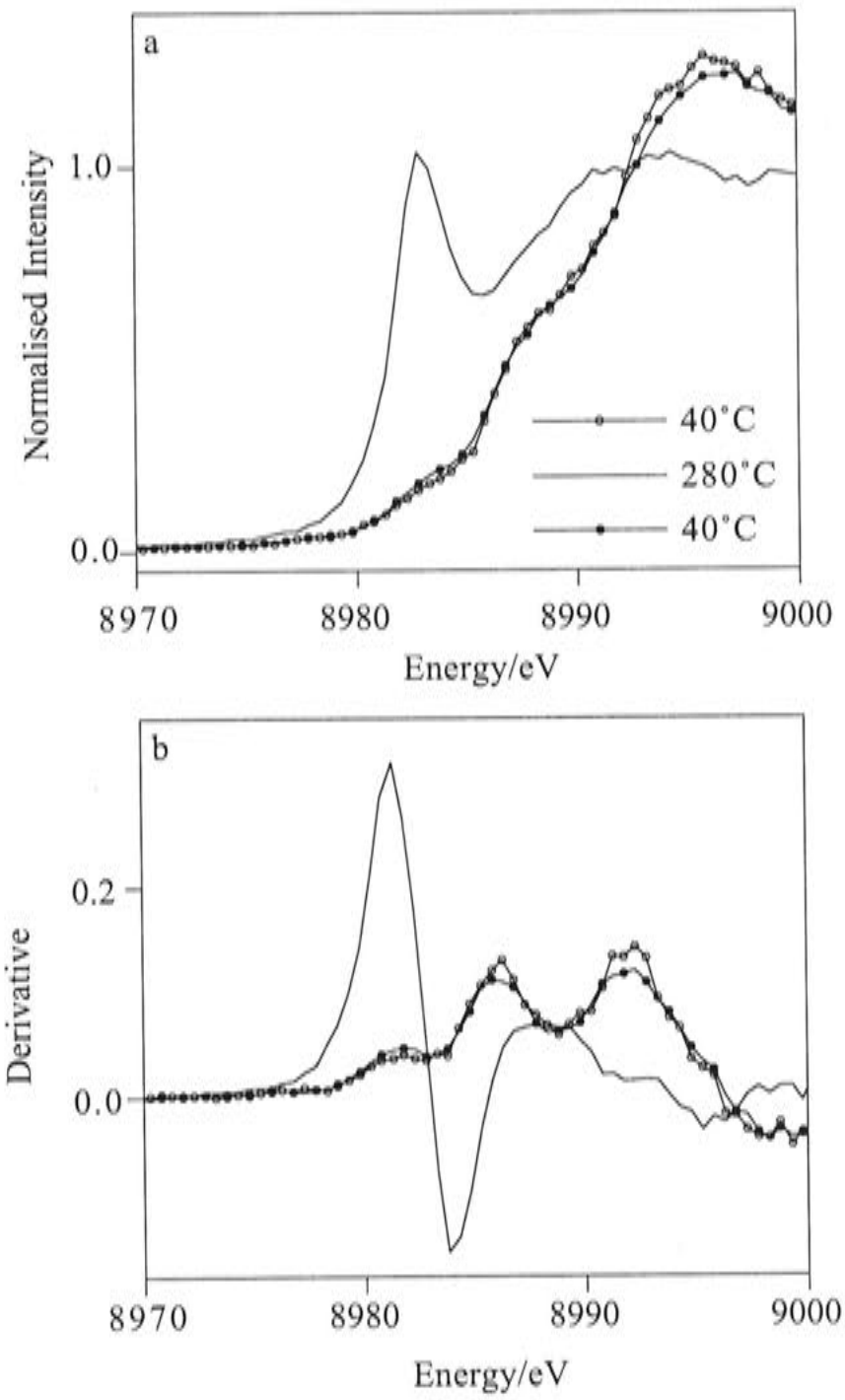

Figure 3.34 Cu *K*-edge (a) normalised XANES and (b) derivative spectra for AH88 recorded before, during and after heating. At high-*T*, Cu^{+} is stable and the Cu^{+}/Cu^{2+} *T* dependence is completely reversible.

Preliminary extended X-ray absorption fine structure (EXAFS) spectra were also recorded for an inclusion in sample AH87 at ~ 400 °C and can be satisfactorily modelled as $CuCl_2^-$ with Cu–Cl bond lengths (2.08 Å) consistent with those found by Fulton *et al.* (2000a). The data can also be modelled by mixed Cl/O coordination (*i.e.* $Cl–Cu–OH_2$), however, the quality of the fit is not statistically improved given the increased number of input parameters. Therefore, $CuCl_2^-$ is favoured as the dominant species in these fluids.

Cu–Cpr–Tc–Qz

Of particular interest are spectra recorded from sample R169 at ~ 280 °C. While these show oxidation to Cu^{2+} as a function of time, the initial spectrum indicates only Cu^{+}. Further, the intensity of the $1s \rightarrow 4p$ transition is strongly indicative of Cu^{+} coordinated to 3 or 4 Cl^-. While O cannot be excluded as a contributing ligand, it is

considered unlikely given the strong dependence of solubility on Cl concentration. At this T the crystal had not completely dissolved and was still clearly visible in the inclusion in a position removed from the beam. As discussed previously, this crystal is expected to be nantokite (CuCl), meaning that for the Cu:Cl ratio of ~ 1:2 determined by LA-ICP-MS for this sample, the presence of $CuCl_{(s)}$ will result in a Cu:Cl ratio in solution that must be > 1:2. Accordingly, higher-coordinated $CuCl(HCl)^{0}_{n-1}$ (or $CuCl_n^{1-n}$) complexes might be expected to occur should they be stable (Figure 3.35). This is the first direct evidence of highly coordinated Cu–Cl complexes at these T. At ~ 500 °C when the crystal has fully dissolved the approximately linear coordination (intense 1s → 4p transition) expected for the Cu:Cl ratio is observed.

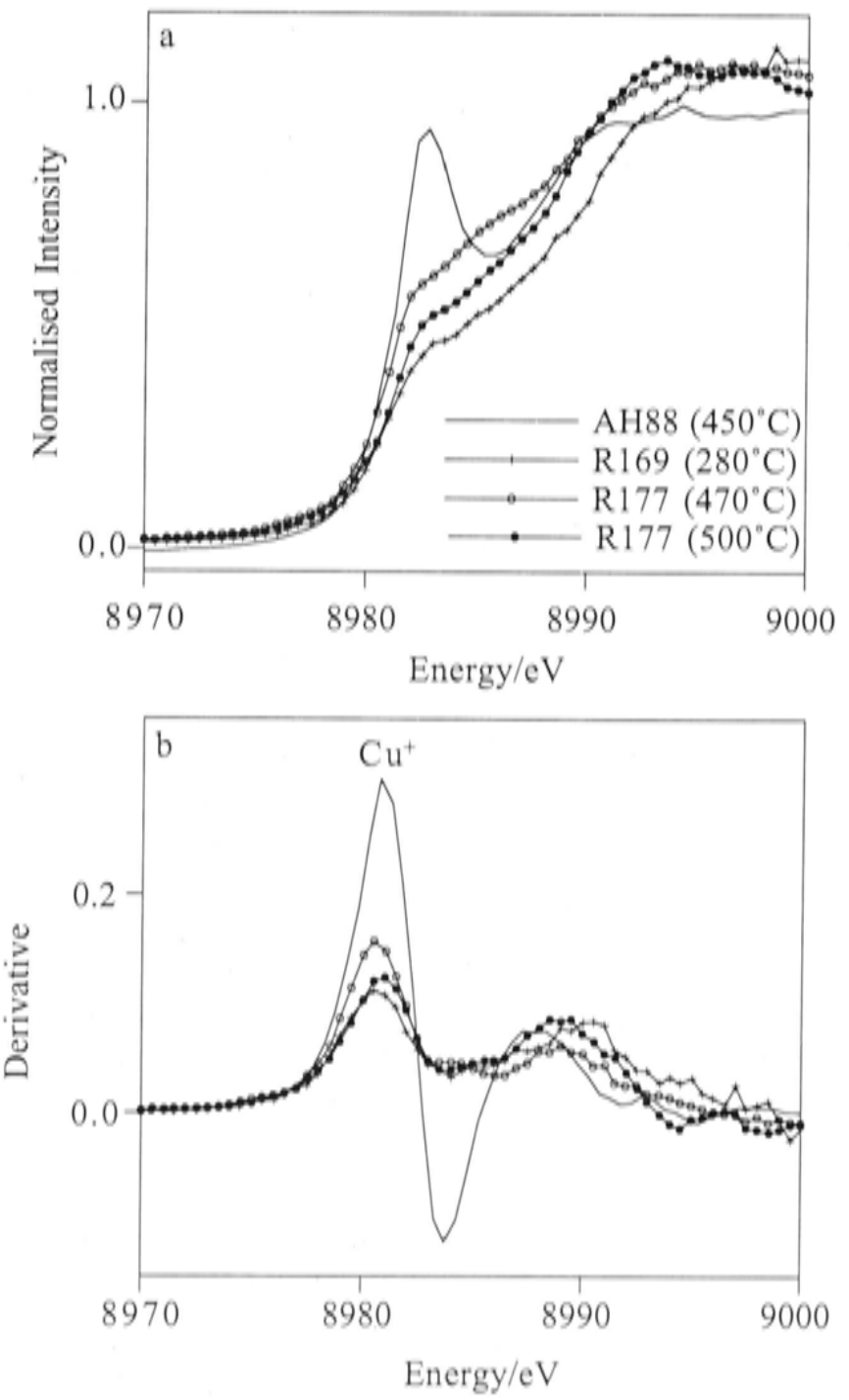

Figure 3.35 High-T, Cu K-edge (a) normalised XANES and (b) derivative spectra indicating linear and higher-order chlorocopper(I) complexes. R169 shows evidence for highly coordinated chlorocopper(I) complexes in solution only while nantokite-saturated (shown), otherwise R169 at $T > T_h$ (not shown) is identical to AH88 in which the linear $CuCl_2^-$ complex predominates. Cu^+ in R177 shows evidence of higher-order coordination (*e.g.* Cu:Cl ~1:3–4) above T_h.

The results for sample R177 are similar to those for R169. The first spectra recorded for a number of inclusions indicate the presence of Cu^+ and again the intensity of the 1s → 4p feature suggests the importance of $CuCl_3^{2-}$ and/or $CuCl_4^{3-}$. These spectra are shown in Figure 3.35. The difference in the spectrum with *T* correlates with a shift of the derivative peak, however, it is not clear if this is indicating the onset of oxidation (although five sequential spectra are identical) given that spectra at 660 °C show evidence for Cu^{2+}, or a shift towards tetrahedral coordination which would produce an increase in the transition energy (as well as a decrease in peak intensity). The significant result is that higher-order Cu–Cl complexes, which may be expected from the Cu:Cl ratio of this sample, are identified.

In addition, the oxidation state of the crystal was determined to be Cu^+ as expected for nantokite. Again, prolonged beam exposure lead to changes in the oxidation state. In one case this oxidation state was maintained throughout a heating and cooling cycle, while in another the crystal oxidised to Cu^{2+} and was then reduced to Cu^+.

9.4 Summary

In sample R177 there is strong evidence for the presence of $CuCl_3^{2-}$ or $CuCl_4^{3-}$ above 400 °C, *i.e.* > T_h (recalling that for R169 such higher-order species were only present < T_h). Noting that the presence of H and thus the nominal charge of the complex cannot be determined, it is possible that higher-coordinated species have the general stoichiometry $CuCl(HCl)_{n-1}^0$ as suggested by the solubility data. This is the first time that complexes of this type have been identified spectroscopically in supercritical fluids, supporting speculation that higher-order species can exist under near-magmatic mineral-buffered conditions.

Two significant observations have been made: 1) higher-order chlorocopper(I) complexes have been identified at supercritical conditions in mineral-buffered fluids; and 2) different chlorocopper(I) complexes predominate at equivalent total Cl concentrations and T–P conditions depending on the buffering mineral assemblage.

With respect to speciation-mineral buffer relations, simplistically, the main difference between the two assemblages investigated is the relative level at which HCl is buffered in the fluid. This is reflected by the order of magnitude difference in equilibrium constants for the acid buffering reactions (*e.g.* $\log K_{Kf-Qz-Sil\ [3.34]}^{700\ ^\circ C,\ 300\ MPa} = 3.6$ and $\log K_{talc-quartz\ [3.3]}^{700\ ^\circ C,\ 300\ MPa} = 2.6$; calculated using the data of: Shock *et al.* 1998 and Helgeson *et al.* 1978). In the case of Cu–Kf–Sil–Qz–Mt–Hm, the strong affinity between K and Cl reduces the potential concentration of HCl, which in turn primarily determines the extent to which highly coordinated chlorocopper(I) complexes are stable. The apparent complexity in a–X relations for fluids buffered by Cu–Kf–Sil–Qz–Mt–Hm does not appear to be related to changes in the chlorocopper(I) speciation. In contrast, HCl concentrations as buffered by Cu–Cpr–Tc–Qz are proportionally much higher at the same Cl concentration, to the extent that higher-order chlorocopper(I) complexes are stable. Given the ubiquity of mineral-buffered fluid KCl and NaCl concentrations in natural systems, the prevalence of copper(I) complexes more highly coordinated than $CuCl_2^-$ (or $CuCl(HCl)_{(aq)}^0$) may be limited. Further investigation, however, is warranted.

10. Application to supercritical hydrothermal phenomena

The experiments reported here document the processes through which rock and fluid compositions may be coupled in nature. Although not sufficiently detailed to derive a complete thermodynamic description of the aqueous complexes observed, and hence quantitative modelling of hydrothermal processes, some significant inferences relevant to a number of geological phenomena may still be drawn.

10.1 Magmatic hydrothermal fluids: Transport and deposition of porphyry copper ores

10.1.1 Copper concentrations in magmatic fluids

The concentration of Cu in magmatic-hydrothermal fluids is thought to be significant as chalcopyrite daughter crystals have been observed in high-salinity aqueous liquid inclusions at numerous localities: Sar Cheshmeh, Iran (Etminan 1977); Panguna, Bougainville, PNG (Eastoe 1978); Red Mountain, Arizona (Bodnar and Beane 1980); Sonora district (breccia pipes), Mexico (Sawkins and Scherkenbach 1981); Santa Rita, New Mexico (Reynolds and Beane 1985); Big Gossan, Ertsberg, Irian Jaya (Meinert 1997); Bajo de la Alumbrera, Argentina (Ulrich *et al.* 1999). More recently, quantitative fluid inclusion measurements by PIXE and LA-ICP-MS have shown Cu is present up to a few weight percent, and preferentially partitions in the vapour phase (Heinrich *et al.* 1992; Ulrich *et al.* 1999; Heinrich *et al.* 1999; Ulrich *et al.* 2001). Further support for extremely high (~ weight percent) Cu concentrations at high-T (> ~ 450°C) is suggested by thermodynamic mineral solubility calculations (based on low-T experimental data) appropriate to porphyry copper environments (*e.g.* Hezarkhani *et al.* 1999).

Not surprisingly, there pervades a general view that at high-T Cu concentrations are extremely high but this has not been substantiated by existing experimental measurements in that they have been restricted to low-T. The present measurements (up to ~ 15 wt.% Cu) are significant because they provide the first direct evidence that mineral-buffered Cu solubility can be at least as high as inferred from the

natural samples and is more than adequate (*e.g.* Cu ≥ 1000 ppm, Rose 1970) for forming a typical porphyry copper deposit at lower *T*.

10.1.2 Geological observations relating to porphyry copper systems

Detailed field studies of porphyry-type hydrothermal ore deposits show they are associated with magmas emplaced at relatively high-levels in the crust (1–3 km depth: *e.g.* Gustafson and Hunt 1975; Titley and Beane 1981; Dilles 1987). Porphyry ores occur as very large (10^7–10^9 tonnes), low-grade deposits (*e.g.* ~ 0.4–1 wt.% Cu) situated as carapaces within the roofs of intermediate to felsic, porphyritic-textured, intrusions and their country rocks. This brecciated zone is conventionally thought to develop in response to volatile saturation of the silicate magma and is typically accompanied by an extensive volume of pervasive hydrothermal alteration (*e.g.* Burnham 1979). In detail, the primary ore minerals (*e.g.* chalcopyrite) are predominantly sited within cross-cutting veins, veinlets and fracture meshes, though fine sulfide disseminations also occur within the altered host-rock. The scale of veining ranges from microscopic to macroscopic. Vein-textures are commonly annealed, a result of contact metamorphism at near-magmatic *T*. Late-stage remobilisation of the primary ore by heated groundwater is common, *e.g.* El Salvador (Gustafson and Hunt 1975).

Though the detailed relations for each deposit vary, some general characteristics are apparent. At the deposit-scale, alteration and mineralisation display vertical and zonal relations to the porphyritic stock (Lowell and Guilbert 1970; Henley and McNabb 1978; Sillitoe 1999). Barren hydrothermal quartz-magnetite alteration is a common feature in the highest *T* regions (Ulrich *et al.* 2001). Cu mineralisation, primarily chalcopyrite, is most commonly associated with the K-silicate altered core (K-feldspar-quartz-biotite±sericite±anhydrite) and inner part of the sericitic (quartz-sericite-pyrite±kaolinite) alteration envelope (*e.g.* Lowell and Guilbert 1970; Henley and McNabb 1978; Dilles 1987; Sillitoe 1999; Hezarkhani *et al.* 1999). In addition to the Cu ore zone, an inner Mo and or Au mineralised zone is sometimes present; bulk metal ratios are highly variable between deposits. Pyrite is ubiquitous, but typically forms a shell mantling the primary distribution of Cu sulfides (*e.g.* San Manuel-Kalamazoo: Lowell and Guilbert 1970; El Salvador: Gustafson and Hunt 1975).

Beyond the sericitic zone, alteration grades into lower *T* propylitic (chlorite-epidote-carbonate-albite-adularia) and argillic (quartz-kaolinite-chlorite) assemblages. In some instances advanced argillic (quartz-kaolinite/dickite-pyrite±alunite) alteration may extend to the paleosurface (Sillitoe 1999). Characteristically Cu ore precipitation occurs over a relatively narrow *T* interval, 400–250 °C (*e.g.* Crerar and Barnes 1976; Henley and McNabb 1978; Dilles 1987; Hezarkhani *et al.* 1999; Ulrich *et al.* 2001).

A combination of fluid inclusion, isotopic and phase equilibria evidence (Sheppard *et al.* 1969, 1971; Roedder 1971; Moore and Nash 1974; Hall *et al.* 1974; Taylor 1974; Gustafson and Hunt 1975; Eastoe 1978; Henley and McNabb 1978; Dilles 1987; Dilles *et al.* 1992; Giggenbach 1992b; Hedenquist and Lowenstern 1994) suggests that the inner K-silicate alteration assemblages developed by reaction with saline aqueous fluid. Liquid-rich fluid inclusions, thought to be remnants of the causative agent, homogenise at 350 to 700 °C and may coexist with low-salinity vapour-rich, commonly CO_2-bearing, inclusions (*e.g.* Henley and McNabb 1978; Hezarkhani *et al.* 1999). Such fluid inclusion assemblages are consistent with liquid-vapour immiscibility, a phenomenon that is experimentally well known in the simple NaCl–H_2O system at similar conditions (Sourirajan and Kennedy 1962; Bodnar *et al.* 1985). Isotopic data indicate there is a significant magmatic component contained within these fluids. While the outer zone of sericitic, argillic and propylitic alteration appears to be developed around 350 °C and involving higher degrees of isotope exchange with meteoric groundwaters (Sheppard *et al.* 1971).

Porphyry Cu ore systems are associated with highly oxidised magmas. For example, the quartz-magnetite-titanite phenocryst assemblage at the Ann Mason Cu porphyry, Yerington, Nevada indicates a magmatic redox state approximately two log units above the synthetic Ni–NiO buffer (Dilles 1987). Similarly, a high magmatic oxidation state can be inferred from primary apatite that contains significant oxidised sulfur, as SO_3 (Streck and Dilles 1998). Other evidence for the existence of relatively oxidised conditions associated with arc magmatism is sulfate-saturation, as demonstrated by the presence of primary anhydrite phenocrysts in erupted volcanic products (*e.g.* El Chichón: Luhr *et al.* 1984, Luhr 1990; Mount Pinatubo: Bernard *et al.* 1991, Imai *et al.* 1993, Hattori 1993).

The oxidised character of Cu mineralised porphyry intrusive rocks is also apparent in their hydrothermal systems. This is indicated by the common, if not voluminous, occurrence of primary hydrothermal phases such as anhydrite ($CaSO_4$) and

barite ($BaSO_4$) in the high-T, K-silicate alteration core (Rose and Burt 1979). Similarly, fluid inclusion studies document hematite (Fe_2O_3) daughter crystals suggesting that high-T fluids are oxidised (*e.g.* Eastoe 1978; Ulrich *et al.* 1999). Furthermore, that arc-related magmatic-hydrothermal systems are oxidised is indicated by redox measurements made on vapours (> 400 °C) emitting from actively degassing volcanoes, such as White Island, New Zealand, where the data indicate they are typically controlled by the SO_2–H_2S gas buffer (Giggenbach 1987, 1992a, 1992b). The high oxidation state of hydrothermal porphyry systems and arc magmas generally, appears to be a feature inherited from the source region as arc-peridotites are significantly oxidised relative to other upper mantle rocks (*e.g.* Wood and Virgo 1989; Brandon and Draper 1996; Johnson *et al.* 1996; Parkinson and Arculus 1999).

These field relations constrain hydrothermal ore deposition and transport processes in porphyry environments. Conspicuously, there is no deposition of Cu ore from 850 °C (*i.e.* near solidus conditions) to ~ 400 °C, despite the inferred magmatic origin of the primary ore fluids. The experimental data presented here are uniquely suited to addressing why this seems to be the case. Three main processes are thought potentially fundamental in controlling primary ore deposition in porphyry hydrothermal fluids (*e.g.* Crerar and Barnes 1976; Brimhall and Crerar 1987; Hezarkhani *et al.* 1999),

1. Fluid mixing
2. Cooling
3. Decompression and "boiling"

10.1.3 Fluid mixing at supercritical conditions

It is widely recognised, on the basis of experimental and field evidence, that copper solubility is influenced by chloride concentration in aqueous hydrothermal fluids. Similarly, it is broadly understood that exsolved magmatic fluids, the principle source of metals and gases, inevitably interact and disperse within ambient dilute convecting groundwaters. Accordingly, numerous workers have proposed that the relatively narrow spatial and T interval in which porphyry deposits form, corresponds to the zone in which magmatic ore fluids and meteoric groundwater initially mix (*e.g.* Hezarkhani *et al.* 1999). The argument being, dilution of saline magmatic fluids by entrainment of relatively pure groundwater drives precipitation because ligand

concentrations decrease significantly. For this process to be effective the solubility curve at the conditions of mixing should be as illustrated in Figure 3.36.

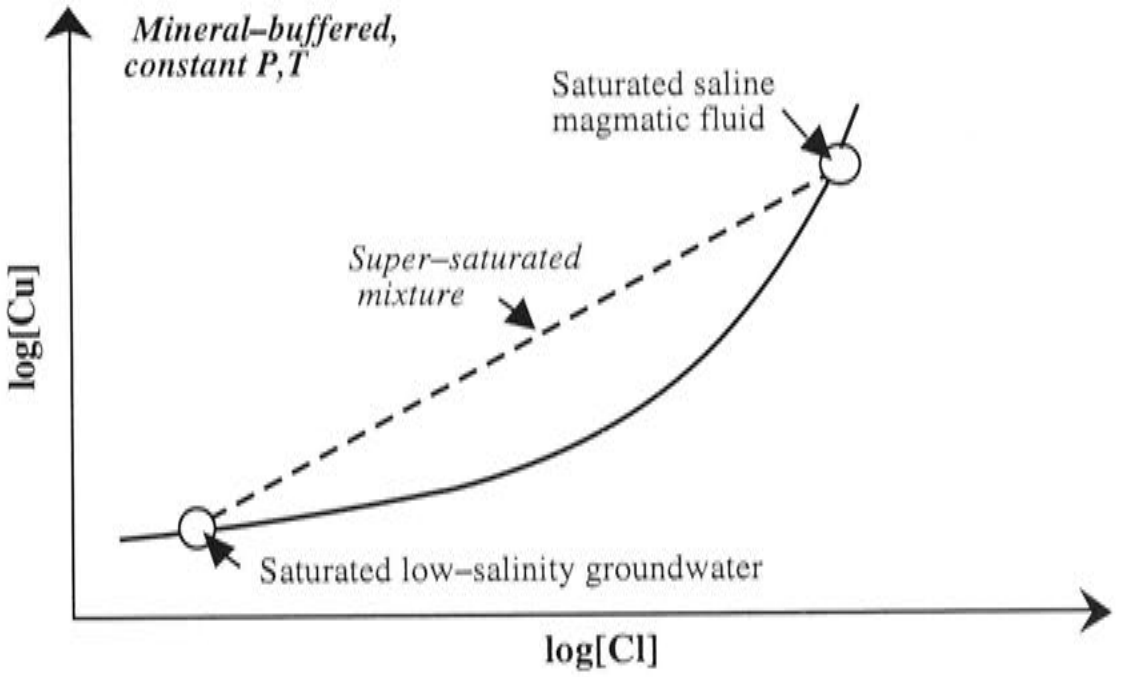

Figure 3.36 The ideal form of the mineral-buffered solubility curve (solid line) as a function of salinity (Cl concentration) required for effective Cu precipitation by fluid mixing at constant *P* and *T*. Dashed line represents the mixing trend between saturated low-salinity convecting groundwater and more saline magmatic fluid.

Fluid mixing as an effective ore depositional mechanism at supercritical *PT* conditions (*e.g.* ≥ 500 °C, ≥ 100 MPa) does not seem to be supported by the salinity series of experiments, in which the Cl concentration was varied under constant mineral-buffered *PT* conditions. As already noted these experimental data clearly show a non-linear relation between saturated Cu and dissolved Cl concentrations exists (Figure 3.3). The form of the solubility curve, however, is not that depicted in Figure 3.36 and suggests that if the limiting case of fluid-rock chemical equilibrium characterises the zone of fluid mixing, then entrainment heated low-salinity groundwater into a more saline magmatic fluid is unlikely to result any significant mineral precipitation. Figure 3.37, based on the salinity series of experiments, illustrates the effect of mixing near-saturated Cu-bearing saline and dilute fluids. This figure shows that composition of the resulting fluid mixture is actually strongly under-saturated with respect to Cu. The extent of under-saturation is determined by the relative masses of fluid mixed. Mixing reduces both the ligand and metal concentration. The point to note is that fluid mixing is more likely to result in dissolution of wall rock minerals rather than precipitation under these conditions.

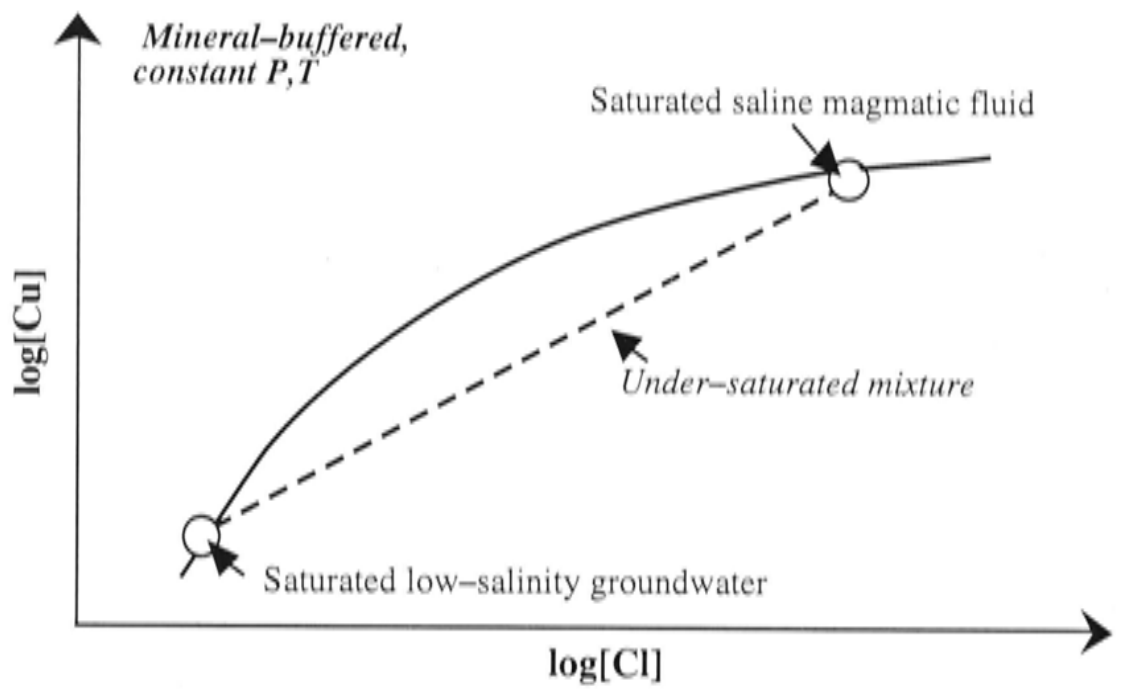

Figure 3.37 Schematic mineral-buffered solubility curve (solid line) as a function of salinity (Cl concentration) at constant *P* and *T*, based on salinity series experimental data. Dashed line represents the mixing trend between saturated low salinity convecting groundwater and more saline magmatic fluid. Note that concentrations *not* activities are plotted.

Admittedly, this is a crude interpretation because the experimental data do not extend to sufficiently low-salinities (excluding the *P* effect data) to determine the stability of hydroxycopper(I) and the minimum Cl concentration at which chlorocopper(I) complexes predominate, which defines the section of the solubility curve shown Figure 3.36. If the "complete" solubility curve is considered, then it is clear that mixing can trigger both mineral precipitation and dissolution depending on the relative compositions and masses of the mixing fluids (Figure 3.38).

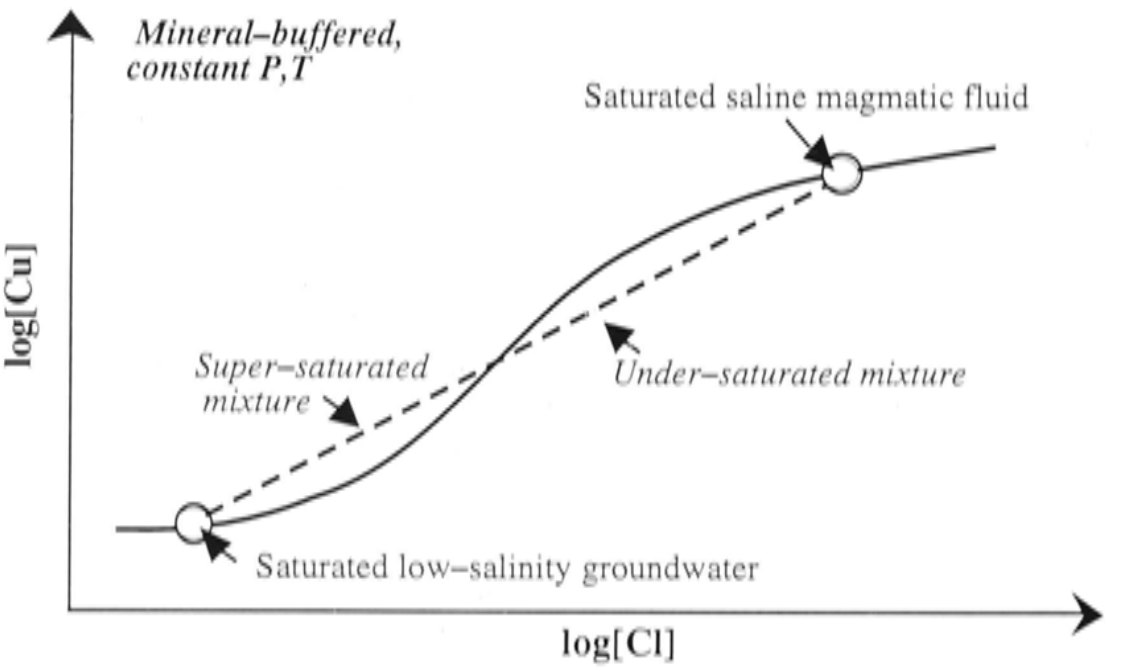

Figure 3.38 Schematic mineral-buffered Cu solubility curve (solid line) as a function of salinity (Cl concentration) at constant *P* and *T*. Dashed line represents the mixing trend between saturated low salinity convecting groundwater and more saline magmatic fluid. Note that fluid mixing may result in either Cu precipitation (super-saturated) or dissolution (under-saturated), depending on the relative masses and compositions of the fluids undergoing mixing. Element concentrations not activities are plotted.

What is significant about the experimental data, however, is that it suggests that chlorocopper(I) complexes are stable over a wide range of salinities at supercritical conditions which potentially reduces the effectiveness of fluid mixing as a depositional process. Perhaps more importantly, the experimental data indicate that copper transport may not be readily perturbed by the entrainment of ambient groundwater at supercritical conditions. This is consistent with the notable absence of Cu mineralisation forming >500 °C.

10.1.4 Isobaric cooling of supercritical ore fluid

Ore deposition in porphyry copper deposits occurs, seemingly universally, once T of the system decreases to approximately 400 °C. Accordingly, this distinctive feature has been attributed to cooling-induced saturation of the primary ore fluid. This is also supported by recent thermodynamic modelling which indicates that chalcopyrite solubility is strongly prograde, that is, Cu concentration increases with T (Hezarkhani *et al.* 1999). Although the present experimental data are not directly relevant to ore depositional conditions, they are applicable to the understanding of transport processes that lead to the locus of mineralisation.

The isobaric T series data indicates that mineral-buffered solubilities are retrograde above approximately 500 °C in supercritical aqueous fluid. Consideration of existing experimental data from lower T conditions, however, indicates that around 500 °C there is a reversal in mineral solubility trends with increasing T (Figure 3.39). The experimental data provide an explanation for the apparent absence of Cu mineralised hydrothermal systems above approximately 500 °C and highlights the potential for transporting ore components considerable distances from the source rocks. Similarly, the dramatic decrease in mineral solubility on cooling below ~ 500 °C, identified in previous studies, is consistent with the depositional conditions inferred for porphyry ores.

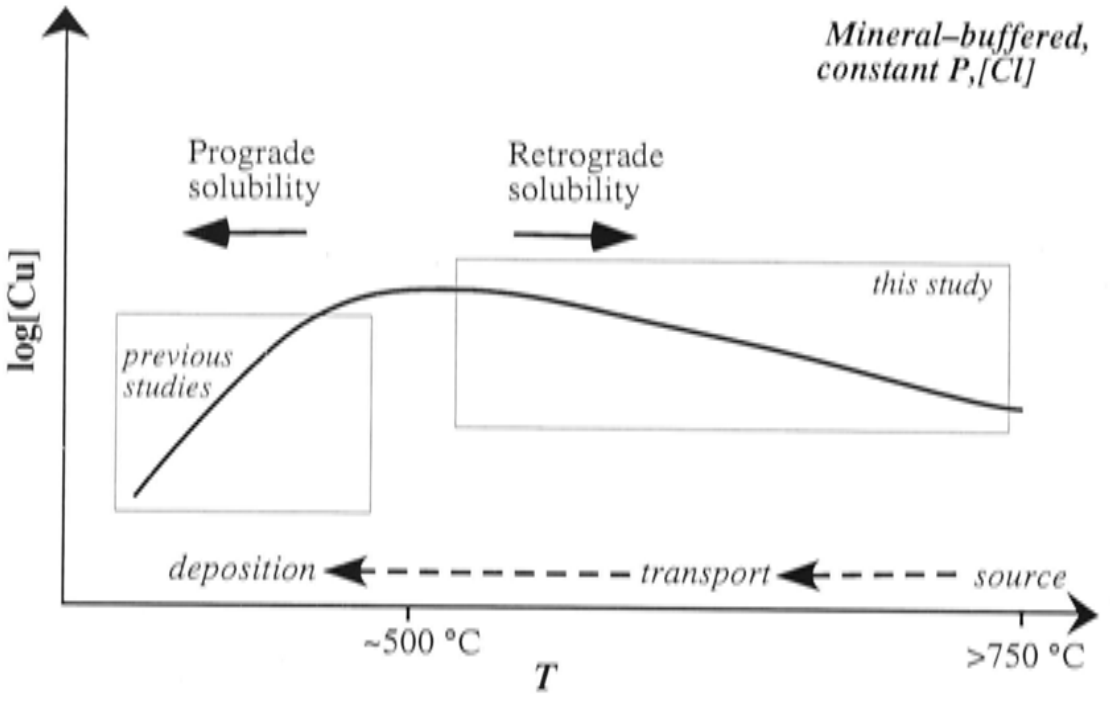

Figure 3.39 Schematic of mineral-buffered Cu solubility along an isobaric *T* gradient from the near-solidus/magmatic source through transport and ore deposition regimes. The approximate regions constrained by the experimental data of this and previous studies indicated by the boxes.

The recognition of retrograde mineral-buffered solubilities in low-*P*, high-*T* supercritical fluids (*e.g.* < 200 MPa, > ~ 500 °C) is not without precedent (*e.g.* Whitney *et al.* 1985; Luce *et al.* 1985; Grabman and Popp 1991; Walther 1997b).

Although not investigated here, it is nonetheless notable that the fO_2 associated with fixed fluid and rock redox buffers increases exponentially with *T* (*e.g.* Eugster and Wones 1962). For example, oxygen fugacity decreases around 20 orders of magnitude from magmatic *T* to 250 °C, which is significant when compared to relative variations in *T* and *P* (Brimhall and Crerar 1987).

Interestingly, redox potential of the fluid phase is buffered by dissolved gaseous components at high-*T* (> ~ 250 °C). In particular, redox measurements made on high-*T* vapours (>400°C) emitting from actively degassing arc volcanoes, such as White Island, New Zealand, indicate they are typically controlled by the SO_2–H_2S gas buffer (*e.g.* Symonds *et al.* 1994; Giggenbach 1987, 1992a, 1992b, 1997),

$$2SO_2 + 2H_2O = 2H_2S + 3O_2$$

This contrasts with most silicate rocks where mineral Fe^{3+}/Fe^{2+} ratios determine the redox state, and typically lie within a few log units of the fayalite-quartz-magnetite (FMQ) reference buffer (*e.g.* Carmichael and Ghiorso 1990; Carmichael 1991).

Because all of the common redox buffers show a strong T dependence it is more instructive to consider the change in the oxidation potential relative to the FMQ reference buffer at the same T. The relative oxidation state is defined as $\log fO_2$ (buffer/sample) - $\log fO_2$ (FMQ) = $\Delta \log fO_2$ (FMQ). Figure 3.40 shows the relation between rock- and fluid-redox buffers and porphyry copper.

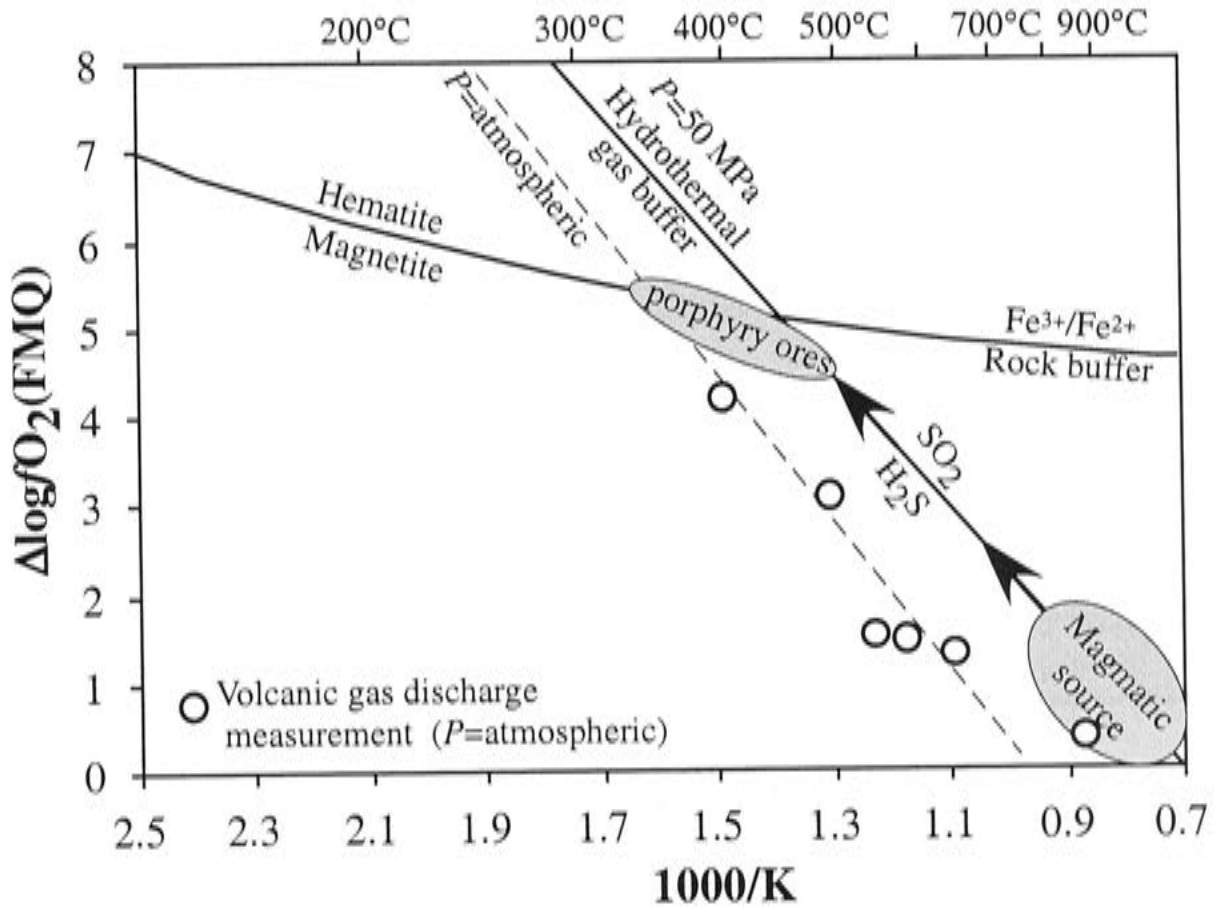

Figure 3.40 General relation between major fluid and rock redox buffers calculated as function of T at 50 MPa (=fH_2O). Isoactivity lines for buffering components, inferred relation between magmatic vapour source and porphyry Cu depositional conditions shown. Circles denote measurements of various arc volcano vapour redox as a function of discharge T and the relation to the SO_2–H_2S gas buffer at atmospheric P (dashed line) (gas redox data from compilation by Giggenbach 1997). Note FMQ rock and sulfur gas redox buffers intersect at near-solidus T.

Porphyry copper field relations and hydrothermal studies in active volcanic arcs reveal a broad coincidence between magnetite (± hematite) alteration, magmatic vapours buffered by SO_2–H_2S and ore deposition at ~ 400 ± 50 °C. Although, the exponential T dependence of the common redox buffers is largely eliminated by plotting relative to the FMQ buffer, nonetheless fluid redox varies ~ 5 log units relative to a typical magmatic rocks near FMQ when internally gas-buffered on cooling. The relative slopes indicate cooling SO_2–H_2S buffered fluids become increasingly oxidised relative to the source rocks and is unlikely to cause precipitation of the ore metals. A transition from gas-buffered to Fe^{3+}/Fe^{2+} rock-buffered fluid redox (*e.g.* magnetite-hematite coexistence in the wall-rock alteration) appears likely to occur in the critical T

interval where most porphyry copper ore occurs. With decreasing T the hematite-saturation curve is intercepted by the sulfur redox-pair fluid buffer at about 450 °C. Although dependent on relative efficiencies of the rock and fluid buffers, continued cooling under approximately rock-buffered conditions causes a relative reduction of the fluid such that H_2S/SO_2 ratio increases which could potentially drive sulfide precipitation, for example,

$$2M^{+}_{(aq)} + H_2S_{(g)} = M_2S_{(\text{sulfide})} + H_{2\,(g)}$$

The general transport and depositional characteristics of ore metals that enter the hydrothermal system in high-T magmatic fluids are reasonably well satisfied by the experimentally observed solubility patterns as a function of T and chloride concentration in the simple system. Equally it can be argued that other phenomena that are strongly coupled to T, like acidity, may be implicated in ore depositional efficiency in natural magmatic-hydrothermal systems. More directly, T appears to be a key variable because all chemical equilibria are irrevocably linked to it, such that in complex systems T cannot be considered in isolation of the equilibria that determine mineral solubility.

10.1.5 Decompression of supercritical ore fluid and vapour-liquid partitioning in "boiling" hydrothermal fluids

The effect of P indicated by the experimental data obtained in this study contrasts with previous investigations by Hemley and co-workers of ore mineral solubilities as a function of P (Whitney *et al.* 1985; Hemley *et al.* 1986; Hemley *et al.* 1992; Fein *et al.* 1992; Cygan *et al.* 1994). These earlier solubility investigations, undertaken at 300 to 700 °C and 50 to 200 MPa, in sulfur-bearing and sulfur-free, supercritical Cl-bearing aqueous fluids, show mineral-buffered solubilities decrease with increasing P. This effect appears to be most dramatic below ~ 500 °C (*e.g.* Whitney *et al.* 1985). However, the present results indicate the opposite, that is, solubilities increase with P (*e.g.* Figure 3.22). The overall solubility behaviour inferred from the various available data is shown in Figure 3.41. Because the datasets represent

mineral solubility at P–T conditions that are not overlapping, it may be that the experimental data are indicating an unanticipated P-related complexity in mineral solubility behaviour.

The solubility minium implied by Figure 3.41 between approximately 200 and 300 MPa could be indicating a potential ore forming window of opportunity in low to medium P crustal metamorphic environments.

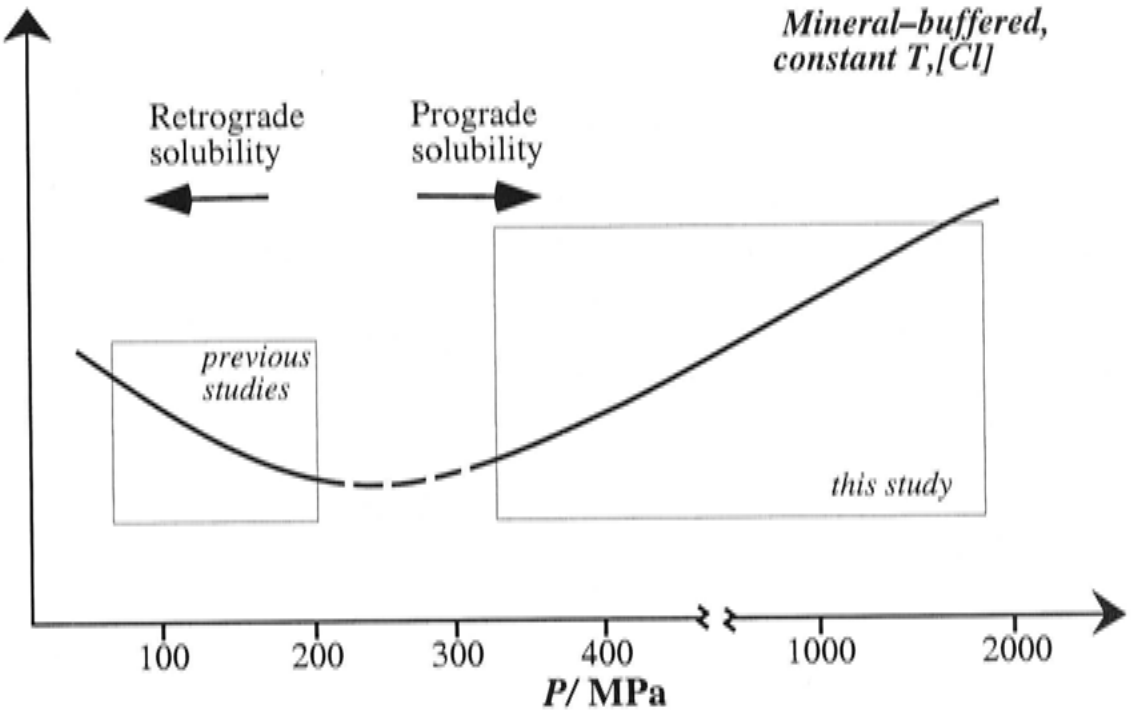

Figure 3.41 Schematic of mineral-buffered Cu solubility along an isothermal *P* gradient from a deep crust-upper mantle source through to near-surface geothermal conditions. The approximate regions constrained by experimental data of this and previous studies indicated by the boxes.

The effect of P on mineral solubility in hydrothermal systems is possibly significant in other respects also. In the limiting case, fluid decompression leads to liquid-vapour immiscibility or "boiling". Boiling is often cited as a major ore precipitation mechanism (*e.g.* Cathles 1977; Henley and McNabb 1978; Drummond and Ohmoto 1985; Giggenbach 1997; Hezarkhani 1999). Whether this is true of porphyry copper systems, however, is not as obvious as usually portrayed. This is because recent studies of natural coexisting liquid and vapour fluid inclusions (unequivocal evidence of "boiling") show that Cu (and Au) preferentially partition into the vapour phase rather the saline brine (Heinrich *et al.* 1992; Audétat *et al.* 1998; Heinrich *et al.* 1999; Ulrich *et al.* 1999; Audétat *et al.* 2000a, b; Ulrich *et al.* 2001). Perhaps a similarity between low-P supercritical fluids and relatively high-density vapours exists, in that the experimental data (below ~ 500 °C at least) indicate that solubilities increase with decreasing fluid density at low-P and high-T (*e.g.* Figure 3.41; Hemley *et al.* 1992).

With decreasing P, the fluid density and dielectric constant of H_2O decreases such that neutral species become increasingly stable. HCl (as opposed to NaCl for example) is known to partition strongly into the low-density, H_2O-dominated vapour relative the brine (Palmer and Simonson 1993; Bischoff *et al.* 1996; Shmulovich and Churakov 1998). This presumably occurs through fractionation of the hydrolysis products between the phases. A general reaction describing this may be written,

$$\underset{liquid}{MCl_n^0} + n\underset{vapour}{H_2O} = \underset{liquid}{M(OH)_n^0} + n\underset{vapour}{HCl^0} \qquad [3.34]$$

where, M refers an alkali or alkaline earth metal and n specifies the stoichiometry required to satisfy the charge balance (n = charge on M), the underscript indicates the preferred phase (liquid or vapour) of each species, but noting their activities in each phase are equivalent at equilibrium (*e.g.* $a_{HCl^0}^{liquid} = a_{HCl^0}^{vapour}$, but $m_{HCl^0}^{liquid} < m_{HCl^0}^{vapour}$). Alkali and alkaline earth chlorides are decoupled from HCl and Cu (and H_2O) during "boiling". Considering equilibrium [3.34] and the identification of a strong affinity between HCl and copper(I) to form neutral complexes in supercritical fluids in the present study, the correlation may be hinting towards the reason that Cu appears to strongly partition, apparently as a hydrated chloride complex (Achibald *et al.* 2002; Mavrogenes *et al.* 2002) into the vapour phase relative to the alkali chloride-rich brine in natural "boiling" hydrothermal systems.

Other potentially important ligands partition strongly into aqueous vapour, such as water (hydroxide complexes), CO_2, and sulfur (SO_2 and H_2S), however, no experimental or thermodynamic data exist which permit evaluation of the relative stabilities of such complexes. Furthermore, some of these gases (or potential ligands) have a profound effect on fluid phase relations and the solubility of other components. For example, CO_2 is known to strongly influence immiscibility and NaCl partitioning between coexisting liquid and vapour in the NaCl–CO_2–H_2O system (Bowers and Helgeson 1983; Frantz *et al.* 1992; Joyce and Holloway 1993). CO_2 is known to drastically (exponentially) reduce the solubility of NaCl in the vapour, but its effect on fractionation of HCl into the vapour is unknown but is possibly significant, as CO_2-bearing vapour inclusions are preferentially enriched in Cu relative to the Cl-rich brine in some magmatic-hydrothermal systems (*e.g.* Mole Granite; Heinrich *et al.* 1992; Mavrogenes *et al.* 2002). Ulrich *et al.* (2001) documented episodic decompression and

"boiling" in the Bajo de la Alumbrera hydrothermal system, but noted that it was not coupled with Cu–Au ore deposition. Accordingly, it is fair to say that at the present time the role of decompression and boiling as depositional (or dissolution?) mechanisms in high-P and T hydrothermal systems remains an interesting but somewhat speculative subject.

10.2 High-pressure metamorphic fluids: Subduction geochemical signatures and the stability and solubility of hydrous minerals

Subduction zone magmas are characterised by being depleted in high field strength elements (HFSE) and enriched in K, Rb, Sr, Ba and Cs (large ion lithophile elements, LILE) and the light rare earth elements (LREE) compared to mid-ocean ridge basalts (MORB; Perfit *et al.*1980; Kay 1980; McCulloch and Gamble 1991; Arculus 1994; Pearce and Peate 1995). The origin of this geochemical signature is thought to be controlled by the phase relations and associated fluid-rock interactions that characterise the descending plate and the overlying mantle wedge.

Interestingly, it is accessory phases that dominate the HFSE (rutile, zircon), P (apatite), LREE, Th, U (allanite), and LILE (phengite) budget in subducted crust (*e.g.* Ryerson and Watson 1987; Tribuzio *et al.* 1996; Rudnick *et al.* 2000; Hermann and Green 2001; Zack *et al.* 2001, 2002; Hermann 2002). Allanite is an epidote-group mineral with the capacity to incorporate Th, LREE, La, Ce and Nd at weight percent concentrations and may also contain significant U (*e.g.* Hermann 2002). Phengite, a silicic white mica, constitutes the main host for H_2O, K and LILE in subducted K-bearing rocks (*e.g.* Herman and Green 2001).

Recent investigations of exposed ultra-high pressure (UHP) rocks and experimental studies have emphasised the apparent stability of all of the key accessory phases in the types of UHP metamorphic assemblages encountered in the subduction regime (*e.g.* Tribuzio *et al.* 1996; Domanik *et al.* 1993; Schmidt 1996; Domanik and Holloway 1996; Sorenson *et al.* 1997; Ono 1998; Zack *et al.* 2001; Hermann and Green 2001). This poses an intriguing problem as it appears to be counterintuitive, considering trace element distributions observed in magmatic arc rocks suggest the stability of trace element-rich hydrous (*e.g.* allanite and phengite) and anhydrous (*e.g.* rutile and zircon) accessory phases are decoupled during subduction. If accessory phases are equally stable, hydrous or not, as implied by recent studies, then specific accessory mineral breakdown reactions are not responsible for decoupling trace element contributions from the slab, and one has to ask, what is the source of the selective depletion and enrichment patterns observed in arc rocks?

10.2.1 Release of LILE, LREE, Th from subducted lithosphere

Melting at subduction zones is thought to be fluxed by fluids derived from the down-going slab. In addition to the characteristic LILE and LREE enrichments, there is unambiguous isotopic evidence of subducted lithosphere components[16] being present in lavas erupted above subduction zones. The conclusion, that all of these features are related to the presence of supercritical hydrous fluids[17] seems unavoidable, what is not clear is whether a simple fluid liberating reaction controls the release of trace elements and/or mineral-fluid partitioning is involved. Three seemingly viable, but somewhat different, mechanisms for liberating trace elements from allanite and phengite have been presented recently (Schmidt 1996; Domanik and Holloway 2000; Hermann and Green 2001),

1. Hot subduction
2. High-P phengite breakdown
3. Fluid-present dissolution

The first two of these are discussed briefly, however, it is fluid-present solubility of trace element-rich hydrous phases in high-P supercritical aqueous fluids that the current experimental data are most suited to addressing.

Some conventional thermal models predict P–T conditions in the subducted lithosphere such that phengite remains a stable phase and does not break down (*e.g.* Davies and Stevenson 1992). In contrast, investigations of exhumed natural UHP metamorphic rocks (up to ~ 4.5 GPa), formed in subduction zones, document P–T conditions that are significantly hotter than some calculations (Figure 3.42; Reinecke 1991; Chopin *et al.* 1991; Schertl *et al.* 1991; Shatsky *et al.* 1995; Hermann *et al.* 2001). Thermal gradients in subduction zones, as inferred from UHP rocks, appear to be

---

16 For example, the short-lived cosmogenic isotope ^{10}Be is concentrated in seafloor sediments and identified in island arc magmas, but is essentially non-existent in other mantle-derived rocks (Brown *et al.* 1982, Morris and Tera 1989).

17 Recognition of the upper second critical point in silicate-H_2O systems means complete miscibility between aqueous fluids and hydrous silicate melts may exist at upper mantle P-T conditions (Kennedy *et al.* 1962; Shen and Keppler 1997; Bureau and Keppler 1999; Stadler *et al.* 2000; Figure 1.10). Consequently, making the distinction between fluids generated by dehydration and silicate partial melting reactions may inappropriate in subduction environments (*cf.* Tatsumi 1989; Ringwood 1990; Schiano *et al.* 1995).

sufficiently high that hydrous phases, like phengite, may melt directly and release LILE before being recycled into the deep mantle.

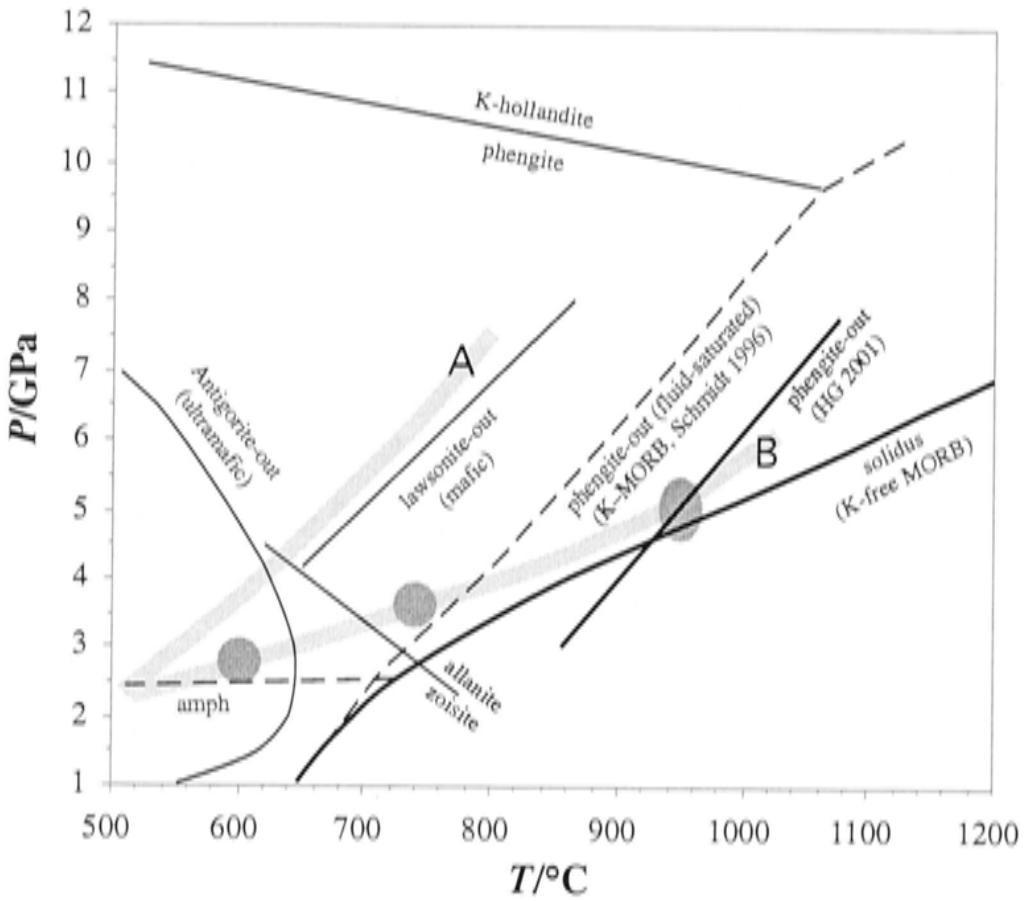

Figure 3.42 Phase stability relations for selected hydrous minerals in various rock types that comprise the subducted lithosphere (after Schmidt 1996 and Hermann and Green 2001). Grey line "A" is a calculated *P–T* conditions for the top of a slab subducting at 7.2 cm/year at 30° dip (Davies and Stevenson 1992). Dark grey ellipses indicate *P–T* conditions of exhumed coesite- and diamond-facies eclogites and gneisses from subduction zones; grey line "B" which links ellipses represents an inferred subduction zone geotherm. Zoisite to allanite transition indicated. Note, phengite-out boundary of Schmidt (1996) is for fluid-saturated conditions (this was not indicated in original text, but is revealed by K_2O and H_2O mass balance calculations for bulk experimental charge and mineral compositions) and correspondingly should be considered a phengite solubility isopleth in the K–MORB+H_2O system containing approximately 1 to 5 wt.% H_2O. The phengite-out boundary of Hermann and Green (2001; HG2001) is probably closer to the actual fluid-absent breakdown reaction.

In relatively cool slabs, phengite remains stable at depths of more than 300 km, where eventually it decomposes incongruently to K-hollandite ($KAlSi_3O_8$) plus hydrous fluid (8–11 GPa, $T \leq 1050$ °C, Figure 3.42; Schimdt 1996; Ono 1998; Domanik and Holloway 1996, 2000). This breakdown reaction could potentially liberate LILE into the fluid phase. This is speculative, however, because the LILE capacity of K-hollandite is presently unknown, but needs to be considerably lower than phengite, if LILE are to be effectively released from the slab.

Prior to subduction, the oceanic lithosphere is comprised of a variety of hydrated rock types, which form through sea floor hydrothermal alteration, including serpentinised peridotite, altered mafic rocks (essentially MORB) and sediments. Consequently during subduction a relatively large number of major dehydration

reactions are possible and many of these occur within the stability fields of allanite and phengite (Figure 3.42). Accordingly, it may be that it is the major mineral stability fields that determine the loci of fluid release but that it is the solubility of the accessory phases in these fluids that controls trace element mass fluxes into the overlying mantle and hence the distinctive chemistry of magmatic arc rocks. In this case, it is trace element partitioning between accessory phases and supercritical hydrous fluid that is important, implying solubilities must vary significantly from mineral to mineral. Furthermore, because minerals such as allanite occur as a minor phase they are potentially susceptible to complete dissolution, if soluble, in coexisting hydrous fluids and thus can be eliminated from having a trace element-buffering role in the subducting slab.

Trace element partitioning relations and the solubility of hydrous phases, however, are much less understood than are their *P–T* stability fields and in the case of allanite even this is not well defined. Perhaps the best indication that fluid-mineral trace element partitioning behaviour in subduction zones could be significant is from recent experiments by Hermann and Green (2001) and Hermann (2002) in which it was observed that hydrous granitic melts coexisting with phengite are strongly enriched in LILE. These investigations, however, also reveal that LREE and Th are still preferentially retained in residual allanite and that solubility is controlled primarily by *T* (Hermann 2002).

The present mineral-buffered solubility experiments suggest that the presence of Cl in high-*P* supercritical fluids may significantly enhance the solubility of hydrous minerals (*e.g.* several orders of magnitude) at subduction *P–T* conditions (Figure 3.22). Though it was talc and not allanite solubility that was determined, given the hydrous nature of both phases it may be reasonable to assume they have similar solubility behaviours. It can be inferred that the efficiency that fluids extract LREE and Th from the slab is probably at least as sensitive to the presence of chlorine (and so possibly other ligands also) as it is to *T*. The Cl budget in subducted materials is poorly constrained, but possibly significant given the Cl flux observed venting from degassing arc volcanoes and Cl concentrations preserved in non-degassed melt inclusions found in primative lavas (*e.g.* 400–1400 ppm; Ito *et al.* 1983). Similarly, it is probably no coincidence that Keppler (1996) noted that experimental silicate melts acquire trace element patterns reminiscent of natural arc magmas when equilibrated with a Cl-bearing aqueous fluid (as opposed to Cl-free, *cf.* Brenan *et al.* 1995).

It is noteworthy, however, that Cl does not universally enhance mineral solubilities in supercritical high-P fluids. For example, Newton and Manning (2000) found no increase in quartz solubility in NaCl–H_2O fluids compared with H_2O-only fluids at high-P, but on the other hand, they did discover that silica solubility was substantially higher in NaCl-bearing relative to CO_2-bearing fluids at the same a_{H_2O}–P–T conditions. While implying Cl–SiO_2 complexes are unimportant, their data do suggest that solvation requirements of the silica species are lower in Cl–dominated fluids (assuming NaCl–SiO_2 interactions/complexes are negligible) relative to CO_2–H_2O fluids at high-P. Regardless, it is sufficient to note that the study by Newton and Manning (2000) is another, albeit different, example of the way in which additional fluid components may significantly affect mineral solubilities and hence the nature of subsequent fluid-rock interactions.

There is of course no simple answer regarding the origin of the arc geochemical signature. The idea, however, that the decoupling of trace elements in arcs is due to significant differences in partitioning between buffering phases (*e.g.* rutile versus phengite) and supercritical fluid (or hydrous melt), rather than simple fixed P–T breakdown reactions seems plausible at the very least. Variations in fluid ligand components, like changes in P and T, may be partly responsible for second-order variations in trace element ratios observed in different arc magmas. Presumably, in some circumstances subduction zones are hot enough to melt out hydrous phases and/or fluid Cl fluxes (for instance) are sufficiently high to dissolve out trace element-buffering minerals, whether this is the usual condition, however, is not obvious and, importantly, may not be necessary. The role of fluid-mineral solubility at high P–T and the factors affecting it may turn out to be more important than usually assumed.

11. Conclusions and future studies

This study demonstrates how fluid inclusions can be used to yield information on the composition and chemical speciation in hydrothermal fluids coexisting with minerals up to the upper mantle *P–T* conditions. Experimental results bear primarily on mineral-buffered solubility and speciation in the system Cu_2O–MgO–SiO_2–HCl–H_2O, though Cu–FeO–Fe_2O_3–K_2O–Al_2O_3–SiO_2–HCl–H_2O was also investigated. There are substantial differences between the new data and existing predictions. In particular it is found that, neutral highly HCl-coordinated copper(I) complexes (*e.g.* Cu:Cl ≈ 1:3–4) predominate with increasing *T* and Cl concentration in the simplified Cu_2O–MgO–SiO_2–HCl–H_2O system. This is the first experimental evidence that highly-coordinated chlorocopper(I) complexes (*e.g.* $CuCl(HCl)^0_{3\,(aq)}$) can be significant in supercritical mineral-buffered fluids. Similarly, the inferred neutral complex stoichiometry has not been identified by previous studies at lower *P* and *T*. High-*T*, in situ XANES spectroscopy of individual synthetic fluid inclusions confirm the presence, if not the specific identity, of higher-order chlorocopper(I) complexes as proposed based upon interpretation the solubility data. Conspicuously, chlorocopper(I) complexes of higher coordination than $CuCl_2^-$ were not observed in fluids at equivalent salinity, *T* and *P* conditions in the Cu–FeO–Fe_2O_3–K_2O–Al_2O_3–SiO_2–HCl–H_2O system. Although expected on the basis of thermodynamic theory, this is the first time spectroscopic data has been acquired for different mineral-buffered supercritical solutions confirming the dependence of speciation on the coexisting mineral assemblage.

The stability of hydroxycopper(I) complexes was not established but presumed to be stable only at much lower salinities at the *P–T* conditions investigated than suggested by the thermodynamic data of Akinfiev and Zotov (2001). Polynuclear species were found to be unnecessary in interpreting the experiments.

Other highlights include the spectroscopic confirmation that fluid speciation varies between fluid buffered by different mineral-assemblages. Although this might be expected on the basis of existing mineral solubility studies and thermodynamic theory, it has not been previously observed spectroscopically and emphasises the importance of understanding the identity and stability of aqueous species over a wide range of *PTX* and mineral-buffered conditions. Another highlight is the experimental measurement of

extremely high-Cu concentrations in supercritical fluids, directly confirming for first time this widely held, but until now speculative view.

These data provide insights into several aspects of porphyry copper ore genesis, or more particularly, the conspicuous absence of high-T (>500 °C) deposits. The prevalence of progressively higher-order chlorocopper(I) complexes with increasing T in supercritical fluids results in retrograde mineral solubility with increasing T, at least above 500 °C, for a fluid of fixed Cl concentration. Conversely, cooling results in liberation of HCl from high-T complexes and these "freed" ligands may react with the coexisting minerals, increasing solubility with decreasing T, noting that existing experimental data suggest this trend reverses at some lower T. These simple experimental trends are consistent with the presence of barren high-T regions in porphyry copper deposits and the general apparent efficiency of ore transport from near-magmatic conditions to lower T depositional conditions (< ~ 500 °C) indicated by field relations. Similarly, the predominance of chlorocopper(I) complexes suggests entrainment and mixing of dilute heated groundwater may not be an effective ore depositional mechanism at supercritical conditions. This is because the average complex stoichiometry can vary with increasing salinity such that mixing previously Cu-mineral saturated fluids can result in either an under-saturated or over-saturated mixture.

The role of P in near-surface hydrothermal environments is not well understood. The present data, however, which extend to upper mantle P–T conditions, suggest the general topology of Cu–Cpr–Tc–Qz solubility in Cl-bearing fluids approximates that of the SiO_2–H_2O system at high P–T. In particular the increase in Tc solubility with increasing P was unanticipated and may be related to changes in the relative stability of hydroxide and chloride complexes with P. Cu solubility behaves in a similarly unexpected way with increasing P, as dissolved Cu exceeds total Cl. The high-P (> ~ 0.35 GPa) experimental data are not sufficiently extensive, however, to robustly constrain the predominant dissolution mechanisms and warrants further investigation.

A number of specific experimental studies would greatly increase the general utility of the current data. These include,

- Extend the existing solubility data as a function of Cl to constrain fluid speciation at high-P (*e.g.* > 1.0 GPa). Such data could be used to derive the P dependence and hence the complete thermodynamic properties for

the chlorocopper(I) complexes identified. This would enable solubility and speciation predictions to be made more robustly outside of the simple experimental system.

- Extend existing compositional series to lower salinities to define the stability of hydroxide-species, which may become increasingly significant at high-P.
- Investigate the effect of additional mineral components and gases on speciation and solubility behaviour.

Nonetheless, the experimental solubility and speciation data obtained by this study provide an insight into mineral-fluid interactions at PTX conditions, which although encountered in natural hydrothermal environments, were hitherto poorly known and largely unconstrained experimentally.

References

Ague, J.J., 1994. Mass transfer during Barrovian metamorphism of pelite, south-central Connecticut. I: Evidence for changes in composition and volume. *American Journal of Science* 294: 989–1057.

Ahrland, S. and Rawsthorne, J., 1970. The stability of metal chloride complexes in aqueous solution VII: the chloride complexes of copper(I). *Acta Chemica Scandinavica* 24: 157–172.

Akinfiev, N.N. and Zotov, A.V., 2001. Thermodynamic description of chloride, hydrosulfide, and hydroxo complexes of Ag(I), Cu(I) and Au(I) at temperatures of 25–500 °C and pressures of 1–2000 bar. *Geochemistry International* 39: 990–1006 (*translated from Russian*).

Alcacio, T.E., Hesterberg, D., Chou, J.W., Martin, J.D., Beauchemin, S. and Sayers, D.E., 2001. molecular scale characteristics of Cu(II) bonding in goethite-humate complexes. *Geochimica et Cosmochimica Acta* 65: 1355–1366.

Anderson, A.J. and Bodnar, R.J., 1993. An adaptation of the spindle stage for geometric analysis of fluid inclusions. *American Mineralogist* 78: 657–664.

Anderson, A.J., Clark, A.H., Ma, X–P., Palmer, G.R. and MacArthur, J.D., 1989. Proton-induced X-ray and gamma-ray emission analysis of unopened fluid inclusions. *Economic Geology* 84: 924–939.

Anderson, A.J., Mayanovic, R.A. and Bajt, S., 1995. Determination of the local structure and speciation of zinc in individual hypersaline fluid inclusions by micro-xafs. *Canadian Mineralogist* 33: 499–508.

Anderson, G.M. and Burnham, C.W., 1965. The solubility of quartz in supercritical water. *American Journal of Science* 263: 494–511.

Anderson, G.M. and Burnham, C.W., 1983. Feldspar solubility and the transport of aluminium under metamorphic conditions. *American Journal of Science* 283–A: 283–297.

Anderson, G.M., Castet, S., Schott, J. and Mesmer, R.E., 1991. The density model for estimation of thermodynamic parameters of reactions at high temperatures and pressures. *Geochimica et Cosmochimica Acta* 55: 1769–1779.

Aranovich, L.Ya, and Newton, R.C., 1996. H_2O activity in concentrated NaCl solutions at high pressures and temperatures measured by the brucite-periclase equilibrium. *Contributions to Mineralogy and Petrology* 125: 200–212.

Aranovich, L.Ya, and Newton, R.C., 1997. H_2O activity in concentrated KCl and KCl–NaCl solutions at high pressures and temperatures measured by the brucite-periclase equilibrium. *Contributions to Mineralogy and Petrology* 127: 261–271.

Archibald, S.M., Migdisov, A.A. and Williams-Jones, A.E., 2002. An experimental study of the stability of copper chloride complexes in water vapour at elevated temperatures and pressures. *Geochimica et Cosmochimica Acta* 66: 1611–1619.

Arculus, R.J., 1994. Aspects of magma genesis in arcs. *Lithos* 33: 189–208.

Audétat, A., Günther, D. and Heinrich, C.A., 1998. Formation of a magmatic-hydrothermal ore deposit: Insights with LA-ICP-MS analysis of fluid inclusions. *Science* 279: 2091–2094.

Audétat, A., Günther, D. and Heinrich, C.A., 2000a. Magmatic-hydrothermal evolution in a fractionating granite: A microchemical study of the Sn-W-F-mineralised Mole granite (Australia). *Geochimica et Cosmochimica Acta* 64: 3373–3393.

Audétat, A., Günther, D. and Heinrich, C.A., 2000b. Causes for large-scale metal zonation around mineralized plutons: Fluid inclusion LA-ICP-MS evidence from the Mole Granite, Australia. *Economic Geology* 95: 1563–1581.

Ayers, J.C., Brenan, J.B., Watson, E.B., Wark, D.A. and Minarik, W.G., 1992. A new capsule techniques for hydrothermal experiments using the piston-cylinder apparatus. *American Mineralogist* 77: 1080–1086.

Bach, R.W., Friedrichs, H.A. and Rau, H., 1977. P–V–T relations for HCl–H_2O mixtures up to 500 °C and 1500 bars. *High Temperatures-High Pressures* 9: 305–312.

Bajt, S., Sutton, S.R. and Delaney, J.S., 1994. X-ray microprobe analysis of iron oxidation states in silicates and oxides using X-ray absorption near edge structure (XANES). *Geochimica et Cosmochimica Acta* 58: 5209–5214.

Ballhaus, C., Ryan, C.G., Mernagh, T.P. and Green, D.H., 1994. The partitioning of Fe, Ni, Cu, Pt, and Au between sulfide, metal, and fluid phases: A pilot study. *Geochimica et Cosmochimica Acta* 58: 811–826.

Barnes, H.L. (ed), 1979. *Geochemistry of hydrothermal ore deposits,* 2nd edn. John Wiley and Sons: New York. 798 pp.

Barnes, H.L., 1981. Measuring thermodynamically-interpretable solubilities at high pressures and temperatures. *In*, Wickman, D.T.A.F.E (ed), *Chemistry and geochemistry of solutions at high pressures and temperatures*, Vol321-338. Pergamon Press

Berman, R.G., 1988. Internally consistent thermodynamic data for minerals in the system Na_2O–K_2O–CaO–MgO–FeO–Fe_2O_3–Al_2O_3–SiO_2–TiO_2–H_2O–CO_2. *Journal of Petrology* 29: 445–522.

Bernard, A., Demaiffe, D., Mattielli, N. and Punongbayan, R.S., 1991. Anhydrite-bearing pumices from Mount Pinatubo: further evidence for the existence of sulfur-rich silicic magmas. *Nature* 354: 139–140.

Berry, A.J., O'Neill, H.S., Jayasuriya, K.D., Campbell, S.J. and Foran, G.J., 2003. XANES calibrations for the oxidation state of iron in a silicate glass. *American Mineralogist* 88: 967–977.

Bischoff, J.L., Rosenbauer, R.J. and Fournier, F.O., 1996. The generation of HCl in the system $CaCl_2$–H_2O: Vapor-liquid relations from 380–500 °C. *Geochimica et Cosmochimica Acta* 60: 7–16.

Bodnar, R.J. and Beane, R.E., 1980. Temporal and spatial variations in hydrothermal fluid characteristics during vein filling in preore cover overlying deeply buried porphyry copper-type mineralisation at Red Mountain, Arizona. *Economic Geology* 75: 876–893.

Bodnar, R.J., 1983. A method of calculating fluid inclusion volumes based on vapor bubble diameters and *P–V–T–X* properties of inclusion fluids. *Economic Geology* 78: 535–542.

Bodnar R.J. and Sterner, S.M., 1985. Synthetic fluid inclusions in natural quartz. II. Application to PVT studies. *Geochimica et Cosmochimica Acta* 49: 1855–1859.

Bodnar, R.J., Burnham, C.W. and Sterner, S.M., 1985. Synthetic fluid inclusions in natural quartz, III: Determination of phase equilibrium properties in the system H_2O–NaCl to 1000 °C and 1500 bars. *Geochimica et Cosmochimica Acta* 49: 1861–1873.

Boettcher, A.L. and Kerrick, D.M., 1971. Temperature calibration in cold–seal pressure vessels. In, *Research Techniques for High Pressure and High Temperature* (ed. G.C. Ulmer). pp. 179–193.

Boettcher, A.L., Windom, K.E., Bohlen, S.R., and Luth, R.W., 1981. Low-friction, anhydrous, low- to high-temperature furnace sample assembly for piston–cylinder apparatus. *Review of Scientific Instruments* 52: 1903–1904.

Bohlen, S.R. and Boettcher, A.L., 1982. The quartz–coesite transformation: a precise determination and the effects of other components. *Journal of Geophysical Research* 87: 7073–7078.

Bose, K. and Ganguly, J., 1995. Quartz–coesite transition revisited: Reversed experimental determination at 500–1200 °C and retrieved thermochemical properties. *American Mineralogist* 80: 231–238.Bowen, N.L., 1928. *The evolution of the igneous rocks*. Princeton University Press, Princeton, N.J. 332 pp.

Bowers, T.S. and Helgeson, H.C., 1983. Calculation of the thermodynamic and geochemical consequences of non-ideal mixing in the system H_2O–CO_2–NaCl on phase relations in geologic systems: Equation of state for H_2O–CO_2–NaCl fluids at high pressures and temperatures. *Geochimica et Cosmochimica Acta* 47: 1247–1275.

Boyd, F.R. and England, J.L., 1960. Apparatus for phase equilibrium measurements at pressures up to 50 kbar and temperatures up to 1750 °C. *Journal of Geophysical Research* 65: 741–748.

Brandon, A.D. and Draper, D.S., 1996. Constraints on the origin of the oxidation state of the mantle overlying subduction zones: an example from Simcoe, Washington, USA. *Geochimica et Cosmochimica Acta* 60: 1739–1749.

Brenan, J.M., Shaw, H.F., Ryerson, F.J. and Phinney, D.L., 1995. Mineral-aqueous fluid partitioning of trace-elements at 900 °C and 2.0 GPa – constraints on the trace-element chemistry of mantle and deep-crustal fluids. *Geochimica et Cosmochimica Acta* 59: 3331–3350.

Brimhall, G.H. and Crerar, D.A., 1987. Ore fluids: magmatic to supergene. *In*, Carmichael, I.S.E. and Eugster, H.P. (eds), Thermodynamic modelling of geological materials: Minerals, fluids and melts. *Mineralogical Society of America, Reviews in Mineralogy* 17: 235–321.

Brodholt, J.P. and Wood, B.J., 1993. Simulations of the structure and thermodynamic properties of water at high pressures and temperatures. *Journal of Geophysical Research* 98: 519–536.

Brodholt, J.P. and Wood, B.J., 1994. Measurements of the PVT properties of water to 25 kbars and 1600°C. *Geochimica et Cosmochimica Acta* 58: 2143–2148.

Brown, L., Klein, J., Middleton, R., Sacks, I.S. and Tera, F., 1982. ^{10}Be in island arc volcanoes and implications for subduction. *Nature* 229: 718–720.

Brugger, J., McPhail, D.C., Black, J. and Spiccia, L., 2001. Complexation of metal ions in brines: application of electronic spectroscopy in the study of the Cu(II)–LiCl–H_2O system between 25 and 90 °C. *Geochimica et Cosmochimica Acta* 65: 2691–2708.

Bureau, H. and Keppler, H., 1999. Complete miscibility between silicate melts and and hydrous fluids in the upper mantle: experimental evidence and geochemical implications. *Earth and Planetary Science Letters* 165: 187–196.

Burnham, C.W., Holloway, J.R. and Davis, N.F., 1969. The specific volume of water in the range 1000 to 8900 bars, 20 ° to 900 °C. *American Journal of Science* 267A: 70–95.

Burnham, C.W., 1979. Magmas and hydrothermal Fluids. *In*, Barnes, H.L. (ed): *Geochemistry of hydrothermal ore deposits,* 2nd edn. pp. 71–136, John Wiley and Sons: New York.

Carmichael, I.S.E., 1991. The oxidation state of basic magmas: a reflection of their source regions? *Contributions to Mineralogy and Petrology* 160: 129–142.

Carmichael, I.S.E. and Ghiorso, M.S., 1990. Controls on oxidation-reduction relations in magmas. *In,* Nicolls, J. and Russell, J.K (eds.): Modern Methods of Igneous Petrology: understanding magmatic processes. *Mineralogical Society of America, Reviews in Mineralogy* 24: 191–210.

Carrol, M.R and Hollway, J.R. (eds.), 1994.Volatiles in magmas. *Mineralogical Society of America, Reviews in Mineralogy* 30, 517 pp.

Cathles, L.M., 1977. An analysis of the cooling of intrusives by ground-water convection which includes boiling. *Economic Geology* 72: 804–826.

Chopin, C., Henry, C. and Michard, A., 1991. Geology and petrology of the coesite-bearing terrain, Dora Maira massif. *European Journal of Mineralogy* 3: 263–291.

Ciavatta, L. and Iuliano, M., 1998. Copper(I) chloride complexes in aqueous solution. *Annali Di Chimica* 88: 71–89.

Crerar, D.A. and Anderson, G.M., 1971. Solubility and solvation reactions of quartz in dilute hydrothermal solutions. *Chemical Geology* 8: 107–122.

Crerar, D.A., 1975. A method for computing multicomponent chemical equilibria based on equilibrium constants. *Geochimica et Cosmochimica Acta* 39: 1375–1384.

Crerar, D.A. and Barnes, H.L., 1976. Ore solution chemistry V. Solubilities of chalcopyrite and chalcocite assemblages in hydrothermal solution at 200–300 °C. *Economic Geology* 71: 772–794.

Crerar, D.A., Susak, N.J., Borcsik, M. and Schwartz, S., 1978. Solubility of the buffer assemblage pyrite + pyrrhotite + magnetite in NaCl solutions from 200 to 350 °C. *Geochimica et Cosmochimica Acta* 42: 1427–1437.

Cygan, G.L., Hemely, J.J. and D'Angelo, M.W., 1994. An experimental study of zinc chloride speciation from 300 to 600 °C and 0.5 to 2.0 kbar in buffered hydrothermal solutions. *Geochimica et Cosmochimica Acta* 58: 4841–4851.

Davis, D.D., Stevenson, K.L. and Davis, C.R., 1978. Photooxidation of dichloro- and trichlorocuprate(I) ions in acid solution. *Journal of the American Chemical Society* 100: 5344–5349.

Davis, J.H. and Stevenson, D.J., 1992. Physical model of source region of subduction zone volcanics. *Journal of Geophysical Research* 97: 2037–2070.

Debout, G.E. and Barton, M.D., 1989. Fluid flow and metasomatism in a subduction zone hydrothermal system: Catalina Schist terrane, California. *Geology* 17: 976–980.

Devore, J. and Peck, R., 1993. *Statistics: The exploration and analysis of data*, 2nd edition. Wadsworth Publishing, Belmont, California.

Dilles, D.H., 1987. Petrology of the Yerington batholith, Nevada: Evidence for evolution of porphyry copper ore fluids. *Economic Geology* 82: 1750–1789.

Dilles, D.H., Solomon, G.C., Taylor, H.P., Jr., Einaudi, M.T., 1992. Oxygen and hydrogen isotope characteristics of hydrothermal alteration at the Ann-Mason porphyry copper deposit, Yerington, Nevada. *Economic Geology* 87: 44–63.

Domanik, K.J., Hervig, R.L., Peacock, S.M., 1993. Beryllium and boron in subduction zone minerals: an ion microprobe study. *Geochimica et Cosmochimica Acta* 57: 4997–5010.

Domanik, K.J. and Holloway, J.R., 1996. The stability of phengitic muscovite and associated phases from 5.5 to 11 GPa: implications for deeply subducted sediments. *Geochimica et Cosmochimica Acta* 60: 4133–4150.

Domanik, K.J. and Holloway, J.R., 2000. Experimental synthesis and phase relations of phengitic muscovite from 6.5 to 11 GPa in a calcareous metapelite from the Dabie Mountains, China. *Lithos* 52: 51–77.

Dorogokupets. P.I., 1995. Equation of state for lambda transition in quartz. *Journal of Geophysical Research* 100(B5): 8489–8499.

Drummond, S.E. and Ohmoto, H., 1985. Chemical evolution and mineral deposition in boiling hydrothermal systems. *Economic Geology* 80: 126–147.

Eastoe, C.J., 1978. A fluid inclusion study of the Panguna porphyry copper deposit, Bougainvillle, Papua New Guinea. *Economic Geology* 73: 721–748.

Eggins, S.M., Kinsley, L.P.J. and Shelley, J.M.G., 1998a. Deposition and element fractionation processes during atmospheric pressure laser sampling for analysis by ICP-MS. *Applied Surface Science* 127–129: 278–286.

Eggins, S.M., Rudnick, R.L. and McDonough, W.F., 1998b. The composition of peridotites and their minerals: a laser-ablation ICP-MS study. *Earth and Planetary Science Letters* 154: 53–71.

Eng, P.J., Newville, M., Rivers, M.L. and Sutton. S.R., 1998. Dynamically conFigured X-ray Kirkpatrick-Baez micro-focusing optics. *SPIE Proceedings* 3449: 145–156.

Etminan, 1977. Le porphyre cuprifère de Sar Cheshmeh (Iran): Rôle des phases fluides dans les mécanismes d'altération et de minéralisation. Sci. Terre. Univ. Nancy (France), Mem. 34: 249.

Eugster, H.P. and Baumgartner, L., 1987. Mineral solubilities and speciation in supercritical metamorphic fluids. *In*, Carmichael, I.S.E. and Eugster, H.P. (eds), Thermodynamic modelling of geological materials: Minerals, fluids and melts. *Mineralogical Society of America, Reviews in Mineralogy* 17: 367–403.

Eugster, H.P. and Wones, DR., 1962. Stability relations of the ferruginous biotite, annite. *Journal of Petrology* 3: 82–125.

Evans, L.F., 1967. Selective nucleation of the high-pressure ices. *Journal of Applied Physics* 38: 4930–4932.

Fiebig, J., Wiechert, U., Rumble, D. and Hoefs, J., 1999. High-precision in situ oxygen isotope analysis of quartz using an ArF laser. *Geochimica et Cosmochimica Acta* 63: 687–702.

Fein, J.B., Hemley, J.J., D'Angelo, W.M., Komninou, A. and Sverjensky, D.A., 1992. Experimental study of iron-chloride complexing in hydrothermal fluids. *Geochimica et Cosmochimica Acta* 56: 3179–3190.

Ferry, J.M., 1994. A historical review of metamorphic fluid flow. *Journal of Geophysical Research* 99: 15,487–15,498.

Folmer, J. and Jellinek, F., 1980. The valence of copper in sulfides and selenides: An X-ray photoelectron spectroscopic study. *Journal of the Less Common Metals* 76: 153–162.

Fournier, R.O. and Potter, R.W., II, 1982. An equation correlating the solubility of quartz in water from 25 °C to 900 °C at pressures up to 10,000 bars. *Geochimica et Cosmochimica Acta* 46: 1969–1973.

Franck, E.U., 1956. Hochverdichteten wasserdampf-III. Iondissoziation von HCl, KOH und H_2O in uberkrishem wasser. *Zeitschrift Fur Physikalische Chemie Neue Folge*. 8: 192–206.

Franck, E.U., 1961 Überkritisches wasser als electrolytisches lösungsmittel *Angewandte Chemie* 73: 309–322.

Frantz, J.D. and Popp, R.K., 1979. Mineral-solution equilibria—I. An experimental study of complexing and thermodynamic properties of aqueous $MgCl_2$ in the system $MgO–SiO_2–H_2O–HCl$. *Geochimica et Cosmochimica Acta* 43: 1223–1239.

Frantz, J.D. and Popp, R.K., 1981. The ionisation constants of aqueous $MgCl_2$ at elevated temperatures and pressures—a revision. *Geochimica et Cosmochimica Acta* 45: 2511–2512.

Frantz, J.D., Popp, R.K. and Hoering T.C., 1992. The compositional limits of fluid immiscibility in the system $H_2O–NaCl–CO_2$ as determined with the use of synthetic fluid inclusions in conjunction with mass spectrometry. *Chemical Geology* 98: 237–255.

Frantz, J.D. and Marshall, W.L., 1982. Electrical conductances and ionisation constants of calcium chloride and magnesium chloride in aqueous solutions at temperatures to 600 °C and pressures to 4000 bars. *American Journal of Science* 282: 1666–1693.

Frantz, J.D. and Marshall, W.L., 1984. Electrical conductances and ionisation constants of salts, acids and bases in supercritical aqueous fluids: I. Hydrochloric acid from 100 ° to 700 °C and pressures to 4000 bars. *American Journal of Science* 284: 651–667.

Fritz, J.J., 1980. Chloride complexes of CuCl in aqueous solution. *Journal of Physical Chemistry* 84: 2241–2246.

Fritz, J.J., 1981, Representation of the solubility of CuCl in solutions of various aqueous chlorides. *Journal of Physical Chemistry* 85: 890–894.

Fritz, J.J., 1982. Solubility of cuprous chloride in various soluble aqueous chlorides. *Journal of Chemical and Engineering Data* 27: 188–193.

Fritz, J.J., 1984. Heats of solution of cuprous chloride in aqueous HCl–HClO mixtures. *Journal of Solution Chemistry* 13: 369–382.

Frost, D.J. and Wood, B.J., 1997. Experimental measurements of the properties of H_2O–CO_2 mixtures at high pressures and temperatures. *Geochimica et Cosmochimica Acta* 61: 3301–3309.

Frost, R.L., 2003. Raman spectroscopy of selected copper minerals of significance in corrosion. *Spectrochimica Acta Part A* 59: 1195–1204

Fulton, J.L, Hoffmann, M. and Darab, J.G., 2000a. An X-ray absorption fine structure study of copper(I) chloride coordination structure in water to 325 °C. *Chemical Physics Letters* 330: 300–308.

Fulton, J.L., Hoffmann, M., Darab, J.G. and Palmer, B.J., 2000b. Copper(I) chloride and copper (II) chloride coordination structure under hydrothermal conditions at 325 °C: an X-ray absorption fine structure and molecular dynamics study. *Journal of Physical Chemistry* A 104: 11651–11663.

Gaetani, G.A., Asimow, P.D. and Stopler, E.M., 1998. Determination of the partial molar volume of SiO_2 in silicate liquids at elevated pressures and temperatures: a new experimental approach. *Geochimica et Cosmochimica Acta* 62: 2499–2508.

Garrels, R.M. and Christ, C.L., 1965. *Solutions, minerals and equilibria*. Harper and Row, New York, 450 pp.

Ghazi, M., McCandless. T.E., Vanko, D.A. and Ruiz, J., 1996. New quantitative approach in trace elemental analysis of single fluid inclusions: applications of laser ablation inductively coupled plasma mass spectrometry (LA-ICP-MS). *Journal of Analytical and Atomic Spectrometry* 11: 667–675.

Gibbs, J.W., 1906. On the equilibrium of heterogeneous substances. In, *The scientific papers of J. Willard Gibbs, Volume I: thermodynamics,* pp. 55–371. Longmans Greens. (reprinted by Dover, 1961).

Giggenbach, W.F., 1981. Geothermal mineral equilibria. *Geochimica et Cosmochimica Acta* 45:393–410.

Giggenbach, W.F., 1987. Redox processes governing the chemistry of fumerolic gas discharges from White Island, New Zealand. *Applied Geochemistry* 2: 143–161.

Giggenbach, W.F., 1992a. Magma degassing and mineral deposition in hydrothermal systems along convergent plate boundaries. *Economic Geology* 87: 1927–1944.

Giggenbach, W.F., 1992b. Isotopic shifts in waters from geothermal and volcanic systems along convergent plate boundaries and their origin. *Earth and Planetary Science Letters* 113: 495–510.

Giggenbach, W.F., 1997. The origin and evolution of fluids in magmatic-hydrothermal systems. *In*, Barnes, H.L. (ed.), *Geochemistry of hydrothermal Ore Deposits*, 3rd edition, pp. 737–796. New York: Wiley–Interscience.

Glasner, A. and Avinur, P., 1961. Absorption bands of cuprous and cupric salts in concentrated alkali halide solutions, and their analytical implications. *Annals. Chim.* 33: 1122–1123.

Grabman. K.B. and Popp, R.K., 1991. Experimental investigation of talc solubility in H_2O–$MgCl_2$–NaCl–HCl fluids in the range 500–700 °C, 2kb. *Geochimica et Cosmochimica Acta* 55: 2819–2829.

Green, T.H., Ringwood, A.E. and Major, A., 1966. Friction effect and pressure calibration in a piston–cylinder apparatus at high pressure and temperature. *Journal of Geophysical Research* 71(14): 3589–3594.

Gu, Y., Gammons, C.H. and Bloom, M.S., 1994. A One-term method for estimating the equilibrium constants of aqueous reactions at elevated temperatures. *Geochimica et Cosmochimica Acta* 52: 1983–1996.

Guissani, Y. and Guillot, B., 1996. A numerical investigation of the liquid-vapor coexistence curve of silica. *Journal of Chemical Physics* 104(19): 7633–7644.

Günther, D., Frischknecht, R., Müschenborn, H.-J. and Heinrich, C.A., 1997. Direct liquid ablation: a new calibration strategy for laser ablation-ICP-MS microanalysis of solids and liquids. *Fresenius Journal of Analytical Chemistry* 359: 390–393.

Günther, D., Audétat, A., Frischknecht, R. and Heinrich, C.A., 1998. Quantitative analysis of major, minor and trace elements in fluid inclusions using laser ablation-inductively coupled plasma mass spectrometry. *Journal of Analytical Atomic Spectroscopy* 13: 263–270.

Günther, D. and Heinrich, C.A., 1998. Enhanced sensitivity in laser ablation-ICP mass spectrometry using helium-argon mixture as aerosol carriers - Plenary lecture. *Journal of Analytical and Atomic Spectrometry* 14: 1363–1368.

Günther, D., Hattendorf, B. and Audétat, A., 2001. Multi-element analysis of melt and fluid inclusions with improved detection capabilities for Ca and Fe using laser ablation with a adynamic reaction cell ICP-MS. *Journal of Analytical and Atomic Spectrometry* 16: 1085–1090.

Gustafson, L.B. and Hunt, J.B., 1975. The porphyry copper deposit at El Salvador, Chile. *Economic Geology* 70: 852–912.

Haar, L., Gallagher, J.S. and Kell, G.S., 1984. *Steam Tables. Thermodynamic and transport properties and computer programs for vapour and liquid states of water in SI units*. Hemisphere Publishing, New York.

Hall, W.E., Friedman, Irving, and Nash, J.T., 1974. Fluid inclusion and light stable isotope study of the Climax molybdenum deposits, Colorado. *Economic Geology* 69: 884–901.

Haselton, H.T., Jr., Chou, I–M., Shen, A.H. and Bassett, W.A., 1995. Techniques for determining pressure in the hydrothermal diamond anvil cell: Behaviour and identification of the ice polymorphs (I,III,V,VI). *American Mineralogist* 80: 1302–1306.

Hattori, K., 1993. High-sulfur magma, a product of fluid discharge from underlying mafic magma: Evidence from Mount Pinatubo, Philippines. *Geology* 21: 1083–1086.

Hayba, D.O., Bethke, P.M., Heald, P. and Foley, N.K., 1986. Geologic, mineralogic and geochemical characteristics of volcanic-hosted epithermal precious metal deposits. *In*, Berger B.R. and Bethke, P.M., (eds), Geology and geochemistry of epithermal systems. *Reviews in Economic Geology, Volume 2*: 126–167.

Heald, P., Foley, N.K. and Hayba, D.O., 1987. Comparative anatomy of volcanic-hosted epithermal deposits: acid-sulfate and adularia-sericite types. *Economic Geology* 82: 1–26.

Hedenquist, J.W. and Henley, R.W., 1985. The importance of CO_2 on freezing point measurements of fluid inclusions: Evidence from active geothermal systems and implications for epithermal ore deposition. *Economic Geology* 80: 1379–1406.

Hedenquist, J.W., Simmons, S.F., Giggenbach, W.. and Eldridge, C.S., 1993. White Island, New Zealand, volcanic-hydrothermal system represents the geochemical environment of high-sulfidation Cu and Au ore deposition. *Geology* 21: 731–734.

Hedenquist, J.W., Matsuhisa, Y, Izawa, E., White, N.C., Giggenbach, W.F. and Aoki, M., 1994. Geology, geochemistry, and origin of high-sulfidation Cu–Au mineralisation in the Nansatsu district, Japan. *Economic Geology* 89: 1–30.

Hedenquist, J.W. and Lowenstern, J.B., 1994. The role of magmas in the formation of hydrothermal ore deposits. *Nature* 370: 519–527.

Hedenquist, J.W., Arribas, Jr., A. and Reynolds, T.J., 1998. Evolution of an intrusion-centred hydrothermal system: Far southeast-Lepanto porphyry and epithermal deposits. *Economic Geology* 93: 373–404.

Heger, K., Uematsu, M. and Franck, E.U., 1980. The static dielectric constant of water at high pressures and temperatures to 500 MPa and 550 °C. Berichte der Bunsen-Gesellschaft – Physical Chemistry, 84: 758–762.

Heinrich, C.A., Ryan, C.G., Mernaugh, T.P. and Edington, P.J., 1992. Segregation of ore metal between magmatic brine and vapor: A fluid inclusion study using PIXE microanalysis. *Economic Geology* 87: 1566–1583.

Heinrich, C.A., Günther, D., Audétat, A., Ulrich, T. and Frischnecht, R., 1999. Metal fractionation between brine and vapour, and the link between porphyry-style and epithermal Cu–Au deposits. *Geology* 27: 755–758.

Helgeson, H.C., 1964. *Complexing and hydrothermal ore deposition*. Pergamon Press, Oxford, 128 pp.

Helgeson, H.C., 1969. Thermodynamics of hydrothermal systems at elevated temperature and pressure. *American Journal of Science* 267: 729–804.

Helgeson, H.C. and Kirkham, D.H., 1974. Theoretical prediction of the thermodynamic behaviour of aqueous electrolytes at high pressures and temperatures: II. Debye-Hückel parameters for activity coefficients and relative partial molal properties. *American Journal of Science* 274: 1199–1261.

Helgeson, H.C., Delany, J.M., Nesbitt, H.W. and Bird, D.K., 1978. Summary and critique of the thermodynamic properties of rock-forming minerals. *American Journal of Science* 278A: 229 pp.

Helgeson, H.C., Kirkham, D.H. and Flowers, G.C., 1981. Theoretical prediction of the thermodynamic behaviour of aqueous electrolytes at high pressures and temperatures: IV. Calculation of activity coefficients, osmotic coefficients, and apparent molal and standard and relative partial molal properties to 600 °C and 5 kb. *American Journal of Science* 281: 1249–1516.

Helz, G.R., Charnock, J.M., Vaughan, D.J. and Garner, C.D., 1993. Multinuclearity of aqueous copper and zinc bisulfide complexes: An EXAFS investigation. *Geochimica et Cosmochimica Acta* 57: 15–25.

Hemley, J.J, Montoya, J.W., Shaw, D.R. and Luce, R.W., 1977. Mineral equilibria in the $MgO–SiO_2–H_2O$ system: II. Talc–antigorite–anthrophyllite–enstatite stability relations and some geological implications in the system. *American Journal of Science* 277: 322–351.

Hemley, J.J., Cygan, G.L., Fein, J.B., Robinson Jr., G.R. and D'Angelo, W.M., 1992. Hydrothermal ore-forming processes in light of studies in rock-buffered systems. I, Iron-copper-zinc-lead sulfide solubility relations. *Economic Geology* 87: 1–22.

Hemley, J.J., Cygan, G.L. and D'Angelo, W.M., 1986. Effect of pressure on ore mineral solubilities under hydrothermal conditions. *Geology* 14: 377–379.

Henley, R.W. and McNabb, A., 1978. Magmatic vapour plumes and groundwater interaction in porphyry copper emplacement. *Economic Geology* 73: 1–20.

Henley, R.W. and Ellis, A.J., 1983. Geothermal systems, modern and ancient: A geochemical review. *Earth Science Reviews* 19: 1–50.

Henley, R.W., Truesdell, A.H. and Barton, P.B., Jr., 1984. Fluid-mineral equilibria in hydrothermal systems. *Reviews in Economic Geology*, *Volume 1:* 1–267.

Henley, R.W. and Berger, B.R., 2000. Self-ordering and complexity in epizonal mineral deposits. *Annual Review of Earth and Planetary Science* 28: 669–719.

Hermann, J. and Green, D.H., 2001. Experimental constraints on high pressure melting in subducted crust. *Earth and Planetary Science Letters* 188: 149–168.

Hermann, J. 2002. Allanite: thorium and light rare earth element carrier in subducted crust. *Chemical Geology* 192: 289–306.

Hezarkhani, A., Wiliams-Jones, A.E. and Gammons, C.H., 1999. Factors controlling copper solubility and chalcopyrite deposition in the Sungun porphyry copper deposit, Iran. *Mineralium Deposita* 34: 770–783.

Hikita, H., Ishikawa, H., and Esaka, N., 1973. Solubility and equilibrium of copper(I) chloride in hydrochloric acid solutions. *Nippon Kagaku Kaishi* 1973: 13–18.

Ho, P.C., Palmer, D.A. and Gruszkiewicz, M.S., 2001. Conductivity measurements of dilute aqueous HCl solutions to high temperatures and pressures using a flow-through cell. *Journal of Physical Chemistry* B105: 1260–1266.

Holland, H.D., 1972. Granites solutions and base metal deposits. *Economic Geology* 67: 281–301.

Holland, T. and Powell, R., 1991. A Compensated-Redlich-Kwong (CORK) equation for volumes and fugacities of CO_2 and H_2O in the range 1 bar to 50 kbar and 100–1600 °C. *Contributions to Mineralogy and Petrology* 109: 265–273.

Holland, T. and Powell, R., 1998, An internally consistent thermodynamic dataset for phases of petrologic interest. *Journal of Metamorphic Petrology* 16: 309–343.

Holland, T.J.B., Redfern, S.A.T., and Pawley, A.R., 1996. Volume behaviour of hydrous minerals at high pressure and temperature: II. Compressibilities of lawsonite, zoisite, clinozoisite and epidote. *American Mineralogist* 81: 341–348.

Hoisieni, K.R., Howald, R.A. and Scanlon, M.W., 1985. Thermodynamics of the lambda transition and the equation of state of quartz. *American Mineralogist* 70: 782–793.

Holmes, H.F., Busey, R.H. Simonson, J.M., Mesmer, R.E., Archer, D.G. and Wood, R.H., 1987. The enthalpy of dilution of $HCl_{(aq)}$ to 648 K and 40 MPa. Thermodynamic properties. *Journal of Chemical Thermodynamics* 19: 863–890.

Hurlen, T., 1961. Electrochemical behaviour of copper in acid solution. *Acta Chemica Scandinavica* 15: 1231–1238.

Ihlemann, J., 1992. Excimer laser ablation of fused silica. *Applied Surface Science* 54: 193–200.

Imai, A., Listanco, E.L. and Fujii, T., 1993. Petrologic and sulfur isotopic significance of highly oxidised and sulfur-rich magma of Mount Pinatubo, Philippines. *Geology* 21: 699–702.

Ito, E., Harris, D.M. and Anderson, A.T., 1983. Alteration of oceanic crust and geologic cycling of chlorine and water. *Geochimica et Cosmochimica Acta* 47: 1613–1624.

Jackson, I., 1976. Melting of the silica isotypes SiO_2, BeF_2 and GeO_2 at elevated pressures. *Physics of the Earth and Planetary Interiors* 13: 218–231.

Johnson, J.M., Oelkers, E.H. and Helgeson, H.C., 1992. SUPCRT92: a software package for calculating the standard molal thermodynamic properties of minerals, gases, aqueous species and reactions from 1 to 5000 bars and 0 ° to 1000 °C. *Computers and Geosciences* 18: 899–947.

Johnson, M.C. and Walker, D., 1993. Brucite [$Mg(OH)_2$] dehydration and the molar volume of water to 15 GPa. *American Mineralogist* 78: 271–284.

Johnson, K.E, Davis, A.M. and Bryndzia, L.T., 1996. Contrasting styles of hydrous metasomatism in the upper mantle: an ion microprobe investigation. *Geochimica et Cosmochimica Acta* 60: 1367–1385.

Joyce, D.B. and Holloway, J.R., 1993. An experimental determination of the thermodynamic properties of H_2O–CO_2–NaCl fluids at high pressures and temperatures. *Geochimica et Cosmochimica Acta* 57: 733–746.

Kau, L.-S., Spira-Solomon, D.J., Penner-Hahn, J.E., Hodgson, K.O. and Solomon, E.I., 1987. X-ray absorption edge determination of the oxidation state and coordination number of copper: application to the type 3 site in rhus vernicifera laccase and its reaction with oxygen. *Journal of the American Chemical Society* 109: 6433–6442.

Kay, R.W., 1980. Volcanic arc magmas: implications of a melting-mixing model for element recycling in the crust-upper mantle. *Journal of Geology* 88: 497–522.

Kennedy, G.C., 1950. A portion of the system silica-water. *Economic Geology* 45: 629–653.

Kennedy, G.C., Wasserburg, G.J., Heard, H.C. and Newton, R.C., 1962. The upper three-phase region in the system SiO_2–H_2O. *American Journal of Science* 260: 501–521.

Keppler, H., 1996. Constraints from partitioning experiments on the composition of subduction-zone fluids. *Nature* 380: 237–240.

Kerrick, D.M. and Jacobs, G.K., 1981. A modified Redlich-Kwong equation for H_2O, CO_2, and H_2O–CO_2 mixtures at elevated pressures and temperatures. *American Journal of Science* 281: 735–767.

Kielland, J., 1937. Individual activity coefficients of ions in aqueous solutions. *Journal of the American Chemical Society* 59: 1675–1678.

Lange, R.A. and Carmichael, I.S.E., 1987. Densities of Na_2O–K_2O–CaO–Fe_2O_3–Al_2O_3–TiO_2–SiO_2 liquids: New measurements and derived partial molar properties. *Geochimica et Cosmochimica Acta* 51: 2931–2946.

Lange, R.A. and Carmichael, I.S.E., 1990. Thermodynamic properties of silicate liquids with emphasis on density, thermal expansion and compressibility. *In,* Nicolls, J. and Russell, J.K (eds.): Modern Methods of Igneous Petrology: understanding magmatic processes. *Mineralogical Society of America, Reviews in Mineralogy* 24: 25–64.

Lasdon. L., Waren, A.D., Jain, A. and Ratner, M., 1978. Design and testing of a Generalised Reduced Gradient code for nonlinear programming. *ACM Transactions on Mathematical Software* 4(1): 34–50.

Larrieu, T.L. and Ayers, J.C., 1997. Measurements of the pressure-volume-temperature properties of fluids to 20 kbar and 1000 °C: A new approach demonstrated on H_2O. *Geochimica et Cosmochimica Acta* 61: 3121–3124.

Lindsay, W.T., Jr., 1980. Estimation of concentration quotients for ionic equilibria in high temperature water: The model substance approach. Abstract, 41st International Water Conference, pp. 284–294.

Liu, L. and Mernagh, T.P., 1990. Phase transitions and Raman spectra of calcite at high pressures and room temperature. *American Mineralogist* 75: 801–806.

Liu, W., McPhail, D.C. and Brugger, J., 2001a. An experimental study of copper(I)-chloride and copper(I)-actetate complexing in hydrothermal solutions between 50 °C and 250 °C and vapour-saturated pressure. *Geochimica et Cosmochimica Acta* 65: 2937–2948.

Liu, W., 2001b. *Hydrothermal geochemistry of copper in chloride and acetate brines.* Unpublished Ph.D. thesis, School of Earth Sciences, Monash University, Melbourne, Australia.

Liu, W., Brugger, J., McPhail, D.C. and Spiccia, L., 2002. A spectrophotometric study of aqueous copper(I)-chloride complexes in LiCl solutions between 100 °C and 250 °C. *Geochimica et Cosmochimica Acta* 66: 3615–3633.

Long, F.A. and Devit, W.F., 1952. Activity coefficients of non-electrolytes in aqueous electrolyte solutions. *Chemical Reviews* 51: 119–169.

Longerich, H.P., Jackson, S.E. and Günther, D., 1996. Laser ablation inductively coupled plasma mass spectrometric transient signal data acquisition and analyte concentration calculation. *Journal of Analytical and Atomic Spectrometry* 11: 899–904.

Loucks, R.R., Eggins, S.M., Shelley, J.M.G. and Kinsley, L.P.J., 1995. Development of the inductively-coupled-plasma mass-spectrometry ultraviolet-laser trace-element micro-analyzer (ICPMS-ULTEMA). In, *Research School of Earth Sciences Annual Report, The Australian National University*, pp. 138–140.

Loucks, R.R. and Mavrogenes, J.A., 1999. Gold solubility in hydrothermal brines measured in synthetic fluid inclusions. *Science* 284: 2159–2101.

Lowell, J.D. and Guilbert, J.M., 1970. Lateral and vertical alteration-mineralisation zoning in porphyry ore deposits. *Economic Geology* 65: 373–408.

Luce, R.W., Cygan, G.L., Hemley, J.J. and D'Angelo, W.M., 1985. Some mineral solubility relations in the system CaO–MgO–SiO_2–H_2O–HCl. *Geochimica et Cosmochimica Acta* 49: 525–538.

Luhr, J.F., Carmichael, I.S.E. and Varekamp, J.C., 1984. The 1982 eruption of El Chichón volcano, Chiapas, Mexico: mineral and petrology of anhydrite-bearing pumices. *Journal of Volcanology and Geothermal Research* 23: 69–108.

Luhr, J.F, 1990. Experimental phase relations of water- and sulfur-saturated arc magmas and the 1982 eruptions of El Chichón volcano. *Journal of Petrology* 31: 1071–1114.

McCulloch, M.T. and Gamble, J.A., 1991. Geochemical and geodynamical constraints on subduction zone magmatism. *Earth and Planetary Science Letters* 102: 358–374.

McDade, P., Wood, B.J., Van Westrenen, W., Brooker, R., Gudmundsson, G., Soulard, H., Najorka, J., and Blundy, J., 2002. Pressure corrections for a selection of piston–cylinder cell assemblies. *Mineralogical Magazine* 66: 1021–1028.

Manning, C.E., 1994. The solubility of quartz in H_2O in the lower crust and upper mantle. *Geochimica et Cosmochimica Acta* 58: 4831–4839.

Manning, C.E. and Boettcher, S.L., 1994. Rapid-quench hydrothermal experiments at mantle pressures and temperatures. *American Mineralogist* 79: 1153–1158.

Mao, H., Sundman, B., Wang, Z. and Saxena, S.K., 2001. Volumetric properties and phase relations of silica – thermodynamic assessment. *Journal of Alloys and Compounds* 327: 253–262.

Marshall, W.L. and Quist, A.S., 1967. A representation of isothermal ion-ion pair solvent equilibria independent of changes in the dielectric constant. *Proceedings of the National Academy of Sciences of The United States of America* 58: 901–906.

Marshall, W.L., 1970. Complete equilibrium constants, electrolyte equilibria and reaction rates. *Journal of Physical Chemistry* 74: 346–355.

Marshall, W.L., 1972. A further description of complete equilibrium constants. *Journal of Physical Chemistry* 76: 720–731.

Marshall, W.L. and Franck, E.U., 1981. Ion product of water substance, 0–1000 °C, 1–10,000 bars, new international formulation and its background. *Journal of Physical and Chemical Reference Data* 10: 295–304.

Marshall, W.L. and Mesmer, R.E., 1984. Pressure-density relationships and ionisation equilibria in aqueous solutions. *Journal of Solution Chemistry* 13: 383–391.

Mavrogenes, J.A., Bodnar, R.J., Anderson, A.J., Bajt, S., Sutton, S.R. and Rivers, M.L., 1995. Assessment of the uncertainties and limitations of quantitative elemental analysis of individual fluid inclusion using synchrotron X-ray fluorescence. *Geochimica et Cosmochimica Acta* 59: 3987–3995.

Mavrogenes, J.A., Berry, A.J., Newville, M. and Sutton, S.R., 2002. Copper speciation in vapour-phase inclusions from the Mole Granite, Australia. *American Mineralogist* 87: 1360–1364.

Mayanovic, R.A., Anderson, A.J. and Bajt, S., 1995. Development of micro-XAFS: Applications to studies of single fluid inclusions. *Physica B* 208&209: 239–240.

Mayanovic, R.A., Anderson, A.J. and Bajt, S., 1997. Microbeam XAFS studies on fluid inclusions on fluid inclusions at high temperatures. *Journal de Physique* IV, C2: 1029–1030.

Meinert, L.D., Hefton, K.K., Mayes, D. and Tasiran, I., 1997. Geology, zonation, and fluid evolution of the Big Gossan Cu–Au skarn deposit, Ertsberg District, Irian Jaya. *Economic Geology* 92: 509–534.

Mesmer, R.E., Marshall, W.L., Palmer, D.A., Simonson, J.M. and Holmes, H.F., 1988. Thermodynamics of aqueous association and ionisation reactions at high temperatures and pressures. *Journal of Solution Chemistry* 17: 699–718.

Mesmer, R.E., Patterson, C.S., Busey, R.H. and Holmes, H.F., 1989. Ionisation of acetic acid in NaCl(aq) media: A potentiometric study to 573 K and 130 bar. *Journal of Physical Chemistry* 93: 7483–7490.

Moissette, A., Shepherd, T. J. and Chenery, S. R., 1996. Calibration Strategies for the Elemental Analysis of Individual Aqueous Fluid Inclusions by Laser Ablation Inductively Coupled Plasma Mass Spectrometry. *Journal of Analytical and Atomic Spectrometry* 11: 667–674.

Mountain, B.W. and Seward, T.M., 1999. The hydrosulfide/sulfide complexes of copper(I): Experimental determination of stoichiometry and stability at 22 °C and reassessment of high temperature data. *Geochimica et Cosmochimica Acta* 63: 11–29.

Moore, W.J. and Nash, J.T., 1974. Alteration and fluid inclusion studies of the porphyry copper ore body at Bingham, Utah. *Economic Geology* 69: 631–645.

Morris, J. and Tera, F., 1989. ^{10}Be and ^{9}Be in mineral separates and whole rocks from volcanic arcs: implications for sediment subduction. *Geochimica et Cosmochimica Acta* 53: 3197–3206.

Müller, B. and Seward, T.M., 2001. Spectrophotometric determination of the stability of tin(II) chloride complexes in aqueous solution up to 300 °C. *Geochimica et Cosmochimica Acta* 65: 4187–4199.

Mysen, B.O. and Acton, A., 1999. Water in H_2O-saturated magma-fluid systems: Solubility behaviour in K_2O–Al_2O_3–SiO_2–H_2O to 2.0 GPa and 1300 °C. *Geochimica et Cosmochimica Acta* 63: 3799–3815.

Mysen, B.O. and Wheeler, K., 2000. Aluminosilicate-saturated aqueous fluids in the Earth's upper mantle. *Geochimica et Cosmochimica Acta* 64: 4243–4256.

Mysen, B.O., 2002. Solubility behaviour of alkaline earth and alkali aluminosilicate components in aqueous fluids in the Earth's upper mantle. *Geochimica et Cosmochimica Acta* 66: 2421–2438.

Nakai, I., Sugitani, Y., Nagashima, K. and Niwa, Y., 1978. X-ray photoelectron spectroscopic study of copper minerals. *Journal of Inorganic Nuclear Chemistry* 40:789–791.

Nakamura, Y., 1974. The system SiO_2–H_2O–H_2 at 15 kbar. *Carnegie Institution of Washington Yearbook* 73: 259-263.

NBS, 1970. *Trace elements in glass SRMs: 610 through 619, inclusive*. National Bureau of Standards (Certificate), 1–4.

Newton, R.C. and Manning, C.M., 2000. Quartz solubility in H_2O–NaCl and H_2O–CO_2 solutions at deep crust-upper mantle pressures and temperatures: 2–15 kbar and 500–900 °C. *Geochimica et Cosmochimica Acta* 17: 2993–3005.

Newton, R.C. and Manning, C.M., 2002. Solubility of enstatite + forsterite in H_2O at deep crust/upper mantle conditions: 4 to 15 kbar and 700 to 900 °C. *Geochimica et Cosmochimica Acta* 66: 4165–4176.

Nordstrom, D.K. and Munoz, J.L., 1994. *Geochemical thermodynamics*, 2nd edition. Blackwell Scientific Publications, Boston, 493pp.

Noyes, A.A. and Chow, M., 1918. The potentials of the bismuth-bismuthoxy chloride and copper -cuprous-chloride electrodes. *Journal of the American Chemical Society* 40: 739–763.

Ochs, F.A. III, and Lange, R.A., 1997. The density of hydrous magmatic liquids, *Science* 283:1314–1317.

Oelkers, E.H. and Helgeson, H.C., 1990. Triple ion anions and polynuclear complexing in supercritical electrolyte solutions. *Geochimica et Cosmochimica Acta* 54: 727–738.

Oelkers, E.H. and Helgeson, H.C., 1991. Calculation of activity coefficients and degrees of formation of neutral ion pairs in supercritical electrolyte solutions. *Geochimica et Cosmochimica Acta* 55: 1235–1251.

Ono, S., 1998. Stability limits of hydrous minerals in sediment and mid-ocean ridge basalt compositions: implications for water transport in subduction zones. *Journal of Geophysical Research* 103: 18253–18267.

Palladino, L., Della Longa, S., Reale, A., Belli, M., Scafati, A., Onori, G. and Santucci, A., 1993. X-ray absorption near edge structure (XANES) of Cu(II)-ATP and related compounds in solution: quantitative determination of the distortion of the Cu site. *Journal of Chemical Physics* 98: 2720–2726.

Palmer, D.A. and Wesolowski, D., 1997. Potentiometric measurements of the first hydrolysis quotient of magnesium (II) to 250 °C and 5 molal ionic strength (NaCl). *Journal of Solution Chemistry* 26: 217–232

Parkinson, I.J. and Arculus, R.J., 1999. The redox state of subduction zones: insights from arc-peridotites. *Chemical Geology* 160: 409–423.

Pawley, A.R., Redfern, S.A.T., and Holland, T.J.B., 1996. Volume behaviour of hydrous minerals at high pressure and temperature: I. Thermal expansion of lawsonite, zoisite, clinozoisite and diaspore. *American Mineralogist* 81: 335–340.

Pawley, A.R., 1994. The pressure and temperature stability limits for lawsonite: Implications for H_2O recycling in subduction zones. *Contributions to Mineralogy and Petrology* 118: 99–108.

Pearce, J.A. and Peate, D.W., 1995. Tectonic implications of the composition of volcanic arc magmas. *Annual Review of Earth and Planetary Science* 23: 251–285.

Pearce, N.J.G., Perkins, W.T., Westgate. J.A., Gorton, M.P., Jackson, S.E., Neal, C.R. and Chenery, S.P., 1997. A compilation of new and published major and trace element data for NIST SRM 610 and NIST SRM 612 glass reference materials. *Geostandards Newsletter* 21: 115–144.

Perfit, M.R., Gust, D.A., Bence, A.E., Arculus, R.J. and Taylor, S.R., 1980. Chemical characteristics of island-arc basalts: implications for mantle sources. *Chemical Geology* 30: 227–265.

Pettke, T., Heinrich, C.A., Ciocan, A.C. and Günther, D., 2000. Quadrupole mass spectrometry and optical emission specroscopy: detection capabilities and representative sampling of short transient signals from laser ablation. *Journal of Analytical and Atomic Spectrometry* 15: 1149–1155.

Plank, T. and Langmuir, C.E., 1993. Tracing elements from sediment input to volcanic output at subduction zones. *Nature* 362: 739–743.

Pokrovskii, V.A., 1999. Calculation of the standard partial molal thermodynamic properties and dissociation constants of aqueous HCl^0 and HBr^0 at temperatures to 1000 °C and pressures to 5 kbar. *Geochimica et Cosmochimica Acta* 63: 1107–1115.

Potts, P.J., 1987. A handbook of silicate rock analysis. Chapman and Hall. 622 pp.

Pownceby, M.I. and O'Neill, H.SC., 2000. Thermodynamic data from redox reactions at high temperatures. VI. Thermodynamic properties of CoO–MnO solid solutions from emf measurements. *Contributions to Mineralogy and Petrology* 140: 28–39.

Pownceby, M.I. and O'Neill, H.SC, 1995. Thermodynamic data from redox reactions at high–temperatures. 5. Thermodynamic properties of NiO–MnO solid-solutions from emf-measurements. *Contributions to Mineralogy and Petrology* 119: 409–421.

Pownceby, M.I. and O'Neill, H.SC., 1994. Thermodynamic data from redox reactions at high–temperatures. 3. Activity–composition relations in Ni–Pd alloys from emf–measurements at 850–1250 K, and calibration of the NiO+Ni–Pd assemblage as a redox sensor. *Contributions to Mineralogy and Petrology* 116: 327–339.

Quist. A.S., 1970. The ionisation constant of water to 800 °C and 4000 bars. *Journal of Physical Chemistry* 74: 3393–3402.

Reardon, E.J. and Langmuir, D., 1976. Activity coefficients of $MgCO_3^0$ and $CaSO_4^0$ ion pairs as a function of ionic strength. *Geochimica et Cosmochimica Acta* 40: 549–554.

Reinecke, T., 1991. Very-high-pressure metamorphism and uplift of coesite-bearing metasediments from the Zermatt-Saas zone, Western Alps. *European Journal of Mineralogy* 3: 7–17.

Reynolds, T.J. and Beane, R.E., 1985. Evolution of hydrothermal fluid characteristics at the Santa Rita, New Mexico, porphyry copper deposit. *Economic Geology* 80: 1328–1347.

Ringwood, A.E., 1990. Slab-mantle interactions 3. Petrogenesis of intraplate magmas and the structure of the upper mantle. *Chemical Geology* 82: 187–207.

Robinson, R.A. and Bates, R.G., 1971. Disssociation constant of hydrochloric acid from partial vapour pressures over hydrogen chloride-lithium chloride solution. *Analytical Chemistry* 43: 969–970.

Roedder, E., 1971. Fluid inclusion studies on the porphyry-type deposits of Bingham, Utah, Butte, Montana, and Climax, Colorado. *Economic Geology* 66: 81–120.

Roedder, E., 1984. Fluid inclusions. *Reviews in Mineralogy* 12, 644 pp.

Romberger, S.B. and Barnes, H.L., 1970. Ore solution chemistry II. Solubility of CuS in sulfide solutions. *Economic Geology* 65: 901–919.

Rose, A.W., 1970. Zonal relations of wallrock alteration and sulfide distribution at porphyry copper deposits. *Economic Geology* 65: 920–936.

Rose, A.W. and Burt, D.M., 1979. Hydrothermal Alteration. *In*, Barnes, H.L. (ed): *Geochemistry of hydrothermal ore deposits, 2nd edn.* John Wiley and Sons, New York, pp: 173–235.

Ruaya, J.R. and Seward, T.M., 1987. The ion-pair constant and other thermodynamic properties of HCl up to 350 °C. *Geochimica et Cosmochimica Acta* 51: 121–130.

Ruaya, J.R., 1988. Estimation of instability constants of metal chloride complexes in hydrothermal solutions up to 300 °C. *Geochimica et Cosmochimica Acta* 52: 1983–1996.

Rudnick, R.L., Barth, M., Horn, I., and McDonough, W.F., 2000. Rutile-bearing refractory eclogites; missing link between continents and depleted mantle. *Science* 287: 278–281.

Ryan, C.G., Heinrich, C.A., van Achterbergh, E., Ballhaus, C. and Mernagh, T.P., 1995. Microanalysis of ore-forming fluids using the scanning proton microprobe. *Nuclear Instruments and Methods in Physics Research B* 104: 182–190.

Ryan, C.G., McInnes, B.I.A., Williams, P.J., Dong, G., Win, T.T., Yeats, C.J., 2001. Imaging fluid inclusion content using the new CSIRO-GEMOC nuclear microprobe. *Nuclear Instruments and Methods in Physics Research B* 181: 570–577.

Ryerson, F.J. and Watson, E.B., 1987. Rutile saturation in magmas: implications for Ti–Nb–Ta depletion in island arc basalts. *Earth and Planetary Science Letters* 86: 225–239.

Saccocia, P.J. and Seyfried, Jr., W.E., 1990. Talc quartz equilibria and the stability of magnesium chloride complexes in NaCl–$MgCl_2$ solutions at 300, 350 and 400 °C, 500 bars. *Geochimica et Cosmochimica Acta* 54: 3283–3294.

Sawkins, F.J., 1972. Sulfide ore deposits in relation to plate tectonics. *Journal of Geology* 80: 377–397.

Sawkins, F.J., 1984. *Metal deposits in relation to plate tectonics* (Minerals and rocks no.17). Amsterdam, Elsevier, 325 pp.

Sawkins, F.J. and Scherkenbach, D.A, 1981. High copper content in fluid inclusions in quartz from northern Sonora: Implications for ore genesis theory. *Geology* 9: 37–40.

Saul, A. and Wagner, W., 1989. A fundamental equation for water covering the range from the melting line to 1273 K at pressures up to 25000 MPa. *Journal of Physical and Chemical Reference Data* 18: 1537–1564.

Schäfer, B., Frischknecht, R., Gunther, D. and Dingwell, D.B., 1999. Determination of trace-element partitioning between fluid and melt using LA-ICP-MS analysis of synthetic fluid inclusions in glass. *European Journal of Mineralogy* 11: 415–426.

Schiano, P., Clocchiatti, N., Shimizu, N., Maury, R.C., Jochum, K.P. and Hoffman, A.W., 1995. Hydrous silica-rich melts in the sub-arc mantle and their relationship with erupted arc magmas. *Nature* 377: 595–600.

Schmidt, M.W. and Poli, S., 1994. The stability of lawsonite and zoisite at high pressures: Experiments in CASH to 92 kbar and implications for the presence of hydrous phases in subducted lithosphere. *Earth and Planetary Science Letters* 124: 105–118.

Schimdt, M.W., 1996. Experimental constraints on recycling of potassium from subducted oceanic crust. *Science* 272: 1927–1930.

Schertl, H.-P., Schreyer, W. and Chopin, C., 1991. The pyrope-coesite rocks and their country-rocks at Parigi, Dora Maira Massif, Western Alps: detailed petrography, mineral chemistry and *PT* path. *Contributions to Mineralogy and Petrology* 108: 1–21.

Setchénow, M. 1892. Action de l'acide carbonique sur les solutions des sels à acids forts. *Annales de Chimie et de Physique* 25: 225–270.

Seward, T.M., 1976. The stability of chloride complexes of silver in hydrothermal solutions up o 350 °C. *Geochimica et Cosmochimica Acta* 40: 1329–1341.

Seward, T.M. and Barnes, H.L., 1997. Metal transport by hydrothermal ore fluids. *In*, Barnes, H.L. (ed.), *Geochemistry of hydrothermal Ore Deposits*, 3rd edition, pp. 435–486. New York: Wiley–Interscience.

Seyfried, W.E. and Ding, K., 1993. The effect of redox on the relative solubilities of copper and iron in Cl-bearing aqueous fluids at elevated temperatures and pressures: An experimental study with application to seafloor hydrothermal systems. *Geochimica et Cosmochimica Acta* 57: 1905–1917.

Shatsky, V.S., Sobolev, N.V. and Vavilov, M.A. 1995. Diamond-bearing metamorphic rocks of the Kokchetav Massif (Northern Kazakhstan). *In*, Coleman, R.G. and Wang, X. (eds), *Ultra-high pressure metamorphism*. Cambridge University Press, Cambridge, pp. 427–455.

Shatsky, V.S., Jagoutz, E., Sobolev, N.V., Kozmenko, O.A., Parkhomenko, V.S. and Troesch, M. 1999. Geochemistry and age of ultrahigh pressure metamorphic rocks from the Kokchetav Massif (Northern Kazakhstan). *Contributions to Mineralogy and Petrology* 137: 185–205.

Shannon, R.D., 1976. Revised effective ionic radii and systematic studies of interatomic distances in halides and chalcogenides. *Acta Crystallographica* A32: 751–767.

Sharma, V.K. and Millero, F.J., 1990. Equilibrium constants for the formation of Cu(I) halide complexes. *Journal of Solution Chemistry* 19:375–390.

Shea, D. and Helz, G., 1988. The solubility of copper in sulfidic waters: sulfide and polysulfide complexes in equilibrium with covellite. *Geochimica et Cosmochimica Acta* 52: 1815–1825.

Shea, D. and Helz, G., 1989. Solubility product constants of covellite and a poorly crystalline copper sulfide precipitate at 298K. *Geochimica et Cosmochimica Acta* 53: 229–236.

Shen, A.H. and Keppler, H., 1997. Direct observation of complete miscibility in the albite–H_2O system. *Nature* 385: 710–712.

Sheppard, S.M.F., Nielsen, R.L. and Taylor, H.P., 1969. Oxygen and hydrogen isotope ratios of clay minerals from porphyry copper deposits. *Economic Geology* 64: 755–777.

Sheppard, S.M.F., Nielsen, R.L. and Taylor, H.P., 1971. Hydrogen and oxygen isotope ratios in minerals from porphyry copper deposits. *Economic Geology* 66: 515–542.

Shettel, D.L., 1974. The solubility of quartz in supercritical H_2O–CO_2 fluids. M.S thesis, The Pennsylvania State University.

Shmulovich, K.I. and Churakov, S.V., 1998. Natural fluid phases at high temperature and low pressures. *Journal of Geochemical Exploration* 62: 183–191.

Shmulovich, K.I. and Graham, C.M., 1999. An experimental study of phase equilibria in the system H_2O–CO_2–NaCl at 800 °C and 9 kbar. *Contributions to Mineralogy and Petrology* 136: 247–257.

Shock, E.L., Sassani, D.C., Willis, M. and Sverjensky, D.A., 1997. Inorganic species in geologic fluids: Correlations among standard molal thermodynamic properties of aqueous ions and hydroxide complexes. *Geochimica et Cosmochimica Acta* 61: 907–950.

Shulman, R.G., Yafet, Y., Eisenberger, P. and Blumberg, W.E., 1976. Observation and interpretation of x-ray absorption edges of iron compounds and proteins. *Proceedings of the National Academy of Science* 73: 1384–1388.

Sillitoe, R.H., 1972. A plate tectonic model for the origin of porphyry copper deposits. *Economic Geology* 67: 184–197.

Sillitoe, R.H., 1973. The tops and bottoms of porphyry copper deposits. *Economic Geology* 68: 799–815.

Sillitoe, R.H., 1975. Subduction and porphyry copper deposits in southwestern North America - a reply to recent objections. *Economic Geology* 70: 1474–1483.

Sillitoe, R.H., 1994. Erosion and collapse of volcanoes: causes of telescoping in intrusion-centred ore deposits. *Geology* 22: 945–948.

Sillitoe, R.H., 1999. Styles of high-sulfidation gold, silver and copper mineralisation in porphyry and epithermal environments. In, *Proceedings of the Pacific Rim conference '99*; Bali, Indonesia, Australasian Institute of Mining and Metallurgy, pp: 399–403.

Simonson, J.M. and Palmer D.A., 1993. Liquid-vapor partitioning of $HCl_{(aq)}$ to 350 °C. *Geochimica et Cosmochimica Acta* 57: 1–7.

Smith, S. and Lasdon, L., 1992. Solving large sparse nonlinear programs using GRG. *ORSA Journal on Computing* 4: 1.

Sorenson, S.S., Grossman, J.N. and Perfit, M.R., 1997. Phengite-hosted LILE enrichment in eclogite and related rocks: implications for fluid-mediated mass transfer in subduction zones and arc magma genesis. *Journal of Petrology* 38: 3–34.

Sourirajan, S. and Kennedy, G.C., 1962. The system H_2O–NaCl at elevated temperatures and pressures. *American Journal of Science* 260: 115–1411.

Sretenskaya, N.G., 1992. The dissociation constants of hydrochloric acid from the electrical conductance data for HCl solutions in water-dioxane mixtures. *Geokhimiya* 447–453 (*in Russian*).

Stalder, R., Ulmer, P., Thompson, A.B. and Günther, D., 2000. Experimental approach to constrain second critical end points in fluid/silicate systems: near-solidus fluids and melts in the system albite-H_2O. *American Mineralogist* 85: 68–77.

Sterner, S.M. and Bodnar, R.J., 1991. Synthetic fluid inclusions. X: Experimental determination of P–V–T–X properties in the CO_2–H_2O system to 6 kb and 700 °C. *American Journal of Science* 291: 1–54.

Sterner, S.M., 1992. Synthetic fluid inclusions: Part XI. Notes on the application of synthetic fluid inclusions to high *P–T* experimental aqueous geochemistry. *American Mineralogist* 77: 156–167.

Stoffregen, R., 1987. Genesis of acid-sulfate alteration and Au–Cu–Ag mineralisation at Summitville, Colorado. *Economic Geology* 82: 1575–1591.

Streck, M.J. and Dilles J.H., 1998. Sulfur evolution of oxidised arc magmas as recorded in apatite from a porphyry copper batholith. *Geology* 26: 523–526.

Student, J.J. and Bodnar, R.J., 1999. Synthetic fluid inclusions XIV; coexisting silicate melt and aqueous fluid inclusions in the haplogranite–H_2O–NaCl–KCl system. *Journal of Petrology*. 40: 1509–1525.

Sugasaka, K. and Fujii, A., 1976. A spectrophotometric study of copper(I) chloro-complexes in aqueous 5M Na(Cl,ClO_4) solutions. *Bulletin of the Chemical Society of Japan* 49: 82–86.

Sukhova T.G., Temkin, O.N., Flid, R.M. and Kaliya, T.K., 1969. Determination of the composition and stability of constants of chloro-cuprate(I) complexes in concentrated solutions. *Russian Journal of Inorganic Chemistry* 13: 1072–1076.

Sutton, S.R., Jones, K.W., Gordon, B., Rivers, M.L., Bajt, S. and Smith, J.V., 1993. Reduced chromium in olivine grains from lunar basalt 15555: X-ray absorption near edge structure (XANES). *Geochimica et Cosmochimica Acta* 57: 461–468.

Sverjensky, D.A., Hemely, J.J., D'Angelo, M., 1991. Thermodynamic assessment of hydrothermal alkali feldspar-mica-aluminosilicate equilibria. *Geochimica et Cosmochimica Acta* 55: 989–1004.

Sverjensky, D.A., Shock, E.L. and Helgeson, H.C., 1997. Prediction of the thermodynamic properties of aqueous metal complexes to 1000 °C and 5 kb. *Geochimica et Cosmochimica Acta* 61: 1359–1421.

Sweeton, F.H., Mesmer, R.E. and Beas, C.F., 1974. Acidity measurements at elevated temperatures. VII. Dissociation of water. *Journal of Solution Chemistry* 3: 191–214.

Symonds, R.B., Rose, W.I., Bluth, G.J.S. and Gerlach, T.M., 1994. Volcanic-gas studies: methods, results and applications. *In*, Carroll, M.R. and Holloway, J.R. (eds), Volatiles in magmas. *Mineralogical Society of America, Reviews in Mineralogy* 30: 1–66.

Tagirov, B.R., Zotov, A.V. and Akinfiev, N.N., 1997. Experimental study of dissociation of HCl from 350 to 500 °C and 500 to 2500 bars: Thermodynamic properties of $HCl^0_{(aq)}$. *Geochimica et Cosmochimica Acta* 61: 4267–4280.

Tanger, J.C. and Helgeson, H.C., 1988. Calculation of the thermodynamic and transport properties of aqueous species at high pressures and temperature: Revised equations of state for the standard partial molal properties of ions and electrolytes. *American Journal of Science* 288: 19–98.

Tatsumi, Y., 1989. Migration of fluid phases and genesis of basalt magmas in subduction zones. *Journal of Geophysical Research* 49: 179–190.

Taylor, H.P., 1974. The application of oxygen and hydrogen isotope studies to problems of hydrothermal alteration and ore deposition. *Economic Geology* 69: 843–883.

Taylor, J.R., Wall, V.J., and Pownceby, M.I., 1992. The calibration and application of accurate redox sensors. *American Mineralogist* 77: 284–295.

Thompson, R.A. and Helz, G.R., 1994. Copper speciation in sulfidic solutions at low sulfur activity: Further evidence for cluster complexes? *Geochimica et Cosmochimica Acta* 58: 2971–2983.

Titley, S.R. and Beane, R.E., 1981. Porphyry copper deposits. Part 1. Geologic settings, petrology and tectogenesis. *Economic Geology 75th Anniversary volume*, pp. 214–235.

Tribuzio, R., Messiga, B., Vannucci, R. Bottazzi, P., 1996. Rare element redistribution during high-pressure low-temperature metamorphism in ophiolitic Fe-gabbros (Liguria, northwestern Italy): implications for light REE mobility in subduction zones. *Geology* 24: 711–714.

Ulrich, T., Günther, D. and Heinrich, C.A., 1999. Gold concentrations of magmatic brines and the metal budget of porphyry copper deposits. *Nature* 399: 676–679.

Ulrich, T., Günther, D. and Heinrich, C.A, 2001. The evolution of a porphyry Cu–Au deposit based on LA-ICP-MS analysis of fluid inclusions: Bajo de la Alumbrera, Argentina. *Economic Geology* 96: 1743–1771.

van der Laan, G., Pattrick, R.A.D., Henderson, C.M.B. and Vaughan, D.J., 1992. Oxidation state variations in copper minerals studied with Cu *2p* X-ray absorption spectroscopy. *Journal of the Physical Chemistry of Solids* 53: 1185–1190.

Var'yash, L.N. and Rekharshiy, V.I., 1982. Behaviour of Cu(I) complexing in chloride solutions. *Geochemistry International* 18: 61–67. (*translated from Russian*)

Var'yash, L.N., 1990. Equilibria in the $Cu–Cu_2O–H_2O$ system at 150–450 °C. *Geochemistry International* 27: 80–90, (*translated from Russian*).

Var'yash, L.N., 1992. Cu(I) complexing in NaCl solutions at 300 and 350 °C. *Geochemistry International* 29: 84–92, (*translated from Russian*).

Wagner, W., Saul, A. and Pruß, A., 1994. International equations for the pressure along the melting and along the sublimation curve of ordinary water substance. *Journal of Physical and Chemical Reference Data* 23: 515–525.

Walther, J.V. and Helgeson, H.C., 1977. Calculation of the thermodynamic properties of aqueous silica and the solubility of quartz and its polymorphs at high pressures and temperatures. *American Journal of Science* 277: 1315–1351.

Walther, J.V. and Orvillle, P.M., 1983. The extraction–quench technique for the determination of the thermodynamic properties of solute complexes: application to quartz solubility in fluid mixtures. *American Mineralogist* 68: 731–741.

Walther, J.V. and Schott, J., 1988. The dielectric constant approach to speciation and ion pairing at high temperature and pressure. *Nature* 332: 635–638.

Walther, J.V., 1991. Determining the thermodynamic properties of solutes in crustal fluids. *American Journal of Science* 291: 453–472.

Walther, J.V., 1997a. Determination of activity coefficients of neutral species in supercritical H_2O fluids. *Geochimica et Cosmochimica Acta* 61: 3311–3318.

Walther, J.V., 1997b. Experimental determination and interpretation of the solubility of corundum in H_2O between 350 and 600 °C from 0.5 to 2.2 kbar. *Geochimica et Cosmochimica Acta* 61: 4955–4964.

Wasserman, E., Wood, B. and Davies, A., 1995. Equation state for aqueous silica species at pressures from 1 bar to 20 kbar and temperatures from 25 ° to 900 °C based on simulated values of the dielectric constant. *Chemical Geology* 121: 3–9.

Waychunas, G.A., Apted, M.J. and Brown Jr., G.E., 1983. X-ray K-edge absorption spectra of Fe minerals and model compounds: near edge-structure. *Physics and Chemistry of Minerals* 10: 1–9.

Weill, D.F. and Fyfe, W.S., 1964. The solubility of quartz in H_2O in the range 1000–4000 bars and 400–550 °C. *Geochimica et Cosmochimica Acta* 28: 1243–1255.

Whitney, J.A., Hemley, J.J., and Simon, F.O., 1985. The concentration of iron in chloride solutions equilibrated with synthetic granitic conditions: The sulfur-free system. *Economic Geology* 80: 444–460.

Wilson, G.A., 1986. *Cassiterite solubility and tin-chloride speciation in supercritical solutions*. Unpublished Ph.D. thesis, John Hopkins University, Baltimore, USA.

Withers, A.C., Kohn, S.C., Brooker, R.A. and Wood, B.J., 2000. A new method for determining the P–V–T properties of high–density H_2O using NMR: Results at 1.4–4.0 GPa and 700–1100 °C. *Geochimica et Cosmochimica Acta* 64: 1051–1057.

Wong, J., Lytle, F.W., Messmer, R.P., and Maylotte, D.H., 1984. *K*-edge absorption spectra of selected vanadium compounds. *Physical Review B* 30: 5596–5609.

Wood, B.J. and Virgo, D., 1989. Upper mantle oxidation state: ferric iron contents of lherzolite spinels by ^{57}Fe Mössbauer spectroscopy and resultant oxygen fugacities. *Geochimica et Cosmochimica Acta* 53: 1277–1291.

Wood, S.A. and Crerar, D.A., 1985. A numerical method for obtaining multiple linear regression parameters with physically realistic signs and magnitudes: Application to the determination of equilibrium constants from solubility data. *Geochimica et Cosmochimica Acta* 49: 165–172.

Wood, S.A., Crerar, D.A. and Borcsik, M.P., 1987. Solubility of the assemblage pyrite-pyrrhotite-magnetite-sphalerite-galena-gold-stibnite-bismuthinite-argentite-moybedenite in H_2O–NaCl–CO_2 solutions from 200 to 350 °C. *Economic Geology* 82: 1864–1887.

Xiao, Z., Gammons, C.H., and Williams, A.E., 1998. Experimental study of copper(I) chloride complexing in hydrothermal solutions at 40 to 300 °C and saturated water vapour pressure. *Geochimica et Cosmochimica Acta* 62: 2949–2964.

Xie, Z. and Walther, J.V., 1993. Quartz solubilities in NaCl solutions with and without wollastonite at elevated temperatures and pressures. *Geochimica et Cosmochimica Acta* 57: 1947–1955.

Zack, T., Rivers, T. and Foley, S.F., 2001. Cs–Rb–Ba systematics in phengite and amphibole: an assessment of fluid mobility at 2.0 GPa in eclogites from Trescolmen, Central Alps. *Contributions to Mineralogy and Petrology* 140: 651–669.

Zack, T., Kronz, A., Rivers, T. and Foley, S.F., 2002. Trace element abundances in rutiles from eclogites and associated mica schists. *Chemical Geology* 184: 97–122.

Zhang, Y-G. and Frantz, J.D., 2000. Enstatite-forsterite-water equilibria at elevated temperatures and pressures. *American Mineralogist* 85: 918–925.

Ziegler, K.J., Lasdon, L., Chlistunoff, J. and Johnston, K.P., 1999. Optimisation models for determining nitric acid equilibria in supercritical water. *Computers and Chemistry* 23: 421–434.

Zotov, A.V., Baranova, N.N., Daryina, T.G. and Bannykh, L.N., 1990. Solubility of gold in aqueous chloride fluids at 350–500 °C, 500–1500 atm pressure and thermodynamic properties of $AuCl_2^-$ (sol) up to 750 °C and 5000 atm. *Geokhimiya*, 979–987, (*in Russian*).

Zotov, N. and Keppler, H., 2000. In–situ Raman spectra of dissolved silica species in aqueous fluids to 900 °C and 14 kbar. *American Mineralogist* 85: 600–604.

Zotov, N. and Keppler, H., 2002. Silica speciation in aqueous fluids at high pressures and high temperatures. *Chemical Geology* 184: 71–82.